Structural and Defect Properties of Strontium Titanate

Alastair George Hartley Smith

A dissertation submitted for the degree of
Doctor of Philosophy
of the
University College London.

Department of Chemistry

2011

Declaration

I, Alastair George Hartley Smith confirm that the work presented in this thesis is my own, except where indicated. Where information has been derived from other sources, I confirm that this has been indicated in the thesis.

Signed: . . . . . .

Abstract

Strontium titanate is a material of considerable interest, with many applications. Though it has been extensively studied experimentally and computationally, there are unresolved issues regarding the structure and defect properties. Experimental examination is challenging due to the propensity of the material to form small domains. Even when single crystals are available, the observed behaviour is an average of these local domains.

In this thesis we undertook an extensive computational investigation of strontium titanate. The material is known to undergo a second order phase transition from cubic ($Pm\bar{3}m$) to tetragonal ($I4/mcm$) at ~ 105 K. We began the investigation by examining the tetragonal phase. Using plane-wave DFT with the LDA, PBE and PBEsol density functionals, we mapped out in three dimensions the $I4/mcm$ space group and fitted the resultant potential energy surfaces to polynomials. Extensive analysis was performed and expectation values for the 0 K octahedral rotation angle were calculated as being between 4.6° and 6.1° for the three functionals.

We continued by carrying out an extensive study, where we examined many different low symmetry saddle points, and minima using the PBEsol functional (which was found to have produced the best results). A total of 38 structures (many of which are unique) were examined in detail and the vibrational and imaginary modes involved in the transitions between higher and lower symmetry structures were identified and described. We identified the lowest energy structure as being monoclinic, with a rhombohedral structure at slightly higher energy. We also note that, as the energy differences are so small between these lower symmetry structures (~ 0.1 meV per formula unit), it is unlikely that these phases will appear in nature.

In the final results chapter we present three new sets of classical pair potentials for modelling strontium titanate. We applied these potentials to model vacancy type defects and investigated the transition pathway for oxygen and strontium migration between adjacent sites. We calculated migration barriers of between 0.96 and 1.35 eV for oxygen and between 3.17 and 3.20 eV for strontium, which are improved estimates over previous pair potential results.

Acknowledgements

I would like to acknowledge the efforts of my supervisor Richard Catlow and of Alexey Sokol, who have assisted me through my PhD and without whom it would not have been possible for me to complete this great task. I also wish to acknowledge Paul Sherwood, Scott Woodley and Aron Walsh for their consultations on scientific methodology and code specific advice.

The following people have also helped me in numerous ways over the years: Stephen Shevlin, François-Xavier Coudert, Jens Thomas, Johannes Kästner, Huub van Dam and Florian Schiffmann. Also Mark Michel for moral support. Finally I would like to thank my parents (Neil and Vicki), who have supported me throughout my journey through life and for tirelessly ferrying me around during my somewhat peripatetic academic career.

The author acknowledges the use of the UCL *Legion* High Performance Computing Facility, and associated support services, in the completion of this work.

Via our membership of the UK's HPC Materials Chemistry Consortium, which is funded by the EPSRC (EP/F067496), this work made use of the facilities of *HECToR*, the UK's national high-performance computing service, which is provided by UoE HPCx Ltd at the University of Edinburgh, Cray Inc and NAG Ltd, and funded by the Office of Science and Technology through EPSRC's High End Computing Programme.

Many of the atomic structure drawings were produced using the *VESTA* package [1, 2]. Other structural drawings and structural files used for calculations were created by *Material Studio 4.0* [3].

---

(1) K. Momma and F. Izumi, "VESTA: A Three-Dimensional Visualization System for Electronic and Structural Analysis", *Journal of Applied Crystallography*, 2008, **41**, 653–658.

(2) K. Momma and F. Izumi, *VESTA Website*, `http://www.geocities.jp/kmo_mma/crystal/en/vesta.html`, 2011.

(3) Accelrys Software Inc., *Material Studio Website*, `http://accelrys.com/products/materials-studio/`, 2005.

Contents

List of Figures

List of Tables

Chapter 1

Strontium Titanate - Background & Literature Review

1.1 Introduction

In this thesis, an in depth computational study of strontium titanate is presented. Strontium titanate, which has the formula $\mathrm{SrTiO_3}$ (abbreviated as STO), is a member of a class of materials known as perovskites, the structure of which we discuss in section 1.2.1.

There are two main areas of study into STO presented here. The majority of the research is based on modelling and characterizing the crystalline phases of STO, with particular emphasis on the tetragonal phase and the determination of the nature of the lowest temperature phase(s). The crystalline phase work is performed with a periodic quantum mechanical (QM) approach (see section 2.2). The second area of study is an investigation of vacancy defects and ion migration pathways/barriers using sets of interatomic potentials (see section 2.3) that were developed in the context of the thesis. We also discuss a relatively new hybrid quantum mechanical, molecular modelling (QM/MM) approach [1] for the study of defects, employed within the *ChemShell* code [1–3].

Useful and potential applications of STO (in some cases doped) include the following: use as the anodes in fuel cells [4], as oxygen sensors [5], in photo-catalysis to hydrolyse water [6, 7], and use as a substrate for growing YBCO superconductors [8], while STO has also been used in so called superlenses, which can be used in microscopy for examining fine structural details (with a resolution of $\lambda/14$) in the mid-infrared range (λ between 10 and $20\,\mu\mathrm{m}$) [9]. STO nano-tubes have been used in medicine for orthopaedic drug administration [10]. There is also a substantial application in the micro-electronics industry as STO can be used in capacitors [11, 12] and varistors [13] and there has been research into reversible electronic switching for use in Resistive RAM (RRAM) in computers [14]. Some images of the material in mineral

and synthetic form are provided in figure 1.1.1.

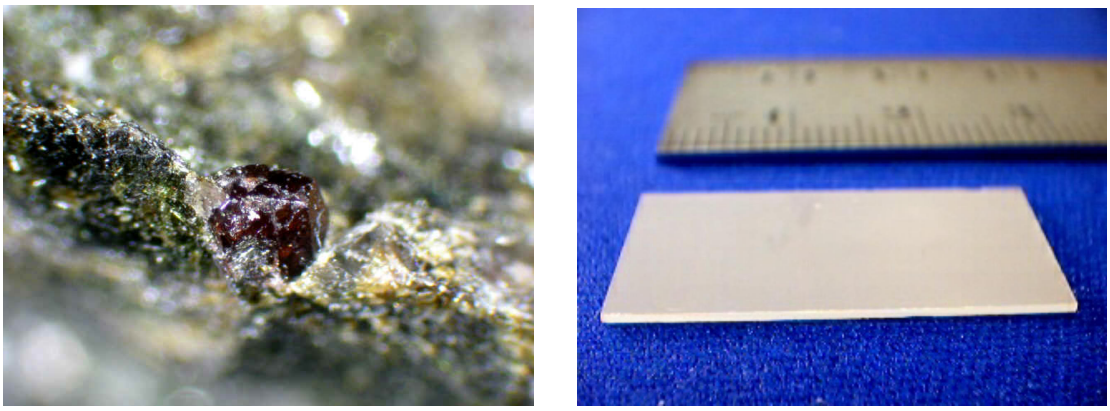

Figure 1.1.1: Images of strontium titanate in mineral form *Tausonite* (left) [15] and manufactured into a slide (right) [16]. Permission to reproduce these images has kindly been given by M. L. D. de Graaf and Commercial Crystal Laboratories, Inc. respectively.

STO has numerous useful electronic properties. It is a wide band-gap semiconductor $e_g \sim 3.22\,\text{eV}$ [17], which is usually of n-type [18]. However, electronic conductivity is highly dependent on the oxygen defect concentration and under certain conditions of oxygen partial pressure, can be made to exhibit p-type conductivity [5, 19, 20]. STO is usually assumed to be ionic, with titanium in the $4+$ state, strontium in the $2+$ state [21] and oxygen in the $2-$ state.

STO has been studied experimentally and has been widely observed to exist in two phases, cubic and tetragonal [22, 23]. Other perovskites are known to have orthorhombic and rhombohedral phases at lower temperatures and there is a small amount of evidence to suggest that these phases may also exist for STO [23, 24]. Due to the formation of small domains, the details of the local structure of STO may not have been detectable to most x-ray crystallography experiments. Currently the local structure of STO at low temperatures is not known accurately. The structure at low temperatures clearly poses fascinating challenges, which will be addressed in this thesis.

As noted, STO has been considered for use as a fuel cell anode. Previous pair potential models of the material give inaccurate values for the heights of the oxygen and strontium migration barriers. Past studies have also assumed that the oxygen migration saddle point would occur directly in between the two oxygen sites, which is unlikely to be the case. Pair potential models have also not previously modelled STO with lattice types of symmetry lower than tetrahedral. This topic is also addressed in the study.

The thesis consists of five main chapters followed by conclusions. Chapter 1 introduces the topic and describes some of the background theory behind STO. In chapter 2 we consider the theory that underlies the various computational techniques employed

in the three results chapters that follow it. In chapter 3 we present a detailed survey of the tetragonal potential energy surface, which has been mapped in three dimensions using multiple density functionals (see section 2.2.6). The surface is fitted to a polynomial and analysed using several different techniques. Chapter 4 contains a study in which several high symmetry starting structures are optimized to form a tree/dendrimer of different structures with the generation of branches at the occurrence of stationary points (zero potential energy gradient). 38 structures were generated this way which have been characterized. Low energy phases have been predicted with low symmetry, including rhombohedral and monoclinic. In chapter 5, we describe related work that was published in *Philosophical Transactions of the Royal Society A* [25]. A new set of molecular mechanical potentials were developed for studying the orthorhombic phase of STO. These potentials were used to perform Schottky defect formation calculations, which involved investigating charged strontium, titanium and oxygen vacancies. We follow by considering the nature of the migration barrier for oxygen and strontium ions.

Overall, the thesis provides new and detailed information on the structural and defect properties of this important material.

1.2 Structural Properties

1.2.1 Introduction

Perovskites, which have the general formula ABX_3 are ternary compounds consisting of two different cations (A and B) in equal ratio and an anion (X), which is usually oxygen (but may be fluorine). Structurally perovskites are made up of corner sharing octahedra with a B site inside each octahedron (BX_6 or TiO_6 for STO). A sites (Sr for STO) are placed in the gaps between groups of eight octahedra and form AX_{12} cuboctahedra, see figure 1.2.1. The TiO_3 sublattice is of the same structure as ReO_3.

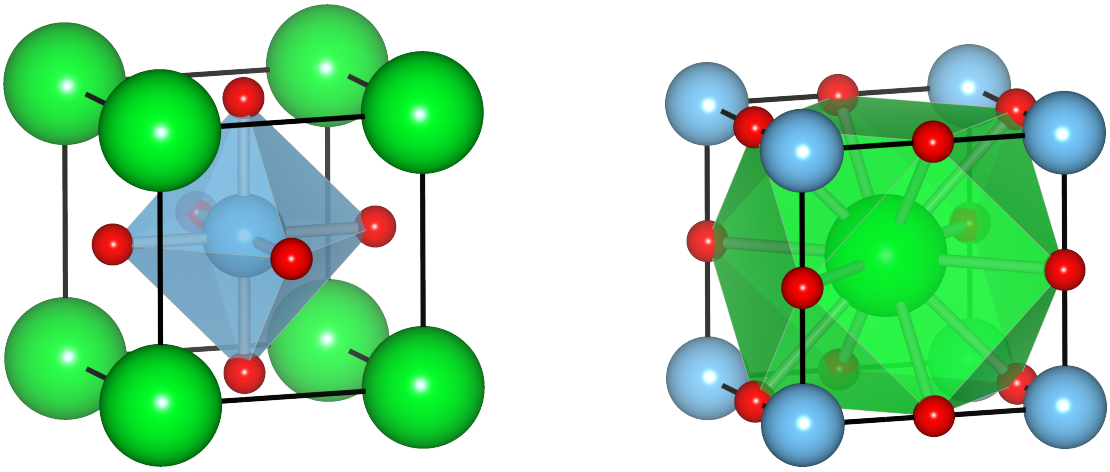

Figure 1.2.1: Representation of ideal cubic $Pm\bar{3}m$ perovskite, B centred (left) and A centred (right). Polyhedra have been drawn on to show the coordination of each cation, the colours of which relate to the cation inside. To represent STO, green, blue and red represent Sr, Ti and O ions respectively.

1.2.2 The Cubic Perovskite

The simplest and highest symmetry phase of the STO is cubic (or a subtle pseudo-cubic variation [24, 26]), with a space group of $Pm\bar{3}m$ and a lattice parameter of 3.905 Å at room temperature [23, 27] (see figure 1.2.1). Cubic symmetry is seen in STO above its transition temperature, which is reported as being between 105.5 and 110 K [23, 24, 26, 28–30]. In the cubic phase the strontium and titanium atoms' mean positions are at the centre of the oxygen cuboctahedra and octahedra respectively. Every oxygen atom perfectly bisects a pair of neighbouring titanium atoms. Each oxygen atom bonds to two titanium atoms (~ 2 Å) and four strontium atoms (~ 2.8 Å). The Wyckoff positions for the $Pm\bar{3}m$ cell, are given in table 1.2.1 (though the unit cell used in this work is translated compared to the coordinates given here).

The cuboctahedral volume is approximately five times greater than the octahedral volume (exactly in the ideal cubic case), which explains the placement of the large cation (strontium) at the A sites and the smaller titanium at the B site.

Table 1.2.1: Wyckoff positions for strontium titanate in the high temperature $Pm\bar{3}m$ setting.

Atom	Position	Coordinates
A(Sr)	1b	$\left(\frac{1}{2},\frac{1}{2},\frac{1}{2}\right)$
B(Ti)	1a	$\left(0,0,0\right)$
X(O)	3d	$\left(\frac{1}{2},0,0\right)$ $\left(0,\frac{1}{2},0\right)$ $\left(0,0,\frac{1}{2}\right)$

1.2.3 The Tetragonal Perovskite

Below the cubic phase transition temperature, the structure undergoes a second order phase transition [22, 26, 28] to a tetragonal structure with $I4/mcm$ symmetry [22, 30]. A second order transition means that there is no sudden change to the properties (structure in this case) of the crystal with changing temperature. A discontinuity is expected in the first derivative of structure (some structural parameter) with respect to temperature.

Although the cubic unit cell (with five atoms) can distort to be tetragonal, the real driving factor behind the cubic to tetragonal phase transition is a rotation of octahedra. Rotation is not possible with the unit cell shown in figure 1.2.1 as oxygen atoms either side of a titanium are images of one another and can only translate in the same direction. A larger unit cell is needed to describe the rotation and typically two different types of unit cell are used [31].

The first (crystallographic) type of tetragonal cell is a super-cell built using two of the cubic cell face diagonals as cell vectors. The third cell vector is simply one of the cubic cell vectors times two (the vector that is perpendicular to the two face diagonals). As a result the tetragonal cell lengths are $a_t = c_t \approx \sqrt{2}a_c$ and $b_t \approx 2a_c$, where a_c is the cubic lattice parameter. As can be seen, the b vector has been chosen to represent the long side of the cell. This first type of tetragonal cell contains 20 atoms and is used for most of the calculations in this thesis. The second type of cell is rather simply built from the cubic unit cell by creating a $2\times2\times2$ super-cell. The second type of cell contains 40 atoms; it is easier to construct, easier to compare to the cubic system and allows more possible structures if the symmetry is lowered. However, it contains twice as many atoms as the first cell, which make calculations with it considerably more computationally expensive. Both types of cell have been depicted in figure 1.2.2. The primitive unit cell of the body centred tetragonal lattice consists of only 10 atoms [32] and is used later in examining a lower symmetry rhombohedral structure (see section 4.6).

The $I4/mcm$ space group has three degrees of freedom, one of which is the rotation of the oxygen octahedra, the other two are the two different lattice parameters,

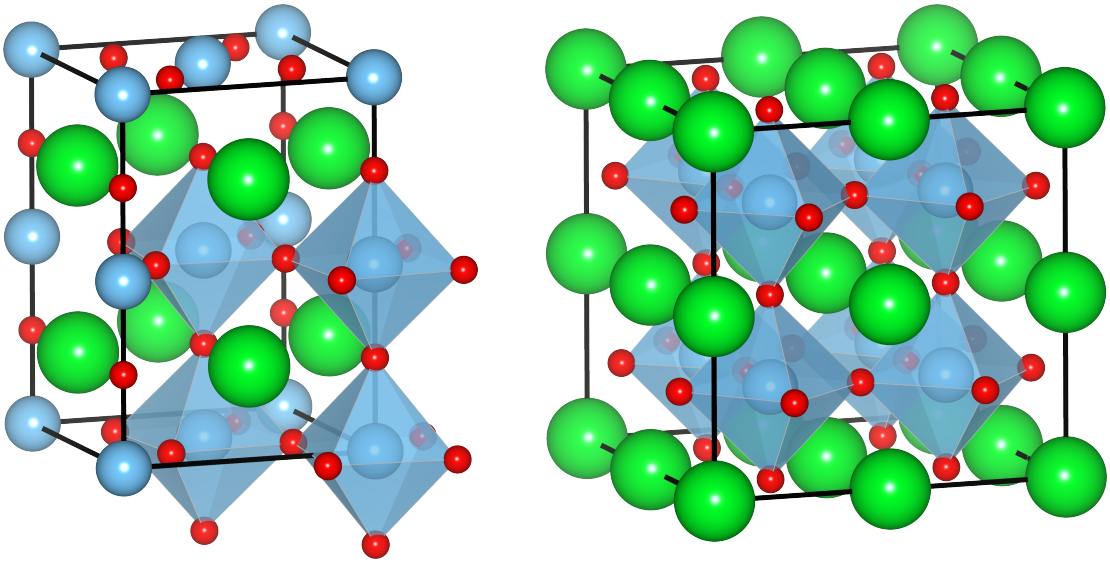

Figure 1.2.2: Representation of $I4/mcm$ perovskite with two different types of cell: B centred with a $\sqrt{2}\times2\times\sqrt{2}$ unit cell and selected octahedra drawn (left) and an A centred $2\times2\times2$ cell, with all octahedra drawn (right). Polyhedra have been drawn on to show the coordination of of each cation, the colours of which relate to the cation inside. To represent STO, green, blue and red represent Sr, Ti and O atoms respectively.

though these three can be re-expressed in terms of another three variables. Chapter 3 is a detailed study of this space group; here the a and b variables are re-expressed in terms of the b/a ratio and a scale factor for the lattice parameters, which changes the volume.

All neighbouring octahedra counter-rotate (rotation in fact is not entirely accurate as the motion is linear in terms of the fractional coordinates of the oxygen atoms). Counter-rotation of octahedra would be expected for octahedra in the plane of the rotation. However, neighbours along the axis of rotation (in the **b** vector) also counter-rotate; this allows for maximum separation between neighbouring planes of oxygen atoms. We consider this again in the chapter (see section 3.4.2). The Wyckoff positions for STO in the $I4/mcm$ space group are shown in table 1.2.2. The cell used within the work in this thesis uses a translated and rotated version of the one described in table 1.2.2 (c and b are swapped).

When the symmetry of a perovskites is lowered from cubic, the structure tends to form domains [31]. The most significant motion in the transition is from oxygen atoms which are smaller and have fewer electrons than the cations. These two effects combined make structural determination very difficult using X-ray and neutron diffraction techniques [31]. Additionally, work by Rimai and deMars [33] shows that at 77 K, the displacement of oxygen is only expected to be ~ 0.6 mÅ, which further contributes to the difficulty in determining low temperature structure.

Table 1.2.2: Wyckoff positions for strontium titanate in the lower temperature $I4/mcm$ setting. The c axis is long, $a = b$.

Atom	Position	Coordinates
A(Sr)	4b	$\left(0, \frac{1}{2}, \frac{1}{4}\right)$ $\left(\frac{1}{2}, 0, \frac{1}{4}\right)$
B(Ti)	4c	$\left(0, 0, 0\right)$ $\left(0, 0, \frac{1}{2}\right)$
X(O)	4a	$\left(0, 0, \frac{1}{4}\right)$ $\left(0, 0, \frac{3}{4}\right)$
X(O)	8h	$\left(x, x+\frac{1}{2}, 0\right)$ $\left(-x, -x+\frac{1}{2}, 0\right)$ $\left(-x+\frac{1}{2}, x, 0\right)$ $\left(x+\frac{1}{2}, -x, 0\right)$

1.2.4 Goldschmidt Tolerance Factors and the Causes of Distortions

It is common for perovskites to undergo phase transitions as their temperatures are lowered, for instance barium titanate, is known to exist in four phases. At high temperatures, $\mathrm{BaTiO_3}$ has a cubic $Pm\bar{3}m$ structure; at 393 K, it undergoes a phase transition to a tetragonal $P4mm$ structure. At 278 K, it undergoes another phase transition to orthorhombic $Amm2$, and below 183 K it has a rhombohedral $R3m$ structure [27, 34].

In general, the perovskite structure is dependent on several determining factors, which are ion size effects, composition and the Jahn-Teller effect [35], though often some combination is involved [27]. Temperature is also a significant determining effect as has been illustrated already. Considerations of the relationship between temperature and the observed structural phase is a highly involved field and covered in part by Landau theory, (see section 1.2.7). It is beyond the scope of this thesis to make temperature based structural predictions. However, the work here does relate directly to the field.

We will now cover briefly the other mentioned structure determining effects. The Jahn-Teller effect comes into play when there are partially filled d orbitals on the B site within the perovskite (inside the octahedra). The degeneracy in the d orbitals causes distortions in the octahedra [27]. As titanium is a d^0 ion, the Jahn-Teller effect does not apply to STO, except when foreign atom impurities are introduced, which is not covered within the thesis.

Changing the relative composition of the atoms in a perovskite, for instance the removal of oxygen atoms (creating vacancies), is another distortive effect. Oxygen and strontium vacancies are covered in section 1.3 and chapter 5, though the emphasis in these sections is not on the nature of the crystallographic distortions but rather the defect formation energies and transition pathways.

The effects of ion size are clearly important in determining structure. In the following, we loosely follow the descriptions given by Johnsson and Lemmens [27], though individual sources have been cited where relevant. During the 1920s, Victor Moritz Goldschmidt carried out work in order to characterize and predict the structure of perovskites. He developed a model based upon ion sizes, making the approximation that

they are rigid spheres. In essence the model compares the atoms along the cell face diagonal (across the middle of the cell's face) with those along a cell vector, $\mathbf{a}$.

$$a = \sqrt{2}(r_{\mathrm{A}} + r_{\mathrm{O}}) = 2(r_{\mathrm{B}} + r_{\mathrm{O}}), \tag{1.2.1}$$

where a is the length of $\mathbf{a}$, r_{A}, r_{B} and r_{O} are respectively the ionic radii of the A, B and O atoms. In (1.2.1), the face diagonal is described by the middle of the equation, while the cell vector (edge) part is covered by the right of the equation, (see figure 1.2.1 (right)). Equation (1.2.1), describes the situation in the perfect cubic perovskite, but in distorted perovskites, one can consider the ratio of the two parts of the equation. The celebrated Goldschmidt tolerance factor is given by:

$$t = \frac{r_{\mathrm{A}} + r_{\mathrm{O}}}{\sqrt{2}(r_{\mathrm{B}} + r_{\mathrm{O}})}. \tag{1.2.2}$$

In STO, the values used for ionic radii are $r_{\mathrm{A}} = 1.44\,\text{Å}$, $r_{\mathrm{B}} = 0.605\,\text{Å}$ and $r_{\mathrm{O}} = 1.40\,\text{Å}$ [27], which gives a value of $t = 1.002$. $t = 1$ of course corresponds to the ideal cubic cell.

The following are approximate guides and do not include temperature effects. The perovskite structure is found when $0.8 < t < 1$. For values of t lower than 0.8, the ilmenite structure is found [21, 36] and for larger values, hexagonal stacking is found [36]. Both of these structures involve octahedral face sharing as opposed to corner sharing found in perovskite. The cubic phase is found for $0.89 < t < 1$ [21, 36] and for $0.8 < t < 0.89$ a distorted perovskite is found [36], which may include orthorhombic distortion [27].

When t decreases, the A ion size decreases relative to the B ion size (the B size determines in part, the size of the octahedra, while the A size determines in part the size of the cuboctahedra). As a consequence, the octahedra tilt/collapse to fill the slack space present in the cuboctahedra. The tilting can occur in more complex ways than in the tetragonal structure, in which octahedra simply rotate about a single X–B–X bond (later referred to as a pseudo-cubic axis). When making predictions about sets of perovskites using Goldschmidt tolerance factors, one can choose a set of self consistent ionic radii, which can make accurate structural predictions under the assumption that only one of either the A ion or the B ion will change. It is not possible to compare sets of perovskites where both A and B ions have been changed as the effective ionic radii are not constant in all crystals [21]. Further information on the development of the Goldschmidt tolerance factors can be found in [37] and references therein.

Table 1.2.3: A comparison of the phases of STO as determined by Lytle [23] and Bogdanov et al. [24].

	Lytle		Bogdanov et al.	
No.	Temp. range (K)	Phase description	Temp. range (K)	Phase description
1	– 110	cubic[a]	– 110	cubic[a]
2	110 – 65	tetragonal	110 – 60	psueudomonoclinic[b]
3	65 – 35	orthorhombic	60 – 20	–
4	10 – [c]	rhombohedral[c]	20 – 4.2[c]	–

a Possibly pseudocubic.
b Based on a determination made at 77 K.
c Only speculative.

1.2.5 Lower Symmetry Structures?

There are various terms related to electrical properties of materials that have been used in the thesis, a short glossary has been provided at the end of the section (see section 1.2.8 on page 29).

STO is predicted by Goldschmidt tolerance factors to be cubic but some expected that like barium titanate, it might have an orthorhombic and rhombohedral phase transition at low temperatures. However, at the present time, there is no strong evidence for the orthorhombic and rhombohedral phases in low temperature STO. There is still debate over the nature of the low temperature dielectric properties of STO, which are strongly related to structure. We attempt therefore to cover a brief history of the understanding of this aspect in the paragraphs that follow.

In 1959, Weaver [38] published a paper based on dielectric measurements, that he believed to offer evidence of a ferroelectric phase of STO at temperatures below 45 K.

Later in the mid 1960s Lytle [23] and Bogdanov et al. [24], published papers demonstrating evidence of multiple low temperature phases. They used X-ray diffraction techniques on monocrystalline STO samples, with temperature ranges from room temperature down to liquid helium temperature (4.2 K). Their findings in terms of the existence of different phases were similar and will be outlined below.

Both authors consider that they found good evidence for the existence of three phases and some less certain evidence towards the existence of a fourth. We summarize the phase determination information in table 1.2.3. We note that Lytle observed the formation of domains in the samples, while Bogdanov et al. did not. Both researchers noted that the cubic phase may not in fact be perfect cubic but instead involve very subtle distortions, making it pseudo-cubic, Bogdanov et al. believe the distortion to be rhombohedral.

A few years later in 1970, Saifi and Cross [26] published a paper based on dielec-

tric measurements, finding evidence for an antiferroelectric phase, occurring at temperatures below $62\,\mathrm{K}$.

Since the publication of these papers the consensus appears to be that undoped STO has a cubic (or pseudo-cubic [26]) state, and a tetragonal state down to low temperatures (the tetragonal phase is often referred to as an antiferrodistortive phase [32, 39] though it is of non-polar character [40]). In a paper by Müller et al. [41] (and references therein), he discusses the possible occurrence of a quantum paraelectric state at $37 \pm 1\,\mathrm{K}$, based upon electron paramagnetic resonance experiments using Fe^{3+} as a dopant. The term quantum paraelectric was previously coined by Müller and Burkard [42] in their 1979 paper involving dielectric measurements at temperatures well below $4\,\mathrm{K}$. In [42] they discuss the large dielectric constant ϵ, which becomes independent of temperature at very low temperatures. They considered this evidence for the "occurrence of a quantum-mechanical regime which stabilizes large ferroelectric f1uctuations in the paraelectric phase". It appears from [42] that the quantum-paraelectric phase is fully established at $\sim 3\,\mathrm{K}$ but starts to deviate from classical behaviour at $\sim 40\,\mathrm{K}$. These ideas contradict the early conclusions by Weaver [38], indicating that there was a ferroelectric phase.

STO is now frequently referred to as an incipient ferroelectric [39, 42–44] (meaning nearly ferroelectric) and a quantum paraelectric.

The work in this thesis on low temperature structure is covered in chapters 3 and 4, most notably the latter and attempts to increase the level of knowledge in the area by determining and analysing the microscopic nature of the many minimum and saddle point structures that can exist in the material via a static lattice *ab-initio* approach i.e. thermal effects are not taken into account and using a quantum mechanical level of theory. Our calculations reveal a fascinating and rich range of structural distortions.

1.2.6 Describing Octahedral Distortions

When perovskites undergo octahedral rotations that are more complicated than the simple tetragonal case (rotation about a single axis), some system of classification is needed to describe it. In the 1970s, Glazer [45, 46] published papers describing a method for doing this. Later on in the mid 1990s, Thomas [47] outlined an alternative approach. Within this thesis, we use an approach that encapsulates the ideas in both methods, at the expense of requiring the output of many numbers in tabular form. A detailed description of this method is given in section 4.2.2.3.

Though making detailed predictions of phase relations is beyond the scope of the thesis, we briefly consider one of the most important and relevant theories in relation to phase determination and the nature of second order phase transitions.

1.2.7 Landau Theory and Phase Determination

The prediction of phase transitions is a complicated field. A detailed overview of displacive phase transitions is given in papers by Dove [48] and Scott [49]. The following brief summary of Landau theory follows the arguments presented in this paper.

Landau theory is a thermodynamic model of second order phase transitions, proposed by Lev Davidovich Landau [50, 51] in 1937. It attempts to relate some order parameter η to the temperature T and the Gibbs free energy G. The order parameter relates to some physical parameter within a crystal, that changes during the phase transition. In the case of STO, the order parameter is equal to or proportional to the octahedral rotation angle θ (we are considering the cubic to tetragonal phase transition). The Gibbs free energy is given by:

$$G(p,T) = U + pV - TS \tag{1.2.3}$$

where U is the internal energy, p is pressure, V is volume and S is entropy. Note that in this thesis only U, the internal energy is calculated and so comparisons that relate to Landau theory are incomplete.

Landau theory assumes that close to the transition point, the free energy can be expressed as a Taylor expansion of the order parameter η:

$$G(\eta) = G_0 + \frac{1}{2}G_2\eta^2 + \frac{1}{4}G_4\eta^4 + \dots. \tag{1.2.4}$$

In (1.2.4), only even terms have been included as the free energy is usually symmetrical with respect to η. This is the case in STO, where it makes no difference which way the octahedra rotate. The expansion is truncated to include only the minimal number of terms needed to describe the system. In [8], the authors experimented with a $(2:4:6)$ parametrization (all even terms up to six), though it is common to only consider two power terms (not necessarily consecutive).

We consider that the expectation structure or phase (in terms of η), will be the one that minimizes the free energy equation:

$$\frac{\partial G}{\partial \eta} = 0, \qquad \frac{\partial^2 G}{\partial \eta^2} > 0. \tag{1.2.5}$$

However, first we must introduce temperature to expression (1.2.4). We define the transition temperature T_c, beneath which the order parameter becomes non-zero. In figure 1.2.3 is a demonstration of the free energy surface above and below T_c.

If we consider the free energy expansion to include only the first two power terms, then it is clear that the free energy will only have a minimum at $\eta = 0$, when the G_2 term

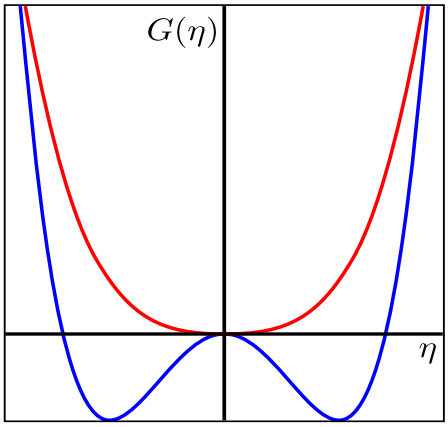

Figure 1.2.3: Plot of free energy G vs. the order parameter η, with two different temperature scenarios. In blue is a representation of the free energy surface for the tetragonal system, where the experimental/expectation value of η is non-zero. In red is the surface above the transition temperature and the expectation value of η is zero.

is zero or positive (and two minima either side of zero when η is negative). Therefore the G_2 term is modified/replaced so as to uphold this relation:

$$G_2 = A(T - T_c), \tag{1.2.6}$$

where A is a constant. Conventionally, letters of the alphabet are used to replace the other coefficients, giving us the relation:

$$G(\eta) = G_0 + \frac{1}{2}A(T - T_c)\eta^2 + \frac{1}{4}B\eta^4. \tag{1.2.7}$$

By applying the conditions in (1.2.5), we see that $\eta = 0$ is the only real solution, when $T > T_c$. For $T < T_c$, there are two real solutions:

$$\eta = \pm \left(\frac{A(T_c - T)}{B} \right)^{\frac{1}{2}}. \tag{1.2.8}$$

The $\frac{1}{2}$ power is known as the critical exponent and is usually represented as β. If we had based the parametrization of the free energy on the second and sixth power terms, which was considered in [8], then a similar formula with $\beta = \frac{1}{4}$ would have been produced. Experimentally determined values have given a range of $0.33 < \beta < 0.42$ (covered in a review in [52]), though more recent results found in [52, 53] state that the value in unstrained STO is 0.35 ± 0.02.

We have only briefly covered Landau theory here. There are also more sophisticated variations of it which can be found in [49]. In section 3.4.6, we relate some of our own results with experimental data fitted to a Landau theory.

1.2.8 Short Glossary of Terms

There are various terms relating to types of polarizing distortions within crystals used in the thesis sections. A brief explanation is provided below.

Ferroelectric materials form permanent electric dipoles in the absence of an applied electric field via the displacement of anions relative to cations. It is energetically favourable for the dipoles to align with one another, with the exception that, given sufficient size, the crystal will form domains with different dipole orientations. The domain size is dependent on the properties of the material. The orientation of the polarization within a crystal can usually be switched upon the application of a sufficiently strong external electric field, with the changes persisting after the external electric field has been removed.

Antiferroelectric materials, as with ferroelectrics, form permanent dipoles without any external field. However, the dipoles orientate themselves in a parallel-antiparallel fashion such that one dipole points in the opposite direction to an adjacent one. An antiferroelectric material has no net dipole moment.

Paraelectric materials form randomly orientated dipoles without the application of an external field. However, when an electric field is applied, then subject to passing though an energy barrier, the dipoles align so as to reduce the strength of the electric field within the material. When the external field is removed, the dipoles return to their disordered state. The quantum-paraelectric effect refers to an energy barrier that is breached through quantum-tunnelling, in the case where the energy barrier is too high to be overcome by the thermal energy and the effect of the applied field. The quantum-tunnelling can facilitate both the alignment of dipoles upon the application of an external field and the subsequent relaxation to a disordered state upon the removal of an electric field.

Dielectric materials, also commonly referred to as insulators, are non-dipolar in the absence of an applied electric field. When an electric field is applied, induced dipoles form in the material to reduce the effect of the applied field within the material. When the applied field is removed, the ions relax back into their original state.

1.3 Defects and Migration Properties

1.3.1 Introduction

STO acquires many of its most interesting and useful properties when the crystal is imperfect (or defective). Amongst the most common defects are oxygen vacancies, which form naturally in the material due to relatively weak binding of the oxygen and high oxygen mobility (though oxygen mobility is highly dependent on temperature [20, 54–56]). Electrical conductivity for example varies significantly with the concentration of vacancy sites [20].

Oxygen and strontium defect calculations, especially the migration barrier and pathway are the main topics of interest in the final results chapter (see chapter 5).

1.3.2 Schottky Defects

We now briefly consider some of the theory behind vacancy formation. There are two main types of spontaneous defect that can form within a crystal. Frenkel defects, first discovered by Yakov Frenkel are a type of defect in which an atom, leaves its normal lattice site, forming a vacancy and an interstitial. Schottky defect formation is a competing process, named after Walter Schottky. In a Schottky defect, separate ions (not interacting with each other) constituting a formula chemical unit of the crystal, leave the bulk of the crystal. As a result the charge and stoichiometry of the crystal are maintained. It has been shown that Schottky defect formation is more energetically favourable than Frenkel defect formation in STO [57] and in barium titanate [58], suggesting that the Schottky defect formation may generally be the dominant method of ionic disorder in perovskites. The closely packed nature of the perovskite crystal can explain the relative difficulty in harbouring interstitial atoms.

Kröger-Vink notation, defines a method for describing vacancy and impurity type defects. With this notation, a defect can be described in the following way:

$$\mathrm{A}_{\mathrm{l}}^{\mathrm{q}}, \tag{1.3.1}$$

where A is the species found at the lattice site l and q defines the charge state of the defect. l is replaced with the chemical element symbol of the lattice site where the defect occurs (what would be there if there was no defect). A is replaced with the element symbol of what is found at the defect site; V is used in place of A to indicate a vacancy. A special notation is used for the charge state, whereby a $\prime$ indicates a single negative charge, a $\bullet$ is used to indicate a single positive charge and repetition of the symbol indicates multiple charges of the respective type. A $\times$ is used in place of q to indicate neutrality, though more commonly in the neutral case q is simply left out. We could describe a defectless titanium site with $\mathrm{Ti}_{\mathrm{Ti}}^{\times}$; likewise a titanium vacancy with a

-4 charge state is represented as: $\mathrm{V}''''_{\mathrm{Ti}}$.

Using this notation, we now describe the full Schottky defect equation for STO:

$$\mathrm{Sr}^{\times}_{\mathrm{Sr}} + \mathrm{Ti}^{\times}_{\mathrm{Ti}} + 3\mathrm{O}^{\times}_{\mathrm{O}} \rightleftharpoons \mathrm{V}''_{\mathrm{Sr}} + \mathrm{V}''''_{\mathrm{Ti}} + 3\mathrm{V}^{\bullet\bullet}_{\mathrm{O}}. \tag{1.3.2}$$

In section 5.4, we calculate the Schottky defect energy, using pair potential techniques, and the Mott-Littleton approach, which will be discussed in the next chapter.

1.3.3 Ion Migration

The diffusion thermodynamics of oxygen is a matter of significant interest. The diffusion barrier is determined by the lowest energy pathway between two equivalent oxygen positions [25]. The transition point is the highest point on the potential energy hypersurface along this trajectory. To a first approximation, the transition point for oxygen lies in the (110) direction, in a linear path equidistant between two oxygen sites [57, 59]. Some curvature in the path may be expected however.

The strontium migration pathway is easier to predict as to transit from one strontium site to a vacant one, it must pass through a symmetrical square face of four oxygen and four titanium atoms. Due to the strong repulsion of the titanium, the transition point can be expected in the mid point.

Determination of the migration barrier for oxygen makes it possible to calculate the oxygen conductivity, which has applications in developing fuel cells [4]. In section 5.5 we present data on ion migration pathways.

Having considered the background behind STO, we now consider the theory behind the theoretical/computational methods used within the thesis.

Chapter 2

Theory

2.1 Preamble

In this chapter we present an introduction to some of the most important theoretical concepts that govern the computer models employed within this thesis. The Quantum Mechanical (QM) and Molecular Mechanical (MM) methods as used in this investigation are all standard methods. However, the QM/MM embedded cluster technique as implemented within *ChemShell* [1–3] is not so widely known, and so the non-standard aspects of this are described at greater length in section 2.5.

2.2 Quantum Mechanical Methodology

2.2.1 Introduction

Quantum Mechanics (QM) governs the behaviour of atomic systems. It can be used to calculate many aspects of atomic behaviour including the calculation of electronic ground states, charge transfer, bond breaking and formation and spin distribution.

The most widespread QM methods attempt to calculate the electronic ground state with fixed nuclear positions i.e. the configuration of electrons around a set of fixed nuclei that has the lowest possible energy. This simplifying method of keeping the nuclei fixed while relaxing the positions of the electrons around them is known as the Born-Oppenheimer approximation [60]. Geometry optimizations, in which the lowest energy configuration of the entire system including the nuclei is calculated are discussed in section 2.4.

The ground state is usually calculated by invoking the variational principle (2.2.3) by finding the wave-function solutions to the Schrödinger equation (2.2.1), that have the minimum mean energy, see (2.2.2):

$$\hat{H}\Psi(\mathbf{x}) = E\Psi(\mathbf{x}); \tag{2.2.1}$$

$$E[\Psi] = \frac{\left\langle \Psi(\mathbf{x})|\hat{H}|\Psi(\mathbf{x})\right\rangle}{\langle\Psi(\mathbf{x})|\Psi(\mathbf{x})\rangle} = \frac{\int \Psi(\mathbf{x})^* \hat{H}\Psi(\mathbf{x})\ \mathrm{d}\mathbf{x}}{\int \Psi(\mathbf{x})^*\Psi(\mathbf{x})\ \mathrm{d}\mathbf{x}}; \tag{2.2.2}$$

$$E[\tilde{\Psi}] \geq E_0, \tag{2.2.3}$$

where Ψ is the complex valued wave function of spin orbitals $\mathbf{x}$, which represent position and spin, $\hat{H}$ is the Hamiltonian, E is energy and $E[\Psi]$ is the mean energy of the state. $\tilde{\Psi}$ is a trial wave function and E_0 is the true ground state energy.

The Hamiltonian varies between QM methods but in general, will include a kinetic energy term and potential energy terms for interactions between the electrons and the nucleus and between the electrons and each other see equations (2.2.4) to (2.2.7).

$$\hat{H} = \hat{T} + \hat{V}_{ne} + \hat{V}_{ee}, \tag{2.2.4}$$

in which:

$$\hat{T} = \sum_{i=1}^{N} \left(-\frac{\nabla_i^2}{2} \right); \tag{2.2.5}$$

$$\hat{V}_{ne} = \sum_{i=1}^{N} \left(-\sum_{\alpha} \frac{Z_\alpha}{r_{i\alpha}} \right); \tag{2.2.6}$$

$$\hat{V}_{ee} = \sum_{i<j}^{N} \frac{1}{r_{ij}}, \tag{2.2.7}$$

where N is the number of electrons in the system, α is the set of all nuclei of charge Z_α, $r_{i\alpha}$ is the distance between pairs of electrons and nuclei and r_{ij} is the distance between all pairs of electrons. This version of the Hamiltonian uses atomic units, whereby length, charge and mass are measured in units of Bohrs (0.5292 Å), electronic charge e and electronic mass m_e respectively [61]. A calculation of the total energy of the system would involve including the Coulombic interaction of the nuclei with one another as a term. However, as an energy calculation considers the nuclei fixed, the energy derivative (force) with respect to nuclear motion is zero and so the term can be left out.

Although in principle QM is an exact description of a system of atoms, in any system that contains more than one electron, approximations have to be made. There are many methods and variations there of, that attempt to make these approximations, the principle approaches, Hartree-Fock (section 2.2.5) and Density Functional Theory (section 2.2.6) are discussed following after we consider approaches to describing the wave function.

2.2.2 Basis Sets

2.2.2.1 Some Prerequisites

Molecular orbitals ψ_i (also called spin orbitals), represent a potential solution to the Schrödinger equation for one electron in a system of atoms. They are known as spin orbitals, as they are composed of the product of a spatially varying function $\phi_i(r)$ and a spin function $\sigma_i(s) = \alpha(s)$ or $\beta(s)$. The α and β functions represent up and down spin respectively.

Molecular orbitals are usually formulated as a Linear Combination of Atomic Orbitals (LCAO) (2.2.8). An atomic orbital is a potential single electron solution for a hydrogen like atom.

$$\psi_i = \sum_{\mu=1}^{n} c_\mu \phi_\mu, \tag{2.2.8}$$

where ψ_i is the i^{th} molecular orbital, ϕ_μ is the μ^{th} atomic orbital, c_μ is a coefficient and n is the number of atomic orbitals in the system.

Atomic orbitals ϕ_μ are usually approximated by a linear combination of, primitive functions (2.2.9)

$$\phi_\mu = \sum c_\nu \phi_\nu. \tag{2.2.9}$$

2.2.2.2 Nuclear Centred Basis Sets

One commonly chosen class of primitive functions are radially varying functions centred on the nuclei of atoms. Traditionally Slater functions (2.2.10) were chosen, which quite accurately represent the single electron wave function. Such orbitals were known as Slater type orbitals.

$$\phi_\nu\left(\zeta, n; r\right) = C r^{n-1} e^{\zeta r} Y_{lm}, \tag{2.2.10}$$

where C is a normalization constant, r is distance from the nucleus, ζ is the exponent, which characterizes the shape of the function, n, l and m are respectively the principle, angular momentum and magnetic quantum numbers. Y_{lm} descries the angular momentum of the system and provides the non-radially symmetric shape of the function [62]. In Cartesian coordinates the angular momentum component is parameterized thus:

$$Y_{lm}(i, j, k; x, y, z) = x^i y^j z^k, \tag{2.2.11}$$

where $i + j + k = l$ are all integers and x, y and z are the Cartesian coordinates. In this representation, i, j and k are combined differently to make the various s, p, d and f functions (e.g. a d_{xy} orbital corresponds to $i = j = 1$). The influence of the magnetic quantum number m on expression (2.2.11) is not demonstrated here; but for a more in depth explanation of the origin of this function in polar coordinates please see reference [63].

Due to the double exponent, Slater functions are very computationally expensive to compute, making calculations on large systems impractical. As a compromise, a series of Gaussian functions may be used to represent the AOs and are denoted Gaussian type orbitals:

$$\phi_\nu\left(\zeta; r\right) = C e^{-\zeta r^2} Y_{lm}. \tag{2.2.12}$$

In combination, Gaussian functions can provide a good approximation to an AO and the use of 4–5 Gaussian type orbitals to replace one Slater type orbital will result in much faster calculations [62].

A basis set is a description of a set of Slater or Gaussian type orbitals (intended as building blocks) known to provide a good initial guess and ultimately allow a good approximation to the ground state wave function to be constructed. Different elements have their own basis sets and there are databases of many different basis sets available.

Very often basis sets are partially contracted. This means that sets of Gaussian

functions have been added together in a fixed ratio, which saves on processing time, as there are fewer variables. A contraction of Gaussian functions would then have a single coefficient as a variable.

Basis sets such as these can be used in both periodic (within a repeating three-dimensional unit cell) systems for studying crystals or within non-periodic systems where one might study a molecule or a local state in the centre of an embedded cluster (see section 2.5).

An alternative type of basis set, commonly used is known as a plane-wave basis.

2.2.2.3 Plane-Wave Basis Sets

In the case of periodic (infinite crystal lattice) systems, an alternative approach can be used to construct the wave function, in which the AOs and MOs are build from a linear combination of plane waves. As both plane waves and crystals are periodic, plane-wave basis sets can be particularly convenient. A one-dimensional non-travelling plane wave can be described as:

$$y(x) = e^{ikx}, \tag{2.2.13}$$

where k is the wave-number and x is distance. For a wave to be periodic when confined within a box of length a, $k = 2n\pi/a$, where n is an integer. This describes an infinite set of waves which can be placed inside a box. For the more general three-dimensional (or multidimensional case), plane waves are described as:

$$\psi_{\nu G}(r) = \tfrac{1}{\sqrt{\Omega}} e^{i\mathbf{G}\cdot\mathbf{r}}, \tag{2.2.14}$$

where Ω is the volume of the real-space cell [64]. $\mathbf{r}$ is the position in real-space and $\mathbf{G}$ is the set (matrix) of all wave-vectors/inverse-vectors (i.e. $\mathbf{G} = \mathbf{k}_j$), which satisfy the periodicity of the given unit cell. A Fourier series can be used to adjust the ratios of the different plane waves in order to fit the MOs as in equations (2.2.8) and (2.2.9).

Plane-wave basis sets are not described by a set of predefined basis functions but rather generated at the time of the calculation based on the unit cell and on a cut-off associated with the largest frequency (highest n) one wishes to consider (this is often done in terms of a maximum energy cut-off). The level of detail that can be described or the quality of the basis set is defined largely by this parameter.

There are several advantages of using a plane-wave basis set, one of which is that the energy of a system of plane waves is easy to calculate. Also the wave functions have no origins i.e. are not centred on nuclei (which can move around during geometry optimizations), which simplifies the set of variables that must be solved. An artefact of force calculations on nuclei centred wave functions is the so called *Pulay forces* [64, 65], which appear when differentiating the wave function with respect to nuclear

coordinates. Pulay forces do not appear in the plane-wave model, simplifying force calculations. Another asset to force calculations is that derivatives in real-space can be carried out as multiplications in G/Fourier-space [64].

A shortcoming of the plane-wave basis set model is the significant need for *pseudo potentials* (see section 2.2.4). Small features such as inner atomic orbitals require larger G-vectors to describe them. As a result, it would require a large number of waves to describe the inner electrons as compared to the valence electrons that are involved in bonding. Pseudo potentials for the plane-wave model can be implemented in various ways including Gaussian functions.

The plane-wave basis set model offers no bias with regard to the level of description of the wave function in different regions of the unit cell, which can be either an advantage or a disadvantage depending on the nature of the system of study.

The plane-wave basis approach is implemented within the *VASP* [66–68] code, which was used for carrying out the energy landscapes investigation in (chapters 3 and 4).

2.2.3 k-Points

In a crystalline system, the wave functions from periodic images of the primitive unit cell interact. In an infinite crystal, the number of allowed electronic states formed is also infinite and as a consequence, the otherwise discrete states form into bands of continua. A gamma point calculation (which is a calculation outside of the Brillouin zone i.e. the reciprocal-space representation of the primitive unit cell) does not take the effect of the infinite lattice on the wave function into account.

The use of k-points in a calculation, considers contributions to the wave function of wave-vectors that lie within the Brillouin zone, which is analogous to the consideration of plane waves that span outside of the real-space primitive cell. By including the effects of a finite number of k-points, the system can behave as if it is part of an infinite crystal.

Most QM codes implement k-point calculations including *VASP*. It is easier to implement in codes that use plane-wave basis sets, as both plane waves and the k-point technique have a reciprocal-space description.

The theoretical basis for the technique is based on Bloch's theorem which is outlined as follows (please see [69] for a fuller description, on which the following derivation is based). Bloch's theorem states that an eigenstate (a basis function) of a one electron Hamiltonian for a system with a periodically varying potential (i.e. the atoms in a unit cell as part of a Bravais lattice) can be described by a plane wave multiplied

by some function that has the same periodicity as the Bravais lattice:

$$\psi_{n\mathbf{k}}(\mathbf{r}) = e^{i\mathbf{k}\cdot\mathbf{r}} v_{n\mathbf{k}}(\mathbf{r}), \tag{2.2.15}$$

where $\psi_{n\mathbf{k}}$ is a basis function; the index n describes the association with a given band (analogous to an orbital) and $\mathbf{k}$ associates the wave function with the choice of k-vector. $e^{i\mathbf{k}\cdot\mathbf{r}}$ is a plane wave (see section 2.2.2.3), where $\mathbf{r}$ is a real-space distance vector. $\mathbf{k}$ has certain requirements in terms of its periodicity and is given by:

$$\mathbf{k} = \sum_{i=1}^{3} x_i \mathbf{b}_i, \tag{2.2.16}$$

where x_i define the allowed values of $\mathbf{k}$ and can be calculated by making use of the Born-von Karman boundary conditions covered later in this section (see equations (2.2.28) to (2.2.30)). $\mathbf{b}_i$ are the reciprocal lattice vectors and satisfy the condition:

$$\mathbf{b}_i \cdot \mathbf{a}_j = 2\pi\delta_{ij}, \tag{2.2.17}$$

where $\mathbf{a}_i$ represents the real-space lattice vectors. $v_{n\mathbf{k}}(\mathbf{r})$ is the function with the same periodicity as the Bravais lattice (see equation (2.2.18)); its representation is often also as a plane wave (though the associated wave-vectors are not represented here).

$$v_{n\mathbf{k}}(\mathbf{r} + \mathbf{R}) = v_{n\mathbf{k}}(\mathbf{r}); \tag{2.2.18}$$

$$\mathbf{R} = \sum_{i=1}^{3} w_i \mathbf{a}_i, \tag{2.2.19}$$

where $\mathbf{R}$ is a displacement vector in real-space pointing to another lattice site and w_i are integers.

By starting with equation (2.2.15) and substituting $\mathbf{r}$ with $\mathbf{r} + \mathbf{R}$ and then using (2.2.18), we have:

$$\psi_{n\mathbf{k}}(\mathbf{r} + \mathbf{R}) = e^{i\mathbf{k}.(\mathbf{r}+\mathbf{R})} v_{n\mathbf{k}}(\mathbf{r} + \mathbf{R}); \tag{2.2.20}$$

$$= e^{i\mathbf{k}.\mathbf{R}} e^{i\mathbf{k}.\mathbf{r}} v_{n\mathbf{k}}(\mathbf{r}). \tag{2.2.21}$$

Finally substituting back equation (2.2.15) we get an alternative form of Bloch's theorem:

$$\psi_{n\mathbf{k}}(\mathbf{r} + \mathbf{R}) = e^{i\mathbf{k}.\mathbf{R}} \psi_{n\mathbf{k}}(\mathbf{r}), \tag{2.2.22}$$

demonstrating the periodicity of the new wave function across the Bravais lattice. The different values of $\mathbf{k}$ represent the different k-points that are sampled in the crystal.

The allowed values of $\mathbf{k}$ can be determined by applying a Born-von Karman boundary condition, which is usually chosen to be that of the periodicity of the wave function:

$$\psi(\mathbf{r}+\mathbf{R}) = \psi(\mathbf{r}+\sum_{i=1}^{3} w_i \mathbf{a}_i) = \psi(\mathbf{r}). \tag{2.2.23}$$

By comparing Bloch's theorem (2.2.22) with (2.2.23), we see that k-points must be chosen such that the plane wave is equal to one:

$$e^{i\mathbf{k}\cdot\mathbf{R}} = 1. \tag{2.2.24}$$

Given the definition of $\mathbf{k}$ and $\mathbf{R}$ in equations (2.2.16) and (2.2.19) respectively and then substituting in the condition in (2.2.17) we have:

$$\begin{aligned}
\mathbf{k}\cdot\mathbf{R} &= (x_1\mathbf{b}_1 + x_2\mathbf{b}_2 + x_3\mathbf{b}_3)\cdot(w_1\mathbf{a}_1 + w_2\mathbf{a}_2 + w_3\mathbf{a}_3); && (2.2.25)\\
&= 2\pi(x_1w_1 + x_2w_2 + x_3w_3); && (2.2.26)\\
&= 2\pi\sum_{i=1}^{3} x_i w_i. && (2.2.27)
\end{aligned}$$

In order to satisfy (2.2.24), all values of $x_i w_i$ must be integral, therefore:

$$\begin{aligned}
x_i w_i &= m_i; && (2.2.28)\\
x_i &= \frac{m_i}{w_i}; && (2.2.29)\\
\mathbf{k} &= \sum_{i=1}^{3} \frac{m_i}{w_i}\mathbf{b}_i, && (2.2.30)
\end{aligned}$$

where m_i is a positive integer. For calculations within the Brillouin zone (outside of the real-space primitive cell) $m_i \leq w_i$.

By considering a single increment of m_i for each index, we describe a parallelepiped with the volume allocated to each k-point for a given set of w_i integers. If $W = w_1w_2w_3$ and represents the total number of real-space primitive cells that the calculation is considering then the volume of a k-point is:

$$\begin{aligned}
\Delta\mathbf{k} &= \frac{1}{W}\mathbf{b}_1\cdot(\mathbf{b}_2\times\mathbf{b}_3); && (2.2.31)\\
&= \frac{(2\pi)^3}{VW}, && (2.2.32)
\end{aligned}$$

where V is the volume of the real-space primitive unit cell and VW is the total real-space volume sampled in the calculation. It follows that the total number of k-points allowed within the Brillouin zone is equal to W as $\mathbf{b}_1\cdot(\mathbf{b}_2\times\mathbf{b}_3)$ is the volume of the

Brillouin zone.

Performing a calculation using k-points significantly improves the accuracy in certain materials. However, the computational load and the number of basis functions required to describe the system (and associated computer memory) increase in proportion to the number of k-points sampled (in most implementations).

A common method for automatically selecting k-points is the Monkhorst-Pack method, developed by Hendrik Monkhorst and James Pack [70]. This method divides the Brillouin zone up into a regular grid and samples the grid on the intersections of the grid. A more dense grid will generally produce more accurate results up to a certain limit which can be determined with some trial calculations (a similar approach is used for the energy cut-off parameter).

2.2.4 Pseudo Potentials

To save on the amount of computer processing required, atoms with many electrons are often modelled with pseudo potentials (also called Effective Core Potentials), in which some or all of the core electrons are replaced with a potential energy term that approximates their collective behaviour. Such approximations can often be made as only the valence electrons are involved in bonding.

In some cases (typically in elements with a large atomic number Z), the use of pseudo potentials can improve the accuracy of a calculation. One reason for this is that the inner electrons of high Z atoms are affected by relativistic effects, which can be taken into account during the development of a pseudo potential. Most QM modelling techniques do not take relativity into account explicitly. Another reason is that as all QM modelling techniques are approximate, the accumulation of errors over the many inner electrons of an atom can result in poorer results than with the use of pseudo potentials.

Pseudo potentials are often created as a contraction of Gaussian functions (centred on the nuclei) or for a plane wave based code they are usually built from plane waves. In the general case one can assume that a pseudo potential is likely to be specifiable in the same ways that the given computer code deals with basis functions.

In the general case, generating pseudo potentials is difficult. There are various methods for achieving this, with varying degrees of automation. One unusually starts by fitting for a single atom/ion of a given material in a vacuum. One method (for an empirical pseudo potential) involves iteratively adjusting the parameters of a pseudo potential in order to fit a set of experimentally known values such as first excited state and ionization energies (focusing on ionization levels that are important to the situation). Developing the pseudo potentials further, one can join the atom/ion to others and through a similar methodology, attempt to accurately reproduce the correct bond

length(s), while maintaining the previous (experimental) values. If done manually, this task can be exceptionally time consuming. Empirical pseudo potentials are often only useful for a given modelling scenario and will perform poorly if used in a different type of system.

Ab-initio pseudo potentials are more versatile and involve a high level of automation. In the general case, these involve matching the properties of an atom with pseudo potentials with that of an all electron atom calculated using an *ab-initio* method. In a paper by Hamann et al. [71], a set of criteria is laid out for the generation of such pseudo potentials. These are that for a chosen prototype atomic configuration: (1) the eigenvalues of the valence electrons of the two systems agree; (2) the atomic wave functions agree outside of a given core-radius distance r_c; (3) outside of the core-radius ($r > r_c$), the integral of charge density over radius from 0 to r i.e. total charge contained within a radius, agree for both full electron and pseudo systems (this is known as norm conservation); (4) for $r > r_c$ there should be agreement between the two systems for the derivatives of the logarithms of the wave functions and also the first derivatives of the systems' energies. Properties (3) and (4) are important for making the pseudo potentials transferable to other systems and (4) is important for reproducing the scattering properties of a full electron atom. The pseudo-potential developer may also need to intervene to make adjustments to a pseudo potential.

Information on one of the *VASP* implementation of pseudo potentials (used in this thesis): the Projector Augmented-Wave method (PAW) can be found in [72, 73].

Having considered the components used for building wave-function based atomic models, we will consider two different approaches for the construction of the wave function and the calculation of energy.

2.2.5 Hartree-Fock Approach

The Hartree approximation begins by assuming that the many electron wave function for the system Ψ_{HF} can be approximated by product of orthonormal molecular orbitals ψ_i. As electrons are Fermions, antisymmetry is one of the requirements of the wave function i.e. swapping any two electrons in the system causes the sign of the wave function to change. The Hartree-Fock approximation improved on the Hartree method and added antisymmetry by means of the Slater determinant:

$$\Psi_{HF} = \frac{1}{\sqrt{N!}} \begin{vmatrix} \psi_1(\mathbf{x}_1) & \psi_2(\mathbf{x}_1) & \dots & \psi_N(\mathbf{x}_1) \\ \psi_1(\mathbf{x}_2) & \psi_2(\mathbf{x}_2) & \dots & \psi_N(\mathbf{x}_2) \\ \vdots & \vdots & \ddots & \vdots \\ \psi_1(\mathbf{x}_N) & \psi_2(\mathbf{x}_N) & \dots & \psi_N(\mathbf{x}_N) \end{vmatrix}, \tag{2.2.33}$$

where N is the number of electrons and $\mathbf{x}$ represents spin orbitals. The determinant combines the N electrons in every combination as a sum of products, applying negative signs appropriately, such that the swapping of electrons causes the sign of the system to change (swapping rows or columns within a determinant has this effect). The normalization factor $\frac{1}{\sqrt{N!}}$, takes account for the extra terms generated by the determinant.

The Hartree-Fock approximation is the method whereby the orthonormal orbitals ψ_i are found that minimize (2.2.2) for Ψ_{HF} [61, 74].

By applying the Hamiltonian from equation (2.2.4) to the Hartree-Fock wave function (2.2.33) the expectation value for the energy is given by:

$$E_{HF} = \left\langle \Psi_{HF} | \hat{H} | \Psi_{HF} \right\rangle = \sum_{i=1}^{N} (H_i) + \tfrac{1}{2} \sum_{i,j=1}^{N} (J_{ij} - K_{ij}) \,. \tag{2.2.34}$$

The first term deals with the kinetic energy and potential energy due to interactions with electrons and the nuclei:

$$H_i = \int \psi_i^*(\mathbf{x}) \left[-\tfrac{1}{2}\nabla^2 + v(\mathbf{x}) \right] \psi_i(\mathbf{x}) \, \mathrm{d}\mathbf{x}, \tag{2.2.35}$$

where $v(\mathbf{x})$ is a sum of potential energies for a given electron (MO) and all nuclei in the system. Equation (2.2.35) is equivalent to equations (2.2.5) and (2.2.6).

The second term in (2.2.34) deals with the interactions of electrons with each other (equivalent to equation (2.2.7)). J_{ij} and K_{ij} are known as the Coulomb and Exchange integrals respectively. Each is an integral over two electrons and three spacial dimensions (an integration over six dimensions), every pair of electrons is considered by the sum in (2.2.34). The Exchange integral takes account of the Pauli exclusion, whereby two electrons may not have the same spin orbital (be in the same orbital and have the same spin).

$$J_{ij} = \iint \psi_i^*(\mathbf{x}_1)\psi_j^*(\mathbf{x}_2) \, \frac{1}{r_{12}} \, \psi_i(\mathbf{x}_1)\psi_j(\mathbf{x}_2) \, \mathrm{d}\mathbf{x}_1 \mathrm{d}\mathbf{x}_2; \tag{2.2.36}$$

$$K_{ij} = \iint \psi_i^*(\mathbf{x}_1)\psi_j^*(\mathbf{x}_2) \, \frac{1}{r_{12}} \, \psi_i(\mathbf{x}_2)\psi_j(\mathbf{x}_1) \, \mathrm{d}\mathbf{x}_1 \mathrm{d}\mathbf{x}_2. \tag{2.2.37}$$

The HF approach uses a Self Consistent Field (SCF) method to find its wave functions, whereby a trial wave function is passed though an algorithm repeatedly until the output is the same as the input to within a given threshold.

A problem with some other methods (including Density Functional Theory, discussed in section 2.2.6) is that the calculation intrinsically considers each electron to interact with itself, which does not happen in nature, so for these methods, it becomes

necessary to attempt to subtract the energetic consequence of the interaction from the total energy. In HF, $J_{ii} = K_{ii}$ and as the J and K terms are subtracted from one another in equation (2.2.34), the so called self interaction is automatically eliminated.

The method described above, also known as Unrestricted Hartree-Fock (UHF) considers each electron to have its own molecular orbital and is used whenever there is an uneven number of electrons (an open shelled system). An alternative method known as Restricted Hartree-Fock (RHF) considers a system with only half as many orbitals as electrons, but multiplies the orbital separately by an $\alpha(s)$ and $\beta(s)$ function for two orbital sharing electrons. This method can be used when there are an even number of electrons (closed shell).

One of the weaknesses of the HF method is that it considers electrons to act only in the mean field of each other. The time dependent effect of correlation, in which, nearby electrons may move under each other's influence allows the energy of the system to reduce. As a consequence HF calculations that do not employ any so called post-Hartree-Fock methods will tend to overestimate the ground state potential energy. The post HF methods involved can include the mixing of millions of determinants [60, 61] and many body perturbation techniques.

2.2.6 Density Functional Theory

2.2.6.1 Introduction

We first note that a functional, in the context of DFT e.g. $E[\rho(\mathbf{r})]$, takes in a function as its argument and returns with a single number. A function will take in a variable (with a range of possible values) and map it to some other value, a functional will in effect consider all, or a large range of possible values of the function and map those to a single number. The functional usually does this via the integration of a function (an integral is an example of a functional).

DFT is a QM method that allows the energy and other properties of a system to be described by functionals of the charge density with respect to space $\rho(\mathbf{r})$ instead of using a many electron wave function [61]. The number of electrons in the system must still relate to the density by:

$$\int \rho(\mathbf{r}) \, \mathrm{d}\mathbf{r} = N, \tag{2.2.38}$$

where N is the number of electrons in the system.

2.2.6.2 The Thomas-Fermi Theory

The development of DFT began in the 1920s with the work of Llewellyn H. Thomas [75] and Enrico Fermi [76–78]. However, these models did not produce useful computer codes until 1964 [61].

The Thomas-Fermi model (in summary) attempts to calculate the electron density

by considering groups of ΔN non-interacting electrons in many boxes of volume ΔV, which behave as infinite potential wells. Quantum states are divided up so that every electron has a unique position in phase-space. Phase-space consists of six dimension with three being position and the other three being momentum. In the Thomas-Fermi model, the ΔV refers to the three momentum-space dimensions only (from which kinetic energy can be calculated).

The theory incorporates statistics on the occupancy of states, using the Fermi-Dirac distribution and then considers the limit as the sizes of the individual boxes tend towards zero. Through some manipulation, it produces an expression for the kinetic energy of the electrons as a functional of the charge density. Similar terms can be produced for the nuclear-electron and electron-electron interactions, allowing the total energy of the system to be calculated in terms of the electron density. This approach became known as the Local Density Approximation (LDA) [79].

The derivation will now be given and a fuller description of the derivation is given in [61].

For a three-dimensional potential energy well of side length l ($l^3 = \Delta V$), the energy of the states is given by:

$$\varepsilon(n_x, n_y, n_z) = \frac{h^2}{8ml^2}(n_x^2 + n_y^2 + n_z^2) = \frac{h^2}{8ml^2}R^2, \tag{2.2.39}$$

where n_x, n_y and n_z represent quantum numbers and so are positive integers, m is the mass of an electron and h is Plank's constant. R in this formula is proportional to the total momentum of an electron. States are expected to fill such that the n_x, n_y and n_z quantum numbers increase in an approximately spherical formation i.e. while populating the sphere: before $n_x^2 + n_y^2 + n_z^2 = R$ can increase, states with all combinations of the quantum numbers producing a lower momentum, must be occupied first. States with equal R will be degenerate and so have equal probability of occurring. As the quantum numbers can only take positive values, they will only fill one octant of the sphere. One eighth of the volume of the sphere of radius R will be approximately equal to the total number of states with an energy smaller than ε:

$$\Phi(\varepsilon) = \frac{1}{8}\left(\frac{4\pi R^3}{3}\right) = \frac{\pi}{6}\left(\frac{8ml^2\varepsilon}{h^2}\right)^{\frac{3}{2}}. \tag{2.2.40}$$

From (2.2.40) the density of states $g(\varepsilon)$ can be calculated:

$$g(\varepsilon) \approx \frac{\pi}{4}\left(\frac{8ml^2}{h^2}\right)^{\frac{3}{2}}\varepsilon^{3/2}. \tag{2.2.41}$$

The final component needed to calculate the actual energy within a ΔV cube is the probability of electrons occupying a given state (see equation (2.2.42)). At 0 kelvin, all the states with an energy lower than the Fermi energy will be occupied, leaving all others unoccupied, above this temperature there is a statistical distribution of occupied states given by the Fermi-Dirac distribution:

$$f(\varepsilon) = \frac{1}{1 + e^{(\varepsilon - \mu)/kT}}, \tag{2.2.42}$$

where k is Boltzmann's constant, T is absolute temperature and μ is the chemical potential, which is equal to the Fermi energy ε_F when the temperature is zero. One can see that in the case of zero, temperature, the exponent on e will either be positive or negative infinity, depending on whether the given state ε is higher or lower in energy than the Fermi energy. This explains the previously described $0\,\mathrm{K}$ occupancy.

By combining expressions (2.2.39), (2.2.41) and (2.2.42) an expression for the kinetic energy ΔE and the number of electrons ΔN within the box can be calculated:

$$\Delta E = 2 \int \varepsilon f(\varepsilon) g(\varepsilon) \, \mathrm{d}\varepsilon; \tag{2.2.43}$$

$$\Delta N = 2 \int f(\varepsilon) g(\varepsilon) \, \mathrm{d}\varepsilon. \tag{2.2.44}$$

The factor of two enters as an orbital/state may have two electrons occupying it. By combining (2.2.43) and (2.2.44), an expression for $0\,\mathrm{K}$ kinetic energy within the box as a function of charge density can be generated:

$$\Delta E = \frac{3h^2}{10m} \left(\frac{3}{8\pi} \right)^{\frac{2}{3}} l^3 \left(\frac{\Delta N}{l^3} \right)^{\frac{5}{3}}. \tag{2.2.45}$$

In the limit as the box sizes shrink to zero, $\Delta N / l^3 \to \rho$ as $l^3 = \Delta V$. Converting this to an integral, to consider the kinetic energy of an entire system of electrons as a function of the electron density, the Thomas-Fermi functional for kinetic energy is given by:

$$T_{TF}[\rho] = C_F \int \rho^{\frac{5}{3}}(\mathbf{r}) \, \mathrm{d}\mathbf{r}, \tag{2.2.46}$$

where $C_F = \frac{3}{10}(3\pi^2)^{2/3}$. The system has been converted to atomic units by the multiplication of $4m\pi^2/h^2$. In the conversion from (2.2.45) to (2.2.46), the l^3 becomes integration over $\mathrm{d}\mathbf{r}$.

By combining the kinetic energy functional with classical terms for the interaction for electrons and nuclei, one can produce the Thomas-Fermi functional for kinetic energy. The Thomas-Fermi functional for an atom is provided in (2.2.47). However,

its expansion to systems of more than one atom is not straightforward as the nature of molecular bonding is not described by the kinetic energy term.

$$E_{TF}[\rho] = C_F \int \rho^{\frac{5}{3}}(\mathbf{r})\ \mathrm{d}\mathbf{r} - Z \int \frac{\rho(\mathbf{r})}{r}\ \mathrm{d}\mathbf{r} + \frac{1}{2} \iint \frac{\rho(\mathbf{r}_1)\rho(\mathbf{r}_2)}{|\mathbf{r}_1 - \mathbf{r}_2|}\ \mathrm{d}\mathbf{r}_1\ \mathrm{d}\mathbf{r}_2. \quad (2.2.47)$$

This method as devised by Thomas and Fermi does not take into account exchange or correlation effects, but provides an approximate energy of the system which can be minimized to find the ground state under the constraint in equation (2.2.38).

As can be seen from the last term of (2.2.47), every point of electron density interacts with every other point of electron density. As electrons are no longer discrete entities, it becomes difficult to remove the component of the interaction where an electron interacts with itself (self-interaction).

2.2.6.3 The Hohenberg-Kohn Theory

The Hohenberg-Kohn theory was developed subsequently to the Thomas-Fermi theory by Pierre Hohenberg and Walter Kohn. A paper was published in 1964 [80] describing their theory, which begins by noting that given a configuration of nuclei (an external potential) $v(\mathbf{r})$ and a number of electrons N, it is possible to completely determine the properties of the ground state. The theory demonstrates that (assuming non-degeneracy) $v(\mathbf{r})$ is a unique functional of $\rho(\mathbf{r})$, apart from a trivial additive constant [80]. Also, it is impossible for two different external potentials to produce the same electron density.

The proof of the theory uses the variational principle by stating that for a given Hamiltonian $\hat{H}$ (which incorporates the external potential), the wave function that minimizes it is the ground state Ψ. Therefore if the ground state wave function Ψ' from another Hamiltonian $\hat{H}'$ is applied to $\hat{H}$, the energy will be greater than E_0.

$$\begin{aligned} E_0 < \left\langle \Psi' \middle| \hat{H} \middle| \Psi' \right\rangle &= \left\langle \Psi' \middle| \hat{H}' \middle| \Psi' \right\rangle + \left\langle \Psi' \middle| \hat{H} - \hat{H}' \middle| \Psi' \right\rangle \\ &= E_0' + \int \rho(\mathbf{r})[v(\mathbf{r}) - v'(\mathbf{r})]\ \mathrm{d}\mathbf{r}, \end{aligned} \quad (2.2.48)$$

$$\begin{aligned} E_0' < \left\langle \Psi \middle| \hat{H}' \middle| \Psi \right\rangle &= \left\langle \Psi \middle| \hat{H} \middle| \Psi \right\rangle + \left\langle \Psi \middle| \hat{H}' - \hat{H} \middle| \Psi \right\rangle \\ &= E_0 - \int \rho(\mathbf{r})[v(\mathbf{r}) - v'(\mathbf{r})]\ \mathrm{d}\mathbf{r}. \end{aligned} \quad (2.2.49)$$

By considering the difference between the two Hamiltonians and assuming that both wave functions produce the same electron density, as in (2.2.48) and (2.2.49), a proof can be made by contradiction. (2.2.50) is produced by adding together the two previous equations:

$$E_0 + E_0' < E_0 + E_0'; \quad (2.2.50)$$

ρ can therefore be used to determine all properties of the system in terms of functionals:

$$E_v[\rho] = V_{ne}[\rho] + F_{HK}[\rho]; \tag{2.2.51}$$

$$F_{HK}[\rho] = T[\rho] + V_{ee}[\rho], \tag{2.2.52}$$

where $E_v[\rho]$ is the total energy functional taking the external potential into account. For the $V_{ne}[\rho]$ functional, one may use a classical charge interaction term:

$$V_{ne}[\rho] = \int \sum_{\alpha} \frac{Z_\alpha \rho(\mathbf{r})}{r_\alpha} \, \mathrm{d}\mathbf{r}, \tag{2.2.53}$$

where Z_α is atomic number of nucleus α and r_α is the distance between the nuclei and point $\mathbf{r}$.

The Hohenberg-Kohn theory makes no statement about the nature of the kinetic energy functional $T[\rho]$, but breaks the electronic repulsion term into two parts:

$$V_{ee}[\rho] = J[\rho] + E_{xc}[\rho], \tag{2.2.54}$$

where $J[\rho]$ is the classical electron repulsive term set out in the last term of (2.2.47) $E_{xc}[\rho]$ is a non-classical term and is composed of correlation and exchange contributions which were mentioned at the end of section 2.2.5. Exchange-correlation values are exceptionally hard to calculate in QM systems, though many advances in these methods have been made over the last 40 years.

The Hohenberg-Kohn theorem restates the variational principle for wave functions (2.2.3) in terms of electron density:

$$E_0 \leq E_v[\tilde{\rho}], \tag{2.2.55}$$

where $\tilde{\rho}$ is a trial density that satisfies the condition in equation (2.2.38).

By minimizing $E_v[\tilde{\rho}]$ under the condition in (2.2.38), e.g. by use of the method of Lagrange multipliers [81], one can determine the ground state density and all of its properties.

$$\mu = \frac{\delta E_v[\rho]}{\delta \rho(\mathbf{r})} = v(\mathbf{r}) + \frac{\delta F_{HK}[\rho]}{\delta \rho(\mathbf{r})}, \tag{2.2.56}$$

where μ is the chemical potential (and also the Lagrange multiplier used in minimization). The right hand side of equation (2.2.56), shows how the external potential can be separated from the $F_{HK}[\rho]$ functional as the $V_{ne}[\rho]$ functional was the integral over the product of density ρ and external potential $v(\mathbf{r})$ (which is known before a DFT calculation starts).

Equation (2.2.56) is one of the basic working equations of DFT [61]. Much of

the difficulty in performing calculations with this method come from determining the proper description of $F_{HK}[\rho]$.

2.2.6.4 The Kohn-Sham Method

The Kohn-Sham method of performing QM calculations was first published in 1965 [82] by Walter Kohn and Lu Jeu Sham. It builds on the Thomas-Fermi theory (section 2.2.6.2) and the Hohenberg-Kohn theory (section 2.2.6.3) by improving on the approximation of the kinetic energy of the system. Kohn-Sham reintroduce the concept of one electron non-interacting antisymmetric orbitals of the Slater determinant type (2.2.33) described earlier in section 2.2.5. The kinetic energy functional is taken as the kinetic energy component of the Schrödinger equation, with the associated electron density resulting from the sum of the squares of the orbital wave functions:

$$T_s[\rho] = \sum_i^N \left\langle \psi_i \left| -\tfrac{1}{2}\nabla^2 \right| \psi_i \right\rangle = \left\langle \Psi_s \left| \sum_i^N (-\tfrac{1}{2}\nabla_i^2) \right| \Psi_s \right\rangle; \tag{2.2.57}$$

$$\rho(\mathbf{r}) = \sum_i^N |\psi_i(\mathbf{r})|^2, \tag{2.2.58}$$

where ψ_i are one electron orbitals, Ψ_s is a Slater wave function for the system and N is the number of electrons. Though the kinetic energy functional itself is calculated using just the standard kinetic energy operator, the Hamiltonian used when fitting the orbitals $\hat{H}_s$, includes an effective potential $v_s(\mathbf{r})$. v_s will be shown later to include aspects of all of the various interactions, i.e. nuclear-electron interaction $V_{ne}[\rho]$ or $v(\mathbf{r})$ and electron-electron interaction $V_{ee}[\rho] = J[\rho] + E_{xc}[\rho]$ where $J[\rho]$ is the classical portion and $E_{xc}[\rho]$ is the exchange-correlation functional.

$$\hat{H}_s = \sum_i^N (-\tfrac{1}{2}\nabla^2) + \sum_i^N v_s(\mathrm{r_i}). \tag{2.2.59}$$

The portions of the kinetic energy that are not included in the $T_s[\rho]$ functional are placed into the $E_{xc}[\rho]$ functional. The $F_{HK}[\rho]$ functional, defined in (2.2.52) and (2.2.54) is rewritten to include the new kinetic energy functional:

$$F_s[\rho] = T_s[\rho] + J[\rho] + E_{xcs}[\rho]; \tag{2.2.60}$$

$$E_{xcs}[\rho] = E_{xc}[\rho] + (T[\rho] - T_s[\rho]), \tag{2.2.61}$$

where $F_s[\rho]$ is the Kohn-Sham version of $F_{HK}[\rho]$, $T[\rho]$ is the exact kinetic energy operator $T_s[\rho]$ is the Kohn-Sham kinetic energy operator, $E_{xc}[\rho]$ is the correlation-exchange energy and $E_{xcs}[\rho]$ is the correlation-exchange functional modified to include the error

from the kinetic energy functional which is relatively small [61].

Equation (2.2.56) with the Lagrange method of optimization can be rewritten:

$$\mu = \frac{\delta E[\rho]}{\delta \rho(\mathbf{r})} = \frac{\delta V_{ne}[\rho]}{\delta \rho(\mathbf{r})} + \frac{\delta J[\rho]}{\delta \rho(\mathbf{r})} + \frac{\delta E_{xcs}[\rho]}{\delta \rho(\mathbf{r})} + \frac{\delta T_s[\rho]}{\delta \rho(\mathbf{r})}; \tag{2.2.62}$$

$$= v(\mathbf{r}) + \int \frac{\rho(\mathbf{r}')}{|\mathbf{r} - \mathbf{r}'|}\, \mathrm{d}\mathbf{r}' + v_{xcs}(\mathrm{r}) + \frac{\delta T_s[\rho]}{\delta \rho(\mathbf{r})}; \tag{2.2.63}$$

$$= v_s(\mathbf{r}) + \frac{\delta T_s[\rho]}{\delta \rho(\mathbf{r})}, \tag{2.2.64}$$

where:

$$v_s(\mathbf{r}) = v(\mathbf{r}) + \int \frac{\rho(\mathbf{r}')}{|\mathbf{r} - \mathbf{r}'|}\, \mathrm{d}\mathbf{r}' + v_{xcs}(\mathrm{r}); \tag{2.2.65}$$

$$v_{xcs}(\mathrm{r}) = \frac{\delta E_{xcs}[\rho]}{\delta \rho(\mathbf{r})}. \tag{2.2.66}$$

Equation (2.2.64) is not usually solved directly as in the case of the Hohenberg-Kohn counterpart (2.2.56). Instead an SCF method is applied in which trial electron densities are repeatedly cycled though an algorithm with the accuracy increasing on each cycle. First an initial guess is made for the density $\tilde{\rho}$, this is passed to (2.2.65) to get an initial guess for the effective potential $\tilde{v_s}(\mathbf{r})$. Next, solutions to the wave functions are calculated by solving (2.2.67):

$$\left[-\tfrac{1}{2}\nabla^2 + v_s(\mathbf{r})\right] \psi_i = \boldsymbol{\varepsilon}_i \psi_i. \tag{2.2.67}$$

An improved estimate of the density is made by passing the solved wave functions into (2.2.58) and the procedure is restarted. The total energy of the system can be calculated at any stage using (2.2.51) with the substituted (2.2.60).

This method proved to be very powerful and is the basis for many DFT methods used today including LDA [79], and the more powerful Generalized Gradient Approximation (GGA) [83, 84]. Also, as this DFT method implements the concept of orbitals, it becomes possible to describe the QM properties of a system in terms of the ubiquitous basis sets. The approach of using orbitals also makes it easier to interpret the electronic and spectroscopic properties of materials.

2.2.6.5 Generalized Gradient Approximation Method

The Local Density Approximation (LDA) was one of the first applications of the Khon-Sham equations. LDA is a closed-shell method, in which orbitals are either doubly occupied or unoccupied; its open shell equivalent (zero, one or two electrons per orbital) is the Local Spin Density approximation (LSD). These functionals were very successful, but only worked well when the electron density was fairly uniform (such as in a metal).

A successor to this method was the Generalized Gradient Approximation (GGA) which takes account both of the electronic charge density and its first derivative (density gradient). GGA deals with inhomogeneous charge distributions more accurately, but is sometimes less accurate for homogeneous charge distributions.

In DFT, the only approximated terms are confined within the exchange-correlation functional and variations between DFT methods are placed within it. The LSD and GGA versions of the exchange-correlation energy can be specified thus:

$$E_{xc}^{\mathrm{LSD}}[\rho_\alpha, \rho_\beta] = \int \rho v_{xc}^{\mathrm{unif}}(\rho_\alpha, \rho_\beta)\ \mathrm{d}\mathbf{r}; \tag{2.2.68}$$

$$E_{xc}^{\mathrm{GGA}}[\rho_\alpha, \rho_\beta] = \int f(\rho_\alpha, \rho_\beta, \nabla\rho_\alpha, \nabla\rho_\beta)\ \mathrm{d}\mathbf{r}, \tag{2.2.69}$$

where electron charge density $\rho = \rho_\alpha + \rho_\beta$, α and β respectively represent up and down spin and v_{xc}^{unif} is the exchange potential for a charge distribution assumed to be uniform.

The general merits of GGA functionals in comparison with LSD functionals were described in [83] and contained references: "GGA's tend to improve total energies, atomization energies, energy barriers and structural energy differences. GGA's expand and soften bonds, an effect that sometimes corrects and sometimes overcorrects the LSD prediction. GGA's favor density inhomogeneity more than LSD does."

For a more in depth explanation of the GGA method, please see [83, 84] which describe the PBE functional and [85], which describes the PBEsol functional. The PBE method was named after its developers John Perdew, Kieron Burke and Matthias Ernzerhof. PBEsol was an adaptation of PBE intended specifically for solids and surfaces. Both of these methods were implemented within *VASP* and used for energy landscape calculations reported in chapters 3 and 4.

2.2.7 Hybrid Methods

Hybrid density functionals use a more computationally expensive technique to deal with inaccuracies in the exchange-correlation functionals. On its own, the single determinantal Hartree-Fock method omits the effects of correlation, one of its strengths is its exact calculation of 'exchange' (see equation (2.2.37)). A hybrid calculation calculates the HF exchange using the one electron orbitals calculated by the Kohn-Sham equations. A portion of the HF exchange is combined with the DFT $E_{xc}[\rho]$ functional with different ratios of mixing being used depending on the hybrid method. The hybrid density functional B97-2 [86, 87], used for the *ChemShell* cluster calculations, described in section 2.5, is a variation of the GGA method, but uses a component of 0.21 exact HF exchange with its own exchange correlation functional.

Having considered the most accurate method used for calculations on atoms, we now consider some of the computationally simpler classical techniques.

2.3 Molecular Mechanical Methodology

2.3.1 Introduction

Quantum mechanical techniques provide the most accurate methods for calculating the electronic and structural behaviour of atomic systems. However, the calculations are computationally expensive and generally scale poorly with system size and the number of processors. One of the great triumphs of 20^{th} century physical theory was the development of Molecular Modelling (also known as force-field methods). These methods model atomic systems in a much simpler way, taking no specific account for individual electrons but instead, using classical physics and parameterized functions, to describe atomic interactions. As a consequence, much larger systems of atoms can be studied compared with QM methods. In the following sub-sections, various MM methods used within this thesis will be described.

MM considers atoms to each consist of one or in the case of the Shell Model (see section 2.3.5) two points, with various forces acting between them and other atoms.

2.3.2 Calculating Energy

The classical model assumes that the energy of a system can be decomposed into an expansion in terms of interactions between different subsets of the total number of atoms [88], N.

$$U = \sum_{i=1}^{N} U_i + \frac{1}{2!}\sum_{i=1}^{N}\sum_{j=1}^{N} U_{ij} + \frac{1}{3!}\sum_{i=1}^{N}\sum_{j=1}^{N}\sum_{k=1}^{N} U_{ijk} + \dots \tag{2.3.1}$$

The first term is the self-energy or internal energy of an atom (such terms arise if the atom polarizes under the influence of external fields). The second term represent interactions between all pairs of atoms, which include Coulombic/long range forces (see section 2.3.3) and short range interactions (see section 2.3.4). Terms that involve three and four atoms at once are used to describe angle-bending, torsion, and other terms within molecules. Third and fourth order terms have not been used in the course of this thesis and will not be described in more detail. Higher order terms than four are not generally used.

2.3.3 Coulombic Interaction

The long range Coulombic potentials usually account for as much as $90\,\%$ of the total internal energy for ionic compounds [88]. For any pair of ions:

$$U_{ij}^{C} = \frac{q_i q_j}{4\pi\varepsilon_0 r_{ij}}, \tag{2.3.2}$$

where q_i represents the charge on ion i. To convert to atomic units (which simplifies the expression), one multiplies by $4\pi\varepsilon_0$.

Despite the simplicity of a single Coulombic calculation (or a sum over a finite number of charges), there are complications associated with performing the calculation for a periodic (infinite lattice) system. The potential contribution of a point-charge is reduced as the reciprocal of the separation r; but the number of charges at distance r is proportional to r^2. As a result, the potential energy of a unit cell, due to the Coulombic interactions will converge only under certain circumstances.

One technique for dealing with this problem is to create charge neutral groups of charges (multi-poles) and sum over these [89] as the potential effects of multi-poles decreases much faster than monopoles. A much more commonly used method of dealing with the electric potential energy contributions on the internal energy of a cell in an infinite lattice is known as Ewald summation.

2.3.3.1 Ewald Summation

The method of Ewald summation [90] was developed by Paul Ewald in the early 20^{th} century to take into account the Madelung field [91] from an infinite lattice. It makes extensive use of Gaussian charge distributions (2.3.3), which at a sufficient distance, behave the same way as point-charges/ions. Gaussian functions (2.3.3) are smoothly varying in space and easier to deal with in reciprocal/Fourier space than delta functions:

$$\rho(r) = z(\zeta/\pi)^{3/2} e^{-\zeta r^2}, \tag{2.3.3}$$

where ρ is charge density, r is distance from the point of origin, z is the integral of the charge (or the charge of the equivalent ion) and ζ characterizes the Gaussians' shape. The description below, loosely follows those found in [88] and [92], where further detail and alternative explanations are provided.

The Ewald method works by taking the original infinite field of point-charges (which must be charge neutral overall) and both adding and subtracting a field of Gaussian functions as described in figure 2.3.1, where ($a + b + c = a$). Each Gaussian function is representative of a point-charge in terms of its integral and position. These three components are combined into two separate summation calculations, both of which converge rapidly. The so called *real-space summation* deals with nearby charges and a *Fourier-space summation* deals with interaction with more distant charges. A third *self-interaction* term is also required.

We first consider the Fourier-space summation in which we sum up the potential at the site of every point-charge/ion within the unit cell due to the *compensating charge* i.e. the infinite field of Gaussian functions of the same sign as the original point-charges (b in figure 2.3.1). The Gaussian field interacts with each point-charge within the unit

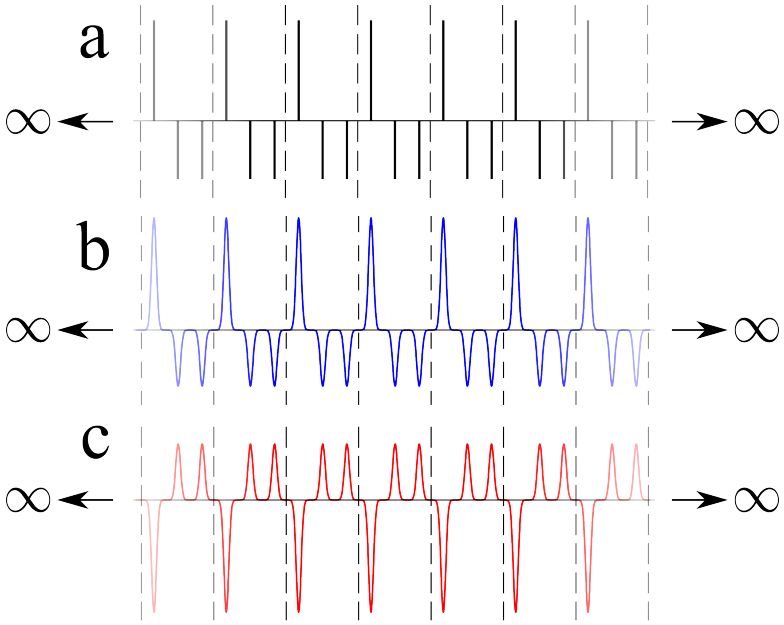

Figure 2.3.1: A diagram representing a one-dimensional periodic unit cell containing three point-charges (one positive and two negative). (a) uses delta functions to represent the conventional point-charges, (b), also known as the compensating charge represents a Gaussian field, which at distances can accurately replace the rôle of a and (c) is a negative version of b and is also known as screening charge.

cell but does not interact with itself. The Fourier transform converges rapidly with the length of the **k** vector:

$$U_{\text{Fourier}} = \frac{1}{2}\sum_{i,j}^{N}\sum_{\mathbf{k}\neq\mathbf{0}}\frac{4\pi z_i z_j}{Vk^2}\exp(i\mathbf{k}\cdot\mathbf{r}_{ij})\exp(-k^2/4\zeta), \tag{2.3.4}$$

where N is the number of point-charges/ions in the periodic cell (usually some super cell of the original unit cell), V is the volume of the cell, z_i represent the charge on point i in atomic units, **k** is a reciprocal-space vector pointing to an ion (see section 2.2.2.3), $\mathbf{r}_{ij}$ is a vector pointing between charges i and j.

Equation (2.3.4) is formulated such that it includes an interaction between each point-charge/ion z_i and its own equivalent Gaussian charge distribution. This over counting is non-physical and so an additional self-interaction term is added to take account of this error (2.3.5). The self-interaction term is simply the (negative) interaction between a point-charge and a single Gaussian of the same sign placed on top of it:

$$U_{\text{Self}} = -\sum_{i}^{N} z_i^2\left(\frac{\zeta}{\pi}\right)^{1/2}. \tag{2.3.5}$$

We now consider the real-space summation in which we sum together a and c

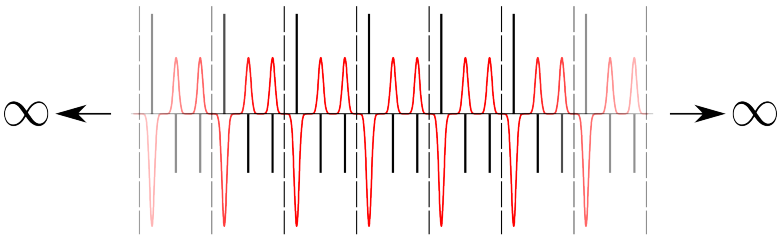

Figure 2.3.2: A diagram showing the addition of the screening potential to the point-charges in a one-dimensional periodic system. This is produced by superimposing components a and c from figure 2.3.1.

from figure 2.3.1, as has been illustrated in figure 2.3.2. The combination of a point-charge, with an oppositely charged but equivalent volume Gaussian function (known as a screening charge), results in an object whose effects decay very rapidly with distance (compared to an unscreened point-charge).

We calculate for every point-charge in the unit cell z_i, the potential due to every other Gaussian screened point-charge. Due to the short ranged nature of the screened charges, one only needs to consider the contribution to the potential energy of the unit cell from point-charges/ions a short distance away. The rapidly converging sum of the contributions to the PE from the screened potentials is evaluated in real-space and is is given by:

$$U_{\text{Real}} = \frac{1}{2}\sum_{i\neq j}^{N} \frac{z_i z_j}{r_{ij}} \operatorname{erfc}\left(\zeta^{1/2} r_{ij}\right), \tag{2.3.6}$$

where

$$\operatorname{erfc}(x) = 1 - \operatorname{erf}(x) = 2\pi^{-1/2}\int_x^{\infty} e^{-t^2}\,\mathrm{d}t. \tag{2.3.7}$$

Unlike equation (2.3.4), (2.3.6) has been formulated so as to exclude any self-interaction. As such no self-interaction term is required to correct the real-space interaction term. The total energy for the system is then given by:

$$U_{\text{Total}} = U_{\text{Fourier}} + U_{\text{self}} + U_{\text{Real}}. \tag{2.3.8}$$

The ζ parameter controls the width of the Gaussian functions, with a larger ζ resulting in their narrowing and closer approximation to a point-charge. A larger ζ allows the size of the real-space region to be decreased as the charges will be completely screened at a shorter distance. This in turn decreases the computational effort required for the real-space calculation. However, the computation effort of the Fourier/reciprocal-space calculation will increase with ζ as the rate of convergence with respect to $\mathbf{k}$ vector decreases.

A method of choosing optimum values for ζ and the corresponding cut-off radius

for the real-space and Fourier-space calculation was presented in reference [88, 93]:

$$\zeta_{\text{opt}} = \left(\frac{N\pi^3}{V^2}\right)^{\frac{1}{3}}; \tag{2.3.9}$$

$$r_{\max} = \left(\frac{-\ln(A)}{\zeta}\right)^{1/2}; \tag{2.3.10}$$

$$k_{\max} = 2\left(-\zeta \ln(A)\right)^{1/2}, \tag{2.3.11}$$

where $A < 1$ is a parameter that allows the precision of the calculation to be controlled (lower values result in a more accurate calculation). Using this method, energy terms that are lower than $Aq^2/V^{1/3}$ are excluded, in the case where all charges are of the same magnitude and the cell is cubic.

2.3.4 Short Range Interactions

2.3.4.1 Introduction

There are various shorter range interactions between atoms, whose effects are a consequence of complex quantum mechanical interactions that take place at small distances. Their effects drop off much faster than those of Coulombic interactions and so it is usually acceptable to use a distance cut-off above which, they are set to zero.

2.3.4.2 Dispersion Interaction

Dispersive forces are the most long ranging after the Coulomb forces [88] and occur as a result of random charge fluctuations in molecules and the interaction of induced temporary dipoles. They can be parameterized as follows:

$$U_{ij}^{\text{Dispersion}} = -\frac{C_6}{r_{ij}^6} - \frac{C_6}{r_{ij}^8} - \frac{C_{10}}{r_{ij}^{10}} - \cdots = \sum_{n=3}^{\infty} -\frac{C_{2n}}{r_{ij}^{2n}} \approx -\frac{C_6}{r_{ij}^6}. \tag{2.3.12}$$

The first term corresponds to the interaction of two instantaneous dipoles, with the subsequent terms corresponding to higher order fluctuating moments [88]. The single C_6 term is generally sufficient in practice. The dispersive forces will converge given a sufficient radial cut-off; however, sometimes, summation techniques similar to the Ewald summation are used to speed up the convergence.

2.3.4.3 Buckingham and Lennard-Jones Interaction

Repulsive short-range forces come in to play when atomic charge clouds overlap. There are two main causes of the atomic repulsion. The first is due to the interaction between the electronic charge clouds themselves, known as *penetration interaction*. The second is nuclei-nuclei repulsion, which is screened by the charge clouds when the atomic separation is great but at small separations, the nuclear screening is reduced. A

schematic of the attractive and repulsive forces experienced between atoms is shown in figure 2.3.3.

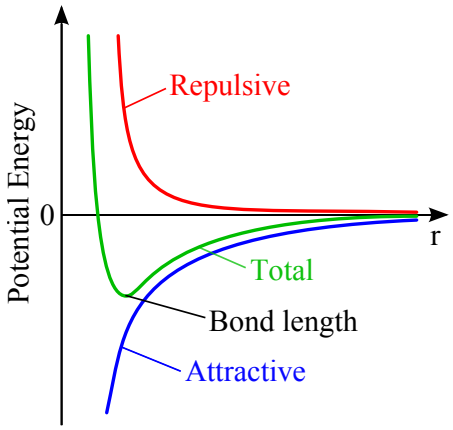

Figure 2.3.3: A schematic of potential energy vs. distance between two atoms. The attractive and repulsive forces compete with each other, the bond length is corresponds to the total potential energy minimum.

Two very commonly used functions for describing the short range forces are the Buckingham [94, 95] (equation (2.3.13)) and Lennard-Jones [96, 97] (equation (2.3.14)) potentials. The Buckingham potential consists of an exponential term added to the most significant term from the dispersion interaction. The Lennard-Jones potential uses a reciprocal power relationship added to a dispersion term:

$$U_{ij}^{\text{Buckingham}} = A\exp\left(\frac{-r_{ij}}{\rho}\right) - \frac{C_6}{r_{ij}^6}; \tag{2.3.13}$$

$$U_{ij}^{\text{Lennard-Jones}} = \frac{C_m}{r_{ij}^m} - \frac{C_6}{r_{ij}^6}, \tag{2.3.14}$$

where A, ρ and $C_{\#}$ are fitting parameters, determined by comparison of the properties of the system with those of experimentally known atomic systems (or sometimes higher level theoretical data e.g. QM). The lattice parameters, crystal symmetry group, internal positions of ions and low frequency (static) dielectric constants are the data of most direct significance for fitting these parameters. Various methods can be employed for the fitting, including automated algorithms and human trial and improvement approaches. Typical values for m are 9–12 [88].

One of the shortcomings of Buckingham potentials is that at very low values of atomic separation r_{ij}, the potential energy decreases very rapidly down to negative infinity (when the radius is zero). The effect is known as a *Buckingham catastrophe*. The Lennard-Jones potential does not suffer from the same shortfall as the power m is greater than six (which is used in the similarly described attractive dispersive term).

For this reason Lennard-Jones potentials are sometimes used in conjunction with Buckingham potentials, to make them more robust.

Unlike QM *ab-initio* methods, MM potentials have to be fitted for particular atomic systems. Sometimes it is sufficient to compose a set of potentials from reusing two bodied terms (from a more general system) describing each pair of atoms in the system. In the case of the work in this thesis, it was necessary to fit sets of potentials to specific low temperature phases of STO as the existing potentials did not reproduce the fine structure of the crystal (see section 5.3).

2.3.5 Shell Model

The model as described so far does not have a way of describing the polarization of atoms. There are two main approaches to modelling this process; one is to use the point dipole or multipole models [88, 98] and the other is the Shell Model proposed by Gale Dick and Albert Overhauser in 1958 [99].

The point dipole model regards an atom or ion to be a single point with a dipole moment proportional to the electric field it experiences from external sources (either other atoms/ions or an externally applied field):

$$\boldsymbol{\mu} = \alpha \mathbf{E}; \tag{2.3.15}$$

$$U^{\text{Polarization}} = -\tfrac{1}{2}\alpha |\mathbf{E}|^2, \tag{2.3.16}$$

where $\boldsymbol{\mu}$ is the dipole moment, α is the polarizability and $\mathbf{E}$ is the electric field strength.

The linear dependence of the dipole on the electric field is a weakness as in real systems the extent of polarization will be influenced by neighbouring atoms which will dampen excessive polarization. As a result of this weakness, polarization catastrophes can occur in strong electric fields, where ions mutually and excessively polarize each other and the model breaks down. This occurrence is often indicated by a large unexpected decrease in the energy of the system (potentially can go to negative infinity, depending on the nature of the model).

The Shell Model (see figure 2.3.4), by contrast, models an atom/ion as consisting of two point-charges, labelled the core and shell and bound together by a spring. The sum of the core and shell charges must equal the charge on the ion. However, they do not specifically represent the nuclei and electrons as separate entities. The core represents the nucleus and innermost electrons while the shell represents the more diffuse outer electrons.

On the application of an electric field, the core and shell separate, limited by the potential in the spring between them. The result is the formation of a real dipole, created by the displacement of charge within the system. Short range repulsion (e.g.

Buckingham potentials) are generally applied only between the shells. The result is a damping effect, which limits the polarization of the atoms as the shells repel other shells. Like in the quantum mechanical model, the Born approximation is used such that shell positions are fitted around a rigid core until a geometry step is made, at which point the cores are moved (sometimes with the shells attached to them, depending on the model).

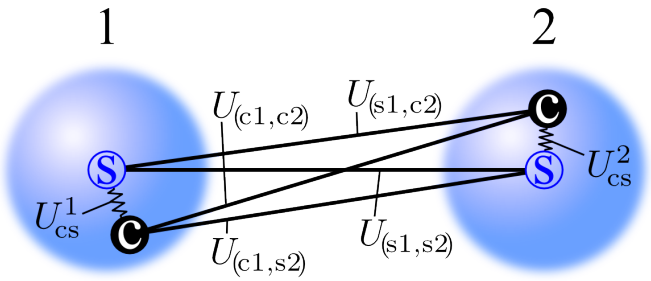

Figure 2.3.4: Diagram showing two differently polarized ions; the blue circles around the shells illustrates the diffuse electron cloud that they model. U_{cs} consists of the potential given in (2.3.17) only. $U_{(c1,c2)}$, $U_{(c1,s2)}$ and $U_{(s1,c2)}$ will usually involve only Coulombic interactions and $U_{(s1,s2)}$ typically includes Coulombic interactions and a short-range pair potential interaction.

In the original formulation of the model [99], there was just a single harmonic spring constant k between the core and shell. More recently another term was in certain systems introduced with an r^4 dependence on energy [100] to increase the dampening at greater core-shell separations and further reduce the danger of a polarization catastrophe.

$$U_{cs}^{\text{Polarization}} = \frac{1}{2}k_2 r_{cs}^2 + \frac{1}{24}k_4 r_{cs}^4, \tag{2.3.17}$$

where U_{cs} is the potential energy of the interaction between the core and shell of one ion, r_{cs} is the corresponding distance between the core and shell and k_2 and k_4 are parameters fitted for a given system. More can be read on the subject of inter-atomic potentials in [101].

The k_2 and k_4 parameters are normally obtained by fitting to experimental data. The high frequency dielectric constants, which relate to how tightly the diffuse charge cloud is bound to the nucleus are most relevant for the fitting of these parameters. For fitting the k_2 term, the dielectric data from the unpolarized crystal (ideal cubic in the case of STO) is most useful. For fitting the k_4 term, which better describes the binding of the shell at large separations, dielectric data from the polarized crystal is more useful (low temperature ideal rhombohedral in the case of STO). In practice, the k_4 term is much harder to fit in a precise way and so a minimum standard is to choose a number sufficiently large that it does not allow a polarization catastrophe in defect calculations.

Part of the work conducted towards this thesis was based around the study of defects within STO. In the next section, we consider one of the methods for performing calculations on defects. The Mott-Littleton approach, which is an MM model, models the effect of defects within an infinite crystal.

2.3.6 Mott-Littleton Method

The methods discussed so far have only dealt with calculations on either an infinite (periodic) crystal, or a system of a finite number of atoms (as in a molecule or cluster of atoms in a vacuum). Another type of system we may wish to consider comprises of an isolated defect within an infinite crystal. One can create an approximation to this in a periodic model by using a large super-cell with the defect. However, there is an intrinsic error associated with this method, arising from defects in neighbouring super-cells interacting with one another. The self-interaction may make the method inappropriate for diluted systems with low defect concentrations.

The Mott-Littleton approach was first published in 1938 [102] by Nevill Mott and Margery Littleton, though the modern implementation differs slightly from the original method [88, 103]. The method uses an embedded cluster approach which proposes that the system be broken down into three concentric regions. Region 1 is centred on the defect or in the mid point between multiple defects. Interactions between atoms in this region are calculated explicitly using Coulombic and short range forces discussed in sections 2.3.3 and 2.3.4 respectively.

Outside region 1, the system is dealt with in a more approximate way, as it is assumed the the system will be perturbed to a lesser degree. Surrounding region 1 are regions 2a and 2b, the latter of which extends to infinity. Regions 1 and 2a are usually defined by either the number of ions within them N or with a cut-off radius from the centre. The total energy of the system is given by:

$$U_{\text{tot}}(\mathbf{x}, \boldsymbol{\xi}) = U_{11}(\mathbf{x}) + U_{12}(\mathbf{x}, \boldsymbol{\xi}) + U_{22}(\boldsymbol{\xi}), \tag{2.3.18}$$

where $\mathbf{x}$ represents the Cartesian coordinates of region 1 ions, $\boldsymbol{\xi}$ represents the Cartesian displacement of ions in region 2 and the pairs of indices in the energy terms represent interactions between the ions of the regions. Regions 2a and 2b are counted together here [88].

The Mott-Littleton method uses approximations to deal with the system without evaluating the self-energy of region 2 (there are no short or long range interactions within the region). This is achieved by careful consideration of the interaction between region 1 and 2. Region 2a is essentially an interface region, as it is assumed that region 2b only experiences Coulombic forces from region 1. If region 2a is made at least the thickness of the short range pair potentials, then it is no longer an approximation

(compared to the non-defective MM methods). It is also advisable for region 1 to have the same radius as the pair potentials.

In order to exclude the self energy of region 2 from equation (2.3.18), one assumes that the perturbing forces from the defect are small enough that the ions in region 2 displace harmonically. The self-energy of such a system is:

$$U_{22}(\boldsymbol{\xi}) = \frac{1}{2}\boldsymbol{\xi}^{\mathrm{T}}\mathbf{H}_{22}\boldsymbol{\xi}, \tag{2.3.19}$$

where $\mathbf{H_{22}}$ is the Hessian matrix of second derivatives of energy with respect to displacement for region 2. By differentiating equation (2.3.18) with respect to $\boldsymbol{\xi}$ and setting equal to zero so as to consider the system at equilibrium we get a force equation:

$$\frac{\partial U_{\mathrm{tot}}(\mathbf{x},\boldsymbol{\xi})}{\partial \boldsymbol{\xi}} = \frac{\partial U_{12}(\mathbf{x},\boldsymbol{\xi})}{\partial \boldsymbol{\xi}} + \mathbf{H}_{22}\boldsymbol{\xi} = 0; \tag{2.3.20}$$

$$\mathbf{H}_{22}\boldsymbol{\xi} = -\frac{\partial U_{12}(\mathbf{x},\boldsymbol{\xi})}{\partial \boldsymbol{\xi}}. \tag{2.3.21}$$

The U_{11} term disappears as it is independent of $\boldsymbol{\xi}$. Equation (2.3.21) is substituted into (2.3.19) and then back into (2.3.18):

$$U_{\mathrm{tot}} = U_{11}(\mathbf{x}) + U_{12}(\mathbf{x},\boldsymbol{\xi}) - \frac{1}{2}\frac{\partial U_{12}(\mathbf{x},\boldsymbol{\xi})}{\partial \boldsymbol{\xi}}\boldsymbol{\xi}. \tag{2.3.22}$$

In a calculation, the system will first be minimized with respect to energy using a geometry optimization method (see section 2.4), once the system has converged to within a certain tolerance, the positions of the ions in region 1 are optimized by way of force balance (it is assumed that the forces are harmonic at this point).

In region 2a, the forces due to interaction with region 1, including Coulombic interactions and short range forces and associated displacements $\boldsymbol{\xi}$ are calculated.

The interaction with region 1 and 2b is more complex (although it only takes Coulombic interactions into consideration). Region 1 is approximated by a single monopole, placed on the defect centre, which works as a good approximation if region 2a and 2b are large. The energy is then summed up using an approach similar to Ewald summation (see section 2.3.3.1).

For a conventional Mott-Littleton calculation, it is a requirement that the bulk structure (before the cluster is cleaved from it) is properly minimized with respect to the internal coordinates and has no imaginary modes within the Brillouin zone [88]. These requirements are equivalent to the first derivative of energy being a good approximation to zero and the matrix of second derivatives having all positive eigenvalues.

A shortfall of using MM methods in general is that they can only be used straight-

forwardly for closed shell systems. There are however, many adaptations that can allow one to deal with this such as the Angular Overlap Model (AOM) [104–106]. MM methods are not well suited to calculations that involve bond breaking and charge transfer.

2.4 Optimization Methods

2.4.1 Introduction

Geometry optimization was touched upon in section 2.3.6 and is a means to find the minimum energy configuration of atoms of a system (or a saddle point in the case of transition state searches). The methods apply a variety of algorithms developed more generally for function minimization.

The system of atoms is seen as a function of potential energy with $3N$ variables, where N is the number of atoms (in fact it is a system of $3(N-1)$ variables as one atom is kept fixed while the others are optimized around it). This set of $3(N-1)$ variables is described as a vector (of structure). The Potential Energy Surface (sometimes called hypersurface or landscape) is a map of the values of the PE function with all possible values for the structural vector within a given range. Such a map can be generated by sampling the PE surface. PE surfaces can be a useful tools for understanding the nature of a system of atoms; however, both visualizing and calculating a PE surface for a system with more than two variables can be difficult. In section 3.4 an STO system with three variables is mapped out, which actually has 20 atoms in it. In this case, constraints of symmetry that relate the motion of atoms to one another mean that there are only three degrees of freedom (variables).

Random searches of a potential energy surface as a means to locate the minimum is very inefficient and will provide a rather coarse approximation to the correct minimum (though it can elucidate the presence of multiple minima if they exist). There are various iterative minimization methods available with different merits and demerits. In general, more sophisticated algorithms will reach a PE minimum with fewer iterations. Different algorithms require different analytical derivatives for the PE to be calculated, though usually not any further than the second derivative.

A detailed discussion of minimization procedures is given in *Numerical Recipes* [107] on which the following discussion is based (with the exception of section 2.4.5, which covers transition-point searches, in which the material was researched elsewhere).

We first assume that the function to be minimized can be described by a polynomial of second order (or by the second order expansion of the Taylor series, see (2.4.1)). Real PE surfaces often have quadratic character close to the minimum. Even away from the minimum the approximation provides a convenient balance between correctly describing the shape of the PE surface and the complexity of dealing with higher order terms.

$$f(\mathbf{x}) \approx \frac{1}{2}(\mathbf{x}-\mathbf{p}) \cdot \mathbf{H}(\mathbf{x}-\mathbf{p}) - \mathbf{b} \cdot (\mathbf{x}-\mathbf{p}) + c, \tag{2.4.1}$$

where for a Taylor expansion, expanded at $\mathbf{p}$:

$$[\mathbf{H}]_{ij} = \frac{\partial^2 f}{\partial x_i \partial x_j}\bigg|_{\mathbf{p}}; \qquad \mathbf{b} = -\frac{\partial f}{\partial x_i}\bigg|_{\mathbf{p}} = -\nabla f(\mathbf{p}); \qquad c = f(\mathbf{p}),$$

in which, $\mathbf{H}$ is the Hessian matrix of second derivatives, $\mathbf{b}$ is a vector and c is a scalar. x_i is the i^{th} component of the structural coordinate vector. The gradient $\nabla f(\mathbf{x}) = \mathbf{H}(\mathbf{x} - \mathbf{p}) - \mathbf{b}$ and points up the slope of the PE surface.

2.4.2 Steepest Descents

A naive (though often sufficient) algorithm for finding the minimum, which does not require second derivatives, is known as the method of steepest descents. In this method a starting position is chosen $\mathbf{p}_i$, ideally close to the minimum. A series of iterations is made whereby one generates a vector pointing down the slope of the PE surface in the steepest direction of descent. This is simply the negative gradient $-\nabla f(\mathbf{x})$ for which it is assumed we can calculate directly (analytically). A line search is carried out whereby multiple points are sampled along the PE surface in the direction of the descent vector. $\mathbf{P_{i+1}}$ is chosen to be at the minimum of this line search where the new gradient $\nabla f(\mathbf{p}_{i+1})$ is guaranteed to be orthogonal to the previous one $\nabla f(\mathbf{p}_i)$. The procedure starts again for $\mathbf{p}_{i+1}$ and repeats until the gradient has reached zero to within a certain tolerance.

As each successive motion to the minimum is at right angles to the previous, it causes the path taken to be a zig-zag. If the PE surface is valley shaped and the starting position is somewhere up the length of the valley then the steps taken are very short and convergence takes a large number of steps.

2.4.3 Conjugate Gradients

Conjugate gradients is a method related to steepest descents and shares its requirement that only the first derivative of energy (force) needs to be calculable for a point (analytically). Also, it is able to find the minimum without generating a Hessian matrix, which can be useful in systems of many atoms where there would be a large memory requirement for the Hessian. The basic aim of the method is to generate a sequence of steps down the slope of the PE surface where some consideration is given to the slope gradient at previous points $\mathbf{p}_{i-n}$ and the direction of the previous steps taken.

The method constructs two vectors each of dimension $3N$ or $3(N-1)$ labelled $\mathbf{g}_i$ and $\mathbf{h}_i$ (see equations (2.4.2) to (2.4.5)), where the index denotes step number. $\mathbf{g}$ and $\mathbf{h}$ are said to be conjugated to one another but are initially set equal to one another $\mathbf{g}_0 = \mathbf{h}_0 = -\nabla f(\mathbf{p}_0)$.

$$\mathbf{g}_{i+1} = \mathbf{g}_i + -\lambda_i \mathbf{H}\mathbf{h}_i; \tag{2.4.2}$$

$$\mathbf{h}_{i+1} = \mathbf{g}_{i+1} + \gamma_i \mathbf{h}_i; \tag{2.4.3}$$

$$\lambda_i = \frac{\mathbf{g}_i \cdot \mathbf{g}_i}{\mathbf{h}_i \cdot \mathbf{H}\mathbf{h}_i}; \tag{2.4.4}$$

$$\gamma_i = \frac{\mathbf{g}_{i+1} \cdot \mathbf{g}_{i+1}}{\mathbf{g}_i \cdot \mathbf{g}_i}. \tag{2.4.5}$$

The $\mathbf{g}$ and $\mathbf{h}$ vectors satisfy the following conditions:

$$\mathbf{g}_i \cdot \mathbf{g}_j = 0; \qquad \mathbf{h}_i \cdot \mathbf{H}\mathbf{h}_j = 0; \qquad \mathbf{g}_i \cdot \mathbf{h}_j = 0, \qquad j < i.$$

In each step, line searches for a minimum are conducted along the direction of the $\mathbf{h}$ vector. The description outlined above requires that the Hessian is known. However, if after each step $\mathbf{g}_{i+1}$ is set to $-\nabla f(\mathbf{p}_{i+1})$, as was done at the initial set up, the set of $\mathbf{g}$ vectors generated is identical to those generated with knowledge of $\mathbf{H}$. Line searches are therefore carried out along a vector which is constructed from a combination of the previous $\mathbf{h}$ vector and the current gradient. Equation (2.4.2) and (2.4.4) do not need to be evaluated and the new $\mathbf{g}$ vector generated in each step can be used to evaluate equations (2.4.3) and (2.4.5). Similar conditions for convergence can be applied as to the steepest descent method.

2.4.4 Quasi-Newton Methods

The Newton-Raphson method was independently developed by Isaac Newton and Joseph Raphson in 1670 and 1690 respectively. The method relies upon being able to calculate the analytical second derivatives of a system. Again it is assumed that PE surface can be approximated to a second order expansion of a Taylor series (2.4.1).

For some quadratic surface $f(\mathbf{x})$ with a starting point of $\mathbf{p}$:

$$\mathbf{H}\Delta\mathbf{p} = \Delta\nabla f = \nabla f(\mathbf{p} + \Delta\mathbf{p}) - \nabla f(\mathbf{p}), \tag{2.4.6}$$

where $\mathbf{H}$ is the Hessian matrix, and Δ represents a change in the proceeding quantity. We wish the next step $\mathbf{p} + \Delta\mathbf{p}$ to lead to the minimum, where the gradient is zero so:

$$\mathbf{H}\Delta\mathbf{p} = 0 - \nabla f(\mathbf{p}), \tag{2.4.7}$$

$$\Delta\mathbf{p} = -\mathbf{H}^{-1}\nabla f(\mathbf{p}). \tag{2.4.8}$$

In the Newton-Raphson method, the Hessian is calculated for a point and then its inverse is calculated from it.

There are two main versions of the Quasi-Newton algorithm called the Broyden-Fletcher-Goldfarb-Shanno (BFGS) method and the Davidon-Fletcher-Powell (DFP)

method. BFGS was developed subsequently to DFP and improves the rate of convergence to the minimum by the addition of an extra term, see equations (2.4.9) and (2.4.10).

A Quasi-Newton method allows the minimum of a function to be found without being able to calculate an analytical Hessian. Instead the inverse Hessian is approximated, the approximation is gradually improved while sampling the gradient during successive steps. The initial guess is usually an identity matrix.

These methods can often get to the minimum more quickly than the Newton-Raphson method. Using Newton-Raphson, if the starting position is far from the minimum, the Hessian is often not positive-definite, which can result in moving up hill away from the minimum. The way that the inverse Hessian is approximated in the Quasi-Newton method, insures that the optimization always travels down the slope of the PE surface.

Successive updates of the inverse Hessian are made thus:

$$\begin{aligned} {}^{\mathrm{DFP}}\mathbf{H}_{i+1}^{-1} =& \mathbf{H}_i^{-1} + \frac{(\mathbf{p}_{i+1} - \mathbf{p}_i) \otimes (\mathbf{p}_{i+1} - \mathbf{p}_i)}{(\mathbf{p}_{i+1} - \mathbf{p}_i) \cdot (\nabla f_{i+1} - \nabla f_i)} \\ & - \frac{\left(\mathbf{H}_i^{-1}(\nabla f_{i+1} - \nabla f_i)\right) \otimes \left(\mathbf{H}_i^{-1}(\nabla f_{i+1} - \nabla f_i)\right)}{(\nabla f_{i+1} - \nabla f_i) \cdot \mathbf{H}_i^{-1}(\nabla f_{i+1} - \nabla f_i)}; \end{aligned} \tag{2.4.9}$$

$${}^{\mathrm{BFGS}}\mathbf{H}_{i+1}^{-1} = {}^{\mathrm{DFP}}\mathbf{H}_{i+1}^{-1} + \left((\nabla f_{i+1} - \nabla f_i) \cdot \mathbf{H}_i^{-1}(\nabla f_{i+1} - \nabla f_i)\right) \mathbf{u} \otimes \mathbf{u}, \tag{2.4.10}$$

where $\otimes$ is the vector direct product which generates a matrix from vectors. For $\mathbf{S} = \mathbf{u} \otimes \mathbf{v}$, $S_{ij} = u_i v_j$. The vector $\mathbf{u}$ in (2.4.10) is given by:

$$\mathbf{u} = \frac{(\mathbf{p}_{i+1} - \mathbf{p}_i)}{(\mathbf{p}_{i+1} - \mathbf{p}_i) \cdot (\nabla f_{i+1} - \nabla f_i)} - \frac{(\mathbf{H}_i^{-1}\mathbf{p}_{i+1} - \mathbf{p}_i)}{(\nabla f_{i+1} - \nabla f_i) \cdot \mathbf{H}_i^{-1}(\nabla f_{i+1} - \nabla f_i)}. \tag{2.4.11}$$

Having considered some of the methods for minimizing functions of atomic structure, we now look at some techniques for calculating and predicting the nature of reaction pathways.

2.4.5 Transition State Searches

2.4.5.1 Introduction

One commonly wishes to calculate the location and height of a transition point in investigating a rate process e.g. a reaction mechanism or an atom/ion migration. Using transition state theory, the activation barrier can be used to estimate the rate of reaction at a given temperature. The transition point has zero gradient and is a minimum in all but one dimension, where it is a maximum. The Rational Function Optimizer (RFO) and Nudged Elastic Band (NEB) technique are two substantially different methods for locating a transition point.

2.4.5.2 Rational Function Optimization

The RFO method was developed by Ajit Banerjee, Noah Adams and Jack Simons [108] and published in 1985. The optimization method resembles the Newton-Raphson method in that the second derivatives are calculated directly and then inverted. The inverted matrix is diagonalized to obtain the eigenvalues and eigenvectors. These are analysed and used to construct a new step vector to move towards the desired stationary point [88].

RFO can be used to find and distinguish maxima, minima or saddle points with a specific number of imaginary frequencies (corresponding to negative eigenvalues). In a system of n variables and Hessian eigenvalues h_i, a minimum is characterised by $0 \leq h_1 \leq \cdots \leq h_n$ and a maximum is characterised by $h_1 \leq \cdots \leq h_n \leq 0$. A saddle point of μ^{th} order is characterised by $h_1 \leq \cdots \leq h_\mu \leq 0 \leq \cdots \leq h_n$. A transition point is a saddle point of first order and so one negative eigenvalue is expected at this point. In the case of a transition point search, it is the second eigenvalue and eigenvector that are used to generate future steps in the search algorithm [108].

Searches for transition points using this method cannot use line searches as the stationary point will not be at a minimum, instead small step sizes are used between Hessian updates. Typically when carrying out a transition point search, the system is configured to be close to the expected transition point (see figure 2.4.1), a series of steps is made until the Hessian has the correct characteristics for the transition point.

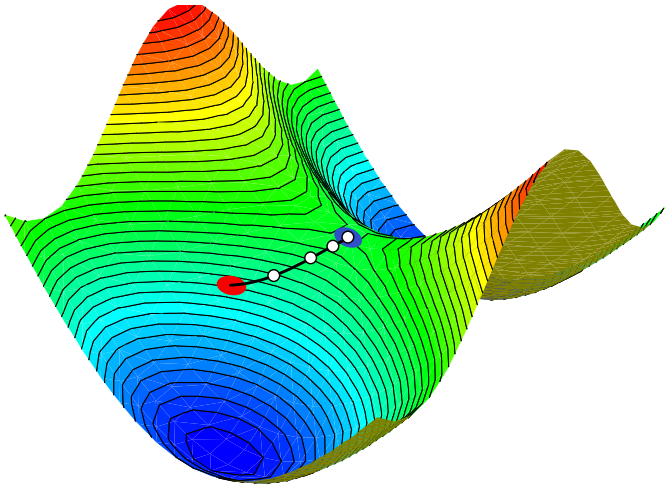

Figure 2.4.1: Representation of an RFO algorithm locating a transition point. The red and blue ellipses respectively represent the starting point and the transition point, the white circles represent successive steps of the optimizer.

2.4.5.3 Nudged Elastic Band

The Nudged Elastic Band method (NEB) [109, 110] can be used to determine the Minimum Energy Pathway (MEP) between two known stable states, with the transition point, somewhere in between their configurations (see figure 2.4.2). The method involves generating a series of intermediate images of the structure that are some kind of interpolation between the initial and final structures (often a linear interpolation). The configuration of each intermediate structure is bound to both of its neighbours by a spring, while the start and end structures are kept fixed in place. The intermediate structures are then geometry optimized using an adapted version of a conventional optimizer. The purpose of the springs is to compel each structure to be similar to its neighbours, thereby encouraging the formation of a pathway between the endpoint structures.

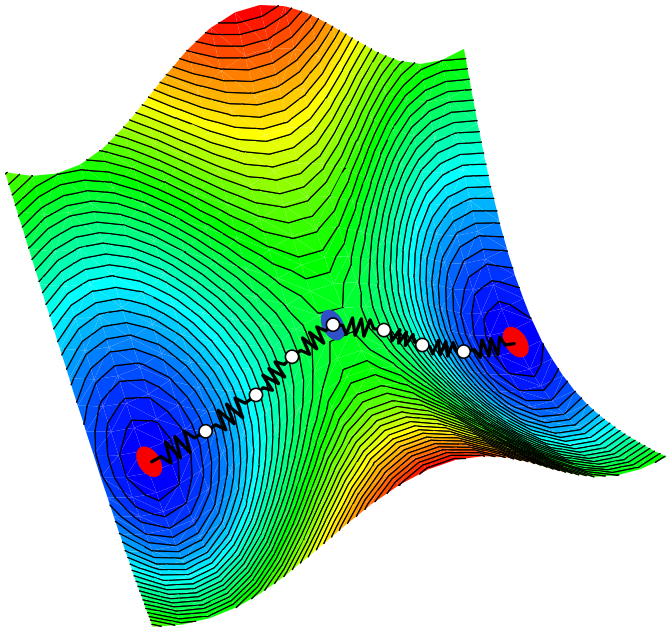

Figure 2.4.2: Representation of an NEB calculation taking place between two known structures, marked as red ellipses. The white circles represent intermediate structures and the interlinking zig-zag lines representing the springs binding one structure to another. The blue ellipse represents the transition point.

In some simpler elastic band methods, the force used in the geometry optimization update algorithm is simply the sum of the real force on the intermediate structures (as if there was no elastic band/spring) and a force proportional to the difference in the configuration of each neighbouring structure (Hooke's law). This method would often result in an incorrect MEP being calculated as the elastic nature of the pathway formed by the intermediate structures would cause the calculated MEP to be shorter than the real MEP, cutting corners around energy barriers and resulting in an overestimation of the saddle point energy. Additionally, the intermediate structures would tend to bunch

together in the potential energy wells (usually near the start and end point structures).

To overcome these issues, the NEB method uses an algorithm to estimate the tangent to the minimum energy path at the point of each intermediate structure. The component of the real force that is perpendicular to the tangent is added to the component of the spring force that is parallel to the tangent. The result is used in the geometry update algorithm. This modification to the elastic band method is referred to as 'nudging'. Some more sophisticated methods, ensure that the structure nearest to the transition point is forced towards it, so that an exact calculation of the saddle point can be made instead of an estimate based upon fitting or interpolation of the images. Additionally, through the manipulation of spring constants, the structures can be encouraged to become more tightly spaced towards the saddle point. Having more resolution near the saddle point can be of benefit as this is usually the feature on the MEP of the greatest interest [110].

As a means of identifying a transition state, the NEB and RFO method are not directly comparable. The NEB method is used for identifying reaction pathways whereas the RFO method identifies the highest point on the reaction pathway. Either method can be most appropriate depending on the circumstances. The NEB method is prejudiced towards finding a saddle point, closest to the midpoint between the two structures. The RFO method does not have the same prejudice, which can, however, lead to it finding the wrong transition point.

We have considered a variety of methods for atomic calculations involving both a QM and an MM approach. In the final section of this chapter, we look at the Hybrid QM/MM, used for calculations within this thesis.

2.5 Embedded Cluster Technique (ChemShell)

2.5.1 Introduction

We have already described the MM Mott-Littleton approach towards calculating the effects of defects in crystals (see section 2.3.6). We now consider a related but more sophisticated approach which uses a hybrid QM/MM model.

There are various QM/MM embedded cluster models implemented today (where QM/MM refers to some technique of using both QM and MM methods together in one model). The general problem that they try to solve is how to model the precise behaviour of a local state (e.g. a defect) in a polar crystal or surface (using QM), while not experiencing interaction from the defects within periodic images and not using a prohibitively large number of QM atoms. In this section, one of the hybrid QM/MM embedded cluster techniques used within the *ChemShell* code [1–3] for solid state embedding in the bulk material will be described.

The concept of the embedded cluster was introduced when discussing the Mott-Littleton approach within section 2.3.6. Earlier attempts at an embedded cluster model, used a QM cluster of atoms located on a region of interest and surrounded by either a set of terminating point-charges [111] or by means of a Shell Model description [112]. More recently, methods employed within the *ICECAP* code [113], the *GUESS* code [114] and the *AIMP* code [115] were of particular significance in the model described in this work (henceforth described as the *QM/MM model*).

2.5.2 The QM/MM Regions

The QM/MM model uses a system of five approximately concentric regions (see figure 2.5.1). Regions 1–3 are part of the active region, which will undergo geometry optimization. Regions 4 and 5 are frozen and no changes can be made to any of the species within them.

Region 1

Region 1 is an embedded cluster of atoms containing the localized state of interest and a number of surrounding atoms. This region is modelled using a QM code of which there are several choices. The work presented in this thesis all use the *GAMESS-UK* code [116, 117].

Region 2

Work carried out on pre-runners to *ChemShell* found that there were several problems with a QM cluster being left unterminated. Electrons on the cluster tended to become delocalized and would spill out towards positive centres, located outside of the cluster [2, 112]. The (band) gap between the HOMO and LUMO would narrow, resulting in unphysical spectroscopic properties. There also needed to be some account taken of

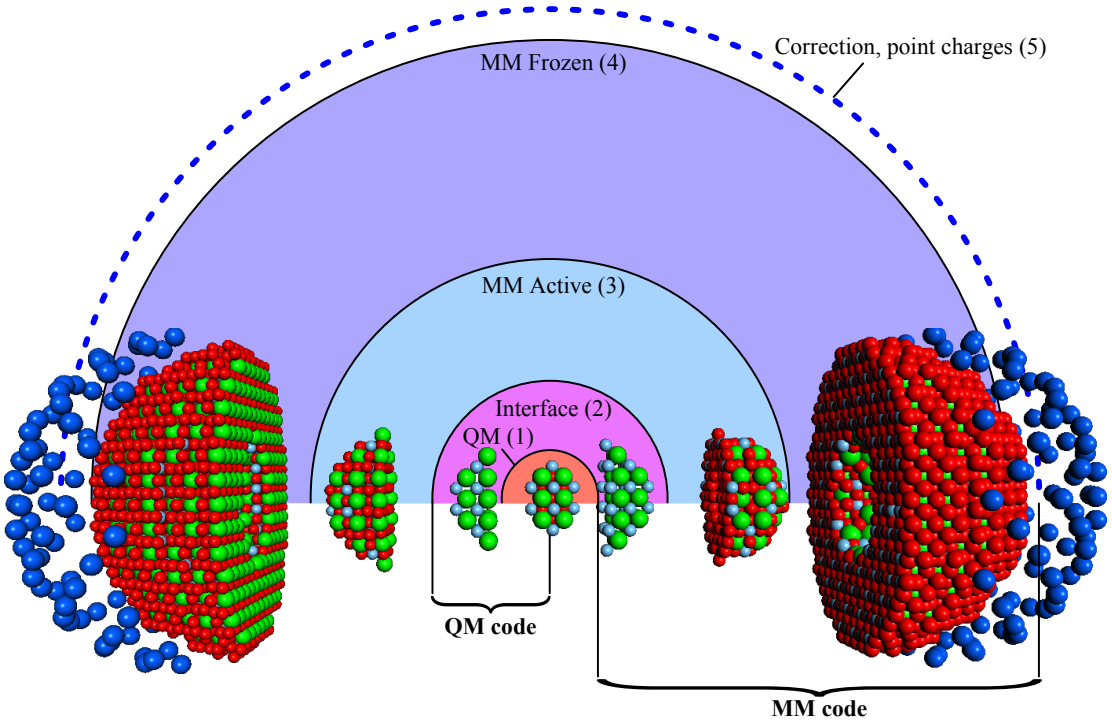

Figure 2.5.1: Diagram of a *ChemShell* QM/MM embedded cluster. The diagram shows a cross section of a diagrammatic cluster with a perspective view of the separated regions of an actual cluster superimposed. In the cluster, green, light blue and red spheres represent respectively strontium, titanium and oxygen atoms. The dark blue spheres represent point-charges (for practical purposes, the six far-field point-charges have not been represented here).

the influence of short range interactions between the QM and MM region.

A solution was to introduce an interface (or boundary) region. The atoms within this region were modelled with both large core pseudo potentials (ECPs, see section 2.2.4) and MM force-fields. This region is usually only one or two atoms thick and consists only of cations. Large core ECPs are intended to model all inner electrons of the atom leaving only valence electrons to be calculated explicitly. As the material is ionic, the ECP atoms are expected to be completely ionized (stripped of all valence electrons). Total ionization is ensured by not associating any basis sets with the region 2 atoms.

There are at least three problems with this usage of large core ECPs: the first is that their availability is not very great in comparison to conventional basis sets; the second is that most large core ECPs were not intended to be used completely ionized, and, as a consequence, they tend to model accurately, the behaviour of the atom in its first or second ionization states, but not very accurately the final and penultimate ionization states; the third is that most available ECPs were developed for Hartree-Fock algorithms instead of DFT. For these last two reasons it is often necessary to refit

the ECPs, which is difficult and time consuming.

In an older version of the model (still in common use), region 2 atoms were modelled as point-charges onto which were placed both the force-field potentials and the ECPs. The model was adapted during the course of the project to include shells on the region 2 atoms. The ideal model would have involved both force-field and ECPs placed on the shells. Unfortunately due to a limitation within *GAMESS-UK*, it was not possible to place ECPs on shells and so the ECPs were placed on the cores.

Regions 3 & 4

In order to embed the QM cluster within a polar environment, which is capable of reacting to changes within the QM region, a Shell Model is placed around the cluster. Both regions 3 and 4 use the Shell Model. Region 3 can be geometry optimized by *ChemShell* and have shell positions optimized by the classical code, of which there are various choices (for this thesis the *GULP* code [88, 118] has been used for all QM/MM calculations). In region 4 neither geometry nor shell optimization are performed, for this reason, it is described as being inactive or frozen. The thickness of region 4 must be at least the distance of the short-range MM cut offs, so as to match the behaviour of the infinite crystal as closely as possible.

The outermost region 4 atoms have their charges adjusted so as to ensure overall charge neutrality of the model (deliberate ionizations are incorporated later), which can be an issue due to bond cleavage. The bond cleavage is a consequence of using a radial cut-off when selecting which atoms to include in the model. Extra atoms are also selectively added to the outside of the model (at correct lattice sites) in order to reduce local multipoles.

Region 5

The outermost region of the QM/MM model is a set of point-charges intended to reproduce the Madelung field accurately within regions 1–3 (the active region). There are two sets of point-charges, one is some large number (selectable via a software parameter) placed roughly equidistantly around the outer surface of the cluster. There are a further six point-charges placed in an octahedral arrangement at some large distance from the cluster and are intended to crudely reproduce most of the net polarization within the crystal. The outer octahedrally arranged charges are calculated directly based on the known polarization within the crystal. The charges on the inner set of points are adjusted subsequently using a least mean square fitting function [2] to reproduce the Madelung field (within the active region) as calculated by an Ewald summation technique (see section 2.3.3.1).

2.5.3 Interactions Between Regions

The optimization duties of the *ChemShell*, the QM code and the MM code are broken down thus: *ChemShell* is responsible for geometry optimization of the system, which in modern implementations involves shifting shells and cores together for the MM active region and shifting QM nuclei, leaving the old wave function as an initial guess for the new one; The QM code optimizes the wave functions of QM atoms and the MM code optimizes the shell positions in the MM active region (and region 2 if the Shell Model is used here).

Table 2.5.1: Two bodied interactions between the QM/MM regions 1–5 as seen by the QM (left) and MM (right) codes. E represents a QM electronic SCF calculation, P represents interactions with ECPs (pseudo potential), Q represents Coulombic (point-charge) interactions, S represents classical short-range force-field interactions (e.g. Buckingham potential) and × represents no interaction. The + represents an additional force term given to the MM code by the QM code via *ChemShell* (see below for details).

QM	1	2	3	4	5
1	E	QP	Q	Q	Q
2		×	×	×	×
3			×	×	×
4				×	×
5					×

MM	1	2	3	4	5
1	×	+	S+	S	×
2		SQ	SQ	SQ	Q
3			SQ	SQ	Q
4				×	×
5					×

In the following section the nature of the calculations within the different regions and how the QM and MM codes each observe and process the system will be described. Table 2.5.1 provides a simple overview of the two bodied interactions in matrix form; higher order interactions will be omitted, but are assumed to be of significantly lower magnitude. These two body interactions, which describe the energy calculation within a single geometry step, will be described in more detail below.

2.5.3.1 The QM Code's Perspective

In the process of calculating the ground state energy of the system, the QM code finds the wave function that minimizes the expectation value of the energy for the region 1 atoms, using nuclear centred basis sets placed on them (see section 2.2.2). The calculation (usually SCF) is performed in the background of large core ECPs from region 2, the cores and shells of regions 2, 3 and 4 (seen as point-charges) and the point-charges of region 5. This procedure facilitates the calculation of the contribution (to the total energy) of the internal energy of region 1 and a large part of the interaction energy between region 1 and regions 2, 3, 4 and 5. Neither internal nor interaction energy within or between regions 2, 3, 4 and 5 are calculated by the QM code. However, the QM

code does calculate the force on each shell in regions 2 and 3 that is a consequence of the electronic distribution within region 1. This information on forces (shown as + in table 2.5.1) is transmitted via *ChemShell* to the MM code, which uses the information in shell optimizations.

2.5.3.2 The MM Code's Perspective

Expanding on the final point from section 2.5.3.1, the atomic model passed to the MM code does not include charges on atoms in region 1. Instead a higher level of theory is used for dealing with the force contribution of the effects of region 1 on MM regions 2–5. The expectation force on every shell (point-charge) due to the effects of region 1 is calculated by the QM code and passed via *ChemShell* to the MM code. The MM code then adds the force terms to the force-field based calculations for the corresponding shells. As the MM code itself only performs shell optimizations, and not geometry optimizations, the force on the cores due to the QM region is not needed (but will be needed internally by *ChemShell*). The QM forces applied to the shells do not make a contribution to the energy reported by the MM code.

Short-range forces between the MM regions and the QM region have not been covered yet. In the previous paragraph we covered a QM/point-charge type interaction between the MM shells and QM region, but the inclusion of classical short range forces brings the system closer to a QM/whole-atom interaction. In some older models, short-range force-fields were applied between regions 2–4 but did not extend to region 1. Despite the gap of several Angstroms between regions 3 and 1, the tail end of the short-range forces was still missing and so the force-field interaction was extended to go from both regions 3 and 4 to region 1. In principle, region 2 ions interact with one another via short-range forces, but the STO Buckingham potentials developed in this thesis have no cation-cation interactions and oxygen is excluded form region 2, so these interactions are excluded.

The internal energy of regions 2 and 3 and the interaction energy between regions 2, 3 and 4 include both Coulombic and short-range forces. The interaction between regions 2 and 5 and between 3 and 5 is purely Coulombic. The internal and interaction energy of and between regions 4 and 5 is excluded as they do not move during any part of the calculation.

2.5.3.3 Differences Between Conventional and Current Methodology

A significant difference to the model presented here and a more common older model in use is related to the shells and pseudo potentials in region 2. In the older model, the region 2 atoms are regarded as fully QM bodies with no charge observed by the MM code. In the model presented here, the region 2 atoms have cores and shells, both have Coulombic charge and the shells have short-range force-field interactions with atoms

in the MM region. The QM code sees the interface atoms as pairs of point-charges with ECPs placed on the shells (in the old model, region 2 atoms were single point-charges with pseudo potentials).

2.5.4 Optimization Procedure Within ChemShell

There are several sophisticated functions within *ChemShell* for carrying out geometry optimization including *DL-Find*, *Newopt* and *HDLCOpt*. These range in capabilities, for such tasks as transition state searches and general purpose optimization and use, several optimization algorithms.

When carrying out a QM/MM model calculation, in between geometry steps *ChemShell* carries out a series of so called 'micro-iterations'. Micro-iterations are a looping system where by cycles of SCF and energy minimizations within the QM code and then the MM code respectively are carried out (the maximum number of micro-iterations is limited by a customizable parameter (called `max_shell_cycles`). After each iteration, the RMS shell displacement is calculated. If the RMS shell displacement is smaller than a certain customizable tolerance (called `shell_tol`) then it breaks out of the loop. After this the energy and gradient are calculated and another geometry step can be taken.

The micro-iteration procedure ensures that the QM electrons and the MM shells are in a mutually relaxed state with respect to each other for a given geometry configuration.

For a geometry optimization, a small value (~ 5) for `max_shell_cycles` is chosen to speed up the processing. For a single point energy calculation (or at the end of a geometry optimization) a much larger value is chosen for maximum accuracy (~ 20).

2.5.5 Procedure for Running a Calculation

In this section we will discuss the general procedure for carrying out a calculation using the above model.

We start by geometry optimizing a periodic crystal within the MM code (*GULP* for the work in this thesis) until the gradient is zero and there are no imaginary frequencies. The optimized crystal data are refactored into the input format that *ChemShell* uses for crystal structures.

At this stage a utility within *ChemShell* called *Construct* [119] is used for generating the QM/MM model. *Construct* adopts the *ChemShell* input format and accepts command line arguments to generate the cluster based on radial cut-offs for the active region and the outer edge of region 4. *Construct* performs the multipole reducing atom additions and the region 5 point-charge fitting (see section 2.5.2). The point-charges are fitted to reproduce the Madelung potential at every core and shell site within the

active region. *ChemShell* outputs a *punch* file (which is the type of structure file that *ChemShell* uses internally) file containing the QM/MM model's structure.

In normal usage the *punch* file will not contain labels indicating the region in which the different ions lie. Typically, the region 1 atoms are selected manually as the choice requires some consideration given that the size of the cluster (region 1) is usually only around 10 atoms. Regions are chosen by postfixing the atomic label with a number.

After the manual labelling of region 1, the model is put through *Construct* again (using a different mode). A thickness of region 2 and a radial cut off for region 3 is entered. A new *punch* file is generated.

A total of either five or six files are needed to run the *ChemShell* calculation, they are: a *ChemShell* input file (`.chm`); an structural *punch* file (`.pun`); for the QM code (*GAMESS-UK* for this thesis) either two or three files are needed, a file describing the basis set (`.basis`), a file describing the set of ECPs (`.ecp`) and optionally a file to describe an initial guess for the electronic configuration of the cluster (`.guess`); finally for the MM code (*GULP* for this work), the file containing the set of classical force-fields (`.ff`).

The force-field file contains sets of force-fields for each set of interactions; this inevitably contains lots of duplicate information (described within section 2.5.3). Atoms from different regions have different labels and so the interactions must be described separately. The force-field file also describes the potential energy exclusions within and between regions 4 and 5 as described earlier. In the context of this work, some more complex force-field interactions are set up to deal with a problem at the interface region.

The *ChemShell* input file warrants some description and the set up will be described in summary. *ChemShell* uses a command interface known as Tool Command Language (TCL). TCL was chosen as its development was already mature and was more sophisticated than the Unix shell scripting languages. Within this file we set up a set of instructions for *GAMESS-UK* and for *GULP*, neither of which is particularly specific to *ChemShell*. We also need to instruct *ChemShell* to perform the hybrid style calculation and either to perform a geometry optimization or a single point energy calculation.

Geometry optimizations can often take more processing time than is allowed for a single job in contemporary supercomputer queueing systems. To deal with this *ChemShell* supports an option to restart from dumped files. Electronic, geometry and shell restarts are allowable as separate options within *ChemShell*.

An output file explaining all the steps taken in the calculation involving the QM and MM codes is produced. The final relaxed energy can be taken from the end of the

ChemShell output file.

At the end of the calculation an additional energy term must be added to the total energy manually (see section 2.5.6).

2.5.6 Jost Correction

When considering what size to make the different regions (and the size of the whole system), one should make the active region large enough for the nature of any structural or electronic defects to present themselves (based on experience and some experimentation). Regardless of the size of the active region, there will always be a contribution to the total energy (of a charged defect) as a consequence of relaxation of the infinite crystal. W. Jost [120] developed a formula (see (2.5.1)) for calculating this contribution:

$$E_{\mathrm{bulk}} = -\frac{q^2}{2r}\left(1 - \frac{1}{\boldsymbol{\varepsilon}_r}\right), \tag{2.5.1}$$

where q is the charge on the defect, r is the radius of the active region and $\boldsymbol{\varepsilon}_r$ is the relative permittivity (or dielectric constant) of the material, which can be provided by the MM code from a calculation on the infinite lattice. In the case of a geometry optimization, the static dielectric constant should be used (as this takes ionic relaxation into account) and in the case of a single point (electronic) calculation, the high frequency dielectric constant should be used (as this only takes electronic/shell relaxation into account).

2.6 Summary

In this chapter, we have covered a wide range of topics covering the principles of several computational techniques for studying materials. Specifically we covered: the principles of quantum mechanical and molecular mechanical methods; various techniques for performing structural (or geometry) optimization; we also discussed the hybrid cluster method of performing calculations on local states (e.g. a defect within a crystal), which was implemented within *ChemShell* for this thesis. The embedded cluster method was considered in some considerable detail as its implementation is not a widely known standard in contemporary solid state physics.

In the following results chapters, the research carried out for this thesis is described in detail. The phase transition work using periodic boundary conditions is presented in chapters 3 and 4 and the results from the defect calculation work are presented in chapter 5.

The majority of the calculations were performed on the supercomputer *HECToR*, with a smaller number run on the University of College London's own supercomputer *Legion*. *VASP* 5.2, *GULP*, *GAMESS-UK* and *ChemShell* were the codes used for performing calculations.

Having considered the theory underlying the various computational methods employed within the course of this thesis, we now move onto our results. There are three results chapters, covering: a detailed analysis of the tetragonal $I4/mcm$ potential energy surface (chapter 3); An analysis of a large number of structures, through a process of optimization and symmetry breaking (chapter 4); defect and ion migration properties of strontium titanate (chapter 5).

Chapter 3

Mapping the *I4/mcm* Potential Energy Landscape

3.1 Preamble

In this chapter, we present work on the determination, modelling and analysis of the nature of the tetragonal potential energy surface of strontium titanate within the $I4/mcm$ space group. The $I4/mcm$ space group has three degrees of freedom, which were analysed over a wide range of values using the LDA, PBE and PBEsol density functionals. The periodic QM plain-wave basis set code *VASP* (see section 2.2.2.3) was used for all calculations except where otherwise indicated. In chapter 4, we consider the potential energy surface of STO in a wider ranging but discontinuous way.

3.2 Introduction

As discussed in section 1.2, STO is known to exist in at least two phases: cubic, with the space group $Pm\bar{3}m$ and tetragonal, with the space group $I4/mcm$. In this chapter we map out the $I4/mcm$ potential energy surface in considerable detail and over a wide range of values that span over the cubic and optimized tetragonal structures. Through a process of sampling of single point calculations using the DFT level of theory, a three-dimensional map of the surface was created. The map has dimensions of octahedral rotation angle, ratio of the two lattice parameters and cell volume. We visualize the potential energy surface using various two-dimensional flattening techniques.

Subsequently, using a residual squares method, we fit the surface to a three-dimensional polynomial (trivariate polynomial). The surface minimum is determined using a Newton-Rahpson optimizer (see section 2.4.4). We also compare a one-dimensional version of the potential energy surface to research by Hayward and Salje [8] involving the fitting of experimental results using Landau theory (see section 1.2.7). Finally we consider the implications of quantum mechanical properties of the atomic nuclei in determining the expectation rotation angle of the octahedra at $0\,\mathrm{K}$. These calculations were all performed using the LDA [79], PBE [83, 84] and PBEsol [85] density functionals, using the *VASP* code [66, 67] and using PAW pseudo potentials [72, 73].

We begin by considering the most appropriate computational parameters to use for our DFT calculations.

3.3 Choosing Accuracy Parameters

3.3.1 Introduction

To begin periodic QM calculations on STO, it was necessary to investigate what energy cut-offs (see section 2.2.2.3) and k-point densities (see section 2.2.3) were necessary to describe properly, the fine structure of the system. For most materials that have harder energy landscapes (landscapes with more positive second derivatives of energy), an energy cut-off of 500 eV is usually sufficient. The knowledge gained in this section is used in the present chapter, chapter 4 and in the QM work presented in chapter 5.

3.3.2 Choosing Plane-Wave Energy Cut off

The calculated energy of the system will be reduced with increasing cut-off energy and converge for values above a certain cut-off energy, as the quality of the wave function of the system increases. A 20 atom $I4/mcm$ tetragonal unit cell and $Pnma$* orthorhombic unit cell (being the lowest symmetry STO structures widely known to exist) were used for testing and were geometry optimized under constant volume conditions (for calculation speed), using a range of different energy cut-offs (500 to 1000 eV). In the *VASP* implementation, constant volume maintains the cell volume, but allows the lattice vectors to change. Symmetry constraints were also turned on, allowing only structural changes that maintained the symmetry group of the given starting structure.

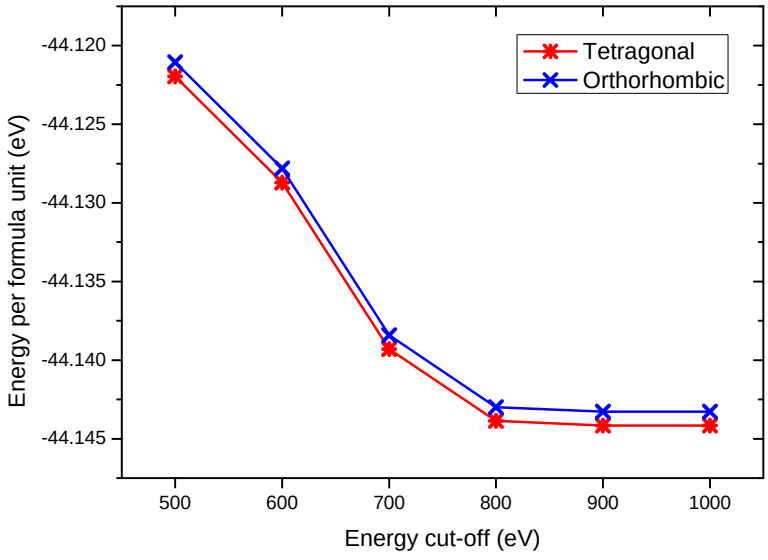

Figure 3.3.1: Plot of converged system energy vs. plane-wave cut-off energy for LDA.

Each system was started with a structure that was approximately optimized for the given functional. In all the plane-wave energy cut-off calculations, a k-point sampling

*It was later discovered that the orthorhombic cell was a near perfect match for both $Pnma$ and $Imma$ space groups (based on trivial modifications of the settings of symmetry recognition software).

grid of $6\times4\times6$ was used (see section 3.3.3), corresponding to the **a**, **b** and **c** lattice vectors respectively (**b** is the long axis).

In figure 3.3.1 we can see that both the tetragonal and orthorhombic systems have almost reached convergence at 800 eV while the system appears to be fully converged at 900 eV. The difference in converged energy was 0.3 meV per formula unit for both tetragonal and orthorhombic structures between cut-off energies 800 and 900 eV. Between 900 and 1000 eV the difference was 10 μeV for the tetragonal system and 4 μeV for the orthorhombic structure.

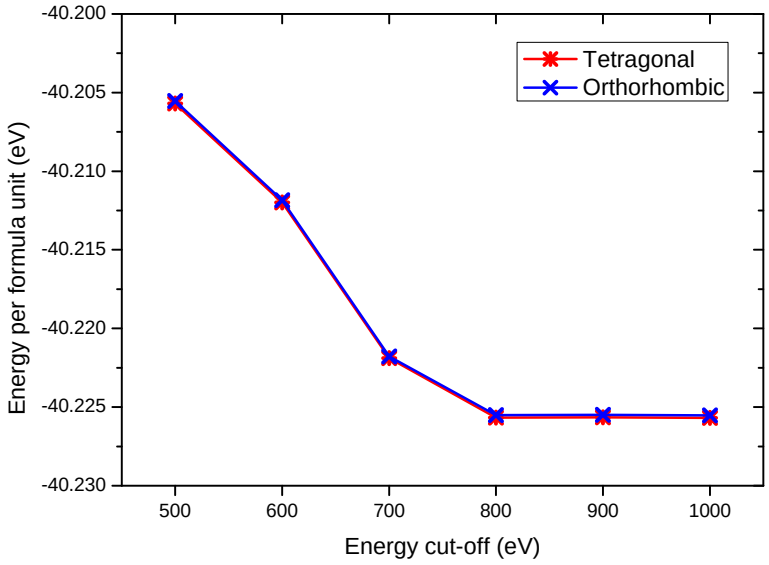

Figure 3.3.2: Plot of converged system energy vs. plane-wave cut-off energy for PBE.

As with the LDA systems, the PBE plot, figure 3.3.2, show convergence at 800 eV upwards. Tetragonal and orthorhombic structures both show a difference in converged energy of 10 μeV between cut-off energies 800 and 900 eV and a slightly larger jump between 900 and 1000 eV of 35 μeV.

Figure 3.3.3 shows some slightly different behaviour in that the system optimized with a cut-off energy of 800 eV has a total energy that is lower than the 900 and 1000 eV calculation. In general we expect system energy to reduce with increasing cut-off energy. In this system, for both tetragonal and orthorhombic systems, the 800 eV energy cut-off gave a system energy that was 0.5 meV lower than the 900 eV system. Going between 900 and 1000 eV calculations, there was a difference of 10 μeV for the tetragonal and 8 μeV for the orthorhombic.

The unexpectedly low system energy in the 800 eV system is likely to be due to an artefact of the plane-wave optimizer within *VASP*, which uses a correction to speed up optimization. A consequence can be a small variation in the calculated system energy. It would therefore be inappropriate to compare two systems that were calculated with

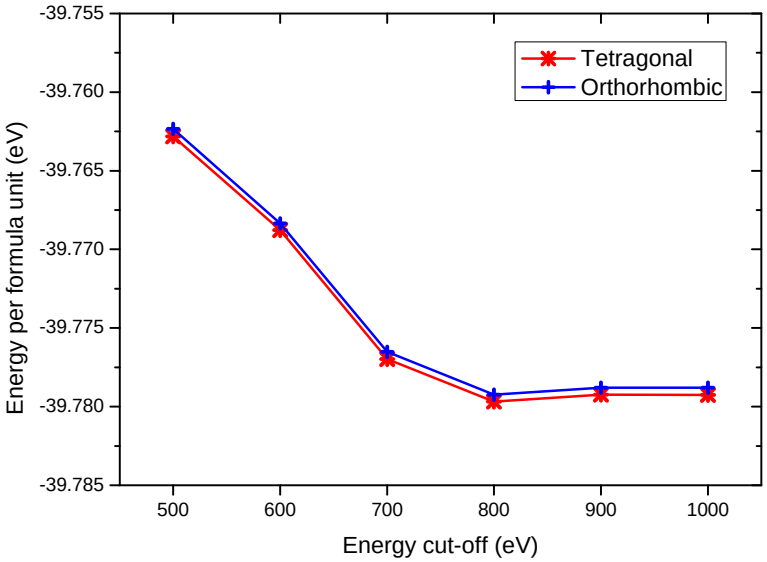

Figure 3.3.3: Plot of converged system energy vs. plane-wave cut-off energy for PBEsol.

different cut-off energies. However, one can see that even in the 800 eV cut-off example, the difference between the tetragonal and orthorhombic system energies converge to be very similar to the 900 eV cut-off example. For the 800 eV, 900 eV and 1000 eV calculations, the difference between tetragonal and orthorhombic energies were respectively: 449 µeV, 450 µeV and 453 µeV.

The cut-off energy that most consistently minimizes system energy is 900 eV and so this value is used in most of the plane-wave calculations presented in this thesis. The only set of calculations not to use the 900 eV cut-off are the $I4/mcm$ energy surface ones (see section 3.4), which were calculated using a cut-off of just 500 eV, in order to reduce the computational resources needed for the task (approximately 8000 calculations for each functional). The very cautious 900 eV calculations were used elsewhere to try and elucidate very low symmetry structures that might appear during geometry optimizations (and for the system energies to be meaningfully comparable to the higher symmetry systems). It is considered as argued below that for the relatively high symmetry tetragonal system, a plane-wave cut-off of 500 eV is sufficient to describe the features.

To gauge a measure of the influence on the system of using 500 eV cut-offs instead of 900 eV, the tetragonal and orthorhombic calculations were compared to one another using the two cut-off energies (see table 3.3.1).

In the table, we present the difference between optimized tetragonal and orthorhombic energies in six different examples i.e. 500 and 900 eV cut-off energies for each of the three functionals. If a given simplification of a method (using a 500 eV cut-

Table 3.3.1: Energy change between optimized orthorhombic and tetragonal systems as determined using both 500 and 900 eV plane-wave cut-off energies and three different functionals. The final column contains the difference between the two previous columns. The constraint of constant volume was used during optimization.

Functional	500 eV (μeV)	900 eV (μeV)	Difference (μeV)
LDA	905	876	29
PBE	153	161	-8
PBEsol	467	450	16

off) for examining the potential energy surface is good then we expect the difference in tetragonal and orthorhombic energy to be similar to the case of the more complete model (using a 900 eV cut-off). We therefore compare the energy differences for the 500 and 900 eV plane-wave cut-off calculations, for each of the three functionals. The greatest deviation between the different cut-off energy calculations is 29 μeV, in the case of LDA. From a fractional point of view, the greatest difference is for the PBE functional where the 500 eV cut-off calculation yields an energy difference (between tetragonal and orthorhombic) within 95 % of the 900 eV cut-off. We consider these to be good approximations and so it is expected that a 500 eV plane-wave cut-off energy will sufficiently model the $I4/mcm$ system when calculating the energy surface (for the work in this chapter). An approximately constant energy offset can be expected between the energy surface calculated with a 500 eV plane-wave cut-off, when comparing it to calculations employing the 900 eV cut-off.

3.3.3 Choosing the k-Point Density

Choosing an appropriate k-point density was performed after the plane-wave cut-off calculations and so 900 eV was used as the cut-off for the following calculations. As with the plane-wave cut-off calculations, one should try to be consistent with using the same k-point density (density in reciprocal-space, see section 2.2.3) for all the systems that are to be compared with one another or as a minimum requirement make sure that the system energy has converged with respect to k-point density for all systems. System energy can go up and down with respect to k-point densities before convergence as can be seen in figures 3.3.4 to 3.3.6.

Again, the tetragonal and orthorhombic systems were used used as the test bed. Table 3.3.2 shows the various k-point samplings that were used in the comparison. In the tetragonal and orthorhombic unit cells, the $\mathbf{b}$ axis is the longest; correspondingly, the number of k-points used along this axis is smaller ($\sim \frac{1}{\sqrt{2}}$ of the number used in the $\mathbf{a}$ and $\mathbf{c}$ axis).

The k-point data were plotted with k-point density in reciprocal-space on the x-

Table 3.3.2: k-point settings used to sample tetragonal and orthorhombic unit cells. These sampling densities are used by a Monkhorst-Pack based algorithm to evenly distribute k-points in reciprocal-space, see section 2.2.3.

k-points in lattice vector			
a	**b**	**c**	Total k-points
1	1	1	1
2	1	2	4
3	2	3	18
4	2	4	32
5	3	5	75
5	4	5	100
6	4	6	144
7	5	7	245
8	6	8	384
10	6	10	600
10	8	10	800

axis. To convert between the figures used in table 3.3.2 to k-point density, the total number of k-points in the Brillouin zone (right hand column) was divided by the volume of the reciprocal-space unit cell:

$$V_{\text{reciprocal}} = \frac{(2\pi)^3}{V}, \tag{3.3.1}$$

where V is the volume of the real-space unit cell. Different unit cells were used for the LDA, PBE and PBEsol systems and obviously for the tetragonal and orthorhombic systems as each calculation was started off at an almost optimized state for the given functional and space group. As a consequence, the cells have different volumes and the data points are not aligned with one another on the horizontal axis. The k-point distributions listed in table 3.3.2 map from top to bottom onto points going left to right in figures 3.3.4 to 3.3.6.

Geometry optimization calculations were run with a constant volume constraint. In all of the k-point plots, two different scales are used for the system energy, with the scale increments on the lower being 250 times finer than on the upper portion.

The LDA, PBE and PBEsol functionals all show similar behaviour. The system energy varies significantly with k-point density up until a density of $\sim$70 k-points per Å^{-3} is reached (henceforth written as Å^3), which corresponds to a Monkhorst-Pack grid of $5\times3\times5$. The energy then rapidly converges. The systems are all well converged at a k-point density of $\sim 130\,\text{Å}^3$, corresponding to a $6\times4\times6$ grid spacing. The difference between this system energy and that of the subsequent sample ($7\times5\times7$) is

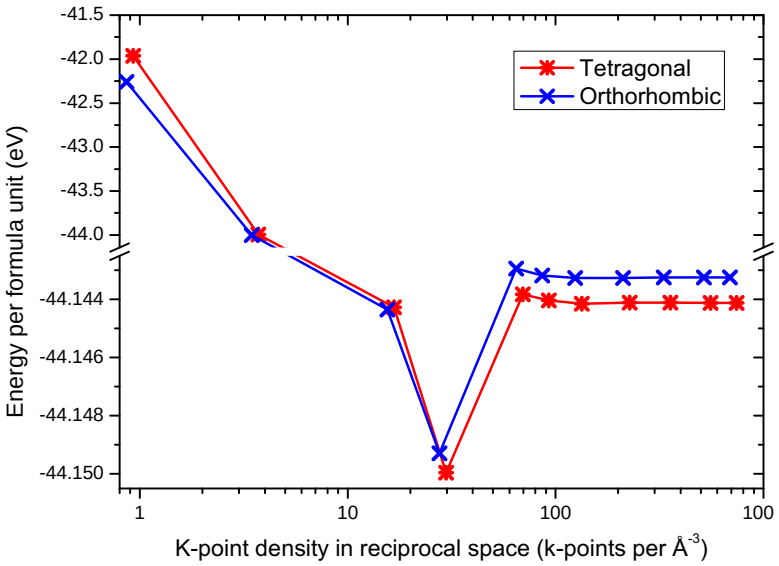

Figure 3.3.4: Plot of converged system energy vs. k-point density in reciprocal-space for LDA.

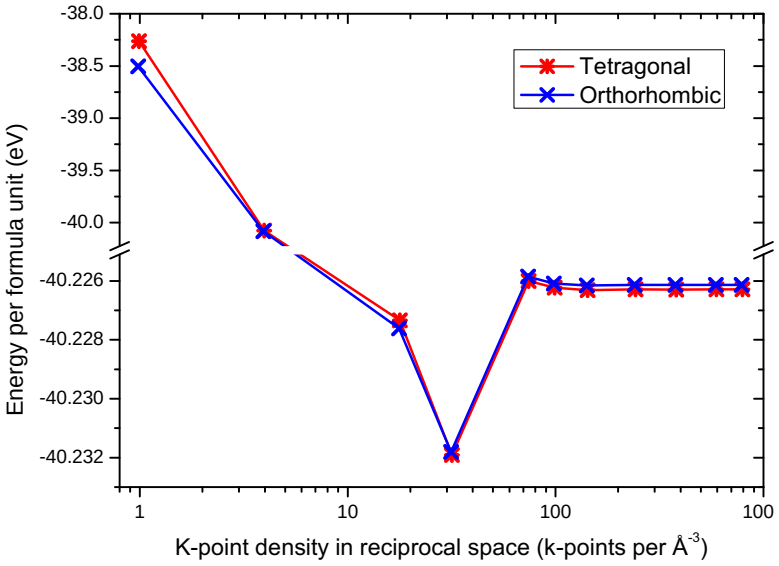

Figure 3.3.5: Plot of converged system energy vs. k-point density in reciprocal-space for PBE.

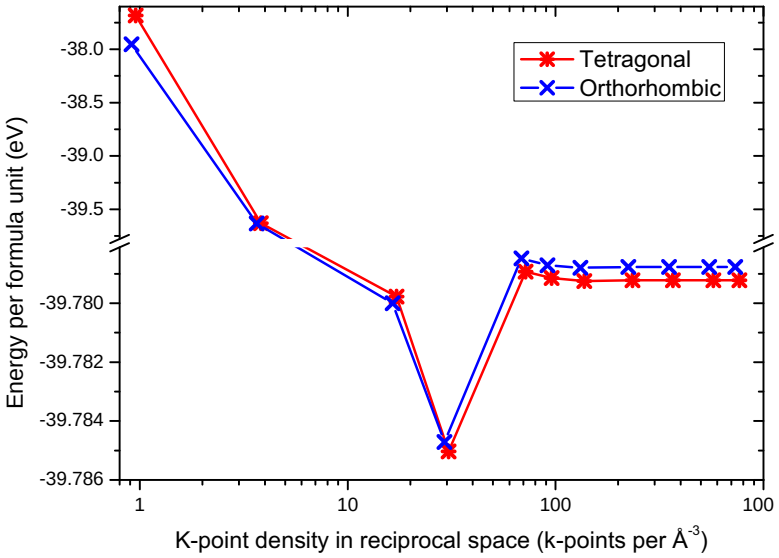

Figure 3.3.6: Plot of converged system energy vs. k-point density in reciprocal-space for PBEsol.

between $20\,\mu$eV and $30\,\mu$eV in every case. Though in principle a higher precision may be achieved with a higher k-point density, the 130 Å^3 density is a good balance and will be used as closely as possible for all systems.

Table 3.3.3 shows the four main unit cells used in the calculations in this thesis. The actual k-point density is approximate as it varies between functional and the symmetry of the atoms within it. The high k-point density for the rhombohedral system was used as a precautionary measure as it was uncertain what the consequence would be of the different angles on the lattice vectors.

Having considered the appropriate analytical parameters to use during calculations, we now move on to the methodology and results.

Table 3.3.3: Different unit cells used in this thesis with corresponding Monkhorst-Pack k-point configurations and approximate k-point density in reciprocal-space. Later in this work, the symmetry of the original cells was allowed to break and so the names given below do not necessarily refer to the space group of the optimized cell.

Number of atoms	Name of Cell	Description	k-point spacing	k-point density (approximate) (Å^3)
5	Cubic	$a \approx b \approx c \approx 3.9$ Å $\alpha \approx \beta \approx \gamma \approx 90°$	$8 \times 8 \times 8$	120
10	Rhombohedral	$a \approx b \approx c \approx 5.5$ Å $\alpha \approx \beta \approx \gamma \approx 60°$	$8 \times 8 \times 8$	245
20	Tetragonal/ Orthorhombic	$a \approx c \approx \frac{b}{\sqrt{2}} \approx 5.5$ Å $\alpha \approx \beta \approx \gamma \approx 90°$	$6 \times 4 \times 6$	140
40	Cubic	$a \approx b \approx c \approx 7.8$ Å $\alpha \approx \beta \approx \gamma \approx 90°$	$4 \times 4 \times 4$	120

3.4 Mapping the *I4/mcm* Energy Landscape

3.4.1 Introduction

In studying the tetragonal system, we use a 20 atom unit cell (see section 1.2.3 and table 3.3.3). The investigation for this structure follows two main branches; the first of which (covered in this chapter), involves the mapping and analysis of the entire $I4/mcm$ system (using the LDA, PBE and PBEsol functionals), which has three degrees of freedom.

The second branch forms part of a more general investigation described in chapter 4 and involves using geometry optimization to explore the unstable vibrational modes of STO and discovering the various saddle point and ground state structures that can be produced by manipulating higher symmetry structures in symmetry breaking ways.

3.4.2 The Set-up and Data Gathering

The tetragonal lattice has two variables corresponding to the different lengths of two lattice vectors ($a = c$, and b), where the $\mathbf{b}$ vector is the long one. Additionally the $I4/mcm$ space group has an extra variable which corresponds to the position of an oxygen atom, which has symmetry related images as discussed in section 1.2.3. The oxygen atom can move on a linear trajectory along the $\mathbf{ac}$ plane between $(\frac{1}{2}\mathbf{a}, 0\mathbf{c})$ and $(0\mathbf{a}, \frac{1}{2}\mathbf{c})$. In the 20 atom cell used in these calculations, there are a total of eight oxygen atoms that move in a symmetry related way (there are another four oxygen atoms that do not move within the unit cell). Though the motion of a given oxygen atom is linear, the collective motion of all the atoms appears as a rotation (of the octahedra that surround the titanium atoms) and is often referred to in this way. As they are corner sharing, every adjacent octahedron in the plane of rotation, rotates in the opposite direction. It also happens that adjacent octahedra on the axis of rotation, rotate in the opposite direction, which allows oxygen ions, separated in the $\mathbf{b}$ direction to gain maximum separation from each other. As there are no net ionic displacements, there are no ferro distortions in the $I4/mcm$ system.

The variables chosen for sampling the potential energy surface were: rotation angle θ (where a 0° rotation represented the cell contents in the cubic case); the ratio of the length of lattice parameters, adjusted to be in the pseudo-cubic context, such that a ratio of 1 represents the lattice in the cubic case:

$$r = \frac{b}{a\sqrt{2}}; \tag{3.4.1}$$

finally a volume parameter V_p which is related to but not proportional to the volume of the unit cell (see (3.4.4)). Ratio and rotation angle appeared to be the most physically

meaningful variables to use while the volume parameter appeared to be the simplest way of controlling the volume.

The lengths of the lattice parameters a and b are given by equations (3.4.2) and (3.4.3):

$$a = \left(\frac{V_T}{r\sqrt{2}}\right)^{\frac{1}{3}}; \tag{3.4.2}$$

$$b = (2V_T)^{\frac{1}{3}}\, r^{\frac{2}{3}}, \tag{3.4.3}$$

where V_T is the volume of the cell and r is the ratio (see above). V_T was taken as the volume of an almost optimized cell with tetragonal symmetry and was a constant, used as a template throughout the calculations, $V_T = 236.773259316\,\text{Å}^3$ exactly*. The actual volume of the unit cell is given by:

$$V = V_T V_p^3 \tag{3.4.4}$$

where V is the volume of the cell and V_p is the aforementioned volume parameter which is a scaling factor used within a *VASP* input file as a multiplier to all lattice vectors.

Calculation of the internal lattice coordinates is more involved. Figure 3.4.1 demonstrates the way that the lattice parameters are governed through a parameter τ, equation (3.4.5) shows the relationship between this and the rotation angle θ.

$$\tau = \frac{1}{4}\tan\theta \tag{3.4.5}$$

A computer code (*genPOSCARs*) was written to generate an $I4/mcm$ cell to a given specification of V_p, r and θ. For each of the three functionals, a series of 7657 cells were generated and given individual file names which included an index number and the specification of the cell (see appendix D.1.9). The ranges are given in table 3.4.1.

Table 3.4.1: The range of variables used to generate the potential energy surfaces. A total of 7657 points produced on the three-dimensional potential energy surface.

Parameter	First value	Last value	Increments	Data points
V_p	0.96	1.08	0.01	13
r	0.92	1.10	0.01	19
θ (°)	0.00	15.0	0.50	31

Single point, energy calculations were run on these structures using a plane-wave

*The large number of significant figures included here have no physical significance, rather their inclusion is to enable the reproduction of this work, without introducing numerical errors at the start.

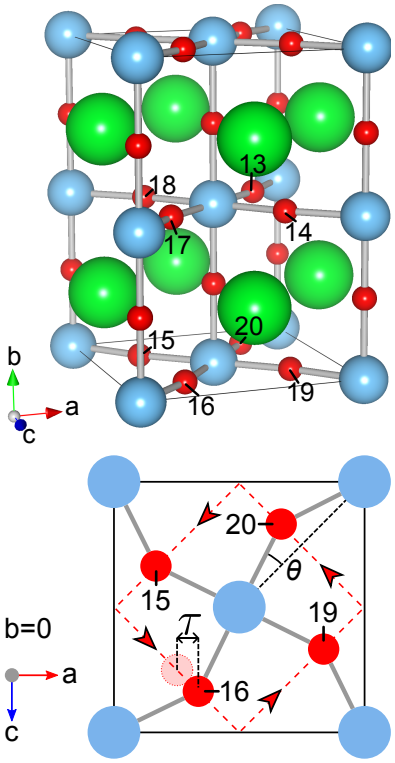

Num.	Type	a	b	c
1	Sr	0.50	0.25	0.00
2	Sr	0.00	0.75	0.50
3	Sr	0.00	0.25	0.50
4	Sr	0.50	0.75	0.00
5	Ti	0.00	0.00	0.00
6	Ti	0.50	0.00	0.50
7	Ti	0.50	0.50	0.50
8	Ti	0.00	0.50	0.00
9	O	0.00	0.25	0.00
10	O	0.50	0.75	0.50
11	O	0.50	0.25	0.50
12	O	0.00	0.75	0.00
13	O	$0.75+\tau$	0.50	$0.25+\tau$
14	O	$0.75-\tau$	0.50	$0.75+\tau$
15	O	$0.25-\tau$	0.00	$0.25+\tau$
16	O	$0.25+\tau$	0.00	$0.75+\tau$
17	O	$0.25-\tau$	0.50	$0.75-\tau$
18	O	$0.25+\tau$	0.50	$0.25-\tau$
19	O	$0.75+\tau$	0.00	$0.75-\tau$
20	O	$0.75-\tau$	0.00	$0.25-\tau$

Figure 3.4.1: Calculation of the internal coordinates of the tetragonal $I4/mcm$ unit cell. The right shows the fractional coordinates of all the atoms in the cell. Only the final eight oxygen atoms can change positions. τ regulates the position of the atoms (in some texts $x = 0.25 - \tau$ is used instead). In the top left is a perspective view of the entire cell, with the mobile atoms enumerated (strontium, titanium and oxygen are respectively represented by green, blue and red balls). On the bottom left is a schematic of a single layer of the cell. The red-dotted lines with arrows represent the motion of oxygen atoms with increasing τ. The rotation angle θ (as measured in this work) is also marked (please see equation (3.4.5)).

cut-off of 500 eV. Using both the facilities of *HECToR* and *Legion*, job scripts were written that would process a range of structure files between a first and last index number. The job submission systems would allow for several script files to be executed simultaneously (though more could be queued up for future processing). Within a job script, structures were processed one at a time, but 64 cores were used in parallel on each. Using the PBEsol functional, a single structure took about 85s to process (190s if an energy cut-off of 900 eV was used instead of 500 eV). After a given PE surface had been processed, there was a set of 7657 output files containing the converged potential energy of each system. The output files were processed by a shell script which produced an indexed list of all the output energies. The lists were manually reprocessed into a plain-text spreadsheet which combined the index numbers, cell specifications and cell energy.

A code was written to read in the spreadsheet, perform some error checking, map

Table 3.4.2: The 0 K minimum energy structure found by sampling the $I4/mcm$ potential energy surface using three functionals. The lattice parameters for the full tetragonal unit cell are given (the pseudo-cubic equivalents are in italics). Volume is per formula unit. The ratio is for a pseudo-cubic system (see equation (3.4.1)). Angle is as described in figure 3.4.1. ΔE is the difference in energy between the cubic $Pm\bar{3}m$ and tetragonal structure (the minimum cubic energy is taken from the geometry optimized cubic system optimized with a 500 eV energy cut-off).

Func.	a (Å)	b (Å)	Volume (Å^3)	Ratio	Angle (°)	ΔE (meV)
LDA	5.4383 (*3.8455*)	7.7679 (*3.8840*)	57.435	1.01	6.5	−11.5
PBE	5.5482 (*3.9232*)	7.9248 (*3.9624*)	60.987	1.01	5.5	−2.1
PBEsol	5.4933 (*3.8843*)	7.8464 (*3.9232*)	59.193	1.01	6.0	−6.8
Exp.	5.4970 (*3.8870*)[a]	7.7976 (*3.8988*)[a]	58.906[a]	1.00030[a]	2.1 (*1.4*)[c]	-
	5.5114 (*3.8972*)[b]	7.7988 (*3.8994*)[b]	59.224[b]	1.00056[b]	1.9 (*1.3*)[d]	-
					1.96 (*1.56*)[e]	-

a X-ray diffraction on a single crystal of $SrTiO_3$ at 77 K [24].
b X-ray diffraction on a single crystal of $SrTiO_3$ at 77 K [23].
c Electron spin-resonance of Fe^{3+} in $SrTiO_3$ with no O-vacancy compensation at 4.2 K (77 K in italics) [30].
d Electron spin-resonance of Fe^{3+} in $SrTiO_3$ with compensating O-vacancies (and factor of 1.4 correction applied to match the non-compensating system) at 4.2 K (77 K in italics) [121].
e Neutron total scattering with Reitveld analysis on a finely ground $SrTiO_3$ sample at 5 K (75 K in italics) [122].

the data points onto an array and analyse the data. Several versions of this code were written to analyse the data in different ways. The first code (*findMinima2*) identified minima by comparing data points on the PE surface to nearest neighbours (see appendix D.1.5). If the data points arranged in a three-dimensional array are imagined as a block of cubes, the code was able to identify separately: minima with respect to neighbours on the faces only; minima with respect to neighbours on faces and corners only; minima with respect to faces edges and corners (all neighbours). Also the global minimum was marked.

Table 3.4.2 shows the details of the minimum energy $I4/mcm$ structures found though this sampling technique. In comparing the DFT results to experiment, we see that all the functionals reproduce the general character of the material in terms of approximate lattice parameters, and a small rotation of the oxygen octahedra. However, qualitatively, the PBEsol functional is the most efficace in terms of matching the experimentally determined lattice parameters with a deviation of at most 0.6 %. LDA underestimates the lattice parameters and PBE overestimates them. The experimentally determined b/a ratio for the tetragonal system is only very slightly different to that of the cubic i.e. unity. Unfortunately the sample points used in the present calculations were placed too sparsely along the ratio dimension to accurately characterize this

slight distortion. All three functionals overestimate the ratio of lattice parameters, but from a qualitative point of view, the distortion is in the correct direction. In all cases the oxygen octahedron rotation angle is overestimated by a factor of between two and three. In reality, even at 0 K, the expectation value for the rotation will be lower than the position of the minimum potential energy, since the potential energy surface generated is only half of the actual surface that mirrors about positive and negative values of rotation. The nuclear wave function for the system which is later calculated (see section 3.4.7), has a maximum amplitude either side of the angle = 0° line. As the expectation value will be some combination of the two possible solutions, the actual rotation can be expected to be lower than in the position of the minimum potential energy position. ΔE shows significant variation between the different functionals with a factor of ~ 6 difference between the highest and lowest. PBEsol predicts the hardest rotational mode (shallowest down slope as rotation increases, also most amenable to inverting) while LDA predicts the softest mode (steepest down slope).

It is worth noting that the differences in energy between neighbouring sample points for θ are 0.1 and 0.5 meV at the minimum for lower and higher angles respectively. These modes are sufficiently soft that it is hard to predict the minimum position with a better precision than $\pm 0.5^\circ$. In the other directions the slope of the surface is steeper with energies differences of 1 and 4 meV respectively for the lower and higher values of ratio and about 30 meV either direction for the volume parameter V_p (corresponding to a 3 % change in actual volume). These values were taken for PBEsol, other functionals produce values of the same order.

3.4.3 Relating the 500 eV Surface to Results Obtained Using a 900 eV Energy Cut-Off

To relate the energy surface as determined with a 500 eV energy cut-off with an energy surface determined with a 900 eV cut-off, two series' of points were compared with one another using both energy cut-offs. Two sets of sample points were taken, the first, arranged at eight corners of an oblong around the region of the cubic to tetragonal transition and an additional two points at the cubic and tetragonal minimum. This region was defined by V_p values of 0.98 and 1.02, r values of 0.98 and 1.02, θ values of 0° and 8° and additionally the two minima, whose positions were dependent on the given functional. The second set of points was placed at the eight most extreme corners of the potential energy surface. Within each set of points the average difference between the energies for the 500 and 900 eV calculations was calculated.

From the results of this sampling, shown in table 3.4.3, we see that the 500 eV energy surface, once applied with an appropriate correction can produce results accurate to ~ 1.5 meV when used in comparisons with the results from a 900 eV calculation,

Table 3.4.3: Samples showing the difference in DFT energy between the 500 and 900 eV energy cut-off PE surfaces. Mean difference was calculated using a set of 10 points close to the cubic-tetragonal transition path way (inner points). The mean difference for the points at the extreme positions of the potential energy surface was almost identical but with a greater variation from the mean, the standard deviation for these eight points has been included here (extreme points). All 900 eV results are lower in DFT energy than the 500 eV results.

Functional	Mean difference (meV)	$\sigma_{\text{inner points}}$ (meV)	$\sigma_{\text{extreme points}}$ (meV)
LDA	22	1.3	4.6
PBE	22	1.5	4.9
PBEsol	17	1.4	4.6

provided that the samples are taken close to the transition path. If the samples are taken at the more extreme points (although there is little change to accuracy with large values of θ), then the accuracy reduces to ~ 5 meV.

3.4.4 Visualizing the Three-Dimensional Data Set

In order to visualize the energy surface, an algorithm was written to flatten the three-dimensional surface into two dimensions. The algorithm was implemented in two ways: the first (*volMatFit2*) flattened the data in the direction of volume (only considering the points of minimum energy w.r.t. volume); the second (*thetaMatFit2*) flattened in the direction of angle θ. So data sets were produced that represented energy structures with respect to volume as a function of θ and ratio r and also the energy minimized with respect to θ as a function of volume and r (more details of these two algorithms can be found in appendices D.1.6 and D.1.7). With these data sets, two-dimensional contour plots were produced.

The first attempt simply involved choosing the lowest energy systems along each line in the data set in the relevant direction. However, this method proved to produce very coarse contours that were hard to interpret. To improve the minimization, a residual squared technique was implemented to fit a set of polynomials to the data (see appendix A.2).

A summary of the algorithm for minimizing with respect to volume is as follows: for every set of volume points corresponding to a point on the $r\theta$-plane, a polynomial of fourth order was fitted (the polynomial was of potential energy in terms of V_p). Subsequently, for every point on the $r\theta$-plane, the polynomial was analytically minimized, with the minimum energy and minimum volume written to separate tables for the production of a pair of contour plots. The second plot of volume vs. θ and r was included so as to represent what was happening in the unplotted dimension. The fourth order fit-

ting was shown to produce good results with an RMS deviation from calculated points of ~ 0.1 meV per formula unit. Fitting to higher order polynomials raised difficulties in terms of coding a minimum finder and additionally did not improve the quality of the fit using the current fitting algorithm.

The contour plots for energy minimized with respect to volume for the LDA, PBE and PBEsol functionals are shown respectively in figures 3.4.2, 3.4.3 and 3.4.4. The plotting software *Origin Pro*, used linear interpolation to produce the plots based on the regular grid of points supplied to it. The white contour line on the plots labelled (a) is used to highlight the region of cubic equivalent energy and to mark the divider between two different energy scales that have been used. In these graphs, energy has been converted into the difference in energy per formula unit compared to the cubic system. The value chosen for the cubic energy was based on the present data set rather than from the separately obtained minimized cubic system mentioned in the caption for table 3.4.2. Likewise for the plot of volume contours, the volume has been expressed as the ratio of cell volume per formula unit V and the ideal cubic volume, with the ideal cubic volume also taken from the present data set rather than the previously obtained geometry optimized system. The reason for taking the ideal cubic system as the reference point for the current data set was so as to keep the plots self consistent such that the cubic system lay on the contour for zero energy and on the contour for unchanged volume. In any case, the fitting was sufficiently good that the deviation between the fitted energy and the energy of the geometry optimized system was between 0.2 and 0.5 meV and the deviation in fractional volumes was between 0.0015 and 0.0017 for the three functionals (all overestimates in the case of volume). The quality of the polynomial fit in predicting the minimum energy point may be superior to the geometry optimization algorithm implemented within *VASP* as the geometry optimization terminates when the magnitude of the energy gradient falls beneath a certain threshold. By comparison, the polynomial fit evens out numerical noise and the actual minimum is found via analytical methods (exact to within the numerical accuracy of the computer).

All three functionals (figures 3.4.2, 3.4.3 and 3.4.4) produced a qualitatively similar potential energy surface (a). Specifically, they predict a valley leading from the cubic structure towards the ideal $I4/mcm$ structure almost directly in the direction of the octahedral rotation angle θ. Due to the slight angle of the valley relative to the ratio r, there is a propensity for θ to increase with increasing r. The gradient of potential energy with respect to θ in the region of the minimum (between 0° and 6°) is very low (between -2.3 and 0.9 meV/$^\circ$ for the PBEsol functional). However, for angles greater 6°, the gradient increases rapidly e.g. 4.2 meV/$^\circ$ at 7° and 8.8 meV/$^\circ$ at 9°. r has the greatest freedom to vary when the system is close to the ideal $I4/mcm$ structure.

By comparing the size of the region on the potential energy surfaces (a), defined by

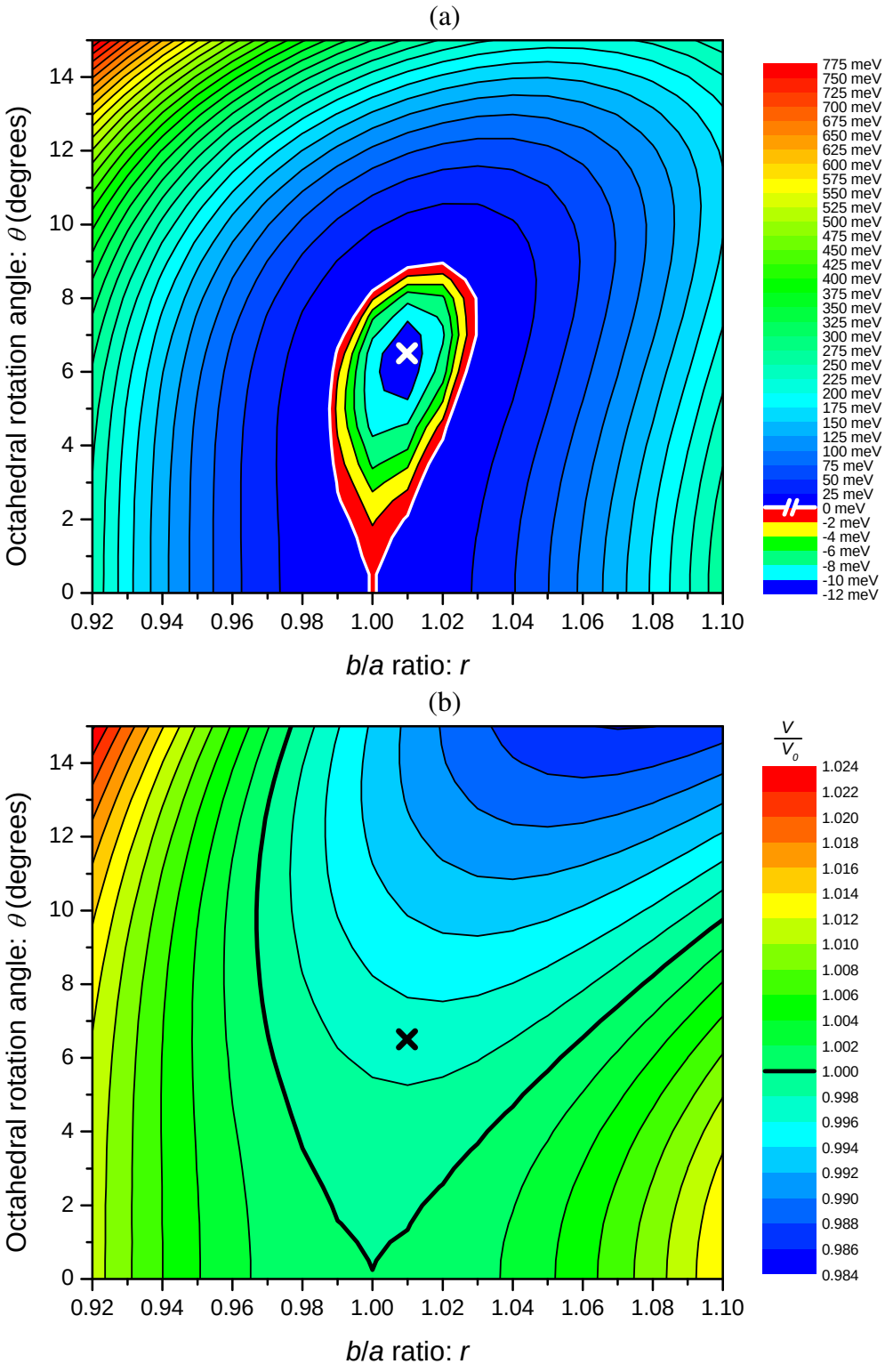

Figure 3.4.2: Contour plots of the $I4/mcm$ potential energy surface using the LDA functional, the minimum is marked ✕: (a) shows the minimized (w.r.t. volume) potential energy per formula unit, relative to the minimum cubic energy (-44.1103 eV, taken from the plot). (b) shows the volume corresponding to the minimum energy in (a) for each point compared to the minimum cubic volume V_0 (57.782 Å^3 per formula unit, taken from the plot).

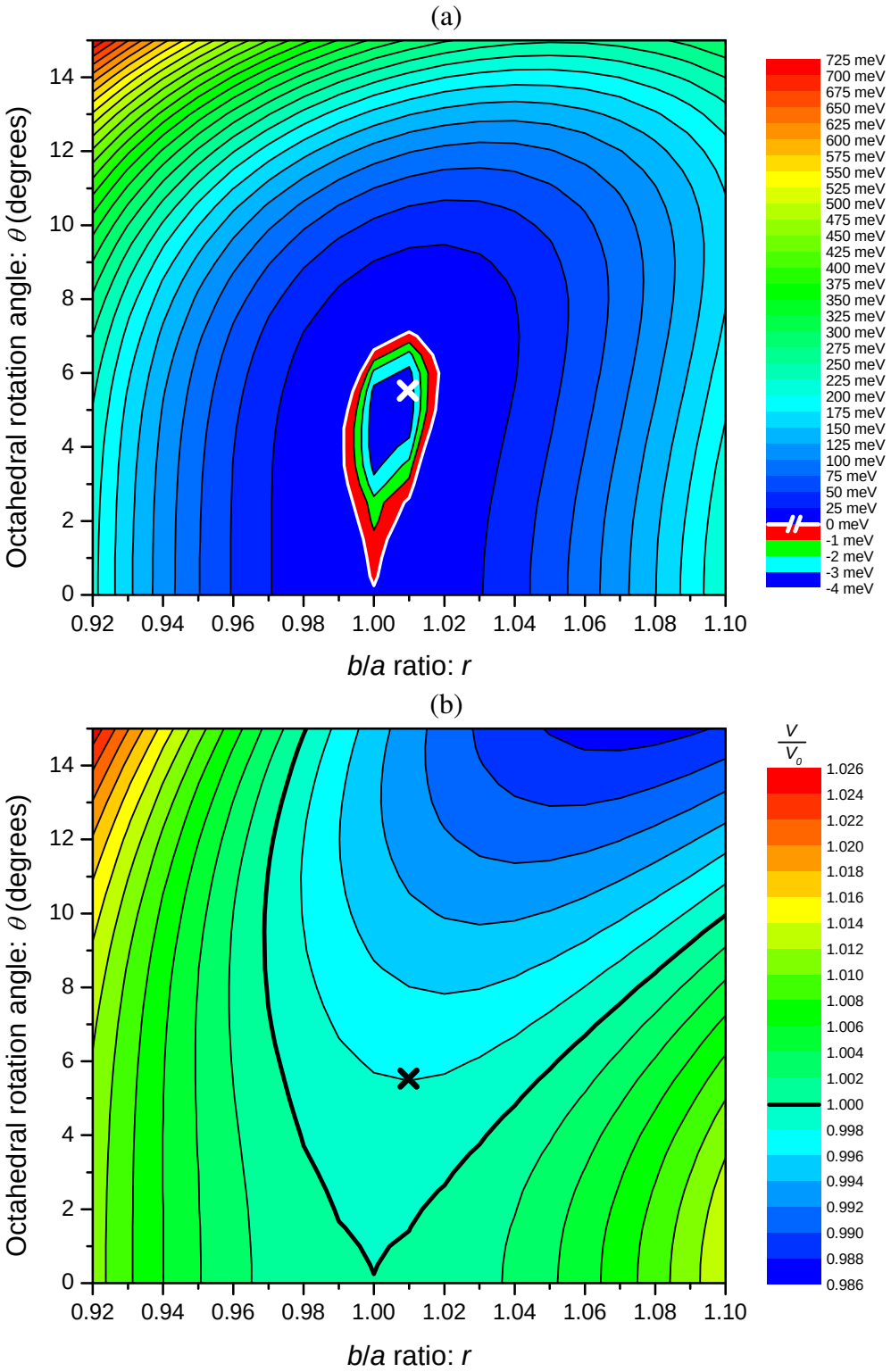

Figure 3.4.3: Contour plots of the $I4/mcm$ potential energy surface using the PBE functional, the minimum is marked ✕: (a) shows the minimized (w.r.t. volume) potential energy per formula unit, relative to the minimum cubic energy (-40.2013 eV, taken from the plot). (b) shows the volume corresponding to the minimum energy in (a) for each point compared to the minimum cubic volume V_0 (61.476 Å^3 per formula unit, taken from the plot).

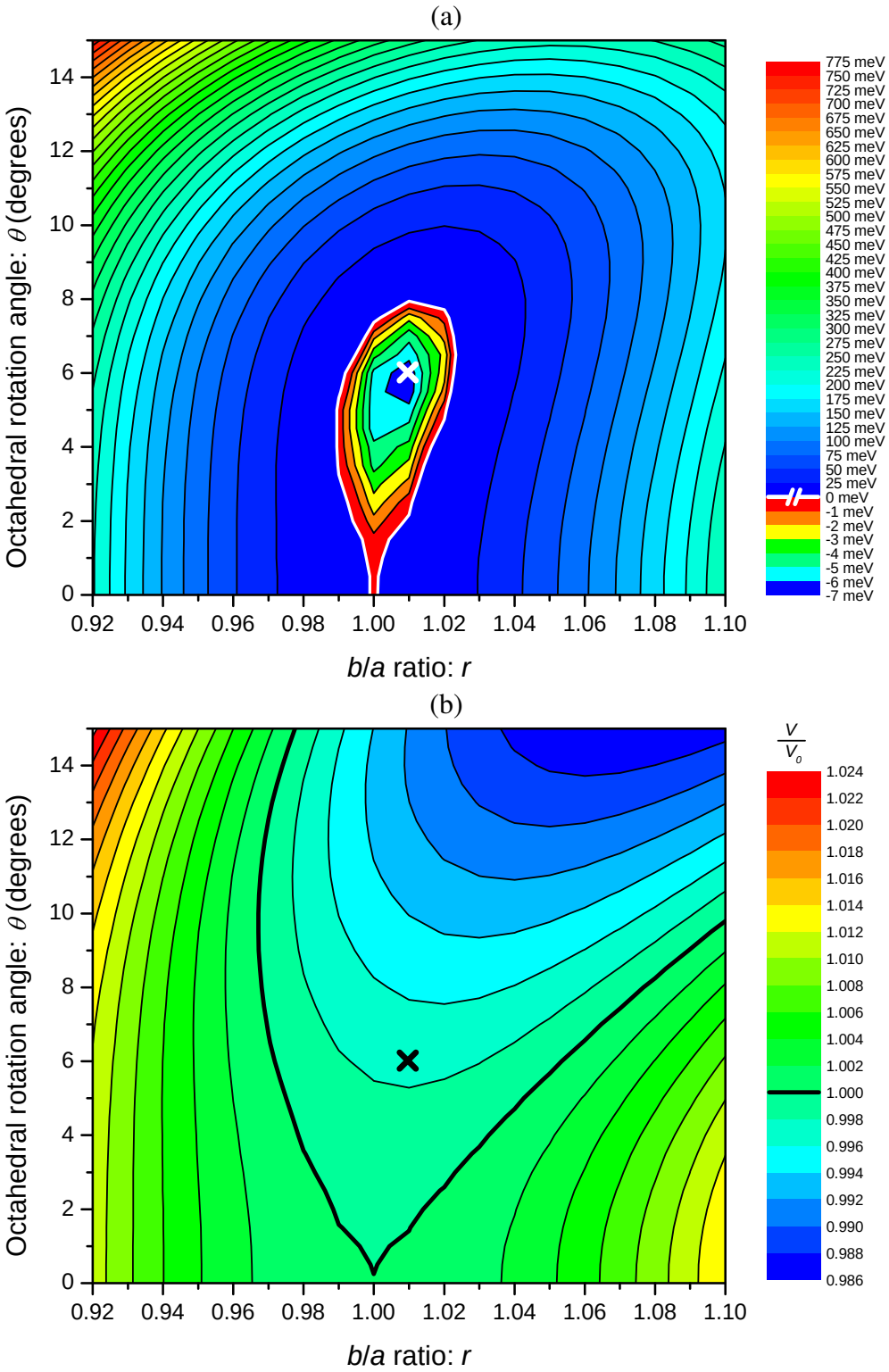

Figure 3.4.4: Contour plots of the $I4/mcm$ potential energy surface using the PBEsol functional, the minimum is marked ✕: (a) shows the minimized (w.r.t. volume) potential energy per formula unit, relative to the minimum cubic energy ($39.7558\,\text{eV}$, taken from the plot). (b) shows the volume corresponding to the minimum energy in (a) for each point compared to the minimum cubic volume V_0 ($59.396\,\text{Å}^3$ per formula unit, taken from the plot).

the cubic contour line (in white), we see that the LDA functional predicts the greatest range of motion while maintaining the same potential energy, while PBE predicts the minimum range of motion (if volume is allowed to relax). In addition, as has already been shown in table 3.4.2, LDA predicts that the valley depth is approximately twice that of PBEsol and three times that of PBE. Despite these differences, the total range of potential energies shown on these volume relaxed systems is approximately equal. When considering the non-volume relaxed case i.e. the difference between the highest and lowest energy system over the entire energy surface, we find a gap per formula unit of 2.36 eV for LDA, 1.98 eV for PBE and 1.93 eV for PBEsol.

From examining the plots of volume at the minimum energy (all labelled (b)) (or ideal volume for a given r and θ), we find that within the region of the cubic to ideal tetragonal transition, the expected volume decreases with increasing θ. If r also increases slightly, the ideal volume will carry on decreasing with increasing θ up to at least $15°$. The smallest crystal cells within this data set occur when r is 1.07 and θ is $15°$ for all functionals. The largest cells appear at the upper and lower limits of r and respectively the lower and upper limits of θ i.e. when $r = 0.92$ and $\theta = 15°$ and when $r = 1.10$ and $\theta = 0°$. The largest cells occur at maximum octahedral rotation and with a highly squashed cell (perpendicular to the plane of rotation) or with no rotation and a highly stretched cell. Comparison of the predictions made by the three functionals, shows that ideal volume (relative to the cubic system) is both qualitatively and quantitatively very similar.

The flattening algorithm was implemented differently in the case of the minimization of energy with respect to θ. As the data set is symmetrical about the Vr-plane, any accurate polynomial fit will only have non-zero coefficients on the even terms (the symmetric terms) so θ^2 was fitted to fourth order, matching the description of the previous set of contour plots. In order to minimize the polynomials with respect to θ, the analytical approach used previously was no longer appropriate as it would require finding the roots of a seventh order polynomial. Instead a one-dimensional Newtonian-Raphson optimizer was implemented, based on equation (2.4.8), which would typically find a minimum within around seven iterations. Additionally, the contour plotting software works best if its horizontal and vertical data points are supplied as a regular grid. Because the volume parameter V_p was sampled in regular intervals instead of actual volume, an interpolation had to be performed to supply the software with data in the preferred form. In this case a simple linear interpolation was used in the direction of volume only. A large number (101) data points were chosen so as to retain as much of the original data as possible. The plotting software's own internal interpolation is also linear.

The contour plots for energy minimized with respect to θ are shown respectively

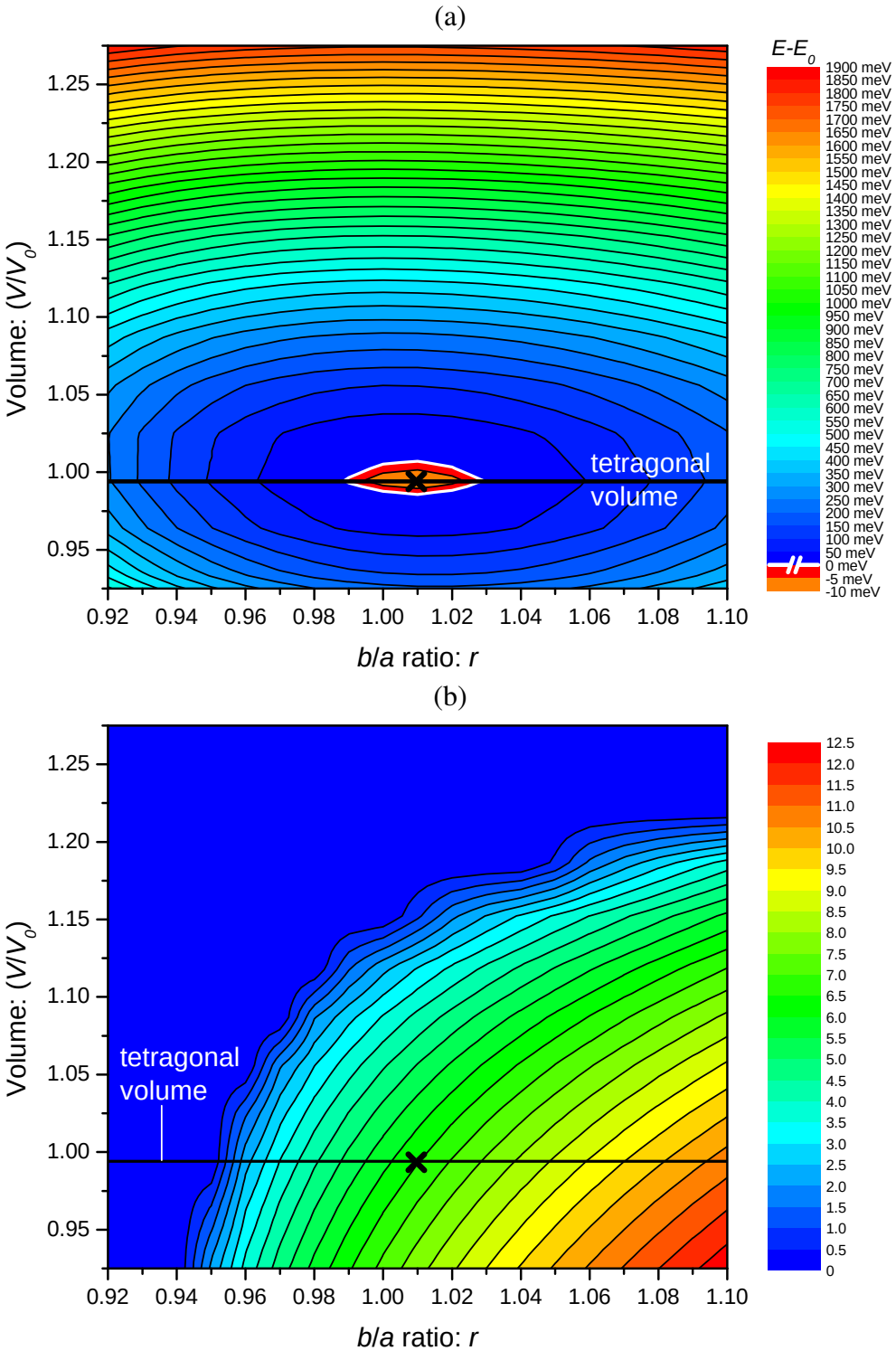

Figure 3.4.5: Contour plots of the $I4/mcm$ potential energy surface using the LDA functional, the minimum is marked ✕: (a) shows the minimized (w.r.t. θ) potential energy per formula unit, relative to the minimum cubic energy ($-44.1103\,\text{eV}$, taken from the minimized with respect to volume data). (b) shows the octahedral rotation angle θ in degrees, corresponding to the minimum energy in (a) for each point.

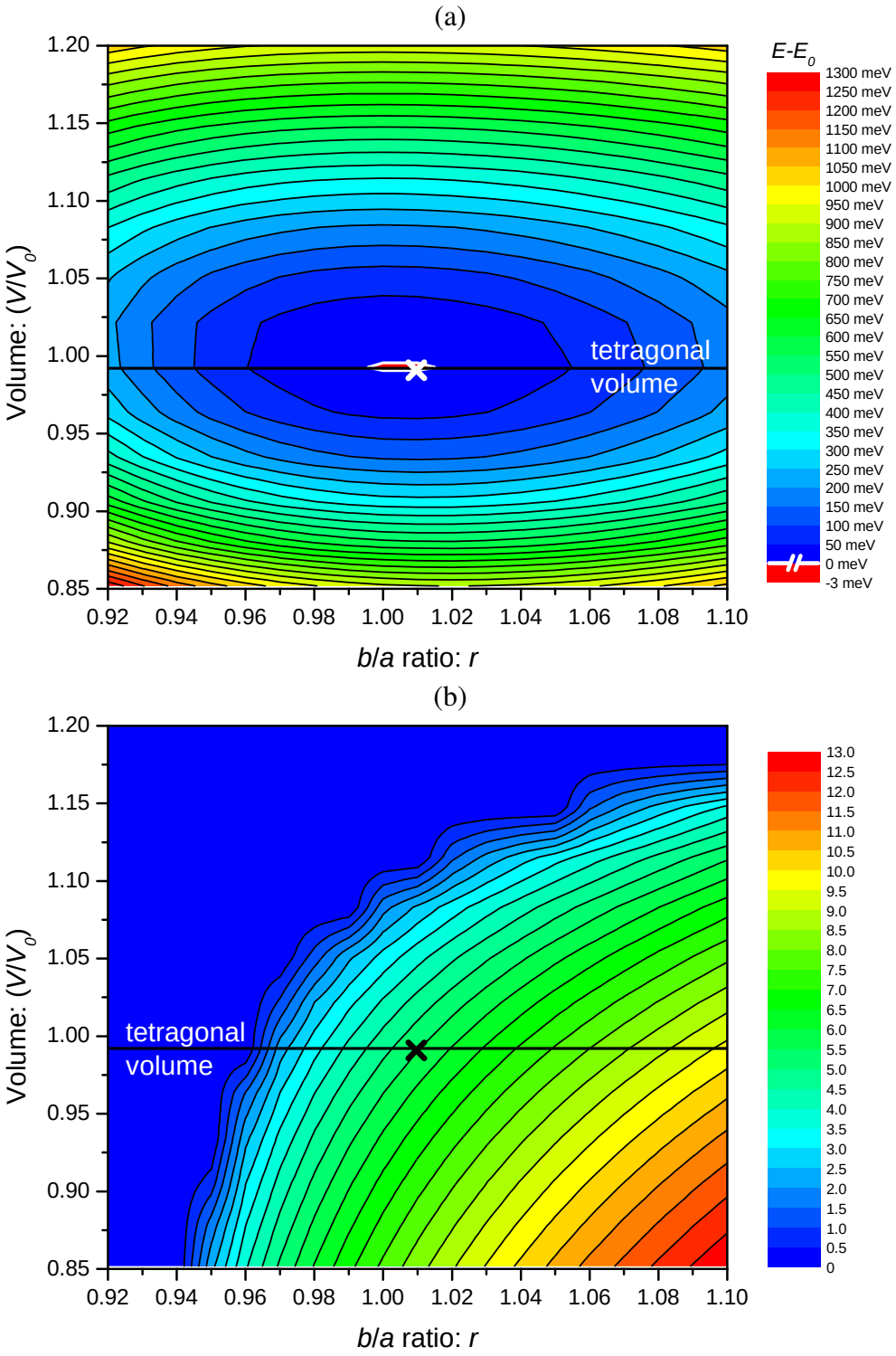

Figure 3.4.6: Contour plots of the $I4/mcm$ potential energy surface using the PBE functional, the minimum is marked ✕: (a) shows the minimized (w.r.t. θ) potential energy per formula unit, relative to the minimum cubic energy (-40.2013 eV, taken from the minimized with respect to volume data). (b) shows the octahedral rotation angle θ in degrees, corresponding to the minimum energy in (a) for each point.

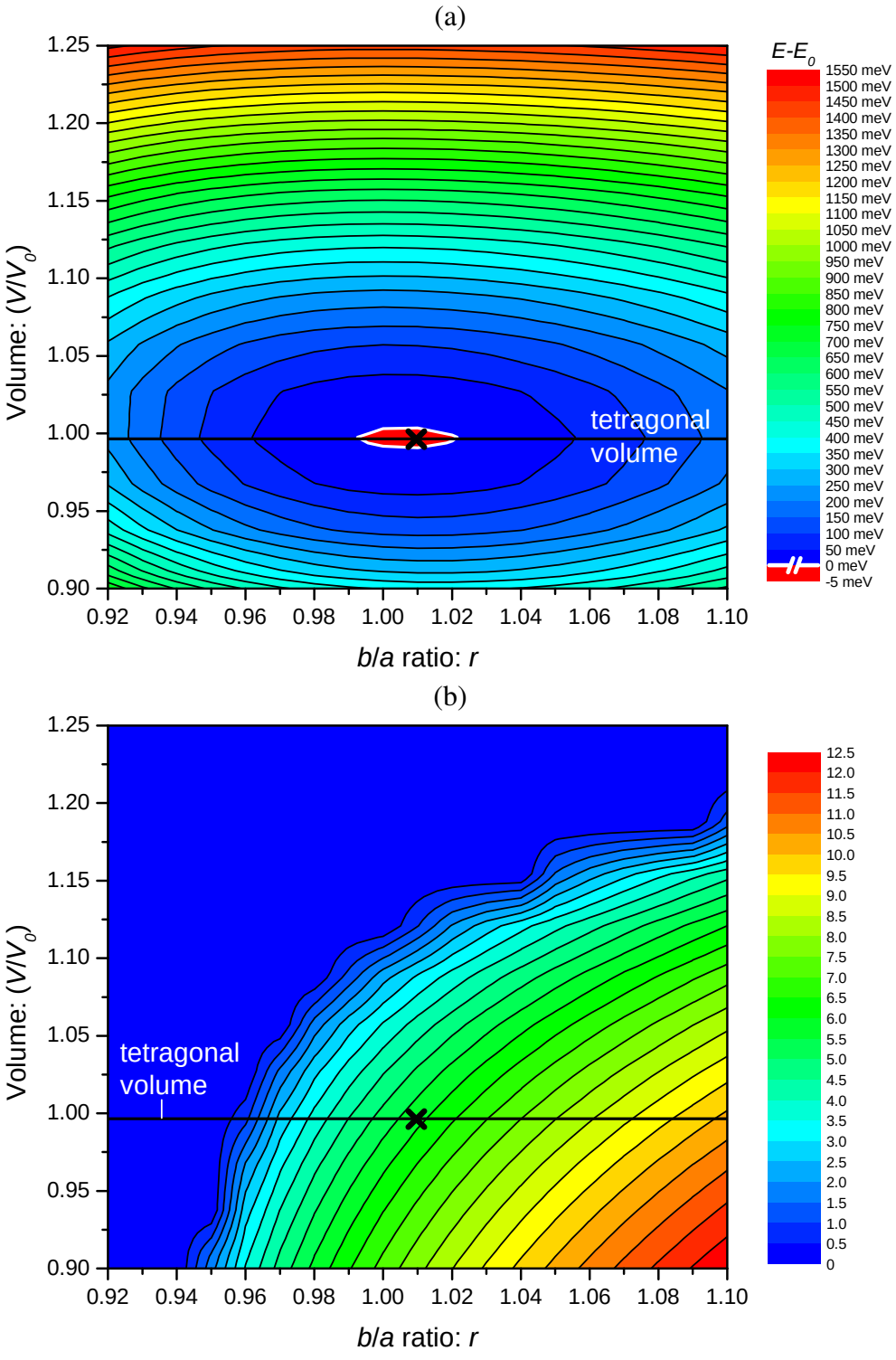

Figure 3.4.7: Contour plots of the $I4/mcm$ potential energy surface using the PBEsol functional, the minimum is marked ✕: (a) shows the minimized (w.r.t. θ) potential energy per formula unit, relative to the minimum cubic energy (-39.7558 eV, taken from the minimized with respect to volume data). (b) shows the octahedral rotation angle θ in degrees, corresponding to the minimum energy in (a) for each point.

for the LDA, PBE and PBEsol functionals in figures 3.4.5, 3.4.6 and 3.4.7. The plots marked (a) show energy per formula unit compared to the cubic case which was taken from the data for energy minimized with respect to volume (figures 3.4.2, 3.4.3 and 3.4.4) for consistency. The data shows that to an approximation, the potential energy profile has mirror symmetry about the minimum, in the direction of both volume and ratio (horizontally and vertically), within the range of the calculations. The variations in the volume ranges as displayed on the plots between the different functionals are due to the different equilibrium volumes. The same set of absolute volumes were used for each functional.

The potential well at the equilibrium position does not sink as low as for the systems minimized with respect to volume, which is an artefact of the sampling and fitting process. When minimizing with respect to volume along lines of constant θ and ratio, there was a set of points in the data set with a perfectly cubic ($Pm\bar{3}m$) structure. The ideal cubic structure lay in between two points and the fitting and minimization process determined its position more precisely. When minimizing with respect to θ along lines of constant ratio and volume, the ideal structure was missed, hence explaining why the lowest values of energy were not obtained here.

The plots marked (b) show the ideal θ as predicted by the potential energy minimum for a given cell volume and ratio r and correspond to the points on the (a) plot. We can see that θ increases with increasing r and decreasing V. Additionally there is a region for low r and high V where the ideal octahedral rotation angle is zero i.e. for large cells or for cells squashed in the direction perpendicular to the plane of rotation. For all functionals, the boundary of this region appears to be at ratios of 0.94 and values of V/V_0 of 1.21, 1.175 and 1.2 for the LDA, PBE and PBEsol functionals respectively. Summarizing, we can say that octahedral rotation in the tetragonal system appears be correlated to the thinness of lattice in the plane of rotation. Inwards pressure applied by the titanium atoms in the plane can drive the octahedra to rotate.

3.4.5 Trivariate Polynomial Fitting of the PE Surface

Having used considerable computer resources to compute the potential energy surface, we set out to try and describe it using a polynomial. A trivariate polynomial is a polynomial in terms of three independent variables and can be expressed as:

$$f(x,y,z) = \sum_{i,j,k=0}^{n} a_{ijk}\, x^i y^j z^k, \tag{3.4.6}$$

where i, j and k are integers, the set of a_{ijk} are the coefficients and n is the order of the polynomial. In the present work, the set of coefficients included in the fit were limited

such that:

$$i + j + k \leq n. \tag{3.4.7}$$

The independent variables, were expressed in the following way:

$$x = V/V_0 - 1; \tag{3.4.8}$$

$$y = r - 1 = \frac{b}{a\sqrt{2}} - 1; \tag{3.4.9}$$

$$z = \theta^2, \tag{3.4.10}$$

where V and V_0 are respectively the volume of the cell and the volume of the ideal cubic cell for the given functional. For the polynomial description of the surface the chosen value for V_0 was based on the independently minimized cubic system using a conjugate gradients optimizer, (V_0: $57.694\,\text{Å}^3$, $61.384\,\text{Å}^3$ and $59.294\,\text{Å}^3$ for the LDA, PBE and PBEsol functionals respectively). b and a are the long and short lattice parameters respectively on the tetragonal unit cell. θ has been expressed in radians. The decision to subtract one from x and y and to express θ in radians instead of degrees was to bring these variables closer to the zero line. This practice can can improve the fitting by reducing numerical noise. As was done in section 3.4.4, θ was squared so that only its even powered coefficients were included in the fit.

The fitting process was performed using a residual squared method, similar to the method used to perform fitting in one dimension. The details have been given in appendix A.3. The code written to perform these calculations was called *multiVariateFit*, see appendix D.1.8.

It was desirable to fit the potential energy surface to the data with a high precision such that the fine detail was retained in it (ideally the polynomial description would have deviated from the data set by no more than $1\,\text{meV}$). In practice the linear solver failed for orders of $n > 6$. At this level of description, the quality of fit is shown in table 3.4.4.

Table 3.4.4: Deviation of *I4/mcm* data set from the polynomial. The maximum deviation and RMS deviation have been shown, for each functional.

Functional	Max. deviation (meV)	RMS deviation (μeV)
LDA	1.3	1.25
PBE	0.56	1.13
PBEsol	0.61	1.14

The 84 coefficients, describing the energy surface using each of the three functionals are too numerous to display in the main text and so have been placed in the

appendix in table B.1. Again, the results are expressed in eV per formula unit.

With the entire energy surface modelled with a polynomial, a new attempt at finding the global minimum was made by implementing a simple Newtonian-Raphson optimizer in three dimensions (see section 2.4.4, specifically equation (2.4.8), which describes the update algorithm).

Table 3.4.5: Minimum energy configurations for *I4/mcm* tetragonal system as determined by the minimization of a fitted polynomial description of it.

Functional	Volume V (Å^3)	V/V_0	Ratio r	Angle θ (°)
LDA	57.617	0.99866	1.0080	6.29
PBE	61.378	0.99989	1.0046	4.99
PBEsol	59.264	0.99949	1.0062	5.59

The improved values for the ideal tetragonal system are shown in table 3.4.5. When comparing these results to the discreetly obtained (taken off a grid) results in table 3.4.2 we see a small reduction in the value for ratio for all functionals, though these results are still approximately an order of magnitude out from the experimental results (after 1 is subtracted). The rotation angles are generally slightly lower (and therefore closer to the experimental value of around 2° [30, 41, 121–123]). However, in the case of the PBE functional, the fitting is clearly imperfect as it places the potential energy minimum closer to 5° than 5.5°. It would have been desirable to use a system of fitting that put a heavier emphasis on accuracy towards the minimum of the data set. However, implementing such fitting methods requires careful consideration in terms of the balance of the fitting quality close to and away from the minimum and would have required a further investment in time to properly research and code.

3.4.6 Comparison to Landau Theory

With the data available from section 3.4.5, we can compare the potential energy surface in one dimension with experimental observations. Hayward and Salje [8] present data on the relationship between free energy and an order parameter, which they label Q (proportional to the octahedral rotation angle). As the potential energy is a component of free energy (see equation (1.2.3) on page 27), a comparison of the two would be appropriate if the other components are small. Hayward and Salje use Landau theory (see section 1.2.7) and multiple sets of experimental data from different sources to derive the free energy with respect to Q and temperature. Their equation for free energy differs slightly from conventional Landau theory and tries to take into account quantum effects:

$$G = \frac{A\theta_S}{2}\left(\coth\frac{\theta_S}{T} - \coth\frac{\theta_S}{T_C}\right)Q^2 + \frac{B}{4}Q^4 + \frac{C}{6}Q^6, \qquad (3.4.11)$$

where θ_S relates to the quantum mechanical character, T is temperature and T_C is the phase transition temperature.

Data on EPR, spontaneous strain, X-ray diffraction and twin angle data (see [8] and references therein) were used to fit values for θ_S, B/A, C/A and T_C. Calorimetric measurements of the excess entropy were used to determine A. For comparison with the present work, their experimentally derived parametrization was simplified (for $T = 0$), formulated in terms of angle in radians and expressed in units of eV.

Table 3.4.6: Coefficients of polynomials in θ (radians), representing potential energy for the ideal cubic and tetragonal systems (in terms of ratio and volume). For a comparison, experimentally derived parameters have been included for the Gibbs free energy, taken from reference [8]. The energy terms described here are in eV per formula unit, the experimental parameters by Hayward and Salje were converted from their presented description. In doing so we assumed that $\theta = 0.04357Q$, where Q was the order parameter used in [8]. This estimate was based on comparing scales on figure 6 of their work and applying a conversion from degrees to radians. We assumed 0 K temperature.

	LDA		PBE		PBEsol		
θ^n	Cubic	Tetragonal	Cubic	Tetragonal	Cubic	Tetragonal	Experiment
0	-44.11	-44.11	-40.20	-40.20	-39.76	-39.75	-
2	-2.017	-2.384	-1.234	-1.388	-1.560	-1.804	-0.09932
4	103.2	102.9	94.01	93.71	98.06	97.76	20.94
6	-241.9	-241.3	-193.0	-192.3	-220.0	-219.7	9916
8	1864	1855	1493	1485	1788	1783	-
10	-7144	-7086	-6231	-6187	-8225	-8192	-
12	8640	8640	12200	12200	18410	18410	-

In the present work, a simple algorithm was written (appended to the end of *multiVariateFit*) to flatten the three-dimensional energy surface down into a single variable polynomial (in θ) of the same order as the polynomial, for a given value of volume and ratio (actually it deals with values of x and y, see equations (3.4.8) and (3.4.9)). The ideal values for volume and ratio in table 3.4.5 were chosen. The results, along with those for the experimentally derived free energy are presented in table 3.4.6.

As can be seen from the data, the fit to the free energy is very poor. Qualitatively, the values for the 2^{nd} and 4^{th} order terms bear a resemblance to the experimental data. The 2^{nd} order term is small and negative in both cases, though out by approximately a factor of 20. The 4^{th} order term is approximately out by a factor of five but is of the correct sign. There is no correspondence between the computational and experimental value for the 6^{th} order term.

To investigate the discrepancy for the 6^{th} order term, the potential energy was refitted to only 6^{th} order with respect to θ (or 3^{rd} order with respect to θ^2 which was used

in the fitting). The higher order terms were removed as we considered that allowing the system these additional degrees of freedom could interfere with the best fit of the lower order terms (used by Hayward and Salje). Most significantly affected was the 6^{th} order term, but this only decreased in magnitude to roughly one third of its previous value. The decrease in magnitude brings its value closer to experiment, but is still not comparable. As an aside, the removal of the higher order terms in θ only doubled the maximum deviation from the data points of the trivariate polynomial.

The differences between these experimental results and our computational results could have two origins: firstly, the DFT functional may not provide a sufficient description of the $I4/mcm$ STO system and secondly, the other terms in the Gibbs free energy (besides potential energy) may be very much more significant than the potential energy. Though it may be the case that Landau theory does not entirely describe the tetragonal system, the errors between the Landau theory fit and experiment were very small in comparison to the deviation of the computational results presented here [8].

Following on from the generation of the one-dimensional polynomials presented here, we take a brief look at the consequences of factoring in QM behaviour of the nuclei.

3.4.7 Calculating the Nuclear Wave Function

In most DFT calculations (including the ones in the present work), the atomic nuclei are assumed to be classical particles, moving under the influence of QM forces from the electrons and only Coulombic forces from the other nuclei. Due to the comparably large masses and slower speeds of the nuclei, this is normally an adequate assumption. However, the nuclei do follow QM rules which could be influential in the case of a system with very small forces holding the nuclei in place.

As the potential energy surface is symmetrical with respect to $\pm\theta$, there is equal probability of a given crystal domain having a clockwise or anticlockwise rotation. The potential energy barrier in between these two configurations keeps one from changing to the other. However, in a model that includes the nuclei as quantum particles (only as point particles, the quantum chromodynamical influences can rest for another thesis), the expectation value of the positions of atoms in the crystal will be a combination of the different possible ground and excited states. A combination of a clockwise and anticlockwise rotation will result in an expectation rotation, closer to $0°$. The experimental evidence suggests that the rotation angle at $0\,\mathrm{K}$ should be close to $2°$[30, 41, 121–123] instead of $\sim 5.5°$ as predicted by the potential energy minima from DFT.

In conjunction with Alexey Sokol (UCL), an algorithm was written to calculate the ground and excited states of a potential energy surface in one dimension. The one-dimensional version was used as it was simpler to deal with. The code was based

around the work by Erik Koch, found on his website (see reference [124]). Much of the detail of the implementation will be left out as the results showed only a minimal improvement in the expectation rotation angle. The algorithm was appended to the end of *multiVariateFit* after the Landau theory comparison work, see appendix D.1.8.

The ground state and first excited state were found to be near-degenerate, with a more significant energy gap for the 2^{nd} excited state. For this reason the expectation value for the rotation angle was based on a wave function in a mixed quantum state, built from a linear combination of the two lowest energy states. The chosen solution was the one that produced the maximum localization (the solution that had the largest amount of probability density over as small an angular separation as possible) and was the result of an equal contribution between the ground and first excited state wave functions. The expectation value of rotation was given by:

$$\Psi(\theta) = \psi_0(\theta) + \psi_1(\theta); \tag{3.4.12}$$

$$\phi_{\text{expect}} = \left\langle \Psi(\theta) \left| \hat{\Theta} \right| \Psi(\theta) \right\rangle = \frac{\int_{-\infty}^{\infty} \Psi^*(\theta)\theta\Psi(\theta)\ \mathrm{d}\theta}{\int_{-\infty}^{\infty} \Psi^*(\theta)\Psi(\theta)\ \mathrm{d}\theta}, \tag{3.4.13}$$

where Ψ, ψ_0 and ψ_1 are the total wave function (as used in these calculation) and the ground and excited state wave functions respectively, θ is the rotation angle and $\hat{\Theta}$ is the rotation operator. No thermodynamic considerations were used in weighting factors for the eigenstates in their combination to form the total wave function. Given the one-dimensional approximation used here, the resultant θ_{expect} can be considered an upper limit on the rotation angle, the inclusion of higher energy states in the total wave function would push the expectation rotation towards zero. If other degrees of freedom (other vibrational modes, including ones that are out of the $I4/mcm$ symmetry system) had been included in a more advanced model, the expectation rotation angle could change in either direction.

At the optimised volume and ratio positions as predicted by the potential energy minimum (found by the NR minimizer), the expectation value for rotation is $6.10°$, $4.99°$ and $5.59°$ for the LDA, PBE and PBEsol functionals respectively (a decrease of between $0.18°$ and $0.35°$ compared to the results shown in table 3.4.5.

These (maximum) rotation angles can be reduced further by sampling on a grid in the plane of volume and ratio to find the lowest ground state energy. In table 3.4.7 we show the results of this and see that the expected volume and ratio have shifted slightly. The expected ratio has decreased slightly (in the direction of the experimental results (see table 3.4.2)). The volume has in all cases increased and in the case of the PBE functional has increased to a volume greater than the ideal cubic system as predicted by potential energy minimization. Through the scanning for ground states method described

above, the lowest energy cubic systems have also been found to change such that the tetragonal systems are still lower in volume. However, the cubic systems also have a significant (maximum) expectation rotation associated with them of between (4.2° and 5.5°), which makes it harder to make clear determinations from the data. For reference the lowest energy cubic volumes are $0.994V_0 = 57.660\,\text{Å}^3$, $1.0003V_0 = 61.403\,\text{Å}^3$ and $1.000V_0 = 59.294\,\text{Å}^3$ for the LDA, PBE and PBEsol functionals respectively (please see the text associated with equation (3.4.8) for the specification of V_0 for the three functionals).

Table 3.4.7: Minimum energy configurations for *I4/mcm* tetragonal system as determined by: 1. sampling a grid of points in the plane of volume and ratio. 2. For each point finding the ground state energy (E_0 eigenvalue for the nuclear wave function), based on the one-dimensional potential energy surface in the direction of rotation angle θ. 3. Finding the configuration with the lowest E_0. The errors underneath the volume and ratio values indicated the granularity of the sampling grid.

Functional	Volume V (Å^3) ± 0.003	V/V_0 ± 0.00005	Ratio r ± 0.00025	Angle θ ($^\circ$)
LDA	57.625	0.9988	1.0075	6.06
PBE	61.391	1.0001	1.0040	4.59
PBEsol	59.276	0.9997	1.0055	5.28

We now draw our analysis of the $I4/mcm$ potential energy surface to an end by reflecting on our findings.

3.5 Concluding Remarks

In this chapter we have performed extensive analysis on strontium titanate in the $I4/mcm$ symmetry group. The entire potential energy surface for this space group has been mapped (500 eV plane-wave energy cut off) within wide variable boundaries and the system has been described in terms of a polynomial, which can be evaluated much more rapidly than a single point DFT calculation.

The calculations performed have made accurate predictions on the unit cell volume with the PBEsol functional providing the most accurate reproduction. The ratio of the b/a lattice parameters has been predicted to be low but not quite matching the subtlety of the experimentally observed system. The coarseness of the sampling grid used was not quite of the level required for an accurate ratio prediction. Later on, in section 4.4.2.1 we consider the same system ($I4/mcm$) using symmetry constrained geometry optimization, where the optimum ratio is more accurately calculated. The calculations have so far failed to model accurately the low experimentally observed oxygen octahedral rotation angle of $\sim 2^\circ$ at 0 K. However, the calculations did recognized that the energy gradient in the transition between cubic and tetragonal is very low in magnitude. A recent paper by Evarestov et al. [32] performs similar calculations as performed here, which compared the plane-wave method (PBE) with the nuclear centred LCAO approach (PBE, PBE0 and B3PW). They found that the LCAO approach was able to obtain more accurate rotation angles of 0.9° and 1.1°.

Future extensions to this work could be made in various ways. The large ranges used for sampling the potential energy surface showed one interesting trend i.e. that for low ratios and large volumes, the potential energy minimum predicts no oxygen rotation. However, for most purposes it would be sufficient to confine the volume sampling to between $0.975V_0$ and $1.025V_0$ (as compared with $\sim 0.85V_0$ to $\sim 1.2V_0$ as in the present work); ratio could more appropriately be measured between 0.98 and 1.03 (as compared with 0.92 to 1.1 as in the present work); the rotation angle need only reach as far as 10° as the remaining 5° in this work showed nothing of real interest. With ranges set as described and approximately 10 sample points in each direction, the surface produced would be more helpful. Volume should also be sampled in even intervals, as the irregular divisions used in this work caused analytical complications. Additionally, due to the propagation of errors effect (translating results from 500 eV calculations to those of 900 eV) and the low transition energies, it would be more valuable to sample the grid using a 900 eV plane-wave cut off. The PBEsol functional has been shown to produce the results most closely matching experiment so it is unnecessary to use any older functionals (though with the proposed reduction in data points, using hybrid functionals may be a possibility).

The research could be extended by including thermal effects, which would include

vibrational modes, besides the one in the direction of the octahedral rotation.

With the potential energy surface now parametrized for the $I4/mcm$ space group and the coefficients reported in appendix B, further investigations based upon the system can be undertaken cheaply. Although the trivariate polynomial has many terms, the potential energy at a point can be evaluated in well under a second by any modern computer. As the energy surface is described by a polynomial, it is easy to perform analysis involving the derivatives and integrals also.

In the next chapter, we continue our analysis of the STO potential energy surface in a wider ranging but discretized way.

Chapter 4

The Descent from High to Low Symmetry Structures

4.1 Preamble

In this chapter, we extend our work in chapter 3, by analysing via a variety of techniques, the structural, polar and vibrational properties of a large number of STO structures. Much is known about the cubic and tetragonal phases of STO. However, relatively little is known about the microscopic/local structure at low temperatures. We investigate this by mapping out a large portion of the potential energy landscape of STO and getting an estimate of the barrier heights between structures. We observe that STO appears to undergo most of the types of distortions displayed by the perovskite family.

The work involves a small number of relatively high symmetry starting structures with several types of unit cell. These structures are geometry optimized using a multi-stage approach that results in the generation of a large number of descendant structures. Some of these resulting structures are saddle points (with regard to energy) and some are ground state structures. All structures found with zero energy gradient were analysed in terms of their transition pathways, internal structure (including octahedral rotation), their polar properties and vibrational properties (see section 4.2.1). The work is split up into sections relating to the different starting structures; a summary of the observations is present at the end of each section.

Again *VASP* is used for the QM calculations, though only the PBEsol functional was employed in the work presented in this chapter as it was found to perform best from our results presented in chapter 3. The accuracy parameters such as k-point sampling density and plane-wave cut-off energy (900 eV), determined in section 3.3 were used throughout the calculations presented in this chapter.

The hybrid density functional PBE06 (also called HSE) was experimented with but found to be to computationally expensive to use for this type of work.

4.2 Introduction

4.2.1 Introduction and Methodology

In the following sections, we consider a different approach to the examination of the phases of strontium titanate. Five different starting structures (of contemporary interest) are used: a cubic cell of five atoms with $Pm\bar{3}m$ symmetry (see section 4.3); a tetragonal cell of 20 atoms with $I4/mcm$ symmetry (see section 4.4); an orthorhombic cell, also with 20 atoms (very similar to the tetragonal) but with $Pnma$ or $Imma$ symmetry (see section 4.5); finally two rhombohedral cells, one with 10 atoms and a second with 40 atoms; the 10 atom unit cell has $R\bar{3}c$ symmetry and the large 40 atom unit cell which is essentially a supercell of the cubic system has $R3c$ symmetry (see section 4.6 for both rhombohedral cells.

The approach adopted here involves taking a starting structure and geometry optimizing it using a combination of CG and QN optimization methods (see sections 2.4.3 and 2.4.4 respectively). The low potential energy gradients on the structure makes optimization difficult and sometimes one of the two methods can prevail where another falters. The structures were allowed to undergo full cell optimization under symmetry constraints. The symmetry of the cell that was used to constrain the optimization was determined by *VASP* at run time. The default precision of 10^{-5} Å was used to make the judgements which often resulted in *VASP* judging a given cell to be of lower symmetry than reported in the thesis (see section 4.2.2.2). Neither of these methods can distinguish a saddle point (a point at which there is a path to lower energy but the gradient is zero) from a minimum and so optimization ends if one is found. The saddle points were interesting and were investigated, but we were also interested in the path all the way to the ground state systems.

After finding a saddle point (or point of zero gradient), the next stage is to calculate the second derivatives of potential energy with respect to ionic position, expressed as a Hessian matrix $\mathbf{H}$ of $3N$ by $3N$ elements (N is the number of ions in the unit cell). An analytical method was used for this based upon perturbation theory and is fairly new to the *VASP* 5 code [68]. A common alternative method, used in some earlier studies (not presented) is known as finite difference and is based on calculating the potential energy of the system with each ion displaced by a finite distance from its equilibrium position in each direction. The approximation is made that the potential energy well that each ion sits in is harmonic (parabolic) and any variation of this from higher levels of theory or experiment are referred to as dampening. Under this approximation, the frequency with which a set of ions will vibrate together can be calculated from the Hessian matrix:

The Hessian matrix is diagonalized to produce a set of eigenvectors $\mathbf{R}$ and a set of eigenvalues $\boldsymbol{\lambda}$. $\mathbf{R}$ has the same dimensionality as $\mathbf{H}$ and represents the nature of the $3N$

different vibrational modes expressed in the cell. $\boldsymbol{\lambda}$ is most directly computed as a diagonal matrix but can be expressed as a vector with $3N$ elements (eigenvalues). A single eigenvalue corresponds to the vibrational frequency of a mode, via the expression:

$$f \propto \sqrt{\lambda}, \tag{4.2.1}$$

where f is the frequency of a given mode (usually expressed in cm^{-1}) and λ is the corresponding eigenvalue.

Though obviously an approximation (and failing to take into account the way that vibrations/phonons will interact with one another), such information can be used to predict/explain the spectroscopic properties of the material. $3N$ frequencies are generated, each presented with an eigenvector $\mathbf{r}$ ($\mathbf{R}$ is the set of all eigenvectors), describing the collective motion of the ions in the unit cell, corresponding to a single vibrational mode (expressed as a set of displacements d**x**, d**y** and d**z** for each ion). The magnitude of the eigenvector $\mathbf{r}$ with $3N$ elements is normally normalized to one. The complete set off $3N$ eigenvectors for a given structure forms an orthogonal basis, in terms of which, any motion of ions within the unit cell can be described through a linear combination.

There are several systems for characterizing and labelling the nature of vibrational modes, which describe the symmetry inherent within them and relate to experimental methods for their identification. For instance: Γ_{15} (TO1), refers to a specific type of vibration at the gamma point (not considering any super cell) involving motion of atoms that is transverse to the direction a phonon wave propagating through the crystal (which might be generated by infra-red spectroscopy). The nature of the labelling scheme will not be described in detail here but further information can be found in [125].

The combination of the sets of frequencies can be used to produce a spectrum and can be compared with the experimental results. Higher frequencies correspond to steeper potential energy wells. In a given set of results, three sets of vibrational modes are expected to have frequencies of zero or very close to zero (corresponding to so called translational modes). These modes are unphysical and their presence trivially states that the entire crystal can translate in three orthogonal directions without any change in energy i.e. there are no restoring forces preventing the crystal from translating its position. However, if the structure is at a saddle point, there will be some imaginary frequencies, whose magnitude corresponds to the frequency of the associated mode if downward components were reflected upwards.

The eigenvectors of the imaginary modes point in the direction that ions must move to lower the potential energy of the system. When imaginary modes were identified, the ionic positions were 'nudged' (manually using some scripting in *MS Excel*) in the direction denoted by the eigenvectors before restarting geometry optimization.

The magnitude of the nudge was scaled for all ions in the cell, such that the greatest absolute motion of any ion was a fixed distance. In most cases, the distance was 0.1 Å, but in a small number of problematic systems, a different magnitude was used. This process is referred to in the thesis as 'nudging'. In the case of there being more than one imaginary mode (with different frequencies), the system was nudged down each of them separately. In the case of degenerate imaginary modes (having the same frequency and with eigenvectors that are analogous to one another), the n degenerate mode's eigenvectors were combined linearly to produce a set of n nudging vectors as:

$$\mathbf{n}_j = \sum_{i=1}^{j} \mathbf{r}_i \qquad\qquad j = 1, \cdots, n, \tag{4.2.2}$$

where $\mathbf{n}_j$ is the resultant nudging vector (not yet scaled), $\mathbf{r}_i$ is the eigenvector for one degenerate mode and i loops over the n degenerate modes.

The nudging and optimization method was repeated until structures were generated with no imaginary modes indicating that a local or global minimum had been found. A dendrimer diagram (see figure 4.2.2) has been produced to summarize these calculations for the five starting systems. The enumerations on the plot are referred to in the subsequent sections.

Through this method, 38 structures were generated including the parent and all descendant structures. Following the generation of the structures, Nudged Elastic Band calculations (see section 2.4.5.3) were run on each transition between cells. The main objective being to identify any potential energy barriers that may exist between the structures. NEB is one of the inbuilt features within the *VASP* code and considers two end point structures (start and finish) fixed in position, while a line of intermediate structures (eight were used unless otherwise stated) are allowed to optimize under certain additional constraints (each structure is compelled to be similar to its neighbour through the addition of a spring force; absolute cell volume is held constant though the lattice vectors can change; the optimization is not restrained by symmetry). Fortunately for the sake of wall time, *VASP* allows each structure to run on its own set of processors during the optimization and in this case 64 cores were used per intermediate structure in unison.

The intermediate structures were generated by interpolation using a code, *interpPos* (see appendix D.1.1), which performs two types of manipulation on the crystal (which must be described in fractional coordinates). First to make the interpolation easier, the code re-expresses the coordinates of one of the end point structures, such that the periodic nature of the crystal can be ignored in terms of relating the positions of equivalent atoms between cells e.g. if structure a has an atom with a coordinate at

0.99 and in structure b the position was 0.01, the value would be changed in b to be 1.01. The next stage is the generation of the intermediate structures themselves. Ideally we would have used linear interpolation of all the atomic positions between the two unit cells. To save time in the coding, an approximation was made. Linear interpolation of the volume parameter V_p (see equation (3.4.4)), the lattice vectors and the atomic positions in fractional coordinates was performed. Assuming that in all cases, these quantities will be similar to one another for the two end point structures, the approximation is good. The approximation does not cause the intermediate cells to move off the line between start and end structures.

It has been shown in section 3.4, that out of the density functionals trialled, PBEsol produces the results that are closest to experiment and so only this functional was used for these calculations. In section 3.3 we found that the most appropriate plane-wave cut-off energy was 900 eV and so this value has been used throughout. Additionally the precision (`PREC`) parameter in *VASP* was set to `ACCURATE`.

We now discuss the various ways in which we analyse structural and polar properties of the generated structures.

4.2.2 Analysis of Structures

4.2.2.1 Transition Pathway

There are two main methods in which the transition pathway between a parent and child structure is analysed. One method is to examine the data from the NEB calculation (see sections 2.4.5.3 and 4.2.1). In the scope of this thesis, the NEB data only undergoes some basic analysis, whereby we check if there is an activation barrier between the two structures and report its height if present. However, none of the transition pathways had an activation barrier, except in one case where the transition between the top level orthorhombic and tetragonal structures was considered.

The other type of transition analysis employed in this thesis is to examine the frequencies and eigenvectors for the structures at either end of the transition pathway and identify which vibrational modes point in the direction of the transition. A code was written for this *cds3* (see appendix D.1.2), which was originally intended to compare cells that had been assembled in different ways and as a consequence, the atoms in the cell descriptions are not required to correspond directly in terms of their listing order. The program analyses the `OUTCAR` files produced by a *VASP* frequency calculation and extracts the lattice parameters, atomic positions (in Cartesian coordinates), frequencies (real and imaginary) and the corresponding eigenvectors of both start and end structures. This information is first used to determine which atoms are equivalent to one another by doing a nearest atom search between every pair of ions in the start and end structures (the periodicity of the cell is taken into account during this). As with the

interpolation code for carrying out NEB, the end structure is re-expressed in terms of the start structure (such that periodicity is no longer a concern). It is not possible to use the code (as is) to compare two structures where one is significantly translated or rotated relative to the other or to compare cells of different types i.e. different numbers of atoms.

With equivalent atoms identified in the two structures, the code then performs a subtraction of one structure from the other to create a difference vector in Cartesian coordinates. Next it calculates the angular separation between the difference vector and in turn, each of the eigenvectors of the starting structure using the general angular separation formula:

$$\theta = \arccos\left(\frac{\mathbf{g}\cdot\mathbf{h}}{|\mathbf{g}|\,|\mathbf{h}|}\right), \tag{4.2.3}$$

where $\mathbf{g}$ and $\mathbf{h}$ are any pair of vectors (expressed using the same basis i.e. representing the same thing and therefore having the same number of dimensions) and θ is the angle between them. The angular separation between hyper-dimensional vectors cannot readily be visualized. However, there is the same principle, that the closer θ is to 0° or to 180°, the better aligned the vectors are. If the difference vector and a given eigenvector are closely aligned then it suggests that one structure can be obtained from the other through motion in the direction of the vibrational mode. Both angular separation and the components of the vibrational mode corresponding to the complete transition are calculated.

4.2.2.2 Cell Description

One of the first ways that we characterize a given structure is with a description of the lattice parameters and the space group. For analysing the symmetry we use a package called *Endeavour* [126, 127], which was designed for analysing powder diffraction data, but includes a tool for crystal structure determination. The structure determination is performed by two algorithms, the first of which determines crystal symmetry (*SFND* [128]) and the second uses the symmetry data to determine the space group (*RGS* [129]). *Endeavour* in fact uses four parameters to determine symmetry: tolerance factors for matching n-fold axes; tolerance used for symmetry checks; tolerance for the search for translational symmetry and tolerance for merging of symmetry-related atoms. These options were not documented and so some trial and error combined with the general philosophy that as the phase transitions in STO are subtle, fairly fine tolerances should be used. 0.001 was chosen for all the tolerances with some exceptions.

The tolerance for symmetry checks of 1 mÅ was used for most symmetry determinations. However, in cases where the cell matched other space groups, within tolerances of up to 10 mÅ, these were also noted, along with their deviations from the ideal space-group. In some rare cases the lowest matching non-$P1$ symmetry group had a

tolerance above this, in these cases the least symmetric matching symmetry group is provided with its deviation from the ideal.

4.2.2.3 Distortion of the Octahedra

Defining the way that the octahedra distort is difficult in the general case and there is no perfect way to do it, that is compatible with all the different unit cells, as the types of distortion that are possible within a given space group and the shape of the unit cell can change. For instance, an algorithm that calculated the rotation of octahedra assuming that the titanium ion would remain central to the octahedra (true for the high symmetry systems), would break down and result in an inaccurate description for the lower symmetry systems. Likewise, an algorithm that assumed orthorhombicity in all unit cells and based rotation angles on variations from the ideal lattice vector directions would also produce inaccurate results (although it happens that non-orthorhombic distortions are slight in the systems presented in this thesis). The descriptive system that was chosen was based approximately on the works by Noel Thomas in his paper [47] and is as follows.

We start by defining a set of pseudo-cubic axes $\mathbf{x}'$, $\mathbf{y}'$ and $\mathbf{z}'$. In the ideal cubic system, the pseudo-cubic axes will be very similar to the $\mathbf{x}$, $\mathbf{y}$ and $\mathbf{z}$ axes in terms of which the lattice vectors are described. In the cubic unit cell, each axis will have an oxygen atom comprising part of an octahedron lying on it. For the other starting point structures, which define the crystal in different orientations from the cubic, the pseudo-cubic axes are significantly different from those of the cubic system. For each starting structure in the following sections, the pseudo-cubic axes are defined within the introductions to the sections, in terms of some combination of the lattice vectors $\mathbf{a}$, $\mathbf{b}$ and $\mathbf{c}$. The choice of pseudo-cubic vectors is made such that the oxygen atoms still lie on or close to the pseudo-cubic vectors. The pseudo-cubic axes will in the general case not be orthogonal (but approximate orthogonality). Non-orthogonality in the pseudo cubic axes can occur via two mechanisms: a tetragonal or orthorhombic distortion, where the pseudo-cubic vectors are made from a combination of multiple symmetry breaking lattice vectors; also lower symmetry distortions where the cell angles change.

For a given octahedron, we define three sticks, each going between a pair of opposing oxygen atoms. We label these $s_{x'}$, $s_{y'}$ and $s_{z'}$. For each stick, we define the angular separation from its equivalent pseudo-cubic axis $\theta_{x'}$, $\theta_{y'}$ and $\theta_{z'}$. When these angles are presented in tabular form in the results, sections 4.4 to 4.6, a column heading θ is used to describe them all, with an appropriate row label.

To illustrate more clearly the nature of the octahedral rotations, some further data on the components of the rotation for each stick are reported. Specifically, we report the rotation of each stick, projected separately in the plane of its corresponding pseudo-

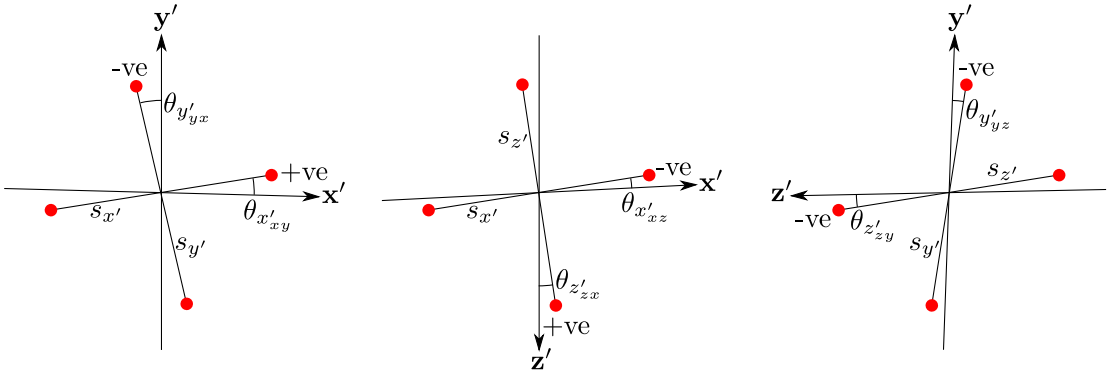

Figure 4.2.1: Description of the variables used to describe the components of rotation of the sticks in the octahedra ($\theta_{x'_{xy}}$, $\theta_{x'_{xz}}$, $\theta_{y'_{yz}}$, $\theta_{y'_{yx}}$, $\theta_{z'_{zx}}$ and $\theta_{z'_{zy}}$). Each of these variables describe motion of sticks within the plane of two pseudo-cubic axes. In each example, two pseudo-cubic axes (not necessarily at right angles) have been included with the other omitted for practical reasons. The red balls represent oxygen atoms. The signs of rotation are marked in each of the example cases.

cubic axis and each of the other two pseudo-cubic axes (see figure 4.2.1).

If a given stick vector $\mathbf{v}$ has a projection $\mathbf{v}_p$ on the plane of two pseudo-cubic vectors, for example $\mathbf{x}'$ and $\mathbf{y}'$, then we can write this as:

$$d\mathbf{x}' + e\mathbf{y}' = \mathbf{v}_p, \tag{4.2.4}$$

where d and e are scalar coefficients. We then recall the angular separation formula (4.2.3) and measure the angle between $\mathbf{v}_p$ and $\mathbf{x}'$ (in the case of the $S_{x'}$ stick), which we represent as $\theta_{x'_{xy}}$ in figure 4.2.1 i.e. the angle between the $\mathbf{x}'$ axis and projection of the s_x stick vector on the $\mathbf{x}'\mathbf{y}'$-plane. In the example of $\theta_{x'_{xy}}$, the sign of e, is inherited by the angle, indicating if the stick points towards or away from the $\mathbf{y}'$ axis (as we move in the $\mathbf{x}'$ direction). The derivation of e and d is provided in appendix A.4.

As the octahedra themselves can distort (as well as just rotate), we also define the angular separation between the sticks using: s_α, s_β and s_γ representing the angles respectively between $s_{y'}$ and $s_{z'}$, between $s_{x'}$ and $s_{z'}$ and between $s_{x'}$ and $s_{y'}$. We also record the stick lengths $l_{x'}$, $l_{y'}$ and $l_{z'}$. The angular components of rotation, described above, can also be used to describe the distortion of the octahedra e.g. for a given plane shown in figure 4.2.1, the angles of the two sticks should be identical for an undistorted octahedron. The calculation of these parameters is performed by a computer code (*rotAngles2*) that analyses *VASP* structure files, see appendix D.1.4.

In the results, we summarize the characteristics of octahedra in tabular form. Columns are given such labels as θ_1 and θ_2, which are used to represent the components of stick rotation. A key for these is provided in table 4.2.1, though we will go over this again when the results are discussed in detail.

Table 4.2.1: A description of abbreviations used in tables to describe the various rotation parameters.

Stick	θ_1	θ_2
$s_{x'}$	$\theta_{x'_{xy}}$	$\theta_{x'_{xz}}$
$s_{y'}$	$\theta_{y'_{yz}}$	$\theta_{y'_{yx}}$
$s_{z'}$	$\theta_{z'_{zx}}$	$\theta_{z'_{zy}}$

The octahedral volumes as well as the overall cell volumes and lattice parameters are reported. These were calculated by bolting on some additional code to *rotAngles2*. The octahedral volumes were evaluated by decomposing the octahedra into eight irregular tetrahedra and evaluating the tetrahedral volume equation:

$$V_{\text{tetrahedral}} = \frac{1}{6} \left| (\mathbf{a} - \mathbf{d}) \cdot ((\mathbf{b} - \mathbf{d}) \times (\mathbf{c} - \mathbf{d})) \right|, \tag{4.2.5}$$

where, $\mathbf{a}$, $\mathbf{b}$, $\mathbf{c}$ and $\mathbf{d}$ are the coordinates of the vertices of the tetrahedron. There is a function implemented within the molecular visualization package *VESTA* [130, 131] which employs a method developed by Swanson and Peterson [132] for calculating polyhedral volumes and *VESTA* readily reports basic lattice information. There were two reasons for implementing some of this functionality within *rotAngles2*: the first was that it was simpler to extract data this way as the output format could be controlled; the second was that there appeared to be a bug in the algorithm implemented within *VESTA* which would cause misreporting of octahedral volumes in certain cases.

4.2.2.4 Dipole Moment Calculation

For each cation in a given unit cell, the dipole moment was calculated via a custom code called *getPolar* (see appendix D.1.3). The method involved cycling through the cation list, and for each, finding the positions of the nearest oxygen ions (the six nearest ions for titanium and 12 nearest for strontium). Vectors pointing from the oxygen anions to the strontium or titanium cations were summed for each cation to generate a displacement vector pointing from the central position of the polyhedron to the enclosed cation. The dipole moment was calculated by assigning a charge of +4 for titanium and +2 for strontium and multiplying by the following factor to convert from units of e Å to Debye units (D):

$$\frac{10^{-11}}{ec} = 0.208194, \tag{4.2.6}$$

where e is the charge on an electron in Coulombs and c is the speed of light in $\mathrm{m\,s^{-1}}$.

Retrospectively, the dipole moment was re-expressed via a transformation into

pseudo-cubic coordinates using the following formulae:

$$\mu_{x'} = \frac{\boldsymbol{\mu} \cdot \mathbf{x}'}{|\mathbf{x}'|}; \qquad \mu_{y'} = \frac{\boldsymbol{\mu} \cdot \mathbf{y}'}{|\mathbf{y}'|}; \qquad \mu_{z'} = \frac{\boldsymbol{\mu} \cdot \mathbf{z}'}{|\mathbf{z}'|}, \tag{4.2.7}$$

where $\boldsymbol{\mu}$ is the electric dipole and $\mu_{x'}$, $\mu_{y'}$ and $\mu_{z'}$ are the pseudo-cubic components of the electric dipole. This transformation is only correct when the pseudo-cubic axes are orthogonal, some other methods of transformation were considered, such as expressing the dipole as an exact linear combination of the normalized pseudo-cubic vectors by calculating the inverse matrix for them but this did not appear to offer any advantage in terms of the interpretation of the data. In fact the closeness of the pseudo-cubic axes to orthogonality, means that there is very little error and when comparing the magnitudes of the dipole expressed in Cartesian and pseudo-cubic, one only sees at most, a small change in the third significant figure. Regardless of this, when a magnitude of dipole is expressed, it will be the actual magnitude based on an orthogonal basis, while vector based expressions of dipole moment will have a pseudo-cubic basis. Total dipole moments for the entire unit cell are expressed as dipole (in D) per formula unit.

4.2.2.5 Imaginary Modes

The imaginary modes of each structure are examined to consider the way that the ions in the crystal must move in order to lower the potential energy and to understand the nature of the subsequent nudge performed on the ions in the cell. Directions of vibrational modes have been re-expressed in pseudo-cubic axes (from the native Cartesian form) using the same formula as in equation (4.2.7). Imaginary frequencies are expressed by appending an i after the frequency.

4.2.2.6 Spectroscopic Data

As touched upon in section 4.2.1, the frequency data obtained from the second derivative calculations can be used to calculate the expected spectroscopic behaviour of the crystal. The list of frequencies can also be used as a way of comparing the similarity of structures. If two structures are produced that are degenerate in energy, we consider the possibility that they are identical to one another. Identical structures (excluding some trivial difference such as a reflection or rotation) will have an identical or almost identical set of frequencies. For the cubic, tetragonal, orthorhombic and rhombohedral starting structures, we compare lists of frequencies of every structure with every other. The bulk of the analysis is presented in appendix C on page 249, though we refer again to these in the text, at the end of each results section.

A small code was written to perform the comparison of frequency lists called *compFreq* (see appendix D.1.10).

4.2.3 Phase Transition Summary

Following the optimization and nudging performed on all of the starting structures, a dendrimer map was created (see figure 4.2.2) displaying the relative placing of all the structures and their heredity. In sections 4.3 to 4.6 we examine the transition paths and structures more closely.

In relating transition energies to temperature we use the convention of:

$$E_J \approx k_B T, \tag{4.2.8}$$

where E_J is energy per particle in joules, k_B is the Boltzmann constant and T is temperature, although we note that a coefficient of $3/2$ is sometimes used in other works. Rephrased we can write:

$$\Delta T = \frac{e\Delta E_{\text{eV}}}{5k_B} = 2.3209{\times}10^3 \Delta E_{\text{eV}}, \tag{4.2.9}$$

where e is the elementary charge and E_{eV} is the energy per formula unit in eV. So an energy change of 1 meV corresponds to a temperature change of 2.3 K.

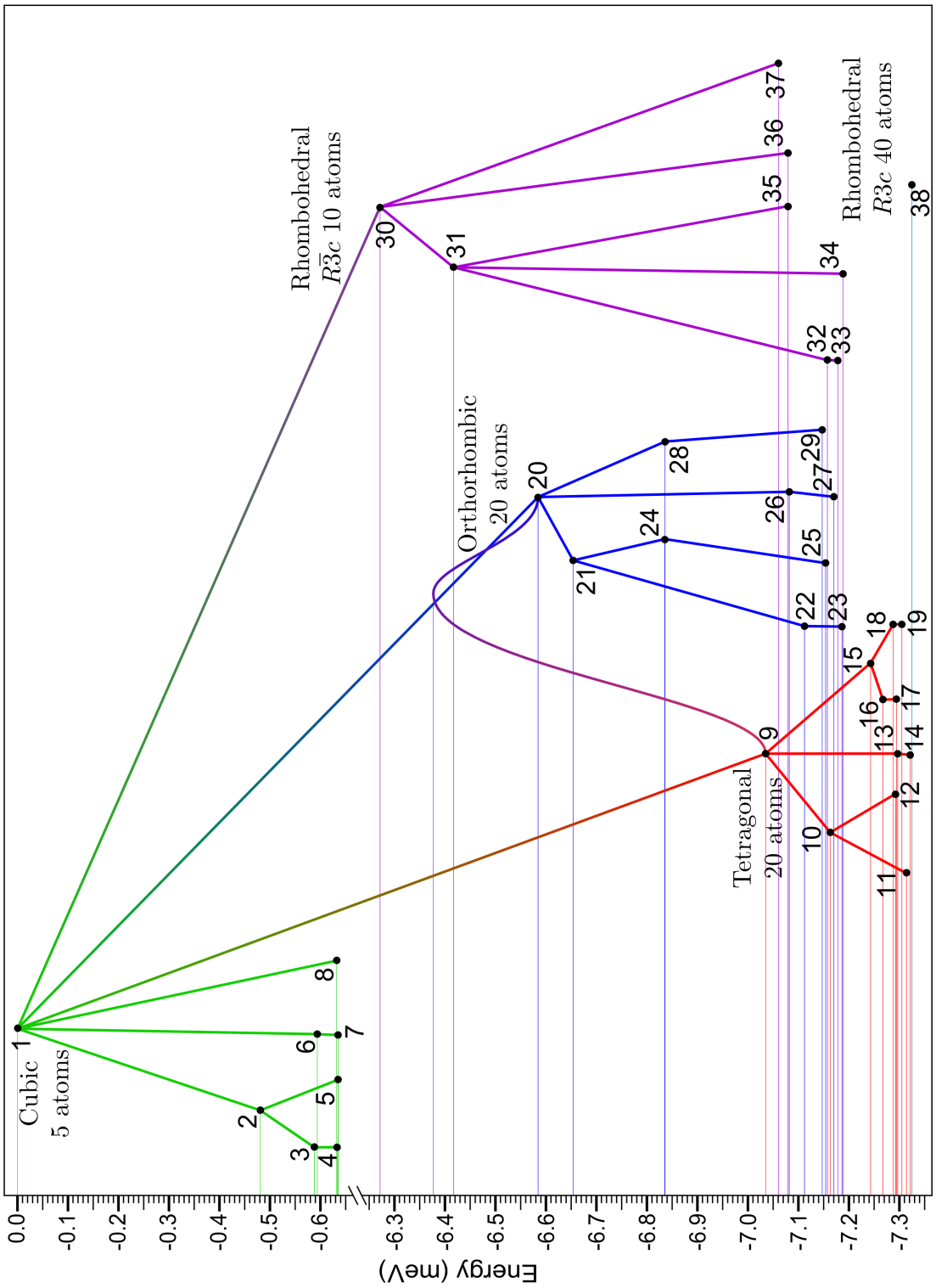

Figure 4.2.2: The dendrimer plot maps the phase transition work presented in this thesis. Each dot denotes, the relative potential energy of the structure, with thick coloured lines denoting the heredity of structures. There are four different trees/dendrimers, each with their own parent structure at the top. Branches are created by nudging/displacing atoms in the direction of imaginary eigenvectors (please see section 4.2.1 for details). The lines with changing colours represent investigations into the transitions between the four top level structures.

4.3 Cubic Unit Cell

4.3.1 Introduction

We now consider the cubic system, the unit cell for which is shown in figure 4.3.1. The enumerations on the oxygen atoms are referred to in the text and tables. We nudge the high symmetry system down along the direction of imaginary modes and optimize until there are no imaginary modes as described in section 4.2.1, creating a set of descendant structures.

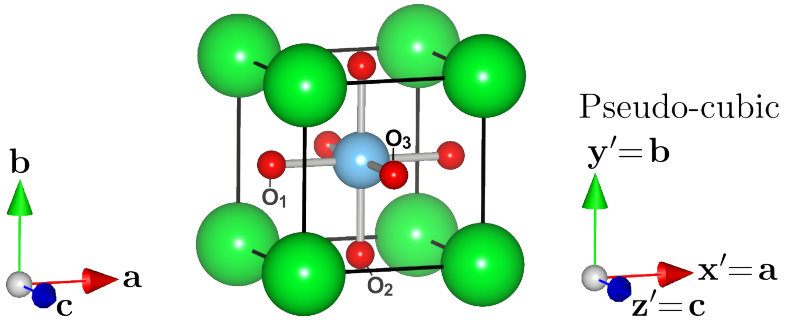

Figure 4.3.1: Structural diagram of the five atom $Pm\bar{3}m$ cubic strontium titanate cell. The direction of the lattice vectors has been shown together with the direction of the pseudo-cubic axes (the same in this case). Green, blue and red balls represent respectively, strontium, titanium and oxygen atoms.

A magnified version of the dendrimer diagram in figure 4.2.2 is presented in figure 4.3.2 to describe the work on the cubic ancestor systems (the ideal cubic and all descendant structures derived from it), together with information on the space group, polarization and imaginary frequencies for every structure.

We now present an analysis of the structures and phase transitions (see section 4.2.2 for information on how the analytical data were obtained). A list of frequencies (table 4.3.5) corresponding to the cubic ancestor structures described here can be found in section 4.3.3 on page 136. Throughout the rest of this chapter, any variable with the subscript '$_0$' refers to that of the ideal cubic as determined by the present set of results, see section 4.3.2.1.

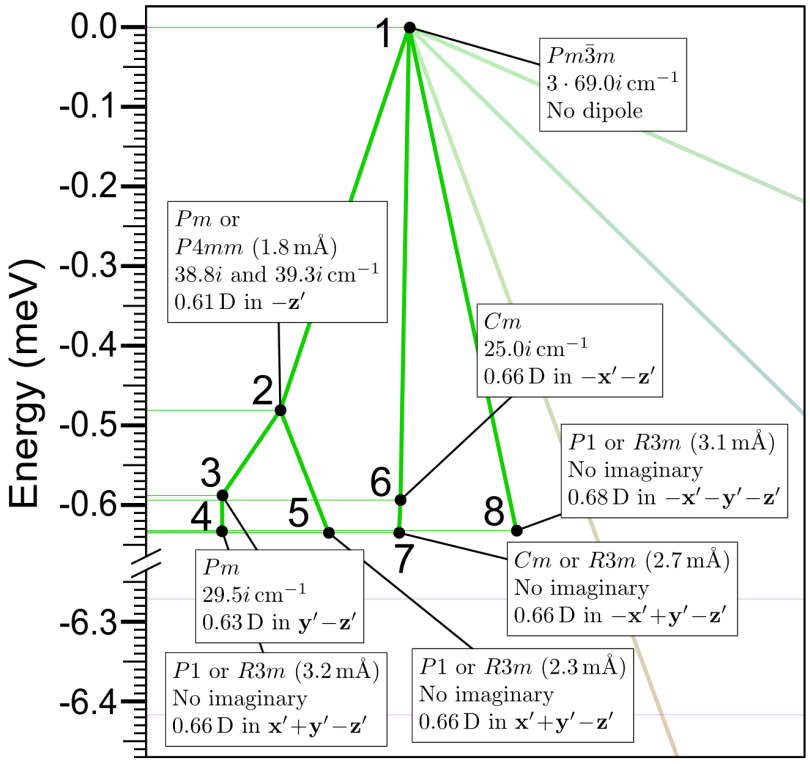

Figure 4.3.2: Dendrimer plot summarizing the cubic ancestor phase transitions. Besides being a zoomed in version of figure 4.2.2, additional information on the structures is provided, namely, the space group (close matches and their deviations are included), the imaginary frequencies and the dipole per formula unit with the approximate direction.

4.3.2 The Structures

4.3.2.1 Structure no. 1 ($Pm\bar{3}m$)

Transitioning: This is a starting structure, though we consider transitions between the present and other starting structures in the relevant sections.

Space group: $Pm\bar{3}m$ (no. 221), which is of course cubic.

Cell definition (Å and degrees): $a = 3.9010$, $b = 3.9010$, $c = 3.9010$;
$\alpha = 90.00$, $\beta = 90.00$, $\gamma = 90.00$.

Cell volume: $59.363\,\text{Å}^3$, $V/V_0 = 1.0000$.

Potential energy (per formula unit): $-39.77221\,\text{eV}^*$

Polyhedral distortion: In this simple system all stick lengths are the 3.901 Å (equal to the lattice parameters). Rotations of octahedra are impossible in a unit cell this size, but in this structure there are no distortions either. The octahedral volume (around the titanium) is $9.8939\,\text{Å}^3$ and the cuboctahedral volume (around the strontium) is $49.4693\,\text{Å}^3$ comprising respectively $1/5$ and $4/5$ of the total cell volume.

*As we deal with some very small energy differences, the energy is given to five decimal places.

Dipole (per formula unit): No dipole.

Imaginary modes: Three degenerate imaginary Γ_{15} modes exist for this structure with frequencies of $69.0i\,\mathrm{cm}^{-1}$ (numbered 13–15). Each describes a ferroelectric motion only in the $\mathbf{x}'$, $\mathbf{y}'$ or $\mathbf{z}'$ directions i.e. along the lattice vectors (see table 4.3.1 and figure 4.3.3). The two oxygen ions that travel across the cell face are compelled to do so in equal measure, while the third oxygen which moves towards the titanium atom, moves to a slightly lesser degree. The titanium and strontium ions move in the opposite direction.

Table 4.3.1: Eigenvectors for one degenerate Γ_{15} (TO1) imaginary mode (13) of structure no. 1. with frequency of $69.0i\,\mathrm{cm}^{-1}$.

Atom	d$\mathbf{x}'$	d$\mathbf{y}'$	d$\mathbf{z}'$
S	0.00	0.00	−0.26
T	0.00	−0.01	−0.47
O_1	0.00	0.01	0.50
O_2	0.00	0.01	0.50
O_3	0.00	0.01	0.45

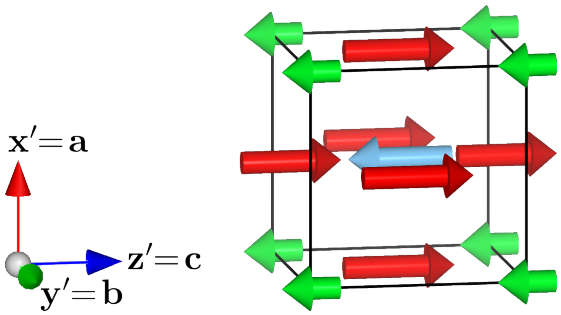

Figure 4.3.3: Graphical representation of the Γ_{15} (TO1) imaginary mode (13) of structure no. 1, see table 4.3.1. Green, blue and red arrows represent vibrations in strontium, titanium and oxygen respectively.

4.3.2.2 Structure no. 2 ($P4mm$)

Transitioning: The parent structure was no. 1 (an ideal cubic $Pm\bar{3}m$ system). The present structure was obtained by nudging down a single Γ_{15} (TO1) imaginary mode (13) in the $\mathbf{z}'$ direction ($j = 1$ in equation (4.2.2)). The ferroelectric transition resulted in an elongation of the unit cell, causing it to become tetragonal.

By comparing the normal modes of both structures with the difference vector between the two (see section 4.2.2.1), we see that two different normal modes lead from structure 1 to structure 2 as some linear combination. The strongest component at $25.4°$ to the difference vector is from mode number 13 (in which structure 1 was nudged prior to optimization). This $69.0i\,\mathrm{cm}^{-1}$ mode becomes hard during the transition to structure 2 with a frequency of $106\,\mathrm{cm}^{-1}$, (mode/frequency number 10 and has the lowest real

frequency, inclined at an angle $37.4°$ to the difference vector). These associated modes are not perfectly aligned, but rather inclined at an angle of $28.5°$ to one another.

The other pair of modes linking the two structures are both real and equivalent in ranking (mode number 7 in both structures, with symmetry label Γ_{15} (TO2)). This threefold degenerate $157\,\mathrm{cm}^{-1}$ mode from structure 1 points at the difference vector with an inclination of $80.2°$, breaking degeneracy by mixing slightly with the TO1 mode no. 13 and rising in frequency up to $184\,\mathrm{cm}^{-1}$ in structure 2 (inclined at $71.5°$ to the difference vector). The number Γ_{15} (TO1) modes from the two structures have the same inclination to one another ($28.5°$) as the imaginary-real pair discussed above. The frequency transitions have been summarized in figure 4.3.4.

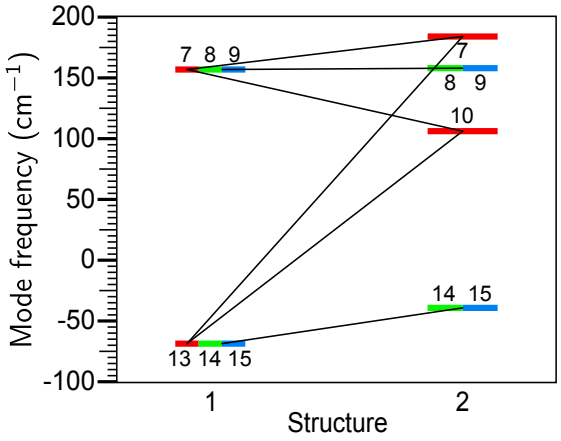

Figure 4.3.4: Energy level diagram, showing the frequency transitions between cubic structure 1 and tetragonal structure 2. The normal modes are enumerated (see table 4.3.5) and multiple colours are used to indicate degeneracy.

Mode 13 in structure 1 describes antiparallel motion of anions and cations along a single lattice vector, to an energetic advantage. As this mode hardens in structure 2, we see a similar antiparallel motion of anions and cations but with very little motion of the titanium ion. Real mode number 7 in structure 1, shows relatively little motion of oxygen but with a strong antiparallel motion of the titanium ion with respect to the strontium ion. As this mode hardens slightly from 157 and $184\,\mathrm{cm}^{-1}$ in structure 2, we see very little change in the relative motion of strontium and titanium. However, the motion of the oxygen relative to the strontium becomes less extreme.

Space group: Pm (no. 6), which is monoclinic; possibly a more suitable candidate is the tetragonal $P4mm$ (no. 99) with a deviation of $3.2\,\mathrm{mÅ}$.

Cell definition (Å and degrees): $a = 3.8994$, $b = 3.8994$, $c = 3.9118$;
$\alpha = 90.00$, $\beta = 90.00$, $\gamma = 90.00$.

Cell volume: $59.480\,\mathrm{Å}^3$, $V/V_0 = 1.0020$. The transition resulted in a small increase in cell volume.

Potential energy (per formula unit): -39.77269 eV, an energy drop of 0.49 meV from the parent, which is equivalent to a decrease in temperature of ~ 1.1 K (see the end of section 4.2.3 for a description of comparisons to temperature).

Polyhedral distortion: No rotations and stick lengths are the same as the corresponding lattice vectors. The octahedral volume was 9.9134 Å^3 which is 1.0020 of the ideal cubic equivalent.

Dipole (per formula unit): 0.612 D in the $-\mathbf{z}'$ direction, of which the titanium is responsible for 0.326 D and the strontium 0.286 D.

Imaginary modes: There are two imaginary modes that are almost certainly degenerate apart from numerical noise, they have frequencies of $38.8i$ and $39.3i$ cm^{-1} (see table 4.3.2 and figure 4.3.5). Each expresses motion in the $\mathbf{x}'$ and $\mathbf{y}'$ directions with approximately a four fold weighting on motion in one of these two, as compared to the other. Anions and cations are shifted in opposite directions to within a few degrees (a ferroelectric distortion), again with the oxygen that moves towards the titanium shifted slightly less than the others.

Table 4.3.2: Eigenvectors for both degenerate imaginary modes of structure no. 2. The Γ_{15} (TO1) modes 14 (left) and 15 (right) have frequencies of $38.8i$ cm^{-1} and $39.3i$ cm^{-1} respectively. We include both for clarity.

Atom	d$\mathbf{x}'$	d$\mathbf{y}'$	d$\mathbf{z}'$
S	0.08	0.28	0.00
T	0.13	0.44	0.00
O_1	−0.12	−0.50	0.00
O_2	−0.14	−0.43	0.00
O_3	−0.13	−0.47	0.00

Atom	d$\mathbf{x}'$	d$\mathbf{y}'$	d$\mathbf{z}'$
S	0.28	−0.08	0.00
T	0.44	−0.12	0.00
O_1	−0.43	0.14	0.00
O_2	−0.50	0.12	0.00
O_3	−0.47	0.13	0.00

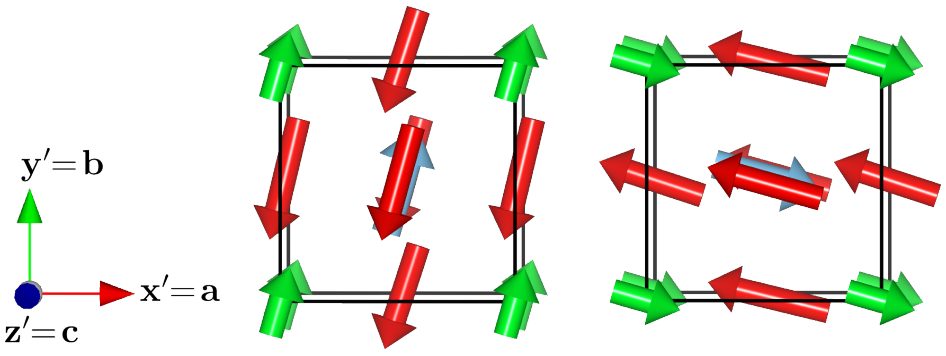

Figure 4.3.5: Graphical representation of the Γ_{15} (TO1) imaginary modes (14 and 15) of structure no. 2, see table 4.3.2. Green, blue and red arrows represent vibrations in strontium, titanium and oxygen respectively.

The small component of the eigenvectors, not in the direction of one of the lattice vectors is most likely due to a small amount of noise in the $\mathbf{y}'$ direction in the vector used to nudge the cubic (1) system into the tetragonal (2).

4.3.2.3 Structure no. 3 (Pm)

Transitioning: The parent structure was the tetragonal $P4mm$ (2). The present structure was obtained by nudging down only the $\mathbf{y}'$ component of the Γ_{15} (TO1) mode no. 14. The decision to exclude the component in the $\mathbf{x}'$ direction was so that the saddle point structure was not excluded in the study. The ferroelectric transition resulted in a slight elongation of the cell in the $\mathbf{y}'$ direction (along the $\mathbf{b}$ vector) and a slight shortening of the cell in the $\mathbf{z}'$ direction (along the $\mathbf{c}$ vector), such that $a < b \approx c$. The shift of the ions, which after this second nudge was along the $\mathbf{b} - \mathbf{c}$ face diagonal, resulted in a subtle narrowing of the angle between the vectors of this face diagonal. α is the relevant lattice parameter, but it was on the other corner on the same face so $\alpha > 90°$, making the structure monoclinic. So the ferroelectric motion along a face diagonal caused an elongation of the face diagonal.

The mixing of the various modes becomes more complex in this transition. The Γ_{15} (TO1) mode 14, in which the system was nudged was most directly responsible for the transition (it is inclined at an angle of $33°$ to the difference vector). The Γ_{15} (TO1) mode becomes hard but has components in multiple modes in structure 3. Other modes involved in the transition from structure 2, were the Γ_{15} (TO2) modes 7 and 8 and the Γ_{15} (TO1) modes 10 and 15. There is a complex interaction between the modes generating the transition.

Space group: The monoclinic Pm (no. 6) space group is the most likely candidate for this system, the orthorhombic $Amm2$ (no. 38) with a deviation of 13 mÅ is another possible candidate.

Cell definition (Å and degrees): $a = 3.8983$, $b = 3.9066$, $c = 3.9039$;
$\alpha = 90.04$, $\beta = 90.00$, $\gamma = 90.00$.

Cell volume: $59.453\,\text{Å}^3$, $V/V_0 = 1.0015$. This represents a small decrease in cell volume from the tetragonal structure (2).

Potential energy (per formula unit): -39.77280 eV, an energy drop of 0.11 meV from the parent, which corresponds to a temperature drop of ~ 0.25 K. The energy change is so small it is unlikely that these phase changes will be observed in nature, especially as actual relaxations to the atomic positions are known to take place over larger numbers of atoms than the five atom unit cell used here.

Polyhedral distortion: The octahedral volume was $9.9088\,\text{Å}^3$ which is 1.0015 of the ideal cubic equivalent.

Dipole (per formula unit): 0.632 D, which acts inclined at $5.9°$ to the face diagonal of the cell in the $0.49\mathbf{y}' - 0.40\mathbf{z}'$ direction. The titanium is responsible for 0.339 D and the strontium 0.293 D.

Imaginary modes: Only one imaginary mode remains in the present system with a frequency of $29.5i\,\mathrm{cm}^{-1}$. This ferroelectric mode expresses motion only in the $\mathbf{x}'$ direction (being the only as yet untravelled direction). The mode is of the same nature as the previous described imaginary modes, with O_1 moving less than the other oxygen atoms as its vibration motion is restricted an adjacent titanium atom (see table 4.3.3).

Table 4.3.3: Eigenvectors for one Γ_{15} (TO1) imaginary mode (15) of structure no. 3. with frequency of $29.5i\,\mathrm{cm}^{-1}$.

Atom	d$\mathbf{x}'$	d$\mathbf{y}'$	d$\mathbf{z}'$
S	0.33	0.00	0.00
T	0.46	0.00	0.00
O_1	−0.44	0.00	0.00
O_2	−0.49	0.00	0.00
O_3	−0.50	0.00	0.00

4.3.2.4 Structure no. 4 ($R3m$ or $P1$)

Transitioning: The parent structure was the monoclinic no. 3. The present structure was obtained by nudging down the Γ_{15} (T01) mode number 15. The final ferroelectric distortion resulted in a slight elongation in the $\mathbf{x}'$ direction (along the $\mathbf{a}$ vector) and a subtle shrink in the other directions resulting in $a \approx b \approx c$ without any significant change in cell volume from the parent. The ferroelectric shift of the ions is now approximately equal in all three directions allowing the remaining angles β and γ to relax from the cubic setting as they had remained in structure 3. As a result, the present structure is rhombohedral as the deviations of α β and γ from $90°$ are about equal. As with the monoclinic system, ferroelectric motion in the direction of a volume diagonal (in this case, the $\mathbf{a}+\mathbf{b}-\mathbf{c}$ diagonal), elongates it, narrowing the surrounding angles. As this diagonal is not the one that passes through the cell origin, some of the cell angles are greater and some are smaller than $90°$.

In this transition, the Γ_{15} (TO1) mode 15 was most directly responsible for the transition, inclined at $30°$ to the difference vector. This mode hardens in structure 4 and appears to most directly contribute to modes 10 and 11. Also responsible for the transition are modes 9 (Γ_{15} (TO2)) and 10 (Γ_{15} (TO1)).

The transition took the system to the minimum energy level. The three Γ_{15} (TO1) modes that were imaginary and degenerate in the cubic system ($69.0i\,\mathrm{cm}^{-1}$) have now all hardened to real modes (numbered 10–12) but have broken degeneracy with frequencies of 93.9, 66.4 and $56.5\,\mathrm{cm}^{-1}$.

Space group: The closest match for this system is $R3m$ (no. 160) which deviates by $3.3\,\mathrm{m\AA}$ from the ideal. Alternatively the space group may be may be $P1$.

Cell definition (Å and degrees): $a = 3.9048$, $b = 3.9031$, $c = 3.9019$;
$\alpha = 90.03$, $\beta = 90.03$, $\gamma = 89.96$.

Cell volume: $59.463\,\text{Å}^3$, $V/V_0 = 1.0016$. Essentially no change since the monoclinic structure 3.

Potential energy (per formula unit): $-39.77284\,\text{eV}$, an energy drop of $45\,\mu\text{eV}$ from the parent and equivalent to a temperature decrease of $\sim 0.10\,\text{K}$.

Polyhedral distortion: The octahedral volume was $9.9104\,\text{Å}^3$ which is 1.0017 of the ideal cubic equivalent.

Dipole (per formula unit): $0.660\,\text{D}$, inclined relative to the volume diagonal at an angle of $5.9°$ (the components are $0.43\mathbf{x}' + 0.38\mathbf{y}' - 0.33\mathbf{z}'$), of which the strontium displacement contributes $0.305\,\text{D}$ and the titanium contributes $0.355\,\text{D}$, both acting in the same direction.

Imaginary modes: This is a minimum energy structure (within the cubic family): no imaginary modes were found.

4.3.2.5 Structure no. 5 ($R3m$)

Transitioning: Structure 5 was obtained by nudging down the sum of the Γ_{15} (TO1) modes 14 and 15 in structure 2 ($j = 1$ in equation (4.2.2)). By nudging in two directions at the same time, the system was able to reach the lowest energy setting allowable with the five atom unit cell with a single nudge (two including the first nudge). The cell appears to be almost identical to structure 4 in terms of space group, ionic structure, potential energy and dipole moment. The transition caused the system to go directly from tetragonal to rhombohedral, with no apparent energy barrier.

The (TO1) modes 14 and 15 were most directly responsible for the transition, inclined at $43°$ and $61°$ to the difference vector. However, all of the Γ_{15} (TO1) and (TO2) have a partial component in the direction of the difference vector.

This transition took the system down to the lowest energy level of the cubic (five atom cell) family. The final frequencies of the three (TO1) modes are 94.2, 66.8 and $61.3\,\text{cm}^{-1}$.

Space group: There are two possible candidates for the space group, either $P1$ or with a deviation of $2\,\text{mÅ}$ $R3m$ (no. 160).

Cell definition (Å and degrees): $a = 3.9037$, $b = 3.9032$, $c = 3.9024$;
$\alpha = 90.03$, $\beta = 90.03$, $\gamma = 89.96$.

Cell volume: $59.460\,\text{Å}^3$, $V/V_0 = 1.0016$, which is identical to structure 3.

Potential energy (per formula unit): $-39.77284\,\text{eV}$, an energy drop of $0.15\,\text{meV}$ from the parent structure no. 3 and equivalent to a reduction in temperature of $\sim 0.36\,\text{K}$.

Polyhedral distortion: The octahedral volume was $9.9101\,\text{Å}^3$ which is 1.0016 of the ideal cubic equivalent.

Dipole (per formula unit): $0.662\,\mathrm{D}$, inclined to the volume diagonal at an angle of $3.3°$, (slightly closer to the diagonal than structure 4). A brief NEB calculation between structures 4 and 5 shows no energy barrier between them and so we can assume that these subtle variations are just noise as a consequence of the limits of the geometry optimization convergence criteria. The slightly larger (and more diagonal) dipole moment on the present structure 5 (than structure 4) is most likely because its initial nudge was a symmetrical shift along the face diagonal (cations shifted in the $\mathbf{x}'$ and $\mathbf{y}'$ direction). The components of the total dipole are $0.40\mathbf{x}' + 0.39\mathbf{y}' - 0.35\mathbf{z}'$, of which the strontium displacement contributes $0.306\,\mathrm{D}$ and the titanium contributes $0.356\,\mathrm{D}$, both in the same direction.

Imaginary modes: This is a minimum energy structure (within the cubic family): no imaginary modes were found.

4.3.2.6 Structure no. 6 (Cm)

Transitioning: The present structure was obtained by nudging the ideal cubic structure (1) down two degenerate imaginary modes (Γ_{15} (TO1) modes 13 and 14), acting in the $\mathbf{x}'$ and $\mathbf{z}'$ directions (the $\mathbf{a}$ and $\mathbf{c}$ vectors). The transition resulted in an equal expansion of the cell along the $\mathbf{a}$ and $\mathbf{c}$ vectors and a slight shortening of the cell along the $\mathbf{b}$ vector. The ferroelectric motion in the direction of the face diagonal allowed the cell's β parameter to reduce while the other two angles remained approximately $90°$. The distortion was from cubic to monoclinic and as such we can compare this structure to the monoclinic structure no. 3, which underwent a similar structural change.

We find that the modes most directly involved in the transition from structure 1 to 6 are the Γ_{15} (TO1) 13 and 14 (frequency of $69.0i\,\mathrm{cm}^{-1}$), which are both inclined at $54°$ to the difference vector. These modes harden, mix and loose their degeneracy to become modes 10 and 11 with frequencies of $100\,\mathrm{cm}^{-1}$ and $77.1\,\mathrm{cm}^{-1}$ respectively. All three of the Γ_{15} (TO2) real modes (7–9) had a small involvement in the transition (inclined $\sim 85°$ to the difference vector).

Space group: The best candidate space group is the monoclinic Cm (no. 8) with a deviation of just $0.06\,\mathrm{m\AA}$. The Cm space group has higher symmetry than the Pm space group of structure 3.

Cell definition (Å and degrees): $a = 3.9061$, $b = 3.8986$, $c = 3.9061$;
$\alpha = 90.01$, $\beta = 89.95$, $\gamma = 90.01$.

Cell volume: $59.482\,\mathrm{\AA}^3$, $V/V_0 = 1.0020$. This is a small expansion of the parent cubic structure (1) and is interestingly the same volume change as in the transition from the cubic to tetragonal system (structure 2). One might expect a volume that is closer to the monoclinic structure no. 3 (which had a V/V_0 ratio of 1.0015) as both this structure and the present have transitioned down two imaginary modes. The difference may be a

consequence of numerical noise.

Potential energy (per formula unit): -39.77281 eV, which involved an energy drop of 0.60 meV, corresponding to ~ 1.4 K from the cubic parent (1). The energy is 6 μeV lower than that of structure 3; we will see other evidence from the dipole and imaginary mode sections that the present structure is better optimized than 3.

Polyhedral distortion: The octahedral volume was 9.9137 Å^3 which is 1.0020 of the ideal cubic equivalent.

Dipole (per formula unit): 0.664 D acting in the face diagonal but with a small component in the $\mathbf{y}'$ direction ($\mathbf{b}$ vector). This small component, which represents a shift of $5.3°$ from the perfect cell face diagonal, is probably due to the small amount of numerical noise that was included in the two eigenvectors in the direction of which we nudged structure 1. The strontium contributed 0.308 D to the net dipole and the titanium contributed 0.356 D.

The total dipole moment strength is greater than in structure 3 (considered to be similar) by 0.032 D, which is possibly due to a more symmetrical initial guess for the structure 1 to 6 transition than obtained by the sequential nudges required to go from structure 1 to 2 to 3. Also the noise in the eigenvectors allowed some ferroelectric motion in the $\mathbf{y}'$ direction, which adds a third degree of freedom. The overall dipole direction is $-0.47\mathbf{x}' + 0.06\mathbf{y}' - 0.47\mathbf{z}'$. The strontium contributes to 0.308 D of the total dipole and the titanium contributes to 0.356 D.

Imaginary modes: Only one imaginary mode remains in the present system; it has a frequency of $25.0i$ cm^{-1}, which is slightly harder than the equivalent imaginary mode in structure 3 ($29.5i$ cm^{-1}), possibly due to the higher degree of optimization (see table 4.3.4). The remaining imaginary mode acts in the $\mathbf{y}'$ direction ($\mathbf{b}$ vector), ignoring small contributions of noise.

Table 4.3.4: Eigenvectors for one Γ_{15} (TO1) imaginary mode (15) of structure no. 6. with frequency of $25.0i$ cm^{-1}.

Atom	d$\mathbf{x}'$	d$\mathbf{y}'$	d$\mathbf{z}'$
S	0.02	0.29	0.02
T	0.02	0.42	0.02
O_1	−0.01	−0.52	−0.01
O_2	−0.01	−0.46	−0.01
O_3	−0.01	−0.52	−0.01

4.3.2.7 Structure no. 7 ($R3m$ or Cm)

Transitioning: Structure 7 was obtained by nudging down the only remaining imaginary Γ_{15} (TO1) mode (15) of structure 6. The transition facilitated a ferroelectric shift involving cationic motion in the $\mathbf{y}'$ direction (or $\mathbf{b}$ vector), during which the cell underwent an equal shrink in the $\mathbf{x}'$ and $\mathbf{z}'$ directions and an elongation in the $\mathbf{y}'$ direction.

The result was $\mathbf{a} \approx \mathbf{b} \approx \mathbf{c}$ and cell angles that were equivalent to one another, each deviating $0.03°$ from a right angle, giving the cell rhombohedral symmetry. The nature of the transition, is identical to that of the structure 3 to structure 4 transition. The present structure is fractionally more of an ideal rhombohedral system due to the simpler and more symmetrical path of its evolution.

In this final transition, we find that the normal mode most directly responsible for the transition, is the imaginary Γ_{15} (TO1) mode (15), inclined to the difference vector at $39°$. The real (TO1) mode no. 12 also played a substantial part in the transition, inclined at $55°$ to the difference vector. Two of the Γ_{15} (TO2) modes (9 and 10) also played a minor rôle.

The transition took the system to the minimum energy level. The final frequencies of the three (TO1) modes are now of 93.9, 65.7 and $61.9\,\mathrm{cm}^{-1}$.

Space group: As with structure 6, the present cell is still a match for Cm symmetry (no. 8), with a deviation of $0.3\,\mathrm{m\AA}$. However, the rhombohedral $R3m$ space group (no. 160) fits with a deviation of $4.7\,\mathrm{m\AA}$. We believe that $R3m$ is the best candidate, given the nature of the transition that has taken place.

Cell definition (Å and degrees): $a = 3.9028$, $b = 3.9038$, $c = 3.9028$;
$\alpha = 90.03$, $\beta = 89.97$, $\gamma = 90.03$.

Cell volume: $59.462\,\mathrm{\AA}^3$, $V/V_0 = 1.0017$. Which is very similar to the minimum energy structures 3 and 5.

Potential energy (per formula unit): $-39.77284\,\mathrm{eV}$, an energy drop of $36\,\mu\mathrm{eV}$ and equivalent to a drop in temperature of $\sim 0.10\,\mathrm{K}$.

Polyhedral distortion: The octahedral volume was $9.9104\,\mathrm{\AA}^3$ which is 1.0017 of the ideal cubic equivalent.

Dipole (per formula unit): $0.660\,\mathrm{D}$, inclined at $2.7°$ to the volume diagonal. The strontium contributes $0.305\,\mathrm{D}$ and the titanium contributes $0.355\,\mathrm{D}$. The components of the dipole are $-0.37\mathbf{x}' + 0.41\mathbf{y}' - 0.37\mathbf{z}'$. The symmetry in the $\mathbf{x}'$ and $\mathbf{z}'$ directions has been retained from structure 6, the component in the $\mathbf{y}'$ direction is not quite equal due to the limits of the geometry optimization.

Imaginary modes: This is a minimum energy structure (within the cubic family): no imaginary modes were found.

4.3.2.8 Structure no. 8 ($R3m$)

Transitioning: The parent structure was no. 1. The present structure was obtained by nudging down an equal superposition of all three of the $69.0i\,\mathrm{cm}^{-1}$ Γ_{15} (TO1) modes, present in structure 1. The ferroelectric shift was along the volume diagonal (with cations shifting towards the cell origin) and caused an approximately isotropic expansion of the cell and a reduction in the cell angles. The resultant structure is almost

certainly rhombohedral in nature (as opposed to the small deviations variations indicating no symmetry).

As was expected, the normal modes most directly involved in the transition were the Γ_{15} (TO1), which were all inclined at 63° to the difference vector. Two real (TO2) modes (7 and 9) also had a minor involvement. The final frequencies for the hardened (TO1) modes are 97.8, 71.7 and $63.3\,\mathrm{cm}^{-1}$.

Space group: $P1$ or $R3m$ (no. 160) with a deviation of $3.1\,\mathrm{m\AA}$.

Cell definition (Å and degrees): $a = 3.9047$, $b = 3.9024$, $c = 3.9036$;
$\alpha = 89.97$, $\beta = 89.96$, $\gamma = 89.97$.

Cell volume: $59.480\,\mathrm{\AA}^3$, $V/V_0 = 1.0020$. This is the largest volumed cubic ancestor structure we have seen and equal to the volumes of structures 2 and 6. All the structures 2–8 have volumes between $1.0015V_0$ and $1.0020V_0$.

As the three structures 2, 6 and 8 are dissimilar except that they were all the result of the first nudge from the cubic system, it is likely that the fractionally larger volumes is a result of the slightly different computational technique used to determine the structures. The other structures were run using full cell geometry optimization (`isif=3`), with a force convergence criterion of $|\mathrm{Force}| = 0.001$ (atomic units). The ideal cubic (1) and the first nudged structures (2, 6 and 8) were optimized with a series of constant cell volume (lattice parameters can change) calculations (`isif=4`) and the use of a least-squares fit algorithm for energy vs. volume, based on the *Birch-Murnaghan* equation of state (see appendix D.2.4). This multiple calculation method, is helpful when low energy cut-offs (e.g. $500\,\mathrm{eV}$) are used, as the plane-wave basis set does not describe the system properly when the cell shape changes. However, with large energy cut-offs it makes little difference.

The multiple point method was found to take an excessive period of time to implement and so it was changed in all of the more complex systems (only the cubic: 1, 2, 6 and 8; tetragonal: 9 and orthorhombic: 20 structures used the multiple calculation per structure technique). Note that only the method of geometry optimization varied between the cubic (and first descendants) systems and the others, the SCF was performed in the same way for all. The different method for geometry optimization may have introduced a bias of $\sim 0.0003V_0$ to the volume calculations, which we do not consider to be significant.

Potential energy (per formula unit): $-39.77284\,\mathrm{eV}$, an energy drop of $0.63\,\mathrm{meV}$ from the cubic parent and equivalent to a temperature drop of $\sim 1.47\,\mathrm{K}$. An immediate drop from the highest to the lowest energy structure, possibly allowable with the current five atom cell.

Polyhedral distortion: The octahedral volume was $9.9134\,\text{Å}^3$ which is 1.0020 of the ideal cubic equivalent.

Dipole (per formula unit): $0.681\,\text{D}$ inclined at 5.1° to the volume diagonal. The current structure displays the largest dipole that has been seen so far, which may be down the the quality of the initial guess, but may also be as a consequence of incomplete convergence in the geometry optimization. The components of the dipole are $-0.43\mathbf{x}' - 0.35\mathbf{y}' - 0.39\mathbf{z}'$, of which the strontium displacement contributes $0.315\,\text{D}$ and the titanium contributes $0.366\,\text{D}$.

Imaginary modes: This is a minimum energy structure, no imaginary modes were found.

Now that we have considered the changes in each structure, we will look at the frequency data gathered in a more general way.

4.3.3 Frequency Analysis

In table 4.3.5, we list all of the vibrational frequencies for the cubic ancestor structures 1–8 that have been produced by the calculations. In section 4.3.2 we confirmed how the Γ_{15} (TO1) modes were most directly involved in the transition down to the lower energy phases and underwent the greatest change in frequency as they hardened from imaginary to real. We also saw that Γ_{15} (TO2) modes played a secondary rôle with a breaking of degeneracy and a weaker degree of hardening. The Γ_{25} and Γ_{15} (TO3) modes have not been mentioned as their involvement was negligible. However, we note that when ideal cubic symmetry is broken, there is a splitting of degeneracy of the (TO3) modes, where two remain the same at $\sim 533\,\text{cm}^{-1}$ and one mode hardens slightly by about 10 wave numbers. This change remains constant during subsequent reductions in cell symmetry.

The Γ_{25} modes behave more subtly though interestingly; from these three modes alone, one can make the distinction between the four types of structure that have been generated from the initially cubic unit cell i.e. cubic, tetragonal, monoclinic and rhombohedral. In the cubic system 1, the three modes are degenerate with a frequency of $226\,\text{cm}^{-1}$. In structure 2 which is the only tetragonal system, we see a slight breaking of degeneracy, with two modes hardening to $231\,\text{cm}^{-1}$ and the third hardening to a slightly greater extent to $233\,\text{cm}^{-1}$. Considering the two monoclinic systems 3 and 6, we find that the degeneracy is broken completely with frequencies of 229, 231 and $\sim 235\,\text{cm}^{-1}$ for both systems. Finally the rhombohedral systems 4, 5, 7 and 8 all display two-fold degeneracy with the lower level at $228\,\text{cm}^{-1}$ and the two higher levels at $\sim 235\,\text{cm}^{-1}$.

In addition to the above, an analysis that compared the frequencies of every structure to every other was performed using a simple custom written tool called *compFreq*

Table 4.3.5: Full frequency listing (in cm^{-1}) of the cubic $Pm\bar{3}m$ ancestor structures. The normal mode labels refer directly to the ideal cubic system (1) and indirectly to the lower symmetry systems, whose modes are some mix of the normal modes of the higher symmetry system's. The labels were determined by comparing frequencies with those in Table V of [44].

Freq. no.	Label	Structure number							
		1	2	3	4	5	6	7	8
1	Γ_{15} (TO3)	533.2	542.9	542.3	542.6	542.7	543.1	542.5	543.3
2	Γ_{15} (TO3)	533.2	533.0	535.1	535.0	535.0	535.4	534.9	535.2
3	Γ_{15} (TO3)	533.2	532.8	533.3	534.7	534.7	533.2	534.8	534.9
4	Γ_{25}	226.2	233.2	235.1	234.8	234.9	235.7	234.8	235.1
5	Γ_{25}	226.2	231.4	231.4	234.0	234.4	231.2	234.5	234.3
6	Γ_{25}	226.2	231.1	228.9	227.6	227.8	228.7	227.8	227.6
7	Γ_{15} (TO2)	156.9	184.0	175.4	172.0	171.9	175.0	171.8	172.7
8	Γ_{15} (TO2)	156.9	158.3	167.1	166.2	166.3	168.6	166.0	166.6
9	Γ_{15} (TO2)	156.9	158.2	158.8	164.0	164.9	158.9	165.1	165.0
10		1.2	106.0	97.2	93.9	94.2	100.4	93.9	97.8
11		$1.2i$	$0.8i$	69.5	66.4	66.8	77.1	65.7	71.1
12		$1.2i$	$0.9i$	1.2	56.5	61.3	0.6	61.9	63.3
13	Γ_{15} (TO1)	$69.0i$	$1.3i$	$0.1i$	$0.2i$	$0.1i$	$1.5i$	$0.1i$	$0.5i$
14	Γ_{15} (TO1)	$69.0i$	$38.8i$	$0.3i$	$0.3i$	$0.2i$	$2.1i$	$0.2i$	$0.9i$
15	Γ_{15} (TO1)	$69.0i$	$39.3i$	$29.5i$	$0.5i$	$0.4i$	$25.0i$	$0.3i$	$2.2i$

(see appendix D.1.10, on page 250). The purpose was to identify identical structures, though the results make similar identifications as have been made above. The comparison data has been summarized in appendix C.2.

4.3.4 Summary of Cubic Ancestor Systems

From the ideal cubic structure and the various descendants produced through manipulations and optimizations that have been performed on it, we have identified three saddle point structures (cubic, tetragonal and monoclinic) and a rhombohedral structure that are allowable. The cubic $Pm\bar{3}m$ structure is the most symmetric but least energetically favourable. Ferroelectric shifts can occur in any and all directions with the most stable resulting in the rhombohedral $R3c$ space group, which forms as a consequence of a ferroelectric shift along the volume diagonal (titanium moving towards an octahedral face). The ferroelectric shifts result in an elongation of the cell in the direction of the transition, which will include a lengthening of a face or volume diagonal (causing the others diagonals to shorten). The maximum dipole moment allowable with the the five atom unit cell is between 0.66 and 0.68 D.

In papers by Zhang et al. [133] and Dove [48], the concepts of displacive phase transitions are discussed in the case of barium titanate and minerals in general (in the two papers respectively). The displacive model describes the shifting of the titanium ion from the central position in the case of the ideal cubic system, along one lattice vector, resulting in a tetragonal cell, two lattice vectors, resulting in an orthorhombic and three, resulting in a rhombohedral cell [133]. The findings presented here differ in

that we do not see an orthorhombic cell in the case of a displacement along two lattice vectors but rather a monoclinic cell with just two different side lengths.

In the case of the rhombohedral distortion, there are eight different directions (the cubic corners) that the titanium can move in order to achieve this distortion of the lattice. However, there are only two equilibrium positions for the titanium to be within a given five atom rhombohedral unit cell (either of the $< 90^\circ$ ends of the cell).

The total energy change between the highest and lowest symmetry cubic ancestor systems is 0.64 meV, which corresponds to a temperature difference of just ~ 1.5 K, we are therefore unlikely to observe these phase transitions, especially as it is known that relaxation of the cell takes place over a larger number of atoms than are modelled here. The simplest symmetry breaking distortion (ferroelectric shift along one lattice vector) results in the greatest energy loss ~ 0.5 meV, a shift down a second lattice vector results in a ~ 1 meV drop in energy and the final shift results in a drop of ~ 0.05 meV. The results, however, illustrate the perplexity of the potential energy landscape for STO.

Also of interest is the fact that in each ferroelectric transition, strontium and titanium have moved in the same direction as each other, which implies correlation. It would be nice to understand the nature of this correlation. Based on the nature of the cages that each atom moves in, it is clear why the titanium favours moving in the direction of the octahedral faces (to get close to as many oxygen atoms simultaneously as possible). The situation with the strontium is more complicated (it may help to consult figure 1.2.1 on page 20). The two most favourable directions of motion for strontium would be in the direction of the octahedral face (close proximity to three oxygens) or at 45° in the direction of a square face (close proximity to four oxygens, though their separation is greater). Structure 2 involves a displacement of titanium towards an octahedral corner and a displacement of strontium towards a cuboctahedral square face. Structure 8 involves a displacement of both cations towards an octahedral face. If we compare the dipole contributions between the strontium and titanium for these two cases, we see that fractionally the strontium contributes more towards the total dipole in structure 2 ($\mathrm{Ti/Sr} = 1.14$) than in structure 8 ($\mathrm{Ti/Sr} = 1.16$). However, overall the strength of both dipoles is greatest in structure 8. It appears that both cations favour motion towards the octahedral face, though this is not certain as there may have been some coercion of the titanium on the strontium in determining the dipole strength. We can reasonably assume though that the effect of correlation (the displacement did not have to be towards equivalent octahedral faces) between the two cations was caused by dipole repulsion.

Now that we have carefully examined the cubic ancestor systems, we now consider the lower symmetry tetragonal ancestor systems which use a four-fold larger unit cell.

4.4 Tetragonal Unit Cell

4.4.1 Introduction

Having examined the five atom cubic ancestor systems of STO, we now look at an expanded supercell shown in figure 4.4.1, which is built from the cubic cell by considering the diagonals in the **a** and **c** vectors ($\sqrt{2}$) in each direction and stacking two such units on top of one another. The tetragonal unit cell therefore has 20 atoms in it and has more degrees of freedom than the cubic unit cell.

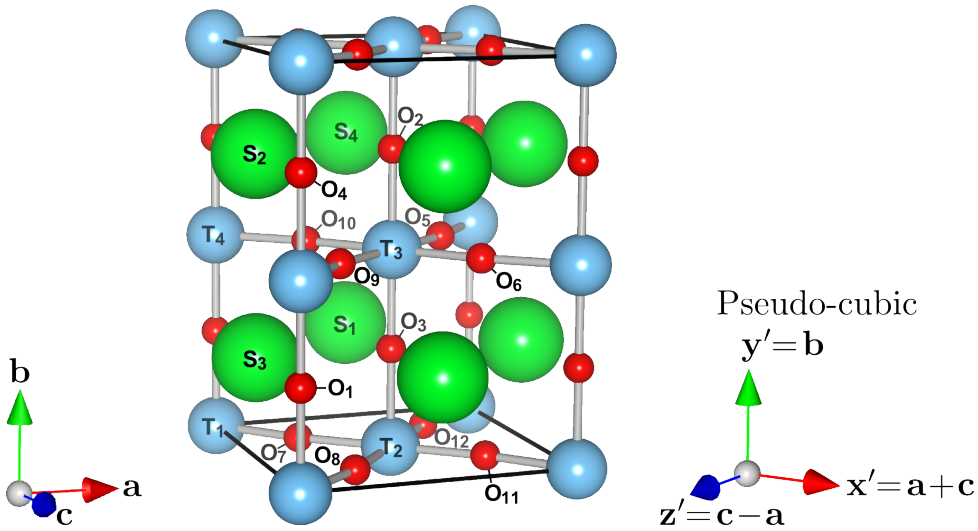

Figure 4.4.1: Structural diagram of the 20 atom $I4/mcm$ tetragonal strontium titanate cell. The direction of the lattice vectors has been shown together with the direction of the pseudo-cubic axis. Green, blue and red balls represent respectively, strontium, titanium and oxygen atoms.

A more detailed version of the dendrimer diagram in figure 4.2.2 has been displayed for the tetragonal ancestor systems in figure 4.4.2.

We will now move through the tetragonal ancestor dendrimer diagram considering the 11 structures in their numerical order. Some consideration of the relationship of the highest symmetry tetragonal structure ($I4/mcm$) to the ideal cubic system ($Pm\bar{3}m$) will be made at the start. A list of frequencies for the tetragonal ancestor structures can be found in table 4.4.18 on page 165.

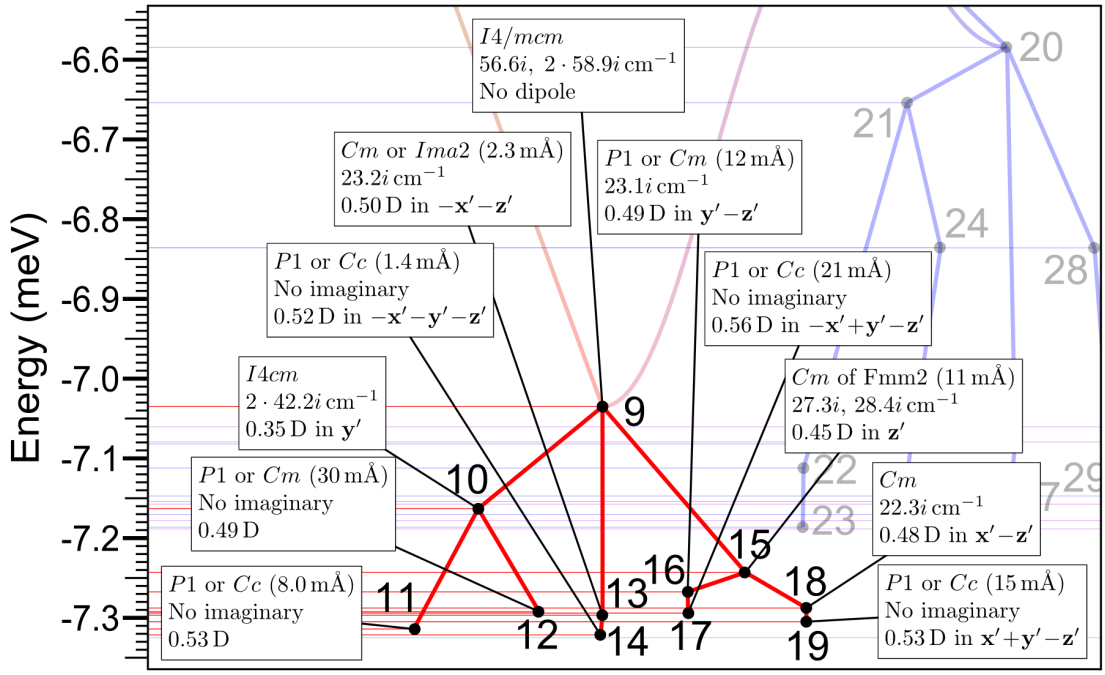

Figure 4.4.2: Dendrimer plot summarizing the tetragonal ancestor phase transitions. Here we provide a magnified version of figure 4.2.2, with labels showing the space groups, imaginary frequencies and dipole moments of the 11 structures that were considered in this part of the study. In some cases the direction of the dipole moment was not simply along or at $45°$ to lattice vectors. In these cases the direction of the dipole was not marked.

4.4.2 The Structures

4.4.2.1 Structure no. 9 ($I4/mcm$)

Transitioning: This high symmetry tetragonal system was a starting structure. However, by generating a supercell $Pm\bar{3}m$ symmetry system using the tetragonal unit cell as in figure 4.4.1, with optimized cubic parameters, it was possible to derive information about a transition between the $Pm\bar{3}m$ and the $I4/mcm$ system.

A NEB calculation showed no energy barrier between the starting and end point structures. The tetragonal (no. 9) system underwent several changes from the cubic system. The overall cell volume decreased, which involved a stretching along the $\mathbf{b}$ vector ($\mathbf{y}'$ axis) and a shortening of a and c. The octahedra rotated around the $\mathbf{b}$ vector and were able to increase in volume as a consequence.

The cubic $Pm\bar{3}m$ system built in the tetragonal unit cell has six imaginary modes in two, three-fold degenerate sets. The softest three modes are numbered 58–60 and have a frequency of $79.6i\,\mathrm{cm}^{-1}$. The slightly harder Γ_{15} (TO1) imaginary modes numbered 55–57, have a small variation from degeneracy, as mode 57 has a frequency of $68.7i\,\mathrm{cm}^{-1}$ and modes 55 and 56 have a frequency of $67.2i\,\mathrm{cm}^{-1}$. We will see that in each of these sets, the one with the highest number has slightly different character to the

others in the set. All of the Γ modes were identified based on the numerical similarity to the Γ modes in the five atom cubic system, see section 4.3, which in turn were based on a slightly looser fit comparison to the works in [44].

Mode no. 60 was most directly responsible for the transition. The eigenvectors of the mode involve only motions of oxygen atoms in a planar fashion with an axis along the **b** vector, it is inclined at 7° to the difference vector and does not appear to posses either ferroelectric or antiferroelectric character. Many other modes had a minor involvement, resulting in the comparatively subtle transformations to the lattice. The other two modes in this set 58–59, like mode 60, only involve the oxygen and consist mostly of a rotation about the titanium atoms, in the $\mathbf{x}'$ and $\mathbf{z}'$ axis. However, they also poses a small amount of antiferroelectric character (with no ferroelectric component). The eigenvectors of the cubic mode 60 and 59 are shown in figure 4.4.3.

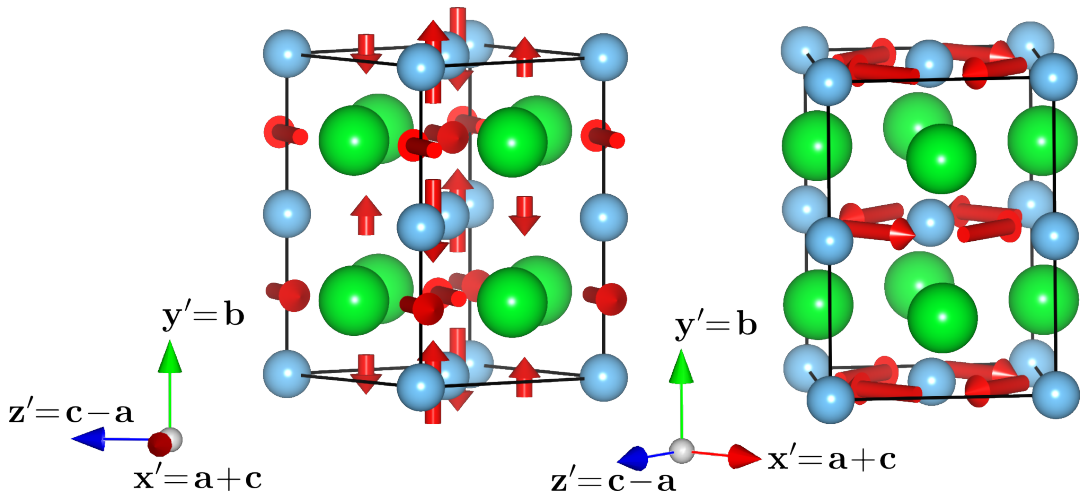

Figure 4.4.3: A representation of the degenerate imaginary modes no. 59 (left) and 60 (right) of the $Pm\bar{3}m$ structure in the tetragonal setting. Green, blue and red respectively represent strontium, titanium and oxygen. Atoms not vibrating are represented as balls, vibrating atoms are arrows.

After the transition, all of the degenerate modes 58–60 become hard with mode 60 hardening to $123\,\mathrm{cm}^{-1}$ (mode number 43) as a pure form of the original i.e. no mixing of other modes. Modes 58 and 59 retained their degeneracy and hardened to $39.1\,\mathrm{cm}^{-1}$ (modes 53 and 54) but included some small amounts of mixing from modes 42 and 41 from the parent $Pm\bar{3}m$ system. The original modes, 58 and 59 were inclined at 7° to their child modes 53 and 54.

Three imaginary modes still remain and are discussed at the bottom of this section on structure 9.

Space group: $I4/mcm$ (no. 140).

Cell definition (Å and degrees): $a = 5.5034$, $b = 7.8290$, $c = 5.5034$;
$\alpha = 90.00$, $\beta = 90.00$, $\gamma = 90.00$;
$a : b : c = 0.9941 : 1 : 0.9941$.

Some additional information on the relative lengths of the **a**, **b** and **c** vectors has been included here. The ratios assume that b is divided by $\sqrt{2}$ to compensate for the tall unit cell. For this tetragonal cell the b/a ratio is 1.0059, the experimental values are 1.00039 [24] and 1.00056 [23].

Cell volume: $237.12\,\text{Å}^3$, $V/4V_0 = 0.9986$. V_0 is the ideal $Pm\bar{3}m$ cubic volume, not the ideal tetragonal volume.

Potential energy (per formula unit): $-39.77924\,\text{eV}$, which is a drop of $7.04\,\text{meV}$ from the ideal cubic system and equivalent to a temperature drop of $\sim 16.3\,\text{K}$.

Polyhedral distortion: In this highly symmetrical tetragonal system, the octahedra now have the freedom to rotate. A summary of the octahedral distortions for the octahedron around titanium atom 1 is in table 4.4.1. The other four octahedra were found to be behaving equivalently i.e. every nearest neighbour octahedron rotated in the opposite direction.

Table 4.4.1: The octahedral tilt and distortion around titanium atom T_1 in structure 9. The octahedral volume was $9.9714\,\text{Å}^3$ which is 1.0078 of the ideal cubic equivalent.

Stick	θ (°)	θ_1 (°)	θ_2 (°)	length l (Å)	l/l_0
$s_{x'}$	5.4911	0.0000	5.4911	3.9095	1.0022
$s_{y'}$	0.0000	0.0000	0.0000	3.9145	1.0035
$s_{z'}$	5.4911	−5.4911	0.0000	3.9095	1.0022

To help interpret table 4.4.1, please refer back to figure 4.2.1 and table 4.2.1 on pages 118 to 119. We find that the octahedra underwent a rotation along the $\mathbf{y}'$ axis (the **b** cell vector) of $5.49°$, which is indicated in the table by the deviation of the $s_{x'}$ and $s_{z'}$ stick vectors from the respective pseudo-cubic axis (indicated in the first column of data (θ)). In this case, the following two columns reiterate that the rotation was only in the plane of the $\mathbf{x}'$ and $\mathbf{z}'$ axis as the rotations are identical. The final column, which demonstrates the change in length of the octahedral sticks ($l_{x'}$, $l_{y'}$ and $l_{z'}$) relative to the ideal cubic stick length l_0 shows an all round expansion of the octahedra with a greater expansion on in the $\mathbf{y}'$ direction.

Dipole (per formula unit): There are no local dipoles and no net dipole in the perfect $I4/mcm$ structure. Though the distortion leading to its creation is often described as antiferrodistortive, this system is not antiferroelectric as the octahedra rotate around the titanium atoms, without changing their relative distances.

Imaginary modes: The high symmetry tetragonal structure has three imaginary Γ_{15} (TO1) modes.

Mode 58 has a frequency of $56.6i$ cm^{-1}, it is purely ferroelectric and expresses its motion in the direction of the b vector ($\mathbf{y}'$ axis). Mode 58 inherited its character mostly from the $Pm\bar{3}m$ Γ_{15} (TO1) mode no. 57 (inclined at $11°$ to it) and a small amount from the Γ_{15} (TO2) mode no. 37.

Modes 59 and 60 are degenerate with one another, with a frequency of $58.9i$ cm^{-1}. These express ferroelectric motion primarily along each of the the $\mathbf{a}$ and $\mathbf{c}$ vectors. However, these two modes also have a weak antiferroelectric component on the titanium as can be seem most clearly in figure 4.4.5. In the right-most diagram for mode 59 we see that the titanium (blue) arrows have different up/down components ($\mathbf{a}$ axis). The eigenvectors for the no. 58 and 59 modes are also provided in table 4.4.2. Similarly to mode 58, modes 59 and 60, inherited most of their character ($8°$) from the $Pm\bar{3}m$ Γ_{15} (TO1) ferroelectric modes 56 and 55 respectively with a weaker component of Γ_{15} (TO2) from modes 38 and 39. However, these two imaginary modes also inherited a small amount of character from $Pm\bar{3}m$ modes 17 and 18. The $Pm\bar{3}m$ Modes 17 and 18 are purely antiferroelectric, involving antiparallel motion of different titanium ions, see figure 4.4.4. This is the most likely origin of the antiferroelectricity in modes 59 and 60.

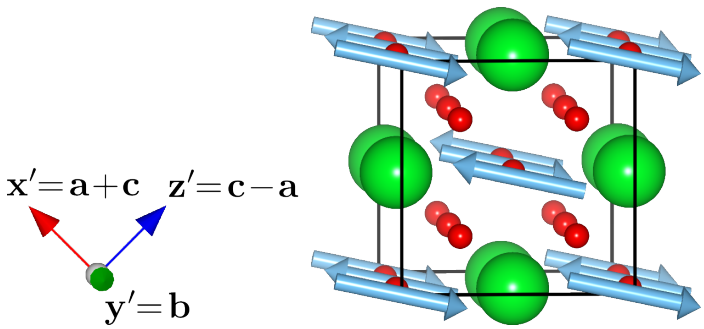

Figure 4.4.4: A representation of the pure antiferroelectric real mode no. 17 of the $Pm\bar{3}m$ structure in the tetragonal setting. Green, blue and red respectively represent strontium, titanium and oxygen. Atoms not vibrating are represented as balls, vibrating atoms are arrows.

Table 4.4.2: Eigenvectors for the non-degenerate and one of the degenerate imaginary modes of structure no. 9. Modes 58 (left) and 59 (right) have frequencies of $56.6i$ cm^{-1} and $58.9i$ cm^{-1} respectively. See figure 4.4.1 for the atom labels.

Atom	dx′	dy′	dz′
S_1	0.00	0.08	0.00
S_2	0.00	0.08	0.00
S_3	0.00	0.08	0.00
S_4	0.00	0.08	0.00
T_1	0.00	0.30	0.00
T_2	0.00	0.30	0.00
T_3	0.00	0.30	0.00
T_4	0.00	0.30	0.00
O_1	0.00	−0.23	0.00
O_2	0.00	−0.23	0.00
O_3	0.00	−0.23	0.00
O_4	0.00	−0.23	0.00
O_5	0.00	−0.23	0.00
O_6	0.00	−0.23	0.00
O_7	0.00	−0.23	0.00
O_8	0.00	−0.23	0.00
O_9	0.00	−0.23	0.00
O_{10}	0.00	−0.23	0.00
O_{11}	0.00	−0.23	0.00
O_{12}	0.00	−0.23	0.00

Atom	dx′	dy′	dz′
S_1	−0.08	0.00	−0.07
S_2	−0.08	0.00	−0.07
S_3	−0.08	0.00	−0.07
S_4	−0.08	0.00	−0.07
T_1	−0.16	0.00	−0.21
T_2	−0.23	0.00	−0.14
T_3	−0.16	0.00	−0.21
T_4	−0.23	0.00	−0.14
O_1	0.18	0.00	0.16
O_2	0.18	0.00	0.16
O_3	0.18	0.00	0.16
O_4	0.18	0.00	0.16
O_5	0.17	0.00	0.15
O_6	0.17	0.00	0.15
O_7	0.17	0.00	0.15
O_8	0.17	0.00	0.15
O_9	0.17	0.00	0.15
O_{10}	0.17	0.00	0.15
O_{11}	0.17	0.00	0.15
O_{12}	0.17	0.00	0.15

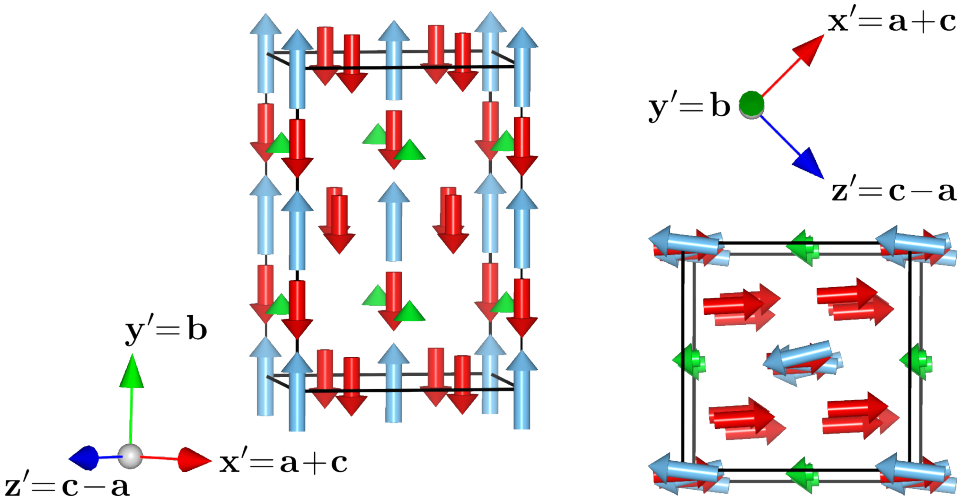

Figure 4.4.5: Graphical representation of the imaginary modes no. 58 (left) and 59 (right) of structure 9. Green, blue and red arrows respectively represent motion of strontium, titanium and oxygen.

4.4.2.2 Structure no. 10 ($I4cm$)

Transitioning: The parent structure was no. 9 and the present structure was obtained by nudging down mode 58. Tetragonal symmetry was preserved during the ferroelectric transition, with an expansion along the $\mathbf{b}$ axis and a small shrinkage in the other axes. There was a small decrease in the cell volume with no significant distortion of the octahedra.

Mode 58 in (structure 9) was the only mode with any significant involvement in the transition. It hardened from $56.6i\,\mathrm{cm}^{-1}$ and split into two parts, going mostly ($22°$) to mode 53 with a frequency of $87.6\,\mathrm{cm}^{-1}$ and to a lesser extent to mode 44 ($69°$) with a frequency of $126.2\,\mathrm{cm}^{-1}$.

Space group: $I4cm$ (no. 108).

Cell definition (Å and degrees): $a = 5.5003$, $b = 7.8364$, $c = 5.5003$;
$\alpha = 90.00$, $\beta = 90.00$, $\gamma = 90.00$;
$a : b : c = 0.9926 : 1 : 0.9926$.

Cell volume: $237.07\,\text{Å}^3$, $V/4V_0 = 0.9984$. A small shrink in overall volume since from structure 9.

Potential energy (per formula unit): $-39.77937\,\mathrm{eV}$, a drop of $0.13\,\mathrm{meV}$ from the $I4/mcm$ structure 9, which correlates to a temperature drop of $\sim 0.30\,\mathrm{K}$.

Polyhedral distortion: The octahedra all distorted in an equivalent way, see table 4.4.3. A small decrease in octahedral volume accompanied a likely inconsequential increased rotation. The rotation has remained in the plane of $\mathbf{x}'$ and $\mathbf{z}'$.

Table 4.4.3: The octahedral tilt and distortion around titanium atom T_1 in structure 10. The octahedral volume was $9.9696\,\text{Å}^3$ which is 1.0077 of the ideal cubic equivalent.

Stick	θ (°)	θ_1 (°)	θ_2 (°)	length l (Å)	l/l_0
$s_{x'}$	5.4982	0.0000	5.4982	3.9073	1.0016
$s_{y'}$	0.0000	0.0000	0.0000	3.9182	1.0044
$s_{z'}$	5.4982	−5.4982	0.0000	3.9073	1.0016

Dipole (per formula unit): $0.354\,\mathrm{D}$ directly in the $\mathbf{y}'$ axis ($\mathbf{b}$ vector), of which the strontium contributes $0.142\,\mathrm{D}$ and the titanium contributes $0.213\,\mathrm{D}$.

Imaginary modes: The present structure has two degenerate imaginary modes with frequency $42.2i\,\mathrm{cm}^{-1}$, see table 4.4.4 and figure 4.4.6. These two modes show some rather complex activity involving a strong ferroelectric component in the $\mathbf{c}$ and $\mathbf{a}$ axis respectively for modes 59 and 60 ($\mathbf{x}' + \mathbf{z}'$ and $\mathbf{x}' - \mathbf{z}'$ respectively). The motions of the titanium atoms are not all aligned, indicating a small antiferroelectric component to the mode. We also see a rocking component on the oxygen atoms with the near atoms

moving up and the far ones moving down (in figure 4.4.6). This component of the distortion would seem to encourage the octahedron to tilt in a direction perpendicular to the **b** vector.

Table 4.4.4: Eigenvectors for the degenerate imaginary mode 59 of structure no. 10 with a frequency of $42.2i\,\mathrm{cm}^{-1}$.

Atom	dx′	dy′	dz′
S_1	0.10	0.00	0.07
S_2	0.10	0.00	0.07
S_3	0.09	0.00	0.07
S_4	0.09	0.00	0.07
T_1	0.18	0.00	0.19
T_2	0.23	0.00	0.11
T_3	0.18	0.00	0.19
T_4	0.23	0.00	0.11
O_1	−0.15	0.00	−0.20
O_2	−0.15	0.00	−0.20
O_3	−0.23	0.00	−0.08
O_4	−0.23	0.00	−0.08
O_5	−0.19	−0.06	−0.13
O_6	−0.18	−0.04	−0.14
O_7	−0.18	−0.04	−0.14
O_8	−0.19	−0.06	−0.13
O_9	−0.19	0.06	−0.13
O_{10}	−0.18	0.04	−0.14
O_{11}	−0.18	0.04	−0.14
O_{12}	−0.19	0.06	−0.13

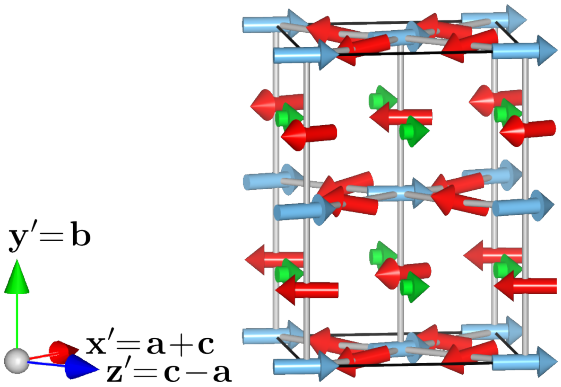

Figure 4.4.6: Graphical representation of the degenerate imaginary modes no. 59 of structure 10. Green, blue and red arrows respectively represent motion of strontium, titanium and oxygen. The bonds have been drawn in grey to make the interpretation of the cell geometry easier.

4.4.2.3 Structure no. 11 (Cc)

Transitioning: The parent structure was the tetragonal no. 10 and the present structure was produced by nudging down the 59^{th} normal mode. The ferro/antiferroelectric transition resulted in a monoclinic structure with approximately equal side lengths **a** and **c**. There was a net increase in the cell volume which involved a shortening of the cell

along the b vector but an expansion of the other two. Also the cells angles have been allowed to relax, one more than the others, resulting in the monoclinic structure.

The mode most directly involved in the transition was mode no. 59, inclined at 34° to the difference vector. However, there was also an involvement of the Γ_{15} (TO3) mode no. 5, the (TO2) mode no. 38, 44, 53, 54, 5, and the imaginary mode 60.

The two degenerate imaginary modes in structure 10, nos. 59 and 60 ($42.2i\,\mathrm{cm}^{-1}$) hardened, breaking degeneracy. Mode 59 hardened (mostly as the angle between the modes was 24°) to mode 53 with a frequency of $91.9\,\mathrm{cm}^{-1}$ and mode 60 hardened (angle between modes was 18°) to become mode 54 with frequency $71.1\,\mathrm{cm}^{-1}$. There was a large degree of mode mixing though, so there modes contaminated other modes and vice versa.

Space group: Cc (no. 9) with a deviation of $8\,\mathrm{m\AA}$, there is no lower symmetry system with a lower deviation, besides $P1$.

Cell definition (Å and degrees): $a = 5.5056$, $b = 7.8245$, $c = 5.5075$;
$\alpha = 90.04$, $\beta = 89.98$, $\gamma = 90.01$;
$a : b : c = 0.9951 : 1 : 0.9954$.

Cell volume: $237.25\,\mathrm{\AA}^3$, $V/4V_0 = 0.9992$.

Potential energy (per formula unit): $-39.77950\,\mathrm{eV}$, a decrease of $0.15\,\mathrm{meV}$ from parent structure no. 10 and is equivalent to a drop of $\sim 0.35\,\mathrm{K}$ in temperature.

Polyhedral distortion: In the present structure we begin to see some small anomalies between the nature of different octahedra in the cell. The descriptions of the stick rotations relative to the pseudo-cubic axes are still equivalent (barring a small amount of noise in the fifth significant figure). However, for the first time, the angles of the sticks relative to one another have departed slightly from 90° and formed two pairs. Titanium atoms 1 and 3 have angles of 90.09°, 89.99° and 90.09° for s_α, s_β and s_γ respectively while titanium atoms 2 and 4 have angles of 90.06°, 89.99° and 90.11° respectively (see figure 4.4.1 and section 4.2.2.3 for a description of the labels). These deviations from orthogonality are small and may be attributed to imperfect optimization.

Table 4.4.5: The octahedral tilt and distortion around titanium atom T_1 in structure 11. The octahedral volume was $9.9766\,\mathrm{\AA}^3$ which is 1.0084 of the ideal cubic equivalent.

Stick	θ (°)	θ_1 (°)	θ_2 (°)	length l (Å)	l/l_0
$s_{x'}$	5.4313	−0.5431	5.4045	3.9120	1.0028
$s_{y'}$	0.9045	−0.7146	0.5543	3.9127	1.0030
$s_{z'}$	5.4512	−5.4069	0.7009	3.9107	1.0025

In table 4.4.5 we see a description of the octahedron around titanium 1 which remains equivalent to the other octahedra in the present structure. We see from the first

column of data that the octahedron now has a substantial deviation from each of the pseudo-cubic vectors, though most of the rotation is still around the $\mathbf{b}$ vector or $\mathbf{y}'$ axis as with structures 9 and 10. The rotation around the $\mathbf{y}'$ axis has fractionally decreased while the octahedron has now rocked over away from this axis by $0.9°$. The θ_1 and θ_2 columns, which for the $s_{y'}$ stick respectively represent $\theta_{y'_{yz}}$ and $\theta_{y'_{yx}}$ (how far the $s_{y'}$ stick rocks over towards the $\mathbf{z}'$ axis and how far it rocks towards the $\mathbf{x}'$ axis), shows that the tilt favours the $\mathbf{z}'$ axis more than the $\mathbf{x}'$.

The various distortions have facilitated a small expansion in the octahedral volume despite a slight shortening of the $s_{y'}$ stick.

Dipole (per formula unit): 0.525 D of which the strontium contributes 0.229 D and the titanium contributes 0.297 D. There is a small angular separation between the strontium and titanium contributions to the total dipole moment of $1.5°$ but this most likely due to imperfect geometry optimization. Overall the dipole acts mostly in the $\mathbf{x}' + \mathbf{z}'$ direction (the projection of the dipole onto the $\mathbf{ac}$ face is $3.8°$ off the $\mathbf{c}$ vector), with a smaller component in the $\mathbf{y}'$ axis. The total dipole moment vector (per formula unit) is $0.371\mathbf{x}' + 0.181\mathbf{y}' + 0.325\mathbf{z}'$. The system has a significant antiferroelectric component with titanium dipoles aligned either parallel or at $7.1°$ to one another. Strontium dipoles are aligned either parallel or at $3.3°$ to one another. A representation of the dipoles on strontium and titanium is shown in figure 4.4.7.

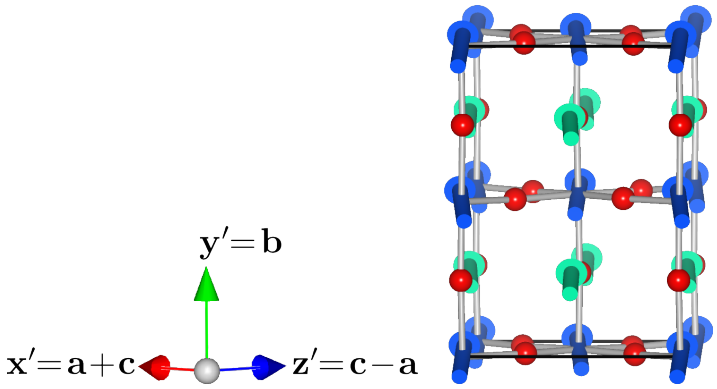

Figure 4.4.7: Representation of the strontium (green) and titanium (blue) dipoles on structure 11. The antiferroelectricity can most readily be seen on the titanium arrows.

Imaginary modes: There are no imaginary modes in this system, which appears to be in a ground state.

4.4.2.4 Structure no. 12 ($P1$ or $I4cm$)

Transitioning: The parent structure was no. 10 and the present structure was obtained by nudging down the sum of the degenerate modes 59 and 60 (with frequency $42.2i\,\mathrm{cm}^{-1}$) and the optimization resulted in a tetragonal to monoclinic lattice distortion. The transition was similar to that of the structure 10 to 11 transition in that it

resulted in similar lattice distortions with ferro and antiferroelectric components and a rotation of the octahedra along multiple axes. The transition resulted as expected in the loss of all unstable modes. As a state with no unstable modes had already been reached in structure 11, there was a degree of redundancy in carrying out the present structural optimization. The calculations were actually run simultaneously and it was not known that two imaginary modes would be lost due to a nudge down a single mode in the 10 to 11 transition until the results were examined. We kept the description of both structures as it adds to the general knowledge of the potential energy surface.

The nudge down both of the imaginary modes has resulted in a somewhat asymmetrical system with possibly $P1$ symmetry. The cell volume increased but to a slightly lesser degree than in structure 11. The $\mathbf{a}$ and $\mathbf{c}$ parameters expanded while the $\mathbf{b}$ parameter shrunk. The rotation of the octahedra along axis besides the $\mathbf{y}'$ was not as substantial as in structure 11. Additionally the magnitude of both the ferro and antiferroelectric effects was slightly weaker than in structure 11.

The modes most directly involved in the transition were mode 59, inclined at $62°$ to the difference vector and mode 60, inclined at $48°$ to the difference vector. Various other modes have a lesser involvement. During hardening, the two degenerate imaginary modes became well mixed into the other modes and so it is hard to determine what frequency they hardened to.

Space group: This is an exceptionally asymmetric system for which the lowest non-$P1$ symmetry group is Cm (no. 8) with a deviation of 30 mÅ.

Cell definition (Å and degrees): $a = 5.5056$, $b = 7.8273$, $c = 5.5044$;
$\alpha = 90.02$, $\beta = 89.92$, $\gamma = 90.02$;
$a : b : c = 0.9947 : 1 : 0.9945$.

Cell volume: $237.20\,\text{Å}^3$, $V/4V_0 = 0.9990$.

Potential energy (per formula unit): -39.77937 eV, a drop of 0.13 meV from the parent structure 10 and equivalent to a ~ 0.37 K temperature drop.

Polyhedral distortion: The qualitative nature of the octahedral tilting is very similar to that of structure 11 (as with the other structures the example of one octahedron is representative of the others). We see from table 4.4.6 that the rotation about the $\mathbf{y}'$ axis is marginally greater than in structure 10. However, the rotation of the octahedra in the other direction is not as great (around $10\,\%$ less). We also see from the θ_1 and θ_2 columns that the octahedra favoured leaning towards the $\mathbf{z}'$ axis much more than the $\mathbf{x}'$ axis i.e. the tilt was mostly about the $\mathbf{x}'$ axis with very little tilt around the $\mathbf{z}'$ axis. In structure 10 we saw that the favoured tilt (after the rotation about the $\mathbf{y}'$ axis) was in between the $\mathbf{x}'$ and $\mathbf{z}'$ axis. As structure 11 had a slightly lower energy, we can assume that the configuration in structure 11 is more energetically favourable.

Table 4.4.6: The octahedral tilt and distortion around titanium atom T_1 in structure 12. The octahedral volume was $9.9752\,\text{Å}^3$ which is 1.0082 of the ideal cubic equivalent.

Stick	θ (°)	θ_1 (°)	θ_2 (°)	length l (Å)	l/l_0
$s_{x'}$	5.4387	0.1726	5.4360	3.9129	1.0031
$s_{y'}$	0.8193	−0.8003	−0.1752	3.9141	1.0034
$s_{z'}$	5.5015	−5.4458	0.7884	3.9079	1.0018

There were some very small distortions to the stick angles: titanium octahedra 1 and 3 have angles of $89.993°$, $90.020°$ and $90.108°$ for s_α, s_β and s_γ respectively and titanium octahedra 2 and 4 have $89.969°$, $90.000°$ and $90.103°$ which excluding noise from the optimization is most likely a single distortion in s_γ of $0.1°$ from orthogonality.

Dipole (per formula unit): $0.494\,\text{D}$ of which the strontium contributes $0.213\,\text{D}$ and the titanium contributes $0.281\,\text{D}$. There is a small angular separation between the components from strontium and titanium of $2.6°$. As with structure 11, the cell has an antiferroelectric component. Titanium dipoles have angular separations of $0°$ and $6.5°$ and the strontium-dipole separations are $0°$ and $1.6°$. Both the ferroelectric and antiferroelectric components of the dipole are weaker in this structure than in structure 11. The qualitative nature of the lattice of dipoles is the same as in figure 4.4.7 so we will not produce another diagram here. The direction of the total dipole is $0.399\mathbf{x}' + 0.236\mathbf{y}' - 0.170\mathbf{z}'$.

Imaginary modes: The present system has no imaginary modes and is one of the ground state structures.

4.4.2.5 Structure no. 13 ($Ima2$)

Transitioning: The parent structure was no. 9 (tetragonal $I4/mcm$ symmetry). The present structure was obtained by nudging down imaginary mode no. 59, which was one of a two fold degenerate set. The ferro/antiferroelectric transition resulted in the introduction of a net dipole to the system and an antiferroelectric component that is present only on the titanium ions. The cell became shorter (shrank in the $\mathbf{b}$ vector or $\mathbf{y}'$ axis) and fatter along the $\mathbf{a}$ and $\mathbf{c}$ vectors though favouring the $\mathbf{c}$ vector slightly. The cell has essentially become orthorhombic, except for a small angle on β of $0.01°$, giving the cell a monoclinic symmetry group.

Mode 59 from structure 9 was most directly responsible for the transition, inclined at $30°$ to the difference vector. A small component of the Γ_{15} real mode 39 ($159.3\,\text{cm}^{-1}$ was also involved in the transition. Mode 59 originally had a frequency of $58.9i\,\text{cm}^{-1}$ and during the transition it split into two parts hardening mostly to mode number 53 (inclined at $17°$) with frequency $92.1\,\text{cm}^{-1}$ and to a lesser extent (inclined at $76°$) to mode 37, with a frequency of $168.5\,\text{cm}^{-1}$.

Mode 60 from structure 9 does not lead to the present structure, but none the less

hardens to $69.5\,\mathrm{cm}^{-1}$, which is mode number 54.

Imaginary mode 58 splits into two parts, one of which hardens and becomes part of mode 56 with frequency $36.2\,\mathrm{cm}^{-1}$, the other part also hardens slightly and becomes part of the new imaginary mode 60 with frequency $23.2i\,\mathrm{cm}^{-1}$.

Space group: Cm (no. 8) or $Ima2$ (no. 46) with a deviation of $2.3\,\mathrm{m\AA}$.

Cell definition (Å and degrees): $a = 5.5052$, $b = 7.8234$, $c = 5.5080$;
$\alpha = 90.00$, $\beta = 89.99$, $\gamma = 90.00$;
$a : b : c = 0.9952 : 1 : 0.9957$.

Cell volume: $237.23\,\mathrm{\AA}^3$, $V/4V_0 = 0.9990$.

Potential energy (per formula unit): $-39.779505\,\mathrm{eV}$, a drop of $0.26\,\mathrm{meV}$ from the parent structure 9, which corresponds to a temperature drop of $\sim 0.61\,\mathrm{K}$.

Polyhedral distortion: Examining table 4.4.7, we see largely similar character to that of structures 9 and 10. The rotation remains only around the $\mathbf{y}'$ axis, though the extent has reduced slightly from the parent ($5.49°$ reduced to $5.48°$). The octahedral volume has increased slightly.

Table 4.4.7: The octahedral tilt and distortion around titanium atom T_1 in structure 13. The octahedral volume was $9.9753\,\mathrm{\AA}^3$ which is 1.0082 of the ideal cubic equivalent.

Stick	θ (°)	θ_1 (°)	θ_2 (°)	length l (Å)	l/l_0
$s_{x'}$	5.4762	0.0000	5.4762	3.9120	1.0028
$s_{y'}$	0.0000	0.0000	0.0000	3.9117	1.0027
$s_{z'}$	5.4778	−5.4778	0.0000	3.9113	1.0026

We also find that the internal octahedral angle s_β (between the $s_{x'}$ and $s_{z'}$ sticks) reduces slightly to $89.97°$ while the others remain at exactly $90°$. This is probably caused by the slight orthorhombic distortion of the cell.

Dipole (per formula unit): $0.505\,\mathrm{D}$ of which the strontium dipoles contribute $0.219\,\mathrm{D}$ and the titanium contribute $0.285\,\mathrm{D}$. The titanium contributes an antiferroelectric effect to the cell and the dipoles vary in angle from one another by either $0°$ or $8.2°$. There is almost no antiferroelectricity deriving from the strontium for this cell as the dipoles are aligned. Strontium-titanium dipole angles are between $4.0°$ and $4.2°$ as the strontium dipoles point in between the titanium dipoles. The overall dipole direction is in the $-0.365\mathbf{x}' - 0.348\mathbf{z}'$ direction i.e. along the cell edge with just a $1.4°$ variation. The antiferroelectric component is also in the $\mathbf{x}'\mathbf{z}'$ plane perpendicular to the ferroelectric component.

Imaginary modes: This structure has one imaginary mode with a frequency of $23.2i\,\mathrm{cm}^{-1}$. The imaginary mode inherited its character from the two real and de-

generate modes 53 and 54 ($39.1\,\mathrm{cm}^{-1}$) and also the imaginary mode 58 ($56.6i\,\mathrm{cm}^{-1}$) (from structure no. 9).

Table 4.4.8: Eigenvectors for the degenerate imaginary mode 60 of structure no. 13 with a frequency of $23.2i\,\mathrm{cm}^{-1}$.

Atom	dx′	dy′	dz′
S_1	−0.02	−0.06	0.02
S_2	−0.02	−0.06	0.02
S_3	0.02	−0.06	−0.02
S_4	0.02	−0.06	−0.02
T_1	0.00	−0.20	0.00
T_2	0.00	−0.20	0.00
T_3	0.00	−0.20	0.00
T_4	0.00	−0.20	0.00
O_1	0.17	0.17	−0.17
O_2	0.17	0.17	−0.17
O_3	−0.17	0.17	0.17
O_4	−0.17	0.17	0.17
O_5	0.00	0.01	0.00
O_6	0.00	0.01	0.00
O_7	0.00	0.01	0.00
O_8	0.00	0.01	0.00
O_9	0.00	0.34	0.00
O_{10}	0.00	0.34	0.00
O_{11}	0.00	0.34	0.00
O_{12}	0.00	0.34	0.00

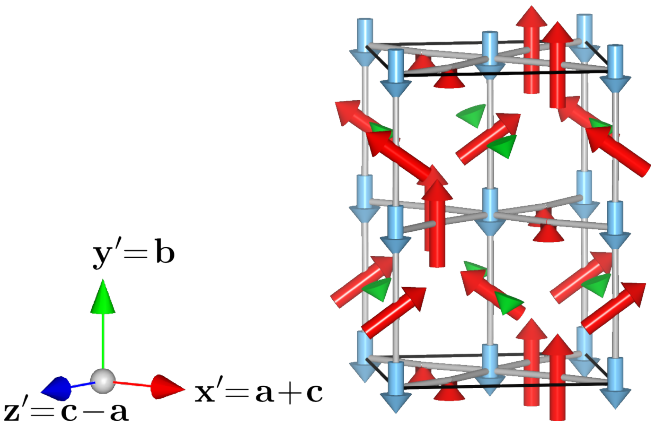

Figure 4.4.8: Graphical representation of the imaginary mode no. 60 of structure 13. Green, blue and red arrows respectively represent motion of strontium, titanium and oxygen.

The ionic motion in this mode is the most peculiar in appearance yet encountered, see table 4.4.8 and figure 4.4.8. There is a purely ferroelectric shift of the titanium ions in the $\mathbf{y}'$ direction and there is a small ferro/antiferroelectric motion of the strontium acting in the same overall direction. Amongst the oxygens though, we see a combination of a strong ferro-electric shift and a substantial rotation of oxygens around the $\mathbf{c}$ cell vector ($\mathbf{x}'$+$\mathbf{z}'$). Looking at the octahedron in the centre of the diagram we see long vectors pointing up on the left of the octahedron and almost zero vectors on the

right. The motion of the octahedron is clockwise relative to the page so on the left, the combined ferroelectric motion and rotation exaggerate the vector length and on the right, they cancel each other out.

4.4.2.6 Structure no. 14 (Cm)

Transitioning: The parent structure was the orthorhombic system no. 13 and the present structure was obtained by nudging down the only remaining mode no. 60 ($23.2i\,\mathrm{cm}^{-1}$). The transition resulted in a monoclinic structure with a small increase in b and a small decrease in a and c and an overall negligible change in volume. The transition which was mostly ferroelectric (barring the introduction of a small component of antiferroelectricity to the strontium) and rotative i.e. causing the oxygen octahedra to rotate over onto their edges by around half a degree.

The transition was almost entirely facilitated by the imaginary mode 60, which is inclined at an angle of 60° to the difference vector. The mode hardened and became most directly a part of mode 57 ($30.3\,\mathrm{cm}^{-1}$), inclined at 30.2° to the new vector. The mode split and became parts of various other modes.

Space group: Cm (no. 9) with a deviation of $1.3\,\mathrm{mÅ}$ or $P1$ for lower deviations.

Cell definition (Å and degrees): $a = 5.5043$, $b = 7.8274$, $c = 5.5063$;
$\alpha = 90.02$, $\beta = 89.99$, $\gamma = 90.00$;
$a : b : c = 0.9945 : 1 : 0.9948$.

Cell volume: $237.23\,\mathrm{Å}^3$, $V/4V_0 = 0.9991$.

Potential energy (per formula unit): $-39.77953\,\mathrm{eV}$, a drop of $25\,\mu\mathrm{eV}$, corresponding to $\sim 0.06\,\mathrm{K}$ from the parent structure 13. This is also the lowest energy structure that was discovered during this thesis, with the exception of a structure made from a 40 atom unit cell (structure no. 38), which was only lower by $3.5\,\mu\mathrm{eV}$ and could easily be attributed to variations due to a different unit cell size.

Polyhedral distortion: In this structure we see from table 4.4.9, a rotation about the $\mathbf{y}'$ axis that is almost identical to the parent structure no. 13 and similar to the starting tetragonal structure no. 9. There is also a tilt in the other two pseudo-cubic axes that is approximately equal around both $\mathbf{x}'$ and $\mathbf{z}'$ ($\sim 0.44^\circ$), which we see from the θ_1 column in the first two rows and the θ_2 column in the second two rows. This could also be described as a rotation of $\sim 5.47^\circ$ about the $\mathbf{b}$ vector and a rotation of $\sim 0.62^\circ$ about the $\mathbf{c}$ vector.

Compared to structures 11 and 12 which were of similar character, the octahedra in the present structure are more symmetrical in the $\mathbf{ac}$ plane of the cell and favour a slightly weaker overall tilt (in addition to a rotation about the $\mathbf{b}$ vector) around just one of the short lattice vectors, such that the octahedra tilt over on an edge instead of a vertex. The marginally lower energy of this system compared to 11 and 12 suggests

Table 4.4.9: The octahedral tilt and distortion around titanium atom T_1 in structure 14. The octahedral volume was $9.9763\,\text{Å}^3$ which is 1.0083 of the ideal cubic equivalent.

Stick	θ (°)	θ_1 (°)	θ_2 (°)	length l (Å)	l/l_0
$s_{x'}$	5.4764	−0.4382	5.4592	3.9109	1.0025
$s_{y'}$	0.6364	−0.4551	0.4446	3.9140	1.0033
$s_{z'}$	5.4781	−5.4601	0.4488	3.9105	1.0024

that there may be a very small energetic advantage to this type of distortion.

The internal angles of the octahedra have all relaxed slightly, we see that s_β is $89.98°$ for all octahedra and s_α and s_γ are $90.05°$ and $90.06°$ in either combination, depending on the octahedron in question.

Dipole (per formula unit): $0.517\,\text{D}$, of which the strontium dipoles contribute $0.223\,\text{D}$ and titanium dipoles contribute $0.295\,\text{D}$ which have an overall angular separation of $2.5°$ from one another. We see antiferroelectricity in both titanium and strontium, though it appears weaker in the strontium. The titanium-titanium dipole angles are $0°$ or $6.8°$ and strontium-strontium dipole angles are $0°$ or $1.7°$. The overall dipole acts in approximately equal measure in all three pseudo-cubic axis: $-0.330\mathbf{x}' - 0.237\mathbf{y}' - 0.320\mathbf{z}'$. The antiferroelectric component acts in the direction of the $\mathbf{b}$ vector or in the $\mathbf{x}'\mathbf{z}'$ plane, perpendicular to the ferroelectric component of the dipole, see figure 4.4.9.

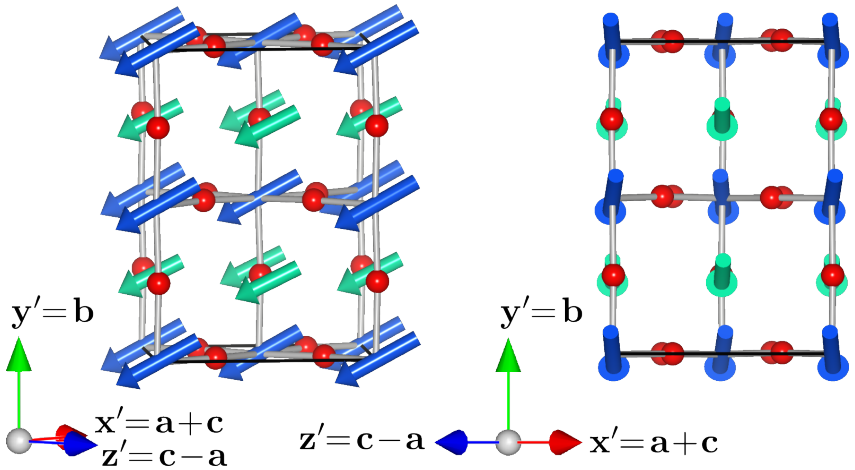

Figure 4.4.9: Representation of the strontium (green) and titanium (blue) dipoles on structure 14. Two different angles are shown, the one on the left most readily shows the overall direction of the dipoles, while the one on the right most readily shows the antiferroelectric dipole component. The bonds have been drawn in grey to make the interpretation of the cell geometry easier.

Imaginary modes: There are no imaginary modes in this structure, which is in the ground state.

4.4.2.7 Structure no. 15 (Cm)

Transitioning: The parent structure was no. 9 and the present structure was obtained by nudging down an equal combination of the degenerate modes no. 59 and 60. The combination did not take the structure into such an energetically favourable configuration as a nudge down just one of the degenerate modes, as was performed in the transition from structure 9 to 13. The transition introduced ferro and antiferroelectric behaviour into the cell.

Nudging the system in both directions at once has caused the cell lengths to stay in the tetragonal setting. A very large distortion (compared to other transitions described so far) in β of 0.1° has pushed the cell into the monoclinic setting. Overall the cell has become shorter and fatter i.e. b has reduced and a and c have increased. Rotations in the octahedra have remained around the $\mathbf{y}'$ axis.

Imaginary modes 59 and 60 from structure 9 were inclined at 52° and 54° to the difference vector, the Γ_{15} (TO2) modes 38 and 39 also played a small rôle, both inclined by 84° to the difference vector.

Experience so far has shown that nudging down j imaginary modes in combination removes all j modes from the system. In this case we are still left with two imaginary modes in structure 15 when three were present in structure 9. We consider the origin of the two remaining imaginary modes at the end of the description of this structure.

Space group: Cm (no. 8) or with a deviation of 11 mÅ $Fmm2$ (no. 42) which is orthorhombic.

Cell definition (Å and degrees): $a = 5.5053$, $b = 7.8243$, $c = 5.5058$;
$\alpha = 90.00$, $\beta = 90.11$, $\gamma = 90.00$;
$a : b : c = 0.9951 : 1 : 0.9952$.

Cell volume: $237.16\,\text{Å}^3$, $V/4V_0 = 0.9988$.

Potential energy (per formula unit): $-39.77945\,\text{eV}$ which is a drop of $0.21\,\text{meV}$, corresponding to $\sim 0.48\,\text{K}$ from the parent structure 9.

Polyhedral distortion: In table 4.4.10 we see that very little has happened to the octahedra in the system. Octahedral rotations increased slightly from the parent and have become less symmetrical according to their stick lengths. s_β has relaxed slightly and has values of 90.01° and 89.98°, while the other two internal octahedral angles remain orthogonal. The distortion of the octahedra is related to the change in the cells β parameter as the cell is otherwise tetragonal.

Dipole (per formula unit): $0.448\,\text{D}$ of which the strontium contributes $0.195\,\text{D}$ and the titanium contributes $0.253\,\text{D}$ acting in the same net direction (mostly in the $\mathbf{z}'$ direction) and with no net component in the $\mathbf{y}'$ direction. We see antiferroelectricity in both the strontium and titanium dipoles. The strontium antiferroelectric component is in the

Table 4.4.10: The octahedral tilt and distortion around titanium atom T_1 in structure 15. The octahedral volume was 9.9730 Å^3 which is 1.0080 of the ideal cubic equivalent.

Stick	θ (°)	θ_1 (°)	θ_2 (°)	length l (Å)	l/l_0
$s_{x'}$	5.5021	0.0000	5.5021	3.9073	1.0016
$s_{y'}$	0.0000	0.0000	0.0000	3.9121	1.0029
$s_{z'}$	5.4836	−5.4836	0.0000	3.9146	1.0035

$\mathbf{y}'$ direction, while the titanium antiferroelectric component is in the $\mathbf{x}'\mathbf{z}'$ plane. Titanium dipoles have an angular separation $0°$ or $8.3°$ from one another while strontium dipoles have a separation of $0°$ or $2.2°$ from one another. The overall dipole direction is $-0.062\mathbf{x}' - 0.444\mathbf{z}'$ ($8°$ from the pure face diagonal along $\mathbf{z}'$).

Imaginary modes: There are two imaginary modes in the present system, 59 with frequency $27.3i$ cm^{-1} and 60 with frequency 28.4 cm^{-1}, see table 4.4.11 and figure 4.4.10. Despite the similarity of the frequencies, they do not appear to be degenerate, based upon their significantly different character.

Table 4.4.11: Eigenvectors for the imaginary modes of structure no. 15. Modes 59 (left) and 60 (right) have frequencies of $27.3i$ cm^{-1} and $28.4i$ cm^{-1} respectively.

Atom	d$\mathbf{x}'$	d$\mathbf{y}'$	d$\mathbf{z}'$
S_1	0.00	0.08	−0.00
S_2	0.00	0.08	−0.00
S_3	−0.00	0.08	0.00
S_4	−0.00	0.08	0.00
T_1	−0.00	0.27	−0.00
T_2	−0.00	0.27	0.00
T_3	−0.00	0.27	−0.00
T_4	−0.00	0.27	0.00
O_1	−0.13	−0.21	0.02
O_2	−0.13	−0.21	0.02
O_3	0.13	−0.21	−0.02
O_4	0.13	−0.21	−0.02
O_5	0.00	−0.19	−0.00
O_6	0.00	−0.09	−0.00
O_7	0.00	−0.09	−0.00
O_8	0.00	−0.19	−0.00
O_9	0.00	−0.22	−0.00
O_{10}	0.00	−0.35	−0.00
O_{11}	0.00	−0.35	−0.00
O_{12}	0.00	−0.22	−0.00

Atom	d$\mathbf{x}'$	d$\mathbf{y}'$	d$\mathbf{z}'$
S_1	0.10	0.00	−0.01
S_2	0.10	0.00	−0.01
S_3	0.10	−0.00	−0.01
S_4	0.10	−0.00	−0.01
T_1	0.25	0.00	0.03
T_2	0.24	0.00	−0.06
T_3	0.25	0.00	0.03
T_4	0.24	0.00	−0.06
O_1	−0.26	−0.00	0.01
O_2	−0.26	−0.00	0.01
O_3	−0.26	−0.00	0.01
O_4	−0.26	−0.00	0.01
O_5	−0.24	−0.00	0.01
O_6	−0.24	−0.00	0.00
O_7	−0.24	−0.00	0.00
O_8	−0.24	−0.00	0.01
O_9	−0.23	−0.00	0.01
O_{10}	−0.24	−0.00	0.01
O_{11}	−0.24	−0.00	0.01
O_{12}	−0.23	−0.00	0.01

In mode 59 we see the eigenvectors have a strong ferroelectric component in the $\mathbf{y}'$ direction, which involves the strontium, titanium and oxygen. We also see a rotation of the octahedra, similar to that observed in figure 4.4.8. The only notable difference is that previously the rotation was hinged on an octahedral edge, whereas in this case it is hinged on a vertex. The rotation is about the $\mathbf{z}'$ pseudo-cubic axis. There are no obvious antiferroelectric components of this eigenvector (if they exist it is in the detail of the oxygen motions).

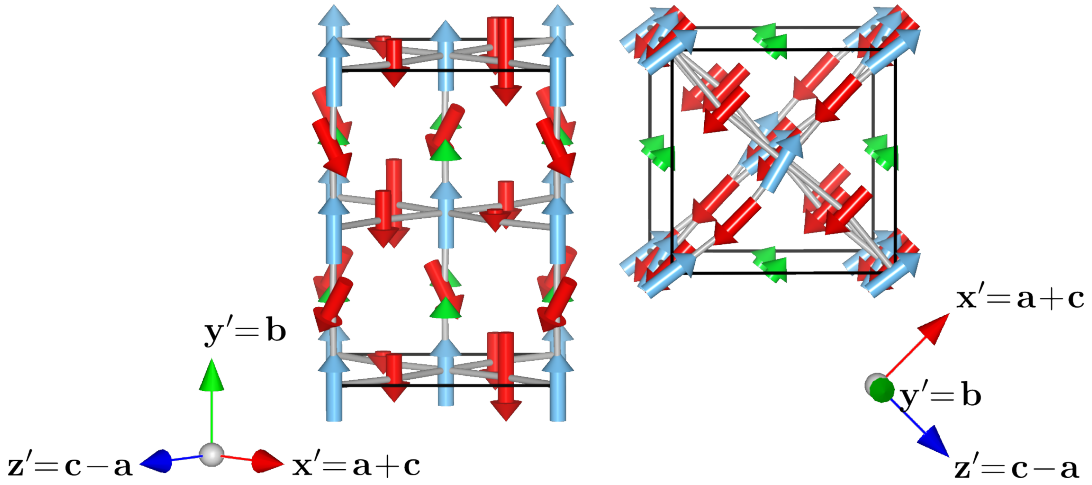

Figure 4.4.10: Graphical representation of the imaginary modes no. 59 (left) and 60 (right) of structure 15. Green, blue and red arrows respectively represent motion of strontium, titanium and oxygen.

In mode 60, the eigenvectors act entirely in the $\mathbf{x}'\mathbf{z}'$ plane. The mode is mostly ferroelectric and there is no significant rotation of the octahedra. Some antiferroelectricity is seen in the titanium.

Mode 59 in the present system is derived mostly from imaginary mode 58 in the parent structure 9 (inclined at 22° to present mode 59), see figure 4.4.5, with a small component from mode 54. Mode 60 is derived in roughly equal measure from imaginary modes 59 and 60 from the parent structure.

4.4.2.8 Structure no. 16 (Cm)

Transitioning: The parent structure was no. 15 and the present structure was obtained by nudging down the eigenvectors of mode no. 59. The ferroelectric transition caused an increase in the net dipole for the cell and introduced a component in the $\mathbf{y}'$ direction. It also caused the octahedra to rock over by about a degree, hinged over a vertex. The cell became taller and thinner (b increased and a and c decreased). The cell lengths still describe a tetragonal system, but the cell angles suggest a monoclinic or triclinic system. *Endeavour*, used to classify the system found it to be of Cm or $P1$ symmetry. With gentle energy gradients, the geometry optimizer may not have found the ideal transition point structure.

Mode 59 of structure 15 ($27.3i\,\mathrm{cm}^{-1}$) was most directly involved in the transition and is inclined at 34° to the difference vector. Several other modes played a minor rôle, the most prominent of which was mode 54 ($41.9\,\mathrm{cm}^{-1}$), inclined at 63° to the difference vector. As the mode hardens, it mixes and becomes part of seven modes with frequencies ranging from 32.0 to $170\,\mathrm{cm}^{-1}$; they will not be listed individually.

Space group: Cm (no. 8) with a deviation of 12 mÅ or $P1$ symmetry with finer tolerances. It should be noted that this structure has the same symmetry group as its parent. At this level it is hard to be certain of the symmetry group and the changes from one structure to another can be subtle.

Cell definition (Å and degrees): $a = 5.5038$, $b = 7.8306$, $c = 5.5040$;
$\alpha = 89.97$, $\beta = 90.08$, $\gamma = 90.03$;
$a : b : c = 0.9940 : 1 : 0.9940$.

Cell volume: 237.21 Å^3, $V/4V_0 = 0.9990$.

Potential energy (per formula unit): -39.77948 eV, which is a drop of 25 μeV from the parent and equivalent to a temperature drop of ~ 0.06 K.

Polyhedral distortion: The octahedra have now rotated, largely around the $\mathbf{z}'$ axis by $\sim 1.1°$, as we can see from the first three columns of data in table 4.4.12. The first column shows the angular separation from the $\mathbf{y}'$ axis, while the second two show that the deviation is mostly towards or away from the $\mathbf{x}'$ axis. This type of rotation is distinct from that of structure 14 (the lowest in energy) which pivoted almost entirely along an edge but is similar to structure 12 which pivoted mostly about a corner but to a slightly lesser extent.

Table 4.4.12: The octahedral tilt and distortion around titanium atom T_1 in structure 16. The octahedral volume was 9.9750 Å^3 which is 1.0082 of the ideal cubic equivalent.

Stick	θ (°)	θ_1 (°)	θ_2 (°)	length l (Å)	l/l_0
$s_{x'}$	5.4849	1.0829	5.3790	3.9069	1.0015
$s_{y'}$	1.1093	0.1657	−1.0969	3.9161	1.0039
$s_{z'}$	5.3741	−5.3717	−0.1632	3.9119	1.0028

The internal angles of the octahedra have distorted remain in two sets, for titanium atoms 1 and 3 the angles are $89.85°$, $90.00°$ and $90.00°$ for s_α, s_β and s_γ respectively. For titanium atoms 2 and 4 they are $89.86°$, $90.01°$ and $89.97°$.

Dipole (per formula unit): 0.490 D of which the strontium contributes 0.210 D titanium contributes 0.281 D, the overall separation of these two is $3°$. The antiferroelectric nature of the crystal appears to have decreased as the angular separation of the dipoles has approximately halved since structure 15 to $4.9°$ for titanium though the strontium-strontium separation has no significant change ($2.3°$). The individual dipole strengths have increased, but not enough to compensate for the decreased angle. The overall dipole in inclined in the direction of the volume diagonal (in the psuedo-cubic context) $-0.072\mathbf{x}' + 0.322\mathbf{y}' - 0.363\mathbf{z}'$.

Imaginary modes: Only one imaginary mode remains in this cell, with a frequency of $23.1i$ cm^{-1} and is represented in table 4.4.13 and figure 4.4.11. In this mode we

see a ferroelectric displacement of ions in the $\mathbf{x}'$ direction. We also see an octahedral rotation about the $\mathbf{x}'$ axis e.g. the octahedron in the centre of the figure shows a counter-clockwise rotation in addition to the ferroelectric displacement.

Table 4.4.13: Eigenvectors for the degenerate imaginary mode 60 of structure no. 16 with a frequency of $23.1i\,\mathrm{cm}^{-1}$.

Atom	$\mathbf{dx}'$	$\mathbf{dy}'$	$\mathbf{dz}'$
S_1	−0.09	0.00	−0.00
S_2	−0.09	0.00	−0.00
S_3	−0.11	0.00	−0.00
S_4	−0.11	0.00	−0.00
T_1	−0.22	−0.01	−0.04
T_2	−0.22	−0.00	0.04
T_3	−0.22	−0.01	−0.04
T_4	−0.22	−0.00	0.04
O_1	0.24	0.00	0.12
O_2	0.24	0.00	0.12
O_3	0.24	0.00	−0.15
O_4	0.24	0.00	−0.15
O_5	0.23	0.14	−0.01
O_6	0.22	0.01	−0.01
O_7	0.22	0.01	−0.01
O_8	0.23	0.14	−0.01
O_9	0.22	−0.13	−0.01
O_{10}	0.22	0.01	−0.01
O_{11}	0.22	0.01	−0.01
O_{12}	0.22	−0.13	−0.01

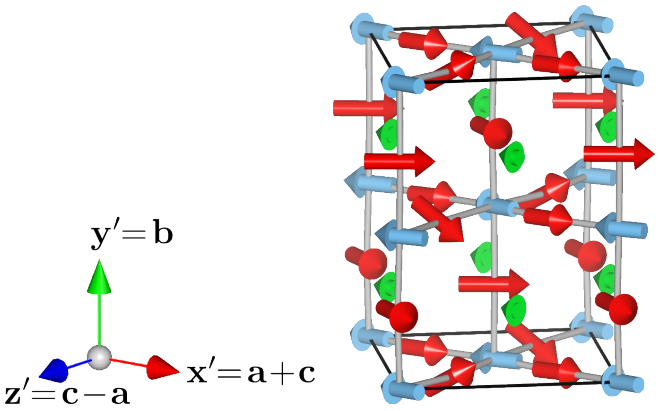

Figure 4.4.11: Graphical representation of the imaginary mode no. 60 of structure 16. Green, blue and red arrows respectively represent motion of strontium, titanium and oxygen.

4.4.2.9 Structure no. 17 (Cc or $P1$)

Transitioning: The parent structure was no. 16 and the present structure was obtained by nudging down the only remaining imaginary mode no. 60. The ferroelectric transition resulted in an increase in the cell dipole moment and caused a rotation of the octahedra about the $\mathbf{x}'$, evening up the tilt/rock of the $s_{y'}$ stick towards the $\mathbf{x}'$ and the $\mathbf{y}'$. The transition was accompanied by a shortening and fattening of the cell with a net

increase of volume. The cell angles, at least two of which deviate from $90°$ significantly in the context of distortions in STO, suggest the lattice may be triclinic.

Mode 60 from structure 16 was inclined at $43°$ to the difference vector, several other real modes were involved in the transition also. The mode hardens and contributes to various real modes with frequencies from $28.0\,\mathrm{cm}^{-1}$ to $169.7\,\mathrm{cm}^{-1}$.

Space group: Cc (no. 9) with a deviation of $21\,\mathrm{m\AA}$ or $P1$ for lower deviations from the ideal*.

Cell definition (Å and degrees): $a = 5.5066$, $b = 7.8253$, $c = 5.5070$;
$\alpha = 89.93$, $\beta = 89.95$, $\gamma = 89.99$;
$a : b : c = 0.9952 : 1 : 0.9952$.

Cell volume: $237.30\,\mathrm{\AA}^3$, $V/4V_0 = 0.9994$.

Potential energy (per formula unit): $-39.77950\,\mathrm{eV}$, a drop of $27\,\mu\mathrm{eV}$ from the parent structure no. 16 and equivalent to a drop of $\sim 0.06\,\mathrm{K}$.

Polyhedral distortion: We see from table 4.4.14 that the rotation about the $\mathbf{y}'$ axis has now decreased slightly from $\sim 5.5°$ to $\sim 5.3°$. We also see that $\theta_{x'_{xy}}$ and $\theta_{y'_{yz}}$ (first two rows of 2^{nd} data column) are much closer to equality, indicating that the octahedra are now much closer to, being hinged on an edge than a vertex as they roll over (as in structure 14).

Table 4.4.14: The octahedral tilt and distortion around titanium atom T_1 in structure 17. The octahedral volume was $9.9775\,\mathrm{\AA}^3$ which is 1.0085 of the ideal cubic equivalent.

Stick	θ (°)	θ_1 (°)	θ_2 (°)	length l (Å)	l/l_0
$s_{x'}$	5.2748	0.9420	5.1916	3.9121	1.0028
$s_{y'}$	1.6847	1.3858	−0.9582	3.9143	1.0034
$s_{z'}$	5.3673	−5.1942	−1.3647	3.9094	1.0022

The internal angles of the octahedra are $89.85°$, $90.02°$ and $89.83°$ for s_α, s_β and s_γ respectively for titanium atoms 1 and 3 and $89.90°$, $90.02°$ and $89.80°$ for atoms 2 and 4.

Dipole (per formula unit): $0.561\,\mathrm{D}$ of which $0.246\,\mathrm{D}$ comes from the strontium dipoles and $0.316\,\mathrm{D}$ comes from the titanium dipoles, which are separated by an angle of $2°$. This structure has the strongest dipole moment of all the tetragonal ancestor systems (some of the cubic and orthorhombic ancestor systems have some stronger dipole moments). The antiferroelectric effect of the dipoles has increased from the previous structure with titanium-titanium dipoles deviating by $5.2°$ and strontium-strontium dipoles by $4.7°$. The overall dipole is in the direction $-0.380\mathbf{x}' + 0.299\mathbf{y}' - 0.285\mathbf{z}'$.

*It was necessary to adjust the n-fold axes tolerance parameter in *Endeavour* to get the non-$P1$ result.

Imaginary modes: There are no remaining imaginary modes in this system.

4.4.2.10 Structure no. 18 (Cm)

Transitioning: The parent structure was no. 15; the present structure was obtained by nudging down imaginary mode 60. The ferroelectric transition resulted in a stretching of the cell's a parameter and a slight shortening of the c parameter. Considering only the cell lengths, the transition was from tetragonal to orthorhombic. However, the non-$90°$ β angle present in both systems means that both parent and child systems are monoclinic. The transition had almost no effect on the octahedra.

Mode 60 ($28.4i\,\mathrm{cm}^{-1}$) from structure 15 is inclined at $31°$ to the difference vector, while modes 52 ($98.6\,\mathrm{cm}^{-1}$) and 39 ($160.5\,\mathrm{cm}^{-1}$) are also implicated in the transition. Mode 60 hardens most directly to mode 53 with frequency $92.2\,\mathrm{cm}^{-1}$ (modes are inclined at $21°$ to one another).

Space group: Cm (no. 8) with a deviation of $1\,\mathrm{mÅ}$.

Cell definition (Å and degrees): $a = 5.5071$, $b = 7.8241$, $c = 5.5048$;
$\alpha = 90.00$, $\beta = 89.95$, $\gamma = 90.00$;
$a : b : c = 0.9954 : 1 : 0.9950$.

Cell volume: $237.19\,\mathrm{Å}^3$, $V/4V_0 = 0.9989$.

Potential energy (per formula unit): $-39.77950\,\mathrm{eV}$, which is a drop of $45\,\mu\mathrm{eV}$ or $\sim 0.10\,\mathrm{K}$ from parent structure 15.

Polyhedral distortion: We note a slightly unusual octahedral distortion in table 4.4.15 in that though the distortion was mostly ferroelectric along $\mathbf{x}'$ resulting in an increase in the $l_{x'}$ parameter; we also see a very small component of rotation, not in the $\mathbf{x}'\mathbf{z}'$ plane. So far we have either seen no out-of-plane rotation or an out-of-plane rotation $\gtrsim 0.1°$, the very small component present in this system is as a consequence of some noise included in the eigenvector used to nudge system 15 into 18, the main component of the motion in the eigenvector was expressed in the $\mathbf{x}'\mathbf{z}'$ plane.

Table 4.4.15: The octahedral tilt and distortion around titanium atom T_1 in structure 18. The octahedral volume was $9.9748\,\mathrm{Å}^3$ which is 1.0082 of the ideal cubic equivalent.

Stick	θ (°)	θ_1 (°)	θ_2 (°)	length l (Å)	l/l_0
$s_{x'}$	5.5048	0.0070	5.5048	3.9128	1.0030
$s_{y'}$	0.0077	−0.0028	−0.0071	3.9120	1.0028
$s_{z'}$	5.5119	−5.5119	0.0029	3.9099	1.0023

The internal angles of the octahedra have a minimal distortion in the present structure and only s_β varies from orthogonality. For titanium atoms 1 and 3 s_β is $90.03°$ and for 2 and 4 s_β is $90.02°$.

Dipole (per formula unit): 0.478 D of which the strontium contributes 0.207 D and the titanium contributes 0.271 D acting in the same net direction. The dipole has strengthened since structure 15 and now acts in the $0.394\mathbf{x}' + 0.004\mathbf{y}' - 0.271\mathbf{z}'$ direction. In the present system, the angular separation of titanium-titanium dipoles is unchanged at $8.3°$ while the antiferroelectric effect involving strontium has almost disappeared, as these dipoles are only separated by $0.8°$.

Imaginary modes: One imaginary mode remains in the present structure. Mode 60 has a frequency of $22.3i$ cm^{-1} and is mostly ferroelectric in the $\mathbf{y}'$ direction. It also displays a tilting/rocking component about $\mathbf{x}' - \mathbf{z}'$ (the $\mathbf{b}$ vector) which involves a hinging along an octahedral edge, see table 4.4.16 and figure 4.4.12. In the figure, we see a counter clockwise rotation of the central octahedron; this type of distortion competes with the ferroelectric motion of the ions.

Table 4.4.16: Eigenvectors for the degenerate imaginary mode 60 of structure no. 18 with a frequency of $22.3i$ cm^{-1}.

Atom	d$\mathbf{x}'$	d$\mathbf{y}'$	d$\mathbf{z}'$
S_1	-0.00	0.08	-0.00
S_2	-0.00	0.08	-0.00
S_3	0.01	0.08	0.01
S_4	0.01	0.08	0.01
T_1	0.00	0.26	0.00
T_2	0.00	0.26	0.00
T_3	0.00	0.26	0.00
T_4	0.00	0.26	0.00
O_1	-0.09	-0.20	-0.13
O_2	-0.09	-0.20	-0.13
O_3	0.09	-0.20	0.13
O_4	0.09	-0.20	0.13
O_5	0.00	-0.33	0.00
O_6	0.00	-0.11	0.00
O_7	0.00	-0.11	0.00
O_8	0.00	-0.33	0.00
O_9	0.00	-0.08	0.00
O_{10}	0.00	-0.29	0.00
O_{11}	0.00	-0.29	0.00
O_{12}	0.00	-0.08	0.00

The motion in the eigenvector is similar to mode 60 of structure 13, shown in figure 4.4.8 on page 151. The character of the present mode is derived from real modes 54 and 55 and the imaginary mode 59 from structure 15 (frequencies are 41.9, 36.9 and $27.3i$ cm^{-1} respectively). The strongest component was from the imaginary mode and was inclined to it with an angle of $25°$.

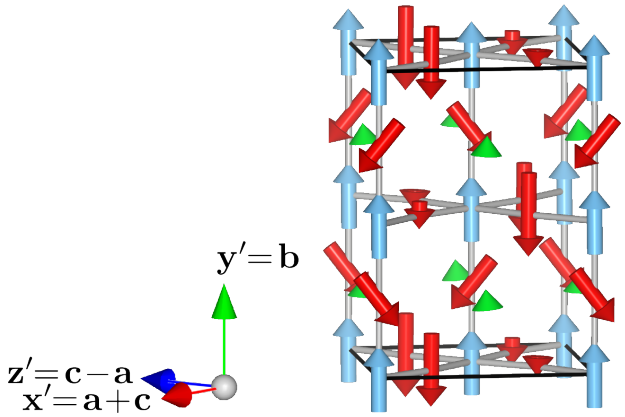

Figure 4.4.12: Graphical representation of the imaginary mode no. 60 of structure 18. Green, blue and red arrows respectively represent motion of strontium, titanium and oxygen.

4.4.2.11 Structure no. 19 (Cc or $P1$)

Transitioning: The parent structure was no. 18 and the present structure was obtained by nudging it the direction of the eigenvectors of the imaginary mode no. 60 ($22.3i\,\mathrm{cm}^{-1}$). During the ferroelectric transition the structure's symmetry may have disappeared or remained as monoclinic depending on what tolerances are chosen (see below). The new component of the dipole was in the $\mathbf{y}'$ direction and accordingly we see a expansion of b and a contraction in a. The c parameter stayed the same, which was probably due to a balance between the contraction driven by the ferroelectric shift and the rocking over of the octahedra in the direction of c by about $1.4°$.

Imaginary mode 60 was inclined to the difference vector by $38°$, though various other modes were involved in the transition, the most important of which was real mode 55, which had a frequency of $41.9\,\mathrm{cm}^{-1}$ and was inclined to the difference vector by $63°$.

Mode 60 in the parent structure, hardened and became part of six other modes with frequencies ranging from 29.5 to $169.5\,\mathrm{cm}^{-1}$. The mode most directly contributed towards was mode 57, which was the softest real mode, with a frequency of $29.5\,\mathrm{cm}^{-1}$.

Space group: Cc (no. 9) with a deviation of $15\,\mathrm{mÅ}$ or $P1$ symmetry with smaller tolerances*.

Cell definition (Å and degrees): $a = 5.5059, b = 7.8274, c = 5.5052;$
$\alpha = 90.01, \beta = 89.97, \gamma = 90.05;$
$a : b : c = 0.9948 : 1 : 0.9947.$

Cell volume: $237.26\,\mathrm{Å}^3$, $V/4V_0 = 0.9992$.

*It was necessary to adjust the n-fold axes tolerance parameter in *Endeavour* to get the non-$P1$ result.

Potential energy (per formula unit): -39.77951 eV, a drop of 17 μeV, corresponding to ~ 0.04 K from the parent structure 18.

Polyhedral distortion: In table 4.4.17 we see a polyhedral distortion similar to that of structure 17, which is on a parallel branch on the dendrimer plot to the present structure. Since structure 18, the rotation about the $\mathbf{y}'$ axis has decreased by $\sim 0.15°$ and the octahedra have rocked over by about a degree, hinging on an edge (approximately around the $\mathbf{a}$ cell vector). The cell length b has lengthened, which is most likely associated with the ferroelectric transition in this direction and the length a has shortened to even up with c. The shortening of a would most likely be associated with the increase of b, while the lack of change in c is most likely due to competition with the rocking of the octahedra encouraging the cell to expand in this direction and the increase in b.

Mode 60 from structure 18 is inclined at $38°$ to the difference vector. Mode 55 (frequency of $41.9\,\mathrm{cm}^{-1}$) also plays an important part, inclined to the difference vector at $63°$, a few other modes played a more minor rôle in the transition. Mode 60 hardened from $22.3i\,\mathrm{cm}^{-1}$ to a spread of other modes ranging in frequency from $29.5\,\mathrm{cm}^{-1}$ (mode 57) to $169.5\,\mathrm{cm}^{-1}$ (mode 37); the most significant contribution was to mode 57 though as the two modes were inclined at $49°$ to one another.

Table 4.4.17: The octahedral tilt and distortion around titanium atom T_1 in structure 19. The octahedral volume was $9.9763\,\text{Å}^3$ which is 1.0083 of the ideal cubic equivalent.

Stick	θ (°)	θ_1 (°)	θ_2 (°)	length l (Å)	l/l_0
$s_{x'}$	5.3586	0.7873	5.3015	3.9111	1.0026
$s_{y'}$	1.3598	−1.0992	−0.8007	3.9148	1.0035
$s_{z'}$	5.4108	−5.3036	1.0820	3.9094	1.0022

Examining the internal angles of the octahedra we see that s_β is $90°$ for all octahedra, indicating that the $s_{x'}$ and $s_{z'}$ sticks remain orthogonal. We also see a $0.1°$ to $0.15°$ deviation of both s_α and s_γ from orthogonality and so the $s_{y'}$ stick has twisted over slightly.

Dipole (per formula unit): 0.532 D of which the strontium contributes 0.231 D and the titanium contributes 0.301 D. These contributions are inclined at $2.4°$ from one another. The titanium-titanium dipoles are inclined at $5.4°$ to one another, which is a substantial decrease in the antiferroelectric contribution. Strontium-strontium dipoles are inclined at $4.3°$ to one another, which is an increase in the antiferroelectric contribution. The overall dipole direction is $0.346\mathbf{x}' + 0.294\mathbf{y}' - 0.276\mathbf{z}'$

Imaginary modes: There are no imaginary modes for this structure.

Now that we have considered the changes in each structure, we will look at the frequency data gathered in a more general way.

4.4.3 Frequency Analysis

In table 4.4.18 we provide as a reference to the material in the previous section, a listing of all of the frequencies for the 11 structures in the tetragonal ancestor dendrimer tree 9–19. Additionally, the frequencies for a system with $Pm\bar{3}m$ cubic symmetry, factored into a tetragonal-like 20 atom unit cell have been included for comparison. Identifying and labelling the irreducible representations of normal modes is quite involved in general. For the cubic system, we labelled the modes according to the works by Wahl et al. [44]. These modes have been marked on the table, but most directly refer to the $Pm\bar{3}m$ symmetry system and indirectly refer to the lower symmetry systems. The remaining modes are unidentified but the degenerate modes (with $Pm\bar{3}m$ symmetry) have been identified with blocks of consecutive $+$ and $-$ signs.

Appendix C.3 (page 250) contains a comparison of the sets of frequencies for all 11 of the structures that evolved from the $I4/mcm$ system. In the analysis presented there, we will see some confirmation of the similarity of the end point structures (with the exception of no. 12) but also find that the distinctiveness of pairings of structures is on a sliding scale, unlike the cubic ancestor structures where a discontinuity demonstrated a clear distinction between similar and dissimilar.

Table 4.4.18: Full frequency listing (in cm^{-1}) of the tetragonal $I4/mcm$ ancestor structures. The frequencies for the cubic $Pm\bar{3}m$ system, factored into the tetragonal unit cell have also been included here. Blocks of $-$ and $+$ indicate degenerate modes, we discuss the symmetry labelling in more detail in the text.

Freq. no.	Label	Structure number											
		$Pm\bar{3}m$	9	10	11	12	13	14	15	16	17	18	19
1	$-$	829.9	816.7	818.3	818.7	818.6	818.6	818.7	818.4	818.6	818.8	818.5	818.8
2	$+$	795.9	782.5	783.7	785.8	785.3	786.0	785.5	785.4	784.9	785.7	785.7	785.5
3	$-$	747.3	735.4	742.2	737.7	738.7	736.1	738.7	736.2	740.8	740.0	736.1	740.0
4	Γ_{15} (TO3)	533.2	529.5	530.7	534.1	529.1	535.5	531.4	529.7	529.9	532.1	533.0	529.6
5	Γ_{15} (TO3)	533.2	525.5	526.1	529.2	528.7	529.7	529.6	529.3	526.9	529.2	529.6	529.3
6	Γ_{15} (TO3)	533.1	521.7	523.0	528.5	527.5	529.7	527.9	528.9	526.8	528.6	529.0	527.7
7	$+$	528.1	521.7	523.0	527.5	527.5	526.6	527.2	526.5	523.1	526.6	526.5	526.4
8	$-$	505.5	498.6	499.8	524.4	523.5	524.3	524.2	523.1	522.1	524.7	523.9	524.4
9	$-$	505.1	495.8	497.4	507.3	505.6	508.3	503.9	507.7	503.9	506.0	507.0	502.9
10	$-$	505.1	495.8	497.4	501.5	502.3	501.8	500.7	503.7	501.7	501.6	501.9	500.7
11	$+$	473.8	471.5	494.8	498.9	496.3	499.0	498.8	494.8	495.5	498.6	497.8	498.6
12	$+$	473.8	465.9	473.9	488.2	484.5	482.0	491.6	468.3	486.2	495.5	479.0	494.8
13	$-$	470.7	465.9	466.1	464.7	465.7	464.4	464.6	466.8	466.4	464.7	464.8	464.8
14	$-$	470.7	463.3	466.1	456.1	457.5	454.2	457.6	454.6	460.3	459.5	454.4	459.4
15	$+$	465.6	455.4	461.6	454.4	454.8	454.1	454.6	453.8	455.2	454.7	453.9	454.9
16	$-$	452.6	451.7	455.9	441.1	444.5	440.0	443.2	443.1	448.6	442.6	441.6	444.6
17	$+$	430.2	428.0	428.3	428.9	428.9	428.9	428.6	429.0	429.0	429.3	428.9	429.0
18	$+$	430.2	428.0	428.3	427.7	427.7	427.4	427.9	427.8	427.5	427.7	427.9	427.7
19	$+$	429.4	427.2	427.4	425.9	426.6	425.9	426.5	427.2	427.3	425.8	426.0	426.1
20	$-$	424.9	427.2	426.6	423.1	424.4	423.6	423.2	424.9	424.9	422.5	423.4	423.1
21	$-$	424.9	426.7	426.6	407.2	411.3	411.7	404.0	423.6	411.6	403.8	415.0	404.7
22	$-$	424.8	423.6	399.3	399.2	398.3	398.9	402.1	397.5	397.3	398.1	399.0	399.8
23	$+$	317.3	332.7	332.5	332.8	333.1	332.9	332.9	333.5	332.7	332.1	333.3	332.4
24	$+$	317.3	332.7	332.5	332.5	332.4	332.7	332.6	332.5	332.0	331.7	332.8	332.1
25	$-$	311.0	309.3	309.1	310.0	309.8	310.2	309.8	309.6	309.3	309.8	310.1	309.6
26	$-$	311.0	309.3	309.1	308.8	308.9	306.8	308.8	309.1	309.2	309.7	308.5	309.4
27	$+$	274.6	289.0	288.9	289.9	289.9	289.6	289.7	289.6	289.7	290.3	289.7	290.0
28	$-$	272.9	280.0	278.5	279.2	279.1	279.7	279.1	279.9	278.5	278.5	279.8	278.7
29	$+$	258.5	261.2	261.5	262.5	262.8	263.1	262.5	263.4	262.2	262.3	263.1	261.9
30	$+$	258.5	261.2	261.5	260.9	260.6	259.0	261.1	260.3	260.7	261.1	260.6	261.4
31	Γ_{25}	228.5	253.2	254.7	256.0	255.9	255.3	255.7	255.0	256.1	257.3	255.4	256.6
32	Γ_{25}	228.5	243.2	244.3	246.9	246.1	247.1	246.8	245.4	245.1	246.4	246.8	246.3
33	Γ_{25}	227.8	243.2	244.3	243.5	244.3	242.2	244.1	244.3	244.5	243.3	243.7	243.7
34	$-$	163.7	183.5	183.4	195.2	193.7	195.9	193.9	195.5	190.9	194.1	195.3	192.7
35	$-$	163.7	177.9	178.6	184.4	182.0	184.6	183.7	181.0	180.4	183.6	183.6	183.1
36	$-$	163.2	177.9	178.6	176.6	177.4	176.9	176.9	178.0	177.4	175.9	177.3	176.4
37	Γ_{15} (TO2)	156.8	166.5	170.6	168.9	169.5	168.5	169.3	171.6	170.1	169.7	169.0	169.5
38	Γ_{15} (TO2)	156.7	159.3	160.2	168.0	168.2	167.8	166.5	167.6	166.9	168.0	167.7	166.7
39	Γ_{15} (TO2)	156.7	159.3	160.2	165.1	161.6	165.5	164.5	160.5	160.8	164.2	163.5	163.7
40	$+$	129.1	141.0	140.6	141.4	141.4	140.9	141.1	141.2	141.6	142.1	141.1	141.8
41	$+$	129.1	136.5	136.7	137.1	136.9	136.5	136.9	140.0	136.9	138.4	136.7	138.0
42	$+$	129.0	136.5	136.7	136.3	136.4	136.1	136.2	136.9	136.3	134.7	136.5	135.2
43	$-$	111.2	123.0	127.6	135.9	136.1	135.6	132.5	136.0	132.4	134.7	136.2	132.3
44	$+$	108.8	111.0	126.2	127.5	122.1	128.3	125.8	121.3	125.3	124.9	123.1	123.5
45	$+$	108.8	111.0	112.9	120.7	117.7	120.7	122.0	113.6	123.1	124.0	121.8	123.0
46	$-$	106.4	105.7	112.9	113.9	117.4	108.0	118.4	107.0	114.5	120.5	107.1	121.5
47	$-$	106.4	105.7	105.9	108.4	108.1	107.0	107.8	106.9	108.6	110.2	107.0	109.4
48	$+$	102.1	105.1	105.9	106.9	106.7	106.8	106.8	106.4	106.5	107.2	106.4	106.9
49	$+$	102.1	102.7	105.1	105.3	105.9	106.0	105.2	105.7	106.1	105.8	105.9	105.4
50	$-$	101.5	99.4	102.4	104.6	103.8	103.8	104.6	104.0	103.5	104.5	103.8	104.3
51	$+$	13.1	91.1	94.2	102.9	101.1	103.7	102.7	99.1	98.8	102.4	103.1	102.2
52		0.2	91.1	94.2	92.8	93.9	93.3	93.7	98.6	94.3	94.4	93.8	92.3
53		0.2	39.1	87.6	91.9	93.1	92.1	89.4	95.1	91.2	90.9	92.2	90.4
54		0.2	39.1	39.2	71.1	66.7	69.5	68.0	41.9	77.2	81.4	58.1	75.6
55	Γ_{15} (TO1)	$67.2i$	0.8	39.2	57.3	42.9	39.4	64.3	36.9	41.0	65.4	41.9	61.4
56	Γ_{15} (TO1)	$67.2i$	$0.1i$	0.2	39.0	30.5	36.2	38.7	1.1	32.0	37.2	39.5	37.3
57	Γ_{15} (TO1)	$68.7i$	$0.1i$	0.2	23.1	26.9	0.2	30.3	0.4	1.2	28.0	0.5	29.5
58	$-$	$79.6i$	$56.6i$	$0.5i$	$0.2i$	$0.3i$	$0.6i$	$0.3i$	$0.3i$	$0.5i$	$0.2i$	$0.3i$	$0.4i$
59	$-$	$79.6i$	$58.9i$	$42.2i$	$0.2i$	$0.4i$	$1.9i$	$0.4i$	$27.3i$	$0.5i$	$0.4i$	$0.5i$	$0.6i$
60	$-$	$79.6i$	$58.9i$	$42.2i$	$0.8i$	$0.6i$	$23.2i$	$0.6i$	$28.4i$	$23.1i$	$0.7i$	$22.3i$	$0.7i$

4.4.4 Summary of Tetragonal Ancestor Systems

We now consider and draw conclusions from all the results presented in this section on the tetragonal ancestor systems. The ionic motion associated with the most significant change in energy was the octahedral rotation, resulting in the cubic (1) to tetragonal (9) transition. The motion resulted in a change of energy of 7.03 meV.

The 20 atom unit cell, used in this set of calculations allowed many more possible distortions than in the cubic unit cell. We saw these changes, resulting in the detection of several saddle point structures. There were two main types of ionic motion that lead to lower energy structures. Ferroelectric distortions along all three pseudo-cubic axes and octahedral rotations that could occur about all of the pseudo-cubic axis (and combinations).

Considering the ferroelectric displacements first, we notice one new feature of the tetragonal ancestor systems is the presence of antiferroelectric flavouring of ferroelectric displacements. The antiferroelectric behaviour appears to happen due to the displacement of a cation, within its polyhedron, generating a dipole (which is ferroelectric on its own) and the rotation of the polyhedron, where neighbouring polyhedra rotate in opposing directions. The nature of the dipole for an individual polyhedron is probably augmented slightly by the interaction with other rotating polyhedra/dipoles. The antiferroelectric effect acts mostly in the $\mathbf{x}'\mathbf{z}'$ plane. We also saw that the overall dipole strength was slightly weaker in the tetragonal ancestor systems than in the cubic ancestor systems. The non-alignment of the individual dipoles due to the antiferroelectricity would be a first suspect but in fact the individual dipole strengths are significantly weaker. Comparing a single strontium and titanium dipole from the lowest energy cubic ancestor structure no. 8 and the lowest energy tetragonal ancestor structure no. 14, we find that a structure 14 strontium dipole is $\sim 27\,\%$ weaker and a titanium dipole is $\sim 14\,\%$ weaker. The reduction in dipole strength may occur as a consequence of antiferroelectric motion as the cations no longer shift in the position most directly in between oxygen ions in the polyhedra, but instead move slightly to one side. The sideways motion would restrict ionic displacment.

Rotations were expressed most strongly around the $\mathbf{y}'$ axis ($\sim 5.45^\circ$). However, this is unsurprising as the starting structure was set up in this configuration and there is an energy barrier to change the main axis of rotation. We found that the octahedra were inclined to rock over no more than 1°, when rotating about one of the $\mathbf{x}'$ or $\mathbf{z}'$ axes, but that the lowest energy configuration appeared to be a hinging on an octahedral edge (rotation around the $\mathbf{a}$ or $\mathbf{c}$ vector), by $\sim 0.6^\circ$. These different sets of ionic motions could occur in many, possibly all combinations.

From the cubic ancestor systems we noted that a ferroelectric transition would cause an elongation of the cell in the direction of the shift, along with a narrowing of

the cell in the other directions. Also that a ferroelectric shift in between lattice vectors will tend to reduce the angle between the vectors. This effects are still observed in the larger unit cell. However, we also observe the following competing processes. An antiferroelectric ionic motion, which has been observed to occur at right angles to the ferroelectric displacements, will cause an expansion or compete with the narrowing of the cell in that direction.

We only have one clear example of rotation about the $\mathbf{b}$ vector ($\mathbf{y}'$ axis), which was in the cubic to tetragonal transition, in this case we saw a thinning and lengthening of the cell. With no other ferroelectric factors to consider in the transition, the explanation will be the octahedral rotation making the cell more efficiently packed in the $\mathbf{ac}$ plane driving the thinning of the cell, but then the increased closeness of the cations driving an expansion in the $\mathbf{b}$ direction. With regard to the less dominant rocking over of the octahedra (hinged on an edge), we found that this would drive an expansion, in the cell one direction (an expansion of a if the rocking was about the $\mathbf{c}$ vector or an expansion of c if the rocking was about the $\mathbf{a}$ vector). Unfortunately, because all of the rocking (rotation not about the $\mathbf{b}$ vector) modes were mixed with ferroelectric motion, it is not straightforward to make comments based on the data about changes to the other cell lengths due to a edge hinged rock or about changes to cell lengths due to vertex based hinging.

The results of the calculations presented in this section have shown the first examples of unequal (orthorhombic-like) a and c cell parameters. As has been alluded to above, the causes of this are the antiferroelectric behaviour and the rocking of octahedra (rotation about $\mathbf{b}$ only causes tetragonal distortions).

From the results, the lowest energy system in this thesis (no. 14, barring the supercell no. 38) is a monoclinic cell with non-equivalent lattice parameters $a = 5.5043\,\text{Å}$, $b = 7.8274\,\text{Å}$, $c = 5.5063\,\text{Å}$, $\alpha = 90.02°$, $\beta = 89.99°$ and $\gamma = 90.00°$. The octahedra rotate about the $\mathbf{b}$ vector by $5.47°$ and about the c vector by $\sim 0.6°$. A dipole induced by the ferroelectric motion of the cations points approximately in the direction of an octahedral face (in the $-\mathbf{b} - \mathbf{c}$ direction). There is additionally an angular separation of the neighbouring titanium dipoles of $\pm 3.4°$ about the $\mathbf{b}$ axis.

An interesting observation of all of the tetragonal ancestor structures is that they have densities equal to or less than that of the ideal cubic structure but the octahedral volumes are all greater than those of the ideal cubic (shown in the figure captions of every octahedral rotation description table). In the experimental/theoretical paper by Hayward and Salje [8], which we used as a source of Landau theory fitting in chapter 3, they propose a model in which octahedral volume increases and cuboctahedral volume decreases in conjunction with the rotation. Our results would appear to be in agreement with theirs.

In further comparison with experiment, we may consider the data in table 3.4.2 on page 91. Additionally, not included on this table are the experimental orthorhombic distortions determined by Lytle [23] which are $0.9998 : 1 : 1.0002$, taken at ~ 40 K. Although the present cell is monoclinic, the angular distortions are sufficiently small that it is reasonable to compare the system cell with an orthorhombic description. Some remapping of cell parameters is required for a comparison here, i.e. expressing the parameters in the present work as: $a : c : b = 0.9996 : 1 : 1.0052$. Interpreting the lattice parameters from the paper is not straightforward but it appears that values are: $a = 5.5122$ Å, $b = 7.7984$ Å and $c = 5.5132$ Å. If the lattice parameters are correct then the PBEsol code overestimates the length of the b parameter by $0.37\,\%$ and underestimates the a and c parameters by $0.14\,\%$. The magnitude of the orthorhombic distortion in the present calculations is somewhat greater than these experimental data. We might, however expect some descrepencies due to thermal effects.

The octahedral rotations also deviate from experiment significantly, though there is no data for orthorhombic or monoclinic octahedral rotations.

We see the most significant change in the drop in the potential energy in the transition between the cubic and the tetragonal system. The drop which is attributed to the octahedral rotation was of 7.04 meV, which correlates to a temperature drop of ~ 16.3 K or an absolute temperature of ~ 88.7 K assuming that the cubic structure occurs at 105 K. The subsequent rotations and ferroelectric shifts taking the system to the ground state resulted in about half the drop of energy (0.29 meV) as in the case of the cubic ancestor systems (0.64 meV). However, if we compare with the tetragonal structure (2) in the cubic ancestor systems (which drop by 0.15 meV before reaching the lowest energy state), the tetragonal ancestor systems undergo around twice the energy drop. We, can therefore conclude that, even after the initial rotation about the axis, the subsequent rotations offer an approximately equal energetic advantage as the ferroelectric shifts (in fact they may be greater as the dipoles generated in the tetragonal ancestor systems were weaker than in the cubic ancestor systems).

Most of the phase transitions described in this section are energetically insignificant, usually relating to small fractions of a kelvin. It is therefore unlikely that the different phases will actually be observed experimentally. It is not the intention of this work to produce accurate phase transition predictions and generate phase diagrams; we include comparisons with temperature as an approximate guide.

We also note, however that the lowest energy structure discovered here, which is believed to be at the ground state has an energy difference from the cubic structure, equivalent to ~ 17 K (the cubic is known experimentally to exist at a minimum temperature of 105 K). Based upon a Landau theory model, the expected temperature of phase transitions is highly dependent on the free energy landscape, of which potential

energy is only a component. Further information on relationships between temperature and phase stability is given in [48].

Having considered the tetragonal ancestor systems, we now consider the set of structures starting from a cell with initial orthorhombic symmetry.

4.5 Orthorhombic Unit Cell

4.5.1 Introduction

We now consider the orthorhombic ancestor systems. The geometry optimized starting cell with atom labels can be seen in figure 4.5.1, though we note that the cell is in essence the same as the tetragonal cell, with small variations of atomic positions. The symmetry-finding software considered that allowing for tolerances, both the $Pnma$ and the $Imma$ space groups were matches for the structure. An astute reader may notice the subtle difference in the configuration of the cell in figure 4.5.1, compared to the tetragonal cell in figure 4.4.1. The present cell has a rotation almost entirely about the **a** vector (what had previously been described as *rocking*, hinging on an edge); the $I4/mcm$ cell had its rotation almost entirely about the **b** vector.

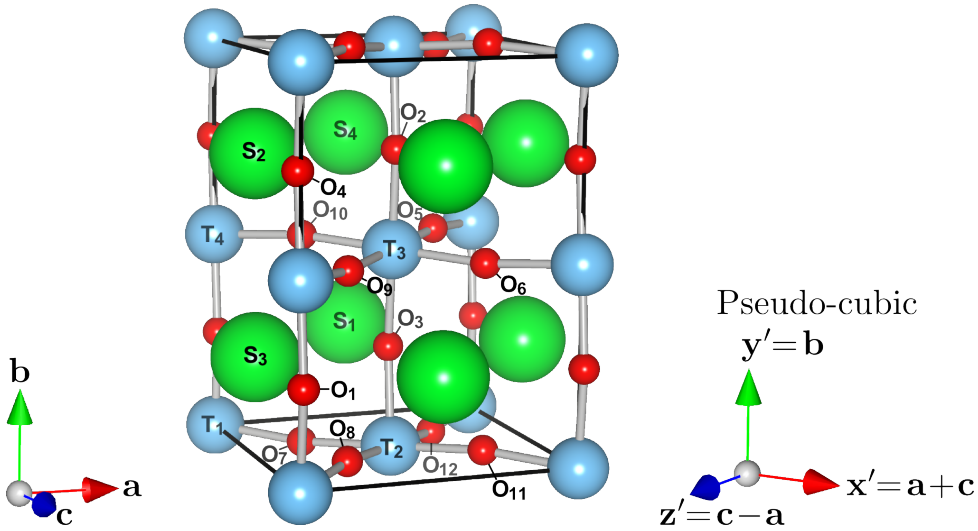

Figure 4.5.1: Structural diagram of the 20 atom $Pnma/Imma$ orthorhombic strontium titanate cell. The direction of the lattice vectors has been shown together with the direction of the pseudo-cubic axis. Green, blue and red balls represent respectively, strontium, titanium and oxygen atoms.

A more detailed version of the dendrimer diagram in figure 4.2.2 has been displayed for the orthorhombic ancestor systems in figure 4.5.2.

We will now move through the orthorhombic dendrimer diagram considering the 10 structures in their numerical order. Some consideration of the relationship of the highest symmetry orthorhombic structure ($Pnma$) to the high symmetry cubic system ($Pm\bar{3}m$) will be made at the start. A list of frequencies for the tetragonal structures can be found in table 4.5.17 on page 199.

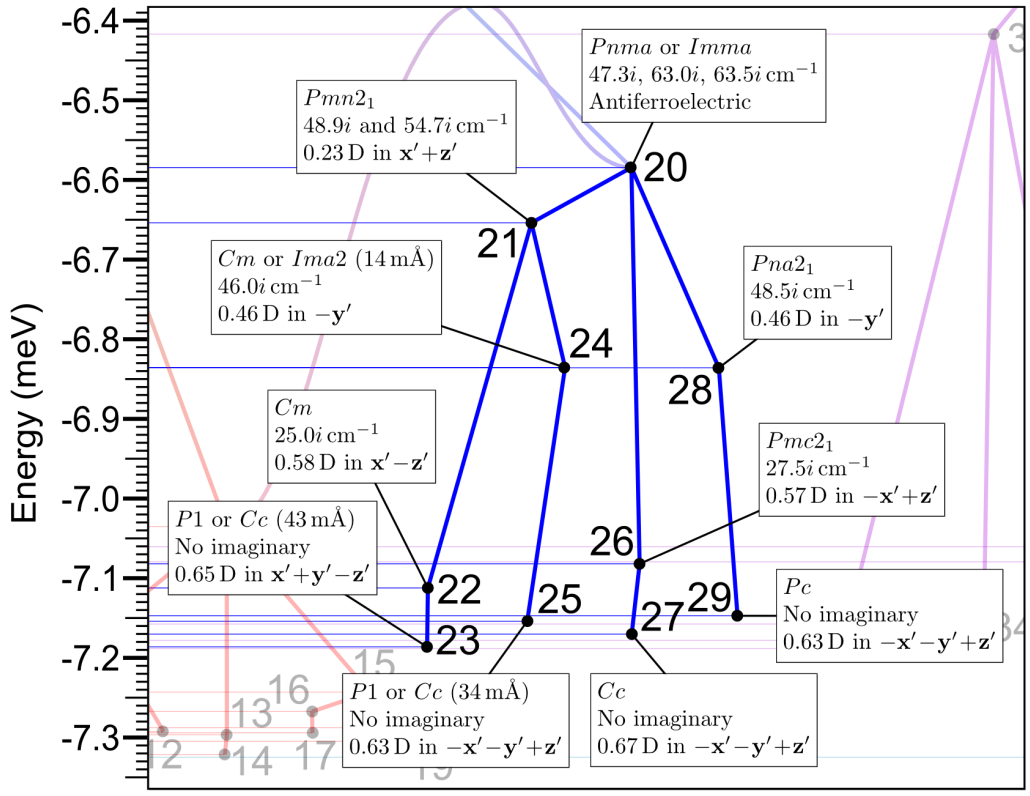

Figure 4.5.2: Dendrimer plot summarizing the orthorhombic phase transitions. Here we provide a magnified version of figure 4.2.2, with labels showing the space groups, imaginary frequencies and dipole moments of the 10 structures that were considered in this part of the study. In some cases the direction of the dipole moment was not simply along or at $45°$ to lattice vectors.

4.5.2 The Structures

4.5.2.1 Structure no. 20 ($Pnma$ or $Imma$)

Transitioning: This was a starting structure. However, as was done for the $I4/mcm$ system (structure 9), we compared the present orthorhombic structure with the optimized $Pm\bar{3}m$ system in the tetragonal/orthorhombic setting. We have already discussed the six imaginary modes of of the cubic system in section 4.4.2.1 and will not consider them in much further detail here. Vibrational mode no. 60 was the main mode involved in the cubic to tetragonal transition. In the present cubic to orthorhombic transition, degenerate modes 58 and 59 ($79.6i\,\mathrm{cm}^{-1}$, see figure 4.5.3) were responsible, though they were unequally balanced with angles of inclination to the difference vector of $20°$ and $71°$. The modes were of rotational and antiferroelectric character.

The transition caused a significant tilt/rocking along the **a** axis and was accompanied by a shortening of a (only small) and b, and a lengthening of c, which was the direction that the octahedron rocked over in. The overall volume decreased and the cell is now become short and fat i.e. a and c are longer than $\frac{b}{\sqrt{2}}$ (the tetragonal cell was tall

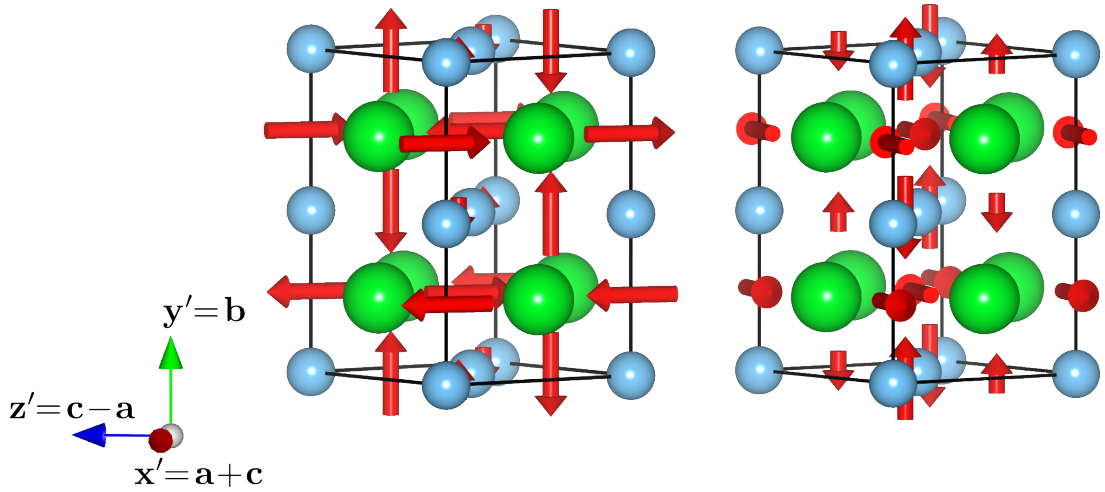

Figure 4.5.3: A representation of the degenerate imaginary modes no. 58 (left) and 59 (right) of the $Pm\bar{3}m$ structure in the tetragonal setting. Green, blue and red respectively represent strontium, titanium and oxygen. The cations are not involved with these modes and are represented as balls, the displacing oxygen atoms are represented with arrows.

and thin). Besides the rotation, the transition introduced antiferroelectricity with no net dipole.

The overall potential energy of the present system is not as low as that of the highest symmetry tetragonal system, for which there are probably two aspects to the explanation: firstly a rotation, hinging on an octahedral edge (on its own) does not have as much freedom of motion as a rotation, hinging on a vertex, due to resistance experienced from two oxygens pressing against strontium atoms e.g. in figure 4.5.1, O_2 presses against S_4 and O_3 against S_1 (see figure 4.5.1 for atom labels). Therefore rotation that is primarily hinging on vertices (or about the pseudo-cubic axes) is favoured. Secondly, the higher potential energy, may be related to the general shape of the unit cell, being $\sim \sqrt{2}$ taller than it is wide, which may make certain rotations in some directions inequivalent to others.

All three of the softest imaginary modes hardened during the transition. Mode 60 ($79.6i\,\mathrm{cm}^{-1}$) hardened to become mode 53 ($37.7\,\mathrm{cm}^{-1}$). Modes 58 and 59 (degenerate with 60) hardened with splitting degeneracy. In fact both modes became part of the same three non-degenerate modes no. 40 ($145.8\,\mathrm{cm}^{-1}$), no. 46 ($114.7\,\mathrm{cm}^{-1}$) and no. 54 ($32.0\,\mathrm{cm}^{-1}$), but with unequal weighting. Mode 58 hardened most directly to mode 46, inclined at $28°$ to it and mode 59 hardened most directly to mode 54, inclined at $20°$ to it.

Space group: $Pnma$ (no. 62) or $Imma$ (no. 74), these are both orthorhombic and fit to the cell, well within 1 mÅ.

Cell definition (Å and degrees): $a = 5.5117$, $b = 7.7854$, $c = 5.5272$;
$\alpha = 90.00$, $\beta = 90.00$, $\gamma = 90.00$;
$a : b : c = 1.0012 : 1 : 1.0040$.

Cell volume: $237.18\,\text{Å}^3$, $V/4V_0 = 0.9988$.

Potential energy (per formula unit): $-39.77879\,\text{eV}$, which is a drop of $6.58\,\text{meV}$ from the ideal cubic structure. The energy drop is equivalent to a temperature change of $\sim 15.3\,\text{K}$.

Polyhedral distortion: From table 4.5.1 we can make several observations about the character of the octahedral distortion. In this instance we have included the description of the octahedra around the T_1 and T_2 atoms as we found that the differences between them were slightly more involved than a change of signs (T_1 and T_4 are similar, as are T_2 and T_3).

The most significant observation on the octahedra is the rotation, almost entirely about the $\mathbf{a}$ vector. The $\theta_{x'}$ and $\theta_{z'}$ values are equal at about $3.8°$, which tells us that the rotation is along the octahedral edge. $\theta_{y'}$ therefore gives us the overall rotation of 5.3 about this vector, which is slightly less than the $5.5°$ initial rotation in the $I4/mcm$ system (which rotated about a vertex).

There is a very small rotation of the octahedra about the $\mathbf{b}$ vector ($\mathbf{y}'$ axis) of just $0.04°$, which we see from studying the $s_{x'}$ and $s_{z'}$ sticks. This rotation is most likely an artefact of the rather contrived evolution of the cell, which originally came from an MM model in which there were different rotations about two axes, before some of these traits were lost through optimization.

Table 4.5.1: The octahedral tilt and distortion around titanium atom T_1 (top) and T_2 (bottom) in structure 20. The octahedral volume was $9.9680\,\text{Å}^3$ which is 1.0075 of the ideal cubic equivalent for both octahedra.

Stick	θ (°)	θ_1 (°)	θ_2 (°)	length l (Å)	l/l_0
$s_{x'}$	3.7916	−3.7914	0.0425	3.9114	1.0027
$s_{y'}$	5.2850	3.7510	3.7441	3.9093	1.0021
$s_{z'}$	3.7917	−0.0425	−3.7914	3.9114	1.0027
$s_{x'}$	3.7917	3.7914	−0.0425	3.9114	1.0027
$s_{y'}$	5.2850	−3.7441	−3.7510	3.9093	1.0021
$s_{z'}$	3.7916	0.0425	3.7914	3.9114	1.0027

We included the descriptions of two octahedra in table 4.5.1; besides the differences in sign between the two octahedra, we also see a juxtaposition of the $\theta_{y'_{yz}}$ and $\theta_{y'_{yx}}$ parameters (θ_1 and θ_2 in the $s_{y'}$ row). The two values here, indicate a slight preference of both the T_1 and T_2 octahedra to rotate counter-clockwise about the $\mathbf{c}$ vector, but this

is in the order of $0.01°$. We also note from looking at this pair of numbers, a $\sim 0.05°$ discrepancy from $\theta_{x'_{xy}}$ and $\theta_{z'_{zy}}$ (both $3.79°$). The discrepancy demonstrates a distortion in the octahedra, which is confirmed by the internal internal angles of the octahedra (T_1) $s_\alpha = s_\gamma = 90.04°$. This distortion is likely to be caused by a restriction in the freedom of the oxygen on the $s_{y'}$ stick due to the surrounding strontium atoms.

The distortion of the octahedron in the **ac** plane, described by s_β is $89.59°$, which is non-90 for two reasons. If the internal fractional coordinates of the octahedra were in the $Pm\bar{3}m$ setting, but with the orthorhombic cell parameters, then we could expect s_β to be $89.84°$ based purely on the distortions of the lattice. By comparing the absolute values of $\theta_{x'}$ with $\theta_{x'_{xy}}$ and $\theta_{z'}$ with $\theta_{z'_{zy}}$ (in table 4.5.1 the first line, θ with θ_1 and last line, θ and θ_2 respectively) we see that the numbers are the same. The fact that for a given line, the two numbers are the same, means that as the octahedra rock over, the octahedral sticks s'_x and s'_z move almost perfectly in the $\mathbf{x}'\mathbf{y}'$ and $\mathbf{z}'\mathbf{y}'$ planes of the cell respectively. This causes a further narrowing of the s_β parameter. The reason for this type of motion of the oxygen atoms may be due to them having their paths confined by the strontium atoms above and bellow (as in figure 4.5.1).

Dipole (per formula unit): There is no net dipole in this system. However, we do see an antiferroelectric displacement of the strontium ions, with an individual dipole strength of $0.022\,\mathrm{D}$ and a maximum dipole-dipole inclination of $18°$. The displacements have been illustrated in figure 4.5.4.

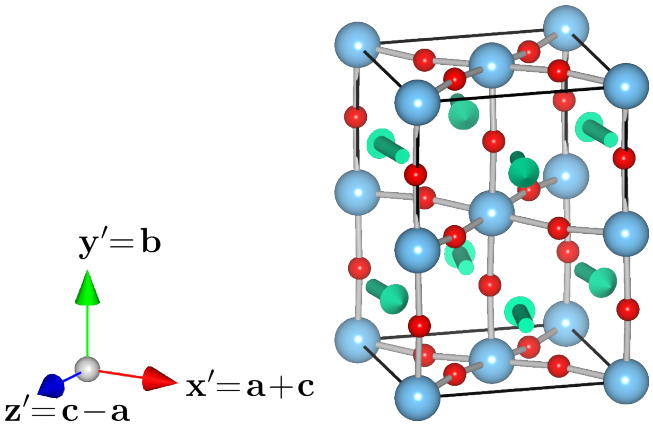

Figure 4.5.4: Representation of the antiferroelectric dipoles on strontium (green arrows) in structure 20. The magnitude of the individual dipoles is not on the same scale as in previous similar diagrams.

Imaginary modes: There are three imaginary modes in this system with frequencies of $47.3i$, $63.0i$ and $63.5i\,\mathrm{cm}^{-1}$, see table 4.5.2 and figure 4.5.5. It is not entirely clear if modes 59 and 60 are degenerate or not, as there is possibly some different character to their eigenvectors. All three modes display mostly ferroelectric character and additionally modes 58 and 60 display some antiferroelectric character. Mode 58 being

the hardest imaginary mode acts mostly in the direction of the $\mathbf{c}$ vector (or the $\mathbf{x}' + \mathbf{z}'$ direction) and the antiferroelectric ionic motion approximately follows the slope of the rocked over octahedra.

Table 4.5.2: Eigenvectors for the imaginary modes no. 58 (left) 59 (middle) and 60 (right) of structure no. 20, frequency are $47.3i$, $63.0i$ and $63.5i\,\mathrm{cm}^{-1}$ respectively.

Atom	dx′	dy′	dz′
S_1	0.05	0.00	0.05
S_2	0.05	0.00	0.05
S_3	0.05	0.00	0.05
S_4	0.05	0.00	0.05
T_1	0.21	−0.05	0.21
T_2	0.21	0.05	0.21
T_3	0.21	−0.05	0.21
T_4	0.21	0.05	0.21
O_1	−0.15	0.00	−0.15
O_2	−0.15	0.00	−0.15
O_3	−0.15	0.00	−0.15
O_4	−0.15	0.00	−0.15
O_5	−0.17	−0.00	−0.16
O_6	−0.16	0.00	−0.17
O_7	−0.16	−0.00	−0.17
O_8	−0.17	0.00	−0.16
O_9	−0.17	−0.00	−0.16
O_{10}	−0.16	0.00	−0.17
O_{11}	−0.16	−0.00	−0.17
O_{12}	−0.17	0.00	−0.16

Atom	dx′	dy′	dz′
S_1	−0.06	0.00	0.07
S_2	−0.07	0.00	0.06
S_3	−0.07	0.00	0.06
S_4	−0.06	0.00	0.07
T_1	−0.16	0.00	0.16
T_2	−0.16	0.00	0.16
T_3	−0.16	−0.00	0.16
T_4	−0.16	−0.00	0.16
O_1	0.18	0.00	−0.19
O_2	0.19	0.00	−0.18
O_3	0.19	0.00	−0.18
O_4	0.18	0.00	−0.19
O_5	0.17	−0.00	−0.17
O_6	0.17	−0.00	−0.17
O_7	0.17	0.00	−0.17
O_8	0.17	0.00	−0.17
O_9	0.17	−0.00	−0.17
O_{10}	0.17	−0.00	−0.17
O_{11}	0.17	0.00	−0.17
O_{12}	0.17	0.00	−0.17

Atom	dx′	dy′	dz′
S_1	0.00	−0.11	0.00
S_2	0.00	−0.11	0.00
S_3	0.00	−0.11	0.00
S_4	0.00	−0.11	0.00
T_1	−0.03	−0.27	−0.03
T_2	0.03	−0.27	0.03
T_3	−0.03	−0.27	−0.03
T_4	0.03	−0.27	0.03
O_1	0.00	0.23	0.00
O_2	0.00	0.23	0.00
O_3	0.00	0.23	0.00
O_4	0.00	0.23	0.00
O_5	0.00	0.23	0.00
O_6	0.00	0.23	−0.00
O_7	0.00	0.23	0.00
O_8	−0.00	0.23	0.00
O_9	0.00	0.23	0.00
O_{10}	0.00	0.23	−0.00
O_{11}	0.00	0.23	0.00
O_{12}	−0.00	0.23	0.00

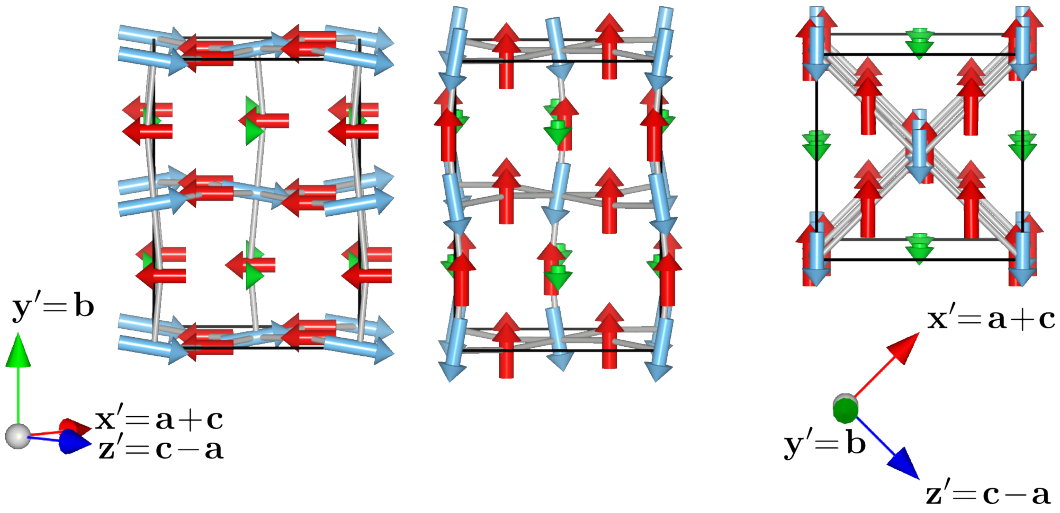

Figure 4.5.5: Graphical representation of the imaginary modes no. 58 (left), 59 (right) and 60 (middle) of structure 20 (note the non-sequential ordering). Green, blue and red arrows respectively represent motion of strontium, titanium and oxygen.

Mode 59 is purely ferroelectric and acts in the direction of the $\mathbf{a}$ vector, there is no antiferroelectric component since the motion is perpendicular to the slopes of the planes made by the octahedra. Mode 60 is mostly ferroelectric and acts primarily in the direction of the $\mathbf{b}$ vector, with the antiferroelectric component of motion almost perfectly matching the slopes created by the rocking octahedra.

Modes 58 and 60 appear to be more similar than 59 and 60, which are near degenerate in energy. Modes 59 and 60 differ in their nature in two ways: 59 is purely ferroelectric and acts in between two pseudo-cubic axes i.e. titanium ions move between two oxygen atoms; mode 60 includes a ferroelectric component and acts in the direction of the ion pseudo-cubic axis i.e. titanium atoms move directly towards an oxygen atom. It is for these reasons that we consider the apparent degeneracy of modes 59 and 60 to be coincidental.

The three imaginary modes originated primarily from the Γ_{15} modes in the cubic system (55–57) with a few components of real modes. Mode 60 in the present system ($63.5i\,\mathrm{cm}^{-1}$) is made up almost entirely from the cubic mode 57 ($68.7i\,\mathrm{cm}^{-1}$), inclined just 8° to it. There is also some flavour from the antiferroelectric real mode no. 18 ($430.2\,\mathrm{cm}^{-1}$). The pure ferroelectric mode no. 59 ($63.0i\,\mathrm{cm}^{-1}$) in the present system was derived from mode 55 ($67.2i\,\mathrm{cm}^{-1}$), inclined at 6° to it. Finally mode no. 58 in the present system was derived mostly from imaginary mode no. 56 ($67.2i\,\mathrm{cm}^{-1}$) with additional components from the real modes 19 ($429.4\,\mathrm{cm}^{-1}$) and 38 ($156.7\,\mathrm{cm}^{-1}$). Mode 19 (of the cubic system set in the present cell size) is antiferroelectric in character and degenerate with no. 17, which was discussed in section 4.4.2.1 and depicted in figure 4.4.4. The cubic (in the present cell) mode 38 is a Γ_{15} mode.

4.5.2.2 Structure no. 21 ($Pmn2_1$)

Transitioning: The parent structure was no. 20 and the present structure was obtained after optimization following a nudge down mode no. 58, with frequency $47.3i\,\mathrm{cm}^{-1}$. The ferro/antiferroelectric transition resulted in a reduction of symmetry, though the lattice remained orthorhombic. Very little rotation took place, except that it became closer to perfect rotation about the **c** vector.

We see that the lattice b parameter is slightly shorter, while there has been virtually no change in the other two cell length parameters. Based on previous examples, we would expect a lengthening of c and a shortening of a as the ferroelectric transition was in the direction of c. There are several possible explanations. The magnitude of the dipole formed (and so the ionic displacement) was small, so we would expect a smaller distortion. As c was already the longest parameter, it may be that it resisted further changes to a greater extent than in previous examples. The reason for the almost absence of shrinkage of a may be due to the substantial reduction in the small rotation about the $\mathbf{y}'$ axis.

Following optimization, the $47.3i\,\mathrm{cm}^{-1}$ mode no. 58 hardened to $41.5\,\mathrm{cm}^{-1}$ (mode 53). There was very little contamination of the mode during the transition as the new and old modes are inclined at 3° to one another. No other modes were involved in causing the transition. However, mode 59 ($63.0i\,\mathrm{cm}^{-1}$) hardened and split to become

parts of modes 59 and 54, with frequencies of $48.9i$ and $38.8\,\mathrm{cm}^{-1}$ respectively. Also mode 60 hardened slightly from $63.5i$ to $54.7i\,\mathrm{cm}^{-1}$.

Space group: $Pmn2_1$ (no. 31), which is orthorhombic.

Cell definition (Å and degrees): $a = 5.5110$, $b = 7.7822$, $c = 5.5274$;
$\alpha = 90.00$, $\beta = 90.00$, $\gamma = 90.00$;
$a : b : c = 1.0015 : 1 : 1.0045$.

Cell volume: $237.05\,\text{Å}^3$, $V/4V_0 = 0.9983$.

Potential energy (per formula unit): $-39.77886\,\mathrm{eV}$, which is $69\,\mu\mathrm{eV}$ lower than the parent structure no. 20. The energy change in equivalent to a drop in temperature of $\sim 0.16\,\mathrm{K}$.

Polyhedral distortion: The octahedral distortions of this structure are almost identical to those of structure no. 20. There has been a small decrease in octahedral volume and the parameters have changed quantitatively in some subtle ways, see table 4.5.3. The main character of the octahedra of this system is a rotation about the **a** vector of $5.3°$. The other less significant features in the distortion of structure 20 such as elements of the rotation along other vectors and the distortion of the octahedra itself are less pronounced.

Table 4.5.3: The octahedral tilt and distortion around titanium atom T_1 in structure 21. The octahedral volume was $9.9640\,\text{Å}^3$ which is 1.0071 of the ideal cubic equivalent.

Stick	θ (°)	θ_1 (°)	θ_2 (°)	length l (Å)	l/l_0
$s_{x'}$	3.8181	−3.8181	0.0158	3.9113	1.0026
$s_{y'}$	5.3265	3.7785	3.7764	3.9080	1.0018
$s_{z'}$	3.8181	−0.0158	−3.8181	3.9113	1.0026

The internal angles of the octahedron around T_1 are $90.04°$, $89.58°$ and $90.04°$ for s_α, s_β and s_γ respectively. We note that as with structure no. 20, the octahedral sticks s'_x and s'_z remain fixed in the $\mathbf{x}'\mathbf{y}'$ and $\mathbf{z}'\mathbf{y}'$ planes respectively.

Dipole (per formula unit): $0.233\,\mathrm{D}$ of which the strontium contributes $0.092\,\mathrm{D}$ and the titanium contributes $0.141\,\mathrm{D}$, both acting directly in the direction of the **c** vector or the $0.165\mathbf{x}' + 0.165\mathbf{z}'$ direction. There is a substantial antiferroelectric divergence of the dipoles of $8°$ for the titanium-titanium dipoles and $4°$ for the strontium-strontium dipoles. The individual dipole strength is fairly low (0.070 and $0.114\,\mathrm{D}$ for strontium dipoles and $0.141\,\mathrm{D}$ for all titanium dipoles). The antiferroelectric component of the net dipole acts in two directions. The strontium atoms continue to display antiferroelectric polarization in the $\mathbf{x}'\mathbf{z}'$ plane as was the case with the parent structure 20. The titanium dipoles though display their antiferroelectric polarization in the $\mathbf{y}'$ direction. The reason for the pure $\mathbf{x}' + \mathbf{z}'$ net dipole is due to the octahedral distortions all being at $90°$ to the

main ionic motion; likewise we can understand the antiferroelectric component of the titanium ions acting just in the $\mathbf{y}'$ direction.

Imaginary modes: There are two imaginary modes in the present saddle point structure with frequencies of $48.9i$ and $54.7i\,\mathrm{cm}^{-1}$ for modes 59 and 60 respectively, they are represented in table 4.5.4 and figure 4.5.6.

Table 4.5.4: Eigenvectors for the imaginary modes no. 59 (left) and 60 (right) of structure no. 21, frequency are $48.9i$ and $54.7i\,\mathrm{cm}^{-1}$ respectively.

Atom	dx′	dy′	dz′
S_1	0.01	0.00	0.00
S_2	0.01	0.00	0.00
S_3	0.01	0.00	0.00
S_4	0.01	0.00	0.00
T_1	0.01	0.00	0.00
T_2	0.01	0.00	0.00
T_3	0.01	0.00	0.00
T_4	0.01	0.00	0.00
O_1	−0.01	0.00	0.00
O_2	−0.01	0.00	0.00
O_3	−0.02	0.00	0.00
O_4	−0.02	0.00	0.00
O_5	−0.01	−0.00	0.00
O_6	−0.01	−0.00	−0.00
O_7	−0.01	−0.00	−0.00
O_8	−0.01	−0.00	0.00
O_9	−0.01	0.00	0.00
O_{10}	−0.01	0.00	−0.00
O_{11}	−0.01	0.00	−0.00
O_{12}	−0.01	0.00	0.00

Atom	dx′	dy′	dz′
S_1	0.00	−0.01	0.00
S_2	0.00	−0.01	0.00
S_3	0.00	−0.00	0.00
S_4	0.00	−0.00	0.00
T_1	0.00	−0.01	−0.00
T_2	0.00	−0.01	0.00
T_3	0.00	−0.01	−0.00
T_4	0.00	−0.01	0.00
O_1	0.00	0.01	0.00
O_2	0.00	0.01	0.00
O_3	0.00	0.01	0.00
O_4	0.00	0.01	0.00
O_5	0.00	0.01	0.00
O_6	0.00	0.01	−0.00
O_7	0.00	0.01	−0.00
O_8	0.00	0.01	0.00
O_9	−0.00	0.01	−0.00
O_{10}	−0.00	0.01	0.00
O_{11}	−0.00	0.01	0.00
O_{12}	−0.00	0.01	−0.00

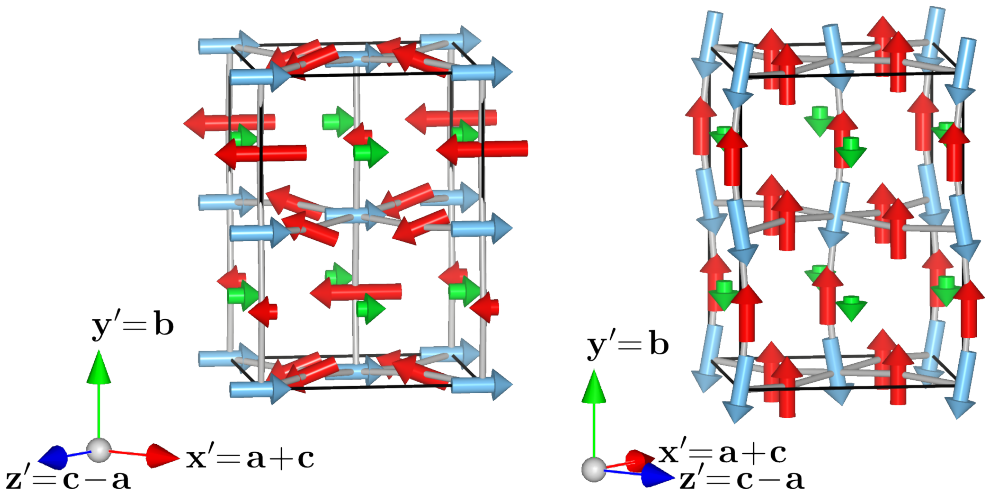

Figure 4.5.6: Graphical representation of the imaginary modes no. 59 (left) and 60 (right) of structure 21. Green, blue and red arrows respectively represent motion of strontium, titanium and oxygen.

Mode 59 in the present structure is a combination of a ferroelectric shift involving all the ions in the $\mathbf{x}' - \mathbf{z}'$ direction (along the $\mathbf{a}$ vector) and a rotation about the $\mathbf{c}$ vector i.e. a rocking motion, perpendicular to the original rotation. In the case of the central

titanium atom (labelled T_3), in figure 4.5.6 (left), the rotation is clockwise relative to the page, while the current atomic configuration consists of the top part of the octahedron leaning towards the reader. Mode 59 inherits mostly from the same mode in structure 20 ($63.0i\,\mathrm{cm}^{-1}$, inclined at 21° to it), having hardened a little. Also a component of real mode 54, with frequency $69.9\,\mathrm{cm}^{-1}$ is introduced (and inclined at 70° to the present mode 59).

Mode 60 has no rotational component, but rather has a ferroelectric component in the $\mathbf{y}'$ direction and an antiferroelectric component in the $\mathbf{x}' + \mathbf{z}'$ direction. Mode 60 in the present structure has been inherited almost unchanged (inclined at 1°) from mode 60 in structure 20 (see figure 4.5.5 (middle)).

4.5.2.3 Structure no. 22 (Cm)

Transitioning: The parent structure was no. 21 and the present structure was obtained by optimization following a nudge down mode no. 59, with frequency $48.9i\,\mathrm{cm}^{-1}$. The transition resulted in the lowering of symmetry from orthorhombic to monoclinic as the β parameter now deviates from 90°. There was a ferroelectric shift along the $\mathbf{a}$ vector which resulted in the elongation of a and the shortening of b; c increased, whereas the ferroelectric shift on its own would be expected to shorten it. The direction of the rocking of the octahedra changed to have a component in the the $\mathbf{c}$ direction, which is probably the explanation for the elongation of c.

Several modes were involved in the transition from structure 21 to 22; the most active was mode 59, inclined at 24° to the difference vector. The most significant other modes that were involved were modes 53 and 54 (frequencies of 41.5 and $38.8\,\mathrm{cm}^{-1}$ respectively) and these were inclined to the difference vector at 77° and 76°.

As a result of the transition, we see that mode 59 hardens and splits to become part of five modes with frequencies ranging from 25.5 to $172.4\,\mathrm{cm}^{-1}$. The most significant part of mode 59 goes to mode no. 52 in the present structure (frequency $98.8\,\mathrm{cm}^{-1}$), inclined at 37° to each other.

Mode 60 in the parent ($54.7\,\mathrm{cm}^{-1}$) hardens and splits to become part of modes 60 ($25.0i\,\mathrm{cm}^{-1}$) and 55 ($48.0\,\mathrm{cm}^{-1}$).

Space group: Cm (no. 8).

Cell definition (Å and degrees): $a = 5.5184$, $b = 7.7775$, $c = 5.5299$;
$\alpha = 90.00$, $\beta = 90.10$, $\gamma = 90.00$;
$a : b : c = 1.0034 : 1 : 1.0055$.

Cell volume: $237.34\,\text{Å}^3$, $V/4V_0 = 0.9995$.

Potential energy (per formula unit): $-39.77932\,\mathrm{eV}$, a drop of $0.46\,\mathrm{meV}$ from the parent structure no. 21, which is equivalent to a temperature drop of $\sim 1.1\,\mathrm{K}$.

Polyhedral distortion: The octahedra now have now rocked over, with components about both $\mathbf{a}$ and $\mathbf{c}$ lattice vectors, we determine this from the unequal components of $\theta_{x'}$ and $\theta_{z'}$ (the θ column in table 4.5.5). There is almost no rotational component around the $\mathbf{y}'$ axis. The angular separation of the $s_{y'}$ stick from the $\mathbf{y}'$ axis has changed very little from the parent structure, meaning that the total amount that the octahedra rocks over is unchanging, only the direction in which it rocks. Despite this change, the octahedra are still effectively hinging about their edges i.e. the new component of rotation, that flavours the octahedral rotation to hinge on a corner is small. We also note that despite a change in the relative motion of the s'_x and s'_z sticks in the $\mathbf{y}'$ direction, the sticks have remained approximately in the $\mathbf{x}'\mathbf{y}'$ and $\mathbf{z}'\mathbf{y}'$ planes. As a consequence, the s_β parameter has increased slightly to $89.65°$. s_α is now $90.03°$ and s_γ is $90.01°$, the inequality is likely related to the asymmetry of the cell (which would previously mirror about the $\mathbf{bc}$ plane).

Table 4.5.5: The octahedral tilt and distortion around titanium atom T_1 in structure 22. The octahedral volume was $9.9763\,\text{Å}^3$ which is 1.0083 of the ideal cubic equivalent.

Stick	θ (°)	θ_1 (°)	θ_2 (°)	length l (Å)	l/l_0
$s_{x'}$	4.4511	−4.4511	0.0104	3.9146	1.0035
$s_{y'}$	5.3537	3.0118	4.4406	3.9058	1.0012
$s_{z'}$	3.0379	−0.0104	−3.0379	3.9150	1.0036

Dipole (per formula unit): $0.583\,\text{D}$ of which the strontium contributes $0.257\,\text{D}$ and the titanium contributes $0.325\,\text{D}$. The net dipoles from each vary by only $0.8°$ in direction from one another. The antiferroelectric component of the dipole is reduced in the case of the titanium, with the maximum titanium-titanium dipole angle separation being just $2°$. While the dipole strength has increased, the overall antiferroelectric contribution from the titanium is reduced. The strontium antiferroelectric contribution has increased with dipoles angled at a maximum of $6°$ to one another. As in the previous orthorhombic structures, the titanium dipoles diverge in the $\mathbf{y}'$ direction and the strontium dipoles diverge in the $\mathbf{x}'\mathbf{z}'$ plane. The overall dipole moment for the system is $0.437\mathbf{x}' - 0.385\mathbf{z}'$.

Imaginary modes: One imaginary mode is present in this system with a frequency of $25.0i\,\text{cm}^{-1}$, see table 4.5.6 and figure 4.5.7. This mode involves a ferroelectric shift in the $\mathbf{y}'$ direction as rotation about the $\mathbf{y}'$ axis. There also appears to be an antiferroelectric component to the distortion due to the titanium atoms shifting along the axis (along the $s_{y'}$ stick) of the rocked over octahedra.

The present mode 60 inherits its character from two different modes in structure 21. The first is the parent's mode 60 with a frequency of $54.7i\,\text{cm}^{-1}$; this is inclined at $34°$ to the present mode 60. The second mode from the parent is real mode 55, with

Table 4.5.6: Eigenvectors for the imaginary mode no. 60 of structure no. 22, with frequency $25.0i\,\mathrm{cm}^{-1}$.

Atom	dx′	dy′	dz′
S_1	0.00	0.12	0.00
S_2	0.00	0.12	0.00
S_3	0.00	0.10	0.00
S_4	0.00	0.10	0.00
T_1	0.03	0.20	0.02
T_2	−0.03	0.20	−0.02
T_3	0.03	0.20	0.02
T_4	−0.03	0.20	−0.02
O_1	0.00	−0.19	0.00
O_2	0.00	−0.19	0.00
O_3	0.00	−0.19	0.00
O_4	0.00	−0.19	0.00
O_5	−0.20	−0.21	0.00
O_6	0.00	−0.20	−0.19
O_7	0.00	−0.20	−0.19
O_8	−0.20	−0.21	−0.00
O_9	0.20	−0.21	0.00
O_{10}	0.00	−0.20	0.19
O_{11}	0.00	−0.20	0.19
O_{12}	0.20	−0.21	0.00

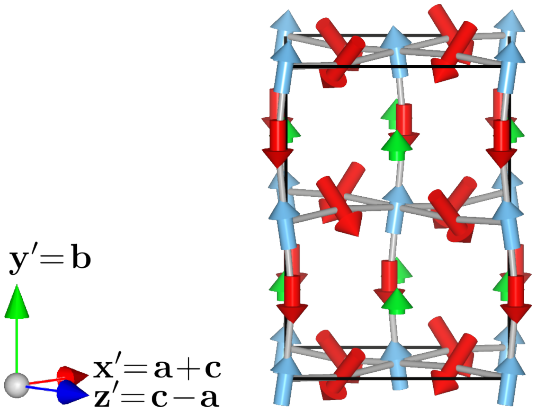

Figure 4.5.7: Graphical representation of the imaginary modes no. 60 of structure 22. Green, blue and red arrows respectively represent motion of strontium, titanium and oxygen.

frequency $38.1\,\mathrm{cm}^{-1}$ and inclined at $57°$ to present mode 60. The latter of the parent modes contains the rotational component and is in fact the almost unaltered mode 60 from the cubic system (in tetragonal setting) that was most directly responsible for the $Pm\bar{3}m$ to $I4/mcm$ transition, see section 4.4.2.1.

4.5.2.4 Structure no. 23 (Cc or $P1$)

Transitioning: The parent structure was no. 22 and the present structure was obtained by nudging down mode 60 ($25.0i\,\mathrm{cm}^{-1}$). The transition has resulted in a very low symmetry structure; the actual space group is not certain. There is now a rotational component along all pseudo-cubic axes, though the structure is dissimilar from the lowest energy structure from the tetragonal ancestor set. The ferroelectric component

of the transition caused b to grow and a and c to shrink, which is typical of these types of transition. All of the cell angles now deviate from $90°$.

Several normal modes were involved in the transition; mode 60 is inclined at $31°$ to the difference vector. The next most involved mode was no. 55 ($48.0\,\mathrm{cm}^{-1}$), which is inclined at $65°$ to the difference vector.

Mode 60 hardened from $25.0i\,\mathrm{cm}^{-1}$ and split to become part of many other modes with frequencies ranging from 24.1 to $99.0\,\mathrm{cm}^{-1}$ (modes 57 to 51)

Space group: $P1$ or with a deviation of $43\,\mathrm{m\AA}$ it is a match for the Cc (no. 9) space group.

Cell definition (Å and degrees): $a = 5.5139$, $b = 7.7944$, $c = 5.5242$;
$\alpha = 89.98$, $\beta = 90.11$, $\gamma = 90.07$;
$a : b : c = 1.0004 : 1 : 1.0023$.

Cell volume: $237.42\,\mathrm{Å}^3$, $V/4V_0 = 0.9998$.

Potential energy (per formula unit): $-39.77939\,\mathrm{eV}$, which is a drop of $74\,\mu\mathrm{eV}$ from the parent structure no. 22, which is equivalent to a temperature difference of $\sim 0.17\,\mathrm{K}$. The present structure is the lowest in energy of all the orthorhombic ancestor structures but $0.14\,\mathrm{meV}$ higher in energy than the lowest energy tetragonal ancestor structure (no. 14).

Polyhedral distortion: In this structure we see a rotation about all three pseudo-cubic axes, see table 4.5.7. The rotation about the $\mathbf{y}'$ axis is $1.89°$, and so it is clearly dissimilar to the lowest energy tetragonal ancestor system. A simple comparison of the θ values for the two systems (considering different orders) would also serve as a useful heuristic as to the similarity of the two systems, but they are clearly distinct.

Table 4.5.7: The octahedral tilt and distortion around titanium atom T_1 in structure 23. The octahedral volume was $9.9785\,\mathrm{Å}^3$ which is 1.0086 of the ideal cubic equivalent.

Stick	θ (°)	θ_1 (°)	θ_2 (°)	length l (Å)	l/l_0
$s_{x'}$	4.5861	−4.1850	−1.8871	3.9114	1.0027
$s_{y'}$	4.9773	2.7321	4.1718	3.9120	1.0028
$s_{z'}$	3.3472	1.8995	−2.7592	3.9129	1.0030

The internal angles of the T_1 octahedron are $89.82°$, $89.68°$ and $90.14°$ for s_α, s_β and s_γ respectively.

Dipole (per formula unit): $0.652\,\mathrm{D}$, of which the strontium contributes $0.294\,\mathrm{D}$ and the titanium contributes $0.358\,\mathrm{D}$, acting in the same direction. The overall overall direction for the dipole of the cell is $0.368\mathbf{x}' + 0.403\mathbf{y}' - 0.356\mathbf{z}'$ and is inclined $3°$ from the volume diagonal of the cell. The titanium-titanium dipole angles have a maximum of $2.8°$ and the strontium-strontium dipoles have a maximum of $4.8°$.

Imaginary modes: There are no imaginary modes present in this system.

4.5.2.5 Structure no. 24 ($Ima2$ or Cm)

Transitioning: The parent structure was no. 21 and the present structure was obtained by optimization following a nudge down mode 60, which had a frequency of $54.7i\,\mathrm{cm}^{-1}$. The transition sees a deformation of the lattice involving an increase in b and a decrease in a and c, which is typical of a ferroelectric shift in the $\mathbf{b}$ ($\mathbf{y}'$) direction. The dipole moment approximately doubles in magnitude and now acts mostly in the $\mathbf{y}'$ direction. There has been very little change to the oxygen octahedra. The ionic shift has changed the cell angle α by just 0.01° so the new structure is classified as monoclinic. Given the slightness of the distortion (even in the context of other STO structures), it is arguable that the structure is still orthorhombic like the parent.

Many modes played a small rôle in the transition, but mode 60 was inclined at 39° to the difference vector. Mode 53 ($41.5\,\mathrm{cm}^{-1}$) contributed the next largest contribution and was inclined at 80° to the difference vector. Mode 60 hardened from $54.7i\,\mathrm{cm}^{-1}$ and became a small part of four modes but made its largest contribution to mode 51 in the present structure, with a frequency of $101\,\mathrm{cm}^{-1}$ and inclined at 21° to it.

Space group: Cm (no. 8) or $Ima2$ (no. 46), with a deviation of $14\,\mathrm{mÅ}$.

Cell definition (Å and degrees): $a = 5.5083$, $b = 7.7968$, $c = 5.5237$;
$\alpha = 90.01$, $\beta = 90.00$, $\gamma = 90.00$;
$a : b : c = 0.9991 : 1 : 1.0019$.

Cell volume: $237.23\,\mathrm{Å}^3$, $V/4V_0 = 0.9991$.

Potential energy (per formula unit): $-39.77904\,\mathrm{eV}$, which is a drop of $0.182\,\mathrm{meV}$ from the parent structure no. 21, which corresponds to a drop of $\sim 0.42\,\mathrm{K}$.

Polyhedral distortion: The octahedra have remained qualitatively similar since the parent structure. In table 4.5.8 we see that the the octahedral volume has increased slightly and the rotation, which is still about the $\mathbf{a}$ axis has decreased slightly ($\sim 0.07^\circ$). The s'_x stick, which was previously slightly out of the $\mathbf{x}'\mathbf{y}'$ plane has moved slightly closer (from table 4.5.8 ($\theta_{x'_{xz}}$ reduces from 0.016° to 0.009°). The s'_z stick also moves a little closer to the $\mathbf{z}'\mathbf{y}'$ plane, but to a lesser degree ($\theta_{z'_{zx}}$ reduces from -0.016° to -0.012°).

Table 4.5.8: The octahedral tilt and distortion around titanium atom T_1 in structure 24. The octahedral volume was $9.9696\,\mathrm{Å}^3$ which is 1.0077 of the ideal cubic equivalent.

Stick	θ (°)	θ_1 (°)	θ_2 (°)	length l (Å)	l/l_0
$s_{x'}$	3.7817	−3.7817	0.0088	3.9090	1.0020
$s_{y'}$	5.2589	3.7292	3.7288	3.9149	1.0036
$s_{z'}$	3.7810	−0.0122	−3.7810	3.9090	1.0020

s_α, s_β and s_γ are $90.06°$, $89.60°$ and $90.06°$ respectively, which describes a small uniform bending of the s'_y stick towards the others and a $0.4°$ contraction of the s'_x and s'_z sticks towards one another.

Dipole (per formula unit): $0.464\,\mathrm{D}$ of which the strontium contributes $0.201\,\mathrm{D}$ and the titanium contributes $0.263\,\mathrm{D}$, the net contributions are inclined $1.6°$ to one another. The overall dipole has components $0.062\mathbf{x}' - 0.456\mathbf{y}' + 0.061\mathbf{z}'$ and is inclined by $11°$ the $\mathbf{y}'$ axis. The dipole is approximately double the magnitude of the dipole in structure 21. The antiferroelectric component involves titanium dipoles inclined at $8°$ to one another and strontium dipoles inclined by $14°$ to one another, which is the largest angular deviation we have seen so far.

One of the more interesting observations of the present structure is that the component of the dipole in the $\mathbf{c}$ (or $\mathbf{x}'+\mathbf{z}'$) direction that was present in the parent has been significantly diminished. In other examples, following sequential ferroelectric shifts in perpendicular directions, the cells tended to retain approximately equal components of the dipole in each of the directions. It is not entirely clear what the cause of the bias towards the $\mathbf{y}'$ direction in the present system is; but one possibility is that the antiferroelectric components of parent structure 21 and the eigenvector in which the system was nudged to get to the present structure interacted with one another to neutralise most of the $\mathbf{x}' + \mathbf{z}'$ component of the dipole moment. The relatively small dipole moment, acting mostly in the direction of one pseudo-cubic axis is probably the cause of the relatively high energy of the system, given that two nudges have taken place.

Imaginary modes: The present structure has only one imaginary mode with a frequency of $46.0i\,\mathrm{cm}^{-1}$ and is described and depicted in table 4.5.9 and figure 4.5.8. In this mode we see three different ionic motions. A ferroelectric motion involving all ions along the the $\mathbf{a}$ vector (or $-\mathbf{x}' + \mathbf{z}'$); a rotation of the octahedra about the $\mathbf{y}'$ axis (which can be seen in figure 4.5.8 as a counter clockwise rotation of the octahedron around T_3 as viewed from above); finally a rotation of the octahedra about the $\mathbf{c}$ vector (which can be seen as a counter clockwise rotation about T_3 as viewed from the front of the figure).

The present mode 60 ($46.0i\,\mathrm{cm}^{-1}$), inherits its character most directly from mode 59 ($48.9i\,\mathrm{cm}^{-1}$) from structure 21 as they are inclined at $21°$ to one another. Present mode 60 also inherits a small amount of character from the near degenerate modes 54 and 44 with frequencies 38.8 and $38.1\,\mathrm{cm}^{-1}$.

Table 4.5.9: Eigenvectors for the imaginary mode no. 60 of structure no. 24 with a frequency of $46.0i\,\mathrm{cm}^{-1}$.

Atom	dx′	dy′	dz′
S_1	−0.08	−0.00	0.08
S_2	−0.08	0.00	0.08
S_3	−0.09	−0.00	0.09
S_4	−0.09	0.00	0.09
T_1	−0.16	0.00	0.16
T_2	−0.17	−0.00	0.17
T_3	−0.16	0.00	0.16
T_4	−0.17	−0.00	0.17
O_1	0.13	0.00	−0.13
O_2	0.13	0.00	−0.13
O_3	0.20	0.00	−0.20
O_4	0.20	0.00	−0.20
O_5	0.05	0.03	−0.15
O_6	0.15	0.04	−0.26
O_7	0.15	0.04	−0.26
O_8	0.05	0.03	−0.15
O_9	0.26	−0.04	−0.15
O_{10}	0.15	−0.03	−0.05
O_{11}	0.15	−0.03	−0.05
O_{12}	0.26	−0.04	−0.15

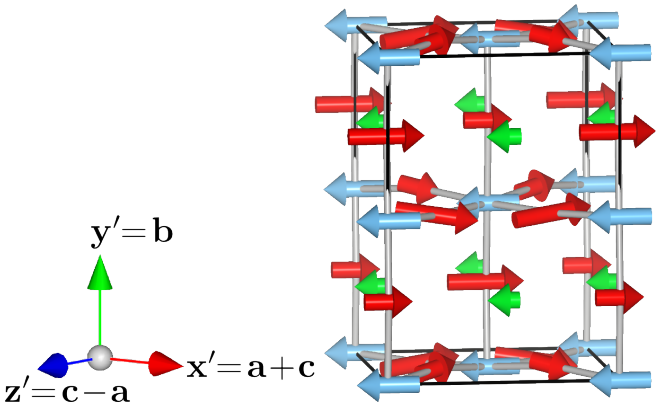

Figure 4.5.8: Graphical representation of the imaginary mode 60 of structure 24. Green, blue and red arrows respectively represent motion of strontium, titanium and oxygen.

4.5.2.6 Structure no. 25 (Cc or $P1$)

Transitioning: The parent structure was no. 24 and the present structure was obtained by nudging down the only remaining imaginary mode no. 60, with a frequency of $46.0i\,\mathrm{cm}^{-1}$. Many changes occur during this transition, in which the monoclinic space group possibly becomes $P1$ as the angles all deviate from $90°$. In the lattice, we see a relatively large increase in the a parameter, and a similar decrease in the b parameter. We also see a small (about half of the change in a) increase in c. We see a substantial increase in the dipole moment of the cell. Also, the octahedral rotation now has a significant (and different) component along all three pseudo-cubic axes, but the parent (24) only had a significant rotation along two axes and they were identical (indicating pure edge based hinging). The rotational components introduced to the cell include an

approximately 1° rotation about the $\mathbf{y}'$ axis.

The increase in a was expected based on previous transitions as the ferroelectric shift was in this direction. The expansion of a may also have been driven by the rocking of the octahedra in the direction of the $\mathbf{a}$ vector, though this effect would have been a smaller contributing factor. The decrease in b was also expected due to the ferroelectric shift in a direction orthogonal to it. However, the new octahedral motion was probably not involved in changing b as the value of $\theta_{y'}$, representing the deviation of the $s_{y'}$ stick from the $\mathbf{y}'$ axis has not changed.

The increase in c was surprising as previous experience has shown that a ferroelectric shift causes a narrowing of the structure in the direction perpendicular to it. It may be helpful to refer back to figure 4.5.8 (which describes the parent structure and the eigenvector that lead to the present structure) and examine table 4.5.10 (describing the present octahedral configuration) in order to consider the situation more carefully. As we have mentioned, the $\theta_{y'}$ parameter, indicating how far the octahedra lean from the $\mathbf{y}'$ axis has not changed significantly (it has actually decreased slightly, indicating more upright octahedra as represented on the page). However, the direction of the lean has changed slightly (not leaning so much towards and away from the page but now a little to the left and right). Generally, we have seen that the rocking over of the octahedra, will lead to an expansion of the cell in the direction in which they leans over, which appears reasonable when one imagines the octahedra concertinaing as they do this (so we would expect a thinning of the cell if they stand more upright). However, another contending contribution is the repulsive force between the oxygen atoms and the titanium atoms. If the Ti–O–Ti bond is bent, then the distance between the titanium atoms will be shorter and also the expected dimensions of the cell (in the same direction). We also note that the octahedra rotated about the $\mathbf{y}'$ axis by $\sim 1^\circ$. On their own, axial rotations have been shown to shrink the lattice parameters perpendicular to the axis of rotation. However, when the octahedra rocked over about the $\mathbf{c}$ vector (or in the direction of the $\mathbf{a}$ vector) and they rotated about the $\mathbf{y}'$ axis in combination with the octahedral edge based rotation that was already present, the $\theta_{x'}$ parameter decreased by 0.25°, pushing the titanium atoms along one diagonal further away (the $\mathbf{a}+\mathbf{c}$ diagonal or $\mathbf{x}'$ direction) while allowing them to contract slightly in the other diagonal (the $\mathbf{c}-\mathbf{a}$ diagonal or the $\mathbf{z}'$ direction). The repulsion of titanium and the different components of rotational motion may explain the expansion of c and the non-90° angles of the cell.

If the above is the explanation for the expansion of c then it seems that there are two competing effects involved, which we will bring up again in our summary (section 4.5.4).

Vibrational mode 60 (in structure 24) hardened from $46.0i\ \mathrm{cm}^{-1}$ during the transition, and mixed into a group of about seven other modes, the most directly related being

mode 52 ($101.1\,\mathrm{cm}^{-1}$) as they are inclined at $35°$ to one another. The other modes range in frequency from 24.8 to $172.5\,\mathrm{cm}^{-1}$ and are inclined at at least $67°$ to mode 60 in the parent.

Space group: Cc (no. 9) with a deviation of $34\,\mathrm{m\AA}^*$ or $P1$ if a tighter tolerance is required.

Cell definition (Å and degrees): $a = 5.5164$, $b = 7.7846$, $c = 5.5281$;
$\alpha = 90.01$, $\beta = 89.95$, $\gamma = 90.04$;
$a : b : c = 1.0022 : 1 : 1.0043$.

Cell volume: $237.39\,\mathrm{\AA}^3$, $V/4V_0 = 0.9997$.

Potential energy (per formula unit): $-39.77936\,\mathrm{eV}$, which is a drop of $0.32\,\mathrm{meV}$, corresponding to a temperature change of $\sim 0.74\,\mathrm{K}$.

Polyhedral distortion: We find from considering table 4.5.10, a similar situation as with structure 23, which is the lowest energy structure from the orthorhombic ancestor systems. In both systems, we see a rotation about all three pseudo-cubic axis. In the present structure, the total octahedral rock/tilt away from the $\mathbf{y}'$ ($\theta_{y'}$) is greater than that of structure 23 by about $0.2°$. $\theta_{x'}$ and $\theta_{z'}$ are closer to equality than in structure 23, indicating that the nature of the rocking is closer to an edge based hinge than in structure 23. By considering the rotational data more closely, we also note that the rotation involves an axial rotation about the $\mathbf{y}'$ axis of about $1.1°$.

Table 4.5.10: The octahedral tilt and distortion around titanium atom T_1 in structure 25. The octahedral volume was $9.9777\,\mathrm{\AA}^3$ which is 1.0085 of the ideal cubic equivalent.

Stick	θ (°)	θ_1 (°)	θ_2 (°)	length l (Å)	l/l_0
$s_{x'}$	3.5347	−3.3605	−1.0996	3.9139	1.0033
$s_{y'}$	5.2114	4.0223	3.3330	3.9084	1.0019
$s_{z'}$	4.1848	1.0954	−4.0405	3.9136	1.0032

The internal octahedral angles are $89.93°$, $89.65°$ and $90.14°$ for s_α, s_β and s_γ respectively. These are identical to structure 23 except for s_α which is distorted to a slightly lesser degree in the present structure.

Dipole (per formula unit): $0.632\,\mathrm{D}$, of which the strontium contributes $0.283\,\mathrm{D}$ and the titanium contributes $0.349\,\mathrm{D}$, both acting in the same direction. The overall dipole acts in the $-0.391\mathbf{x}' - 0.278\mathbf{y}'0.410\mathbf{z}'$ direction. The antiferroelectric component of the dipoles is fairly weak for in the case of titanium-titanium dipoles where are inclined at a maximum of $2.1°$ to one another, while strontium-strontium dipoles are inclined as much as $5.9°$ to one another.

*It was necessary to adjust the n-fold axes tolerance parameter in *Endeavour* to get the non-$P1$ result.

Imaginary modes: There are no imaginary modes in the present structure as it is an endpoint structure.

4.5.2.7 Structure no. 26 ($Pmc2_1$)

Transitioning: The parent structure was no. 20 and the present structure was obtained after optimization, by nudging along the eigenvectors of mode 59. Orthorhombicity was maintained during this transition, in which there was very little change to the octahedra but the ferroelectric shift drove changes to the lattice parameters: a grew and b shrank, both of which were expected based upon the ferroelectric shift in the **a** direction. The c parameter also grew, which may in this case be attributable to the antiferroelectricity on the strontium ions acting in this direction. The octahedral shifting is less suspect in causing these changes due to the slightness of their motion.

The energy change during the transition to the present system is the largest seen in the orthorhombic and tetragonal ancestor systems but is similar to some of the energy changes seen in the cubic ancestor systems. The energy change can be almost completely attributed to the ferro and antiferroelectric ionic motion, but it is not entirely clear why it was greater in magnitude than similar shifts that have happened to other orthorhombic ancestor systems. The explanation may be related to the ferroelectric shift direction being the same as the direction in which the octahedra rock over. Similarly to other transitions the ferroelectric displacement that lead to the present structure was along a cell vector i.e. between two octahedral vertices. However, in this case, the direction that the octahedra were leaning in and the direction of the ferroelectric displacement were the same. Due to the rocking of the octahedra, the shift in this case has been partially towards a third octahedral vertex as well, allowing greater titanium displacements; hence the strength of the dipole and the increased energy drop.

Two normal modes had a significant contribution to the transition — mode 59 ($63.0i\,\mathrm{cm}^{-1}$) and mode 38 ($160.8\,\mathrm{cm}^{-1}$) — which were inclined, respectively by 29° and 83° to the difference vector. During the transition, two imaginary modes hardened to become real and the third hardened to an extent but remaining imaginary. Mode 58 ($47.3i\,\mathrm{cm}^{-1}$) in the parent hardened and most directly became a part of mode 51 ($103\,\mathrm{cm}^{-1}$); they are inclined at 20° to one another. Modes 56 and 37 in the present structure (25.6 and $169.7\,\mathrm{cm}^{-1}$ respectively) are inclined at 72° and 81° respectively to the parent mode 58.

Similarly with parent mode 59 ($63.0i\,\mathrm{cm}^{-1}$), we see the mode become part of three others in the present system: modes 53, 48 and 36 with frequencies of 97.8, 115.6 and $171.2\,\mathrm{cm}^{-1}$ and angular inclinations of 20°, 80° and 74° respectively.

Finally imaginary mode 60 ($63.5i\,\mathrm{cm}^{-1}$), which we discuss further at the end of this structure description splits into two parts. One part contributes to the hard mode

55 in the present structure ($48.0\,\mathrm{cm}^{-1}$) and inclined at $58°$ to it. The other part which remains soft has a frequency of $27.5i\,\mathrm{cm}^{-1}$ and an inclination angle of $32°$ to the parent mode 60.

Space group: $Pmc2_1$ (no. 26), which is orthorhombic.

Cell definition (Å and degrees): $a = 5.5176$, $b = 7.7780$, $c = 5.5302$;
$\alpha = 90.00$, $\beta = 90.00$, $\gamma = 90.00$;
$a : b : c = 1.0032 : 1 : 1.0055$.

Cell volume: $237.33\,\text{Å}^3$, $V/4V_0 = 0.9995$.

Potential energy (per formula unit): $-39.77929\,\mathrm{eV}$, which is a drop of $0.498\,\mathrm{meV}$ and equivalent to a temperature reduction of $\sim 1.2\,\mathrm{K}$.

Polyhedral distortion: The octahedra have distorted similarly to those of structure 21 (which actually involved very little change). From examining table 4.5.11 we see that the octahedra have expanded slightly, since the parent (and slightly larger than in structure 21 also). The rocking of the octahedra is now a purer rotation about the **a** vector than in the parents' case and the extent of the rotation is very slightly greater, by about $0.04°$.

Table 4.5.11: The octahedral tilt and distortion around titanium atom T_1 in structure 26. The octahedral volume was $9.9753\,\text{Å}^3$ which is 1.0082 of the ideal cubic equivalent.

Stick	θ (°)	θ_1 (°)	θ_2 (°)	length l (Å)	l/l_0
$s_{x'}$	3.7985	−3.7985	0.0192	3.9146	1.0035
$s_{y'}$	5.3266	3.7775	3.7749	3.9059	1.0012
$s_{z'}$	3.7985	−0.0192	−3.7985	3.9146	1.0035

We find symmetrical internal angles of the octahedra: $90.02°$, $89.62°$ and $90.02°$ for s_α, s_β and s_γ. The similarity of s_α and s_γ demonstrate the symmetry of the structure about the **cb** plane.

Dipole (per formula unit): $0.571\,\mathrm{D}$ of which the strontium contributed $0.252\,\mathrm{D}$ and the titanium contributed $0.319\,\mathrm{D}$, both acting purely in the $-\mathbf{x}' + \mathbf{z}'$ direction. The titanium dipoles are all aligned with one another, but there is some antiferroelectricity on the strontium as the dipoles have a maximum deviation of $7.2°$ from one another. The antiferroelectric component of the strontium acts largely in the $\mathbf{x}' + \mathbf{z}'$ direction (direction of the **c** vector).

Imaginary modes: Only one imaginary mode remains for the present system with a frequency of $27.5i\,\mathrm{cm}^{-1}$; it has been depicted in table 4.5.12 and figure 4.5.9. Mode 60 of the present system is very similar to the equivalent mode of structure 22 (see figure 4.5.7). The present mode is characterized by a ferroelectric shift in the $\mathbf{y}'$ direction, which has an antiferroelectric component acting in the $\mathbf{x}' + \mathbf{z}'$ direction. We also note

an axial rotation of the octahedra about the $\mathbf{y}'$ axis. There does not appear to be any other type of rotation involved.

Table 4.5.12: Eigenvectors for the imaginary mode no. 60 of structure no. 26, with frequency $27.5i\,\mathrm{cm}^{-1}$.

Atom	$\mathbf{dx}'$	$\mathbf{dy}'$	$\mathbf{dz}'$
S_1	0.00	−0.13	0.00
S_2	0.00	−0.13	0.00
S_3	0.00	−0.13	0.00
S_4	0.00	−0.13	0.00
T_1	−0.02	−0.22	−0.02
T_2	0.02	−0.22	0.02
T_3	−0.02	−0.22	−0.02
T_4	0.02	−0.22	0.02
O_1	0.00	0.19	0.00
O_2	0.00	0.19	0.00
O_3	0.00	0.19	0.00
O_4	0.00	0.19	0.00
O_5	−0.18	0.20	−0.00
O_6	−0.00	0.20	−0.18
O_7	−0.00	0.20	−0.18
O_8	−0.18	0.20	−0.00
O_9	0.18	0.20	0.00
O_{10}	0.00	0.20	0.18
O_{11}	0.00	0.20	0.18
O_{12}	0.18	0.20	0.00

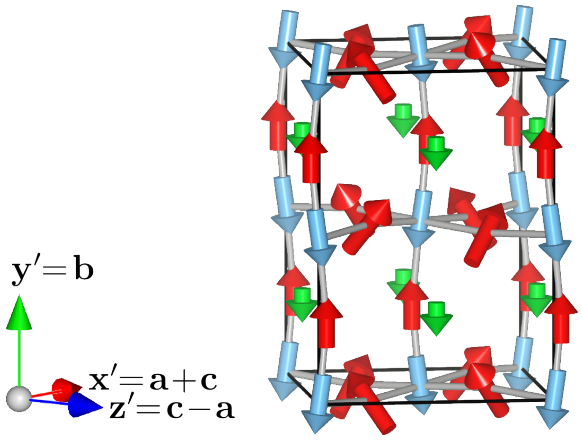

Figure 4.5.9: Graphical representation of the imaginary modes no. 60 of structure 26. Green, blue and red arrows respectively represent motion of strontium, titanium and oxygen.

Mode 60 in the present system is derived from two different modes from structure 20. The structure 20 mode 60 ($63.5i\,\mathrm{cm}^{-1}$) is most closely related and inclined at $32°$ to the present mode. The second significantly contributing mode is mode 53 ($37.7\,\mathrm{cm}^{-1}$), which is inclined at $58°$ to the present mode 60.

4.5.2.8 Structure no. 27 (Cc)

Transitioning: The parent structure was no. 26 and the present structure was obtained by nudging down the only remaining mode 60 ($27.4i\,\mathrm{cm}^{-1}$). The transition saw the

structure change from orthorhombic to monoclinic symmetry, with a single angle γ departing from $90°$. During the transition, there were various changes to the cell and internal structure: b grew and a and c shrank, which is the expected behaviour based on a ferroelectric shift in the b direction. The octahedra rotated about the $\mathbf{y}'$ axis, while the rocking of the octahedra relative to the $\mathbf{y}'$ axis reduced. The octahedra did not start leaning over in the $\mathbf{a}$ direction, as we have seen with other structures. We discuss the octahedral distortion further below.

The dipole moment increased and acts roughly in the in the direction of the octahedral faces (the departure from this is to do with the octahedral rocking).

An interesting observation in the present structure is the very low density (identical to that of the ideal cubic $Pm\bar{3}m$ system). The other systems based on a 20 atom cell have had a higher density than the ideal cubic system.

Mode 60 ($27.5i\,\mathrm{cm}^{-1}$) from the parent structure was inclined at $37°$ to the difference vector and two other modes contributed to the transition. Modes 55 ($48.0\,\mathrm{cm}^{-1}$) and 48 ($115.6\,\mathrm{cm}^{-1}$) were respectively inclined at $66°$ and $80°$ to the difference vector.

During the transition, mode 60 hardens and splits into at least five other modes, the most directly related is mode 54 ($90.6\,\mathrm{cm}^{-1}$), which is inclined at $38°$ to parent mode 60. The other modes that inherit from parent mode 60 are 56, 52, 38 and 36, with frequencies of 31.4, 99.4, 167.6 and $173.1\,\mathrm{cm}^{-1}$ and inclined at angles of $64°$, $67°$, $86°$ and $81°$ respectively to it.

Space group: Cc (no. 9), which is monoclinic.

Cell definition (Å and degrees): $a = 5.5143$, $b = 7.7932$, $c = 5.5253$;
$\alpha = 90.00$, $\beta = 90.00$, $\gamma = 90.07$;
$a : b : c = 1.0007 : 1 : 1.0027$.

Cell volume: $237.44\,\text{Å}^3$, $V/4V_0 = 1.0000$. A small expansion from the previous system which brings the structure to the same volume as the ideal cubic system.

Potential energy (per formula unit): $-39.77938\,\mathrm{eV}$, which is a drop of $88\,\mu\mathrm{eV}$ and equivalent to a temperature change of $\sim 0.20\,\mathrm{K}$.

Polyhedral distortion: From table 4.5.13 we see that the octahedra have twisted to be more closely aligned with the $\mathbf{y}'$ axis, while the deviations of the sticks from the other two pseudo-cubic axes have increased slightly from the previous structure. $\theta_{x'_{xz}}$ and $\theta_{z'_{zx}}$ (θ_2 (top) and θ_1 (bottom) respectively) show that the octahedra have rotated round by $\sim 1.9°$ about the $\mathbf{y}'$ axis, while there has been no rotation about the $\mathbf{c}$ vector i.e. the octahedra rotate on an axis and lean towards only one cell wall. Given that this is an end point structure, these observations are interesting as the type of rotation involved is very similar to the lowest energy tetragonal ancestor system no. 14. The main difference is that in the present system, there is a small rotation about an axis and

a large equal rotation about the other two (an edge) where as in structure 14, we have the opposite situation.

Table 4.5.13: The octahedral tilt and distortion around titanium atom T_1 in structure 27. The octahedral volume was $9.9788\,\text{Å}^3$ which is 1.0086 of the ideal cubic equivalent.

Stick	θ (°)	θ_1 (°)	θ_2 (°)	length l (Å)	l/l_0
$s_{x'}$	3.9987	−3.5246	−1.8966	3.9126	1.0030
$s_{y'}$	4.9457	3.5052	3.5047	3.9112	1.0026
$s_{z'}$	3.9987	1.8966	−3.5246	3.9126	1.0030

The internal octahedral angles corresponding to the octahedra surrounding T_1 are $89.85°$, $89.67°$ and $90.19°$ for s_α, s_β and s_γ respectively. The octahedra are therefore fairly substantially distorted (in terms of the magnitudes we see in this system).

Dipole (per formula unit): $0.672\,\text{D}$, of which the strontium contributes $0.305\,\text{D}$ and the titanium contribute $0.368\,\text{D}$, which both pointing directly between the three pseudo-cubic axis (not quite a volume diagonal as the long $\mathbf{b}$ vector changes the angle), i.e. the net dipole can be given by $-0.387\mathbf{x}' - 0.389\mathbf{y}' + 0.387\mathbf{z}'$. This structure has the strongest dipole moment in the tetragonal and orthorhombic ancestor systems. The antiferroelectric component on the titanium is relatively weak for an end point structure with dipoles diverging by just $2.0°$ or $4.1°$ for strontium.

Imaginary modes: This structure has no imaginary modes as it is an endpoint structure.

4.5.2.9 Structure no. 28 ($Pna2_1$)

Transitioning: The parent structure was no. 20 and the present structure was obtained by nudging the atoms in the direction of mode 60, which has a frequency of $63.5\,\text{cm}^{-1}$. During the transition, the orthorhombic Bravais lattice type is maintained. We note that b increases, while a and c decrease, which is expected, due to the ferroelectric shift of ions along the $\mathbf{y}'$ axis (along the $\mathbf{b}$ vector). There is now a dipole this direction and there has been virtually no change in the nature of the octahedra.

We note, however that the present structure, directly derived from structure no. 20, is almost identical to structure no. 24, which was derived from 20, via structure 21. The structures are degenerate in energy and have almost identical: lattice parameters, octahedra, dipole moments, imaginary frequencies and eigenvectors. The two structures deviate on a few points: structure 24 has a very small angular deviation of from $90°$ on α but the present structure does not; structure 24 also has a small net component of dipole moment acting in the $\mathbf{x}' + \mathbf{z}'$ direction which is not present in the present structure; finally we note that the eigenvectors of the two structures are almost identical, but structure 24 includes a component that causes the octahedra to rock over away from a cell face and towards a cell edge (or in the direction of two faces).

Mode 60 ($63.5i\,\mathrm{cm}^{-1}$), in which the system was nudged in inclined to the difference vector with an angle of $34°$, though we also see a small involvement of real mode 39 ($159.0\,\mathrm{cm}^{-1}$) in the transition.

During the transition, mode 58 ($47.3i\,\mathrm{cm}^{-1}$) hardened to become mode 56 ($24.0\,\mathrm{cm}^{-1}$). Mode 60 hardened from $63.5i\,\mathrm{cm}^{-1}$ and split into three main components, which are as follows: mode 51, 47 and 36 with frequencies of 101.6, 112.6 and $172.5\,\mathrm{cm}^{-1}$ and inclined with angles of $22°$, $80°$ and $71°$ to mode 60 respectively.

Mode 59 ($63.0i\,\mathrm{cm}^{-1}$) split into two parts during the transition, one of which became hard and the other hardened lightly but remained imaginary. The hardened component contributes to mode 54 ($41.6\,\mathrm{cm}^{-1}$) and is inclined at $73°$ to the parent mode 59. The imaginary component is the present mode 60 ($48.5i\,\mathrm{cm}^{-1}$) and is inclined at $18°$ to the parent mode.

Space group: $Pna2_1$ (no. 33), which is orthorhombic.

Cell definition (Å and degrees): $a = 5.5083$, $b = 7.7970$, $c = 5.5235$;
$\alpha = 90.00$, $\beta = 90.00$, $\gamma = 90.00$;
$a : b : c = 0.9991 : 1 : 1.0019$.

Cell volume: $237.23\,\text{Å}^3$, $V/4V_0 = 0.9991$.

Potential energy (per formula unit): $-39.77904\,\mathrm{eV}$, which is a drop of $0.25\,\mathrm{meV}$ and equivalent to a temperature change of $\sim 0.58\,\mathrm{K}$. The present structure is also degenerate with structure no. 24.

Polyhedral distortion: There has been almost no change in the octahedra of the present structure since the parent no. 20. The octahedra lean over equally about two pseudocubic axes, which forms an edge based hinge. The dize of the octahedra is virtually unchanged as is the degree and nature of the tilt. Slightly different to the transitions between the parent and structures 21 and 26 is the more subtle artefact of the $0.04°$ rotation about the $\mathbf{y}'$ axis has not reduced as much in the present system (it is about $0.025°$ in the present).

Table 4.5.14: The octahedral tilt and distortion around titanium atom T_1 in structure 28. The octahedral volume was $9.9692\,\text{Å}^3$ which is 1.0076 of the ideal cubic equivalent.

Stick	θ (°)	θ_1 (°)	θ_2 (°)	length l (Å)	l/l_0
$s_{x'}$	3.7773	−3.7772	0.0254	3.9088	1.0020
$s_{y'}$	5.2515	3.7253	3.7220	3.9149	1.0036
$s_{z'}$	3.7773	−0.0254	−3.7772	3.9088	1.0020

We see a symmetrical set of internal angles in the present system, and additionally note that the distortion of s_β is slightly less than in the parent. Respectively s_α, s_β and s_γ are $90.05°$, $89.59°$ and $90.05°$.

Dipole (per formula unit): $0.461\,\mathrm{D}$ of which the strontium contributes $0.201\,\mathrm{D}$ and the titanium contributes $0.260\,\mathrm{D}$, both inclined directly in the $\mathbf{y}'$ direction. There is however, a strong antiferroelectric element to the dipole configuration, as the titanium dipoles have a maximum inclination of 7.9° to one another and the strontium dipoles have a maximum inclination of 14°. The antiferroelectric component of both titanium and strontium based dipoles acts in the $\mathbf{x}' + \mathbf{z}'$ direction.

Imaginary modes: There is only one imaginary mode in the present system, with a frequency of $48.5i\,\mathrm{cm}^{-1}$; it is depicted in table 4.5.15 and figure 4.5.10. This mode has two components: a ferroelectric ionic shift in the direction of the $\mathbf{a}$ vector ($\mathbf{x}' - \mathbf{z}'$ direction) and a rotation about the $\mathbf{y}'$ axis. The imaginary mode is qualitatively almost identical in character to that of structure no. 24 and only differs in that mode 60 of structure 24 had a component of rotational motion about the $\mathbf{c}$ vector also i.e. a rocking of the octahedra in the direction of the $\mathbf{a}$ vector.

Table 4.5.15: Eigenvectors for the imaginary mode no. 60 of structure no. 28, with frequency $48.5i\,\mathrm{cm}^{-1}$.

Atom	d$\mathbf{x}'$	d$\mathbf{y}'$	d$\mathbf{z}'$
S_1	−0.09	−0.00	0.09
S_2	−0.09	0.00	0.09
S_3	−0.09	−0.00	0.09
S_4	−0.09	0.00	0.09
T_1	−0.17	0.00	0.17
T_2	−0.17	0.00	0.17
T_3	−0.17	0.00	0.17
T_4	−0.17	0.00	0.17
O_1	0.17	0.00	−0.17
O_2	0.17	0.00	−0.17
O_3	0.17	0.00	−0.17
O_4	0.17	0.00	−0.17
O_5	0.06	−0.00	−0.16
O_6	0.16	0.00	−0.26
O_7	0.16	0.00	−0.26
O_8	0.06	0.00	−0.16
O_9	0.26	0.00	−0.16
O_{10}	0.16	−0.00	−0.06
O_{11}	0.16	0.00	−0.06
O_{12}	0.26	0.00	−0.16

The present imaginary mode 60 is derived from two modes in the parent system. The main contributor is the imaginary mode 59 ($63.0i\,\mathrm{cm}^{-1}$), which is inclined at 17° to the present mode. The other contributor is real mode no. 53 ($37.7\,\mathrm{cm}^{-1}$, which is inclined at 73° to present mode 60.

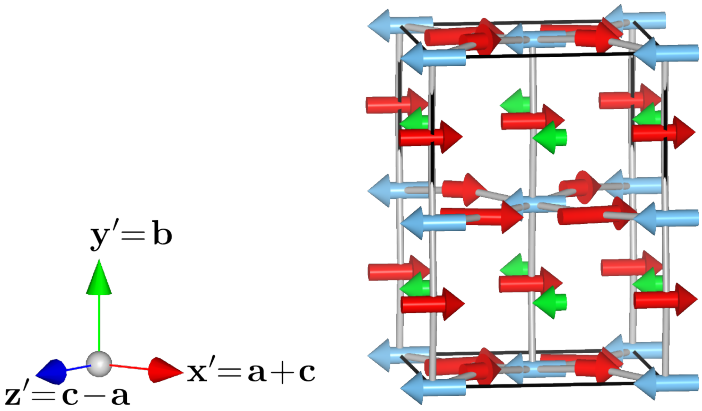

Figure 4.5.10: Graphical representation of the imaginary modes no. 60 of structure 28. Green, blue and red arrows respectively represent motion of strontium, titanium and oxygen.

4.5.2.10 Structure no. 29 (Pc)

Transitioning: The parent structure was no. 28 and the present structure was obtained after optimization by nudging the atoms in the direction of imaginary mode 60, with a frequency of $48.5i\,\mathrm{cm}^{-1}$. During the transition, in which the symmetry of the lattice was reduced from orthorhombic to monoclinic, we see that a increased significantly, while b decreased significantly. Both were expected, based on the ferroelectric transition in the $\mathbf{a}$ direction. We also note that c increased slightly. The octahedral motion involved a rotation about the $\mathbf{y}'$ axis of about a degree, which we expect is the cause of the increase in c as it would not be caued by the ferro and antiferroelectric ionic motion. The explanation for the mechanism of this process (expansion of c due to the given octahedral rotation) was given in the transitioning part of section 4.5.2.6, where structure 25 is described. However we should note that in the transition to structure 25, both a rocking over octahedra (slightly) towards an edge and an axial rotation about the $\mathbf{y}'$ axis interacting with the previous edge based rotation were responsible for the expansion of c. In the present case, there is only an axial rotation interacting with the edge based rotation, resulting in a similar outcome. The distinction in the nature of the rotation in the two structures (25 and 29) suggests that the rocking over of the octahedra, not directly towards a face is at least not a requirement for an expansion in c and is possibly not very relevant.

Several modes had a small involvement in the present transition. However, mode 60 ($48.5i\,\mathrm{cm}^{-1}$) was inclined at $29°$ to the difference vector and so as expected contributed most to the transition. The next two most involved modes were modes 54 and 51 with frequencies of 41.5 and $101.6\,\mathrm{cm}^{-1}$, these were each inclined to the difference vector at $74°$ and $77°$ respectively.

During the transition, mode 60 from the parent, hardened and split to become a

part of at least six modes. The most directly involved was mode no. 52 which had a frequency of $101.5\,\mathrm{cm}^{-1}$ and was inclined at 33° to the parent mode 60. The others ranged in frequency from 33.6 to $172.4\,\mathrm{cm}^{-1}$

Space group: Pc (no. 7), which is monoclinic.

Cell definition (Å and degrees): $a = 5.5162$, $b = 7.7845$, $c = 5.5284$;
$\alpha = 90.00$, $\beta = 90.00$, $\gamma = 90.04$;
$a : b : c = 1.0021 : 1 : 1.0044$.

Cell volume: $237.40\,\text{Å}^3$, $V/4V_0 = 0.9998$.

Potential energy (per formula unit): $-39.77936\,\mathrm{eV}$, which is a drop of $0.312\,\mathrm{meV}$ from the parent structure (28) and equivalent to a temperature drop of $\sim 0.72\,\mathrm{K}$.

Polyhedral distortion: In table 4.5.16, we have displayed two octahedra (the ones around T_1 and T_2 were essentially identical as were the ones around T_3 and T_4, see figure 4.5.1 on page 170) as we observed some slight differences in them besides sign of angles. Though there were variations in previous cases, we ignored these if the differences were lower than 0.01°. The differences are probably not of any physical significance but the two examples were included for completeness.

Examining the oxygen octahedra around T_1 we see that the octahedron rocks in a symmetrical fashion around the $\mathbf{a}$ vector as did its parent. The magnitude of the tilt has reduced by about 0.04°. We also observe a rotation about the $\mathbf{y}'$ axis of $\sim 1.1^\circ$. The octahedron does not lean in any other direction and as such is very similar to the octahedra in structure no. 27 (table 4.5.13). We note though that the octahedra in structure 27 have a smaller rotation about the $\mathbf{a}$ vector and a larger rotation about the $\mathbf{y}'$ axis ($\mathbf{b}$ vector).

Table 4.5.16: The octahedral tilt and distortion around titanium atom T_1 (top) and T_3 (bottom) in structure 29. The octahedral volume was $9.9777\,\text{Å}^3$ which is 1.0085 of the ideal cubic equivalent for both octahedra.

Stick	θ (°)	θ_1 (°)	θ_2 (°)	length l (Å)	l/l_0
$s_{x'}$	3.8659	−3.7142	−1.0771	3.9138	1.0033
$s_{y'}$	5.2070	3.6920	3.6901	3.9084	1.0019
$s_{z'}$	3.8658	1.0771	−3.7141	3.9138	1.0033
$s_{x'}$	3.8744	−3.7140	−1.1080	3.9138	1.0033
$s_{y'}$	5.2071	3.6901	3.6920	3.9084	1.0019
$s_{z'}$	3.8743	1.1080	−3.7140	3.9139	1.0033

For the octahedron around T_1, the internal octahedral angles are 89.93°, 89.63° and 90.12° for s_α, s_β and s_γ respectively, indicating a moderately deformed system.

Dipole (per formula unit): $0.634\,\mathrm{D}$ of which the strontium is responsible for $0.284\,\mathrm{D}$ and the titanium is responsible for $0.350\,\mathrm{D}$, both inclined in the same direction. The overall dipole moment vector is given by $-0.403\mathbf{x}' - 0.276\mathbf{y}' + 0.403\mathbf{z}'$. The antiferroelectric component from the titanium ions is small, as the dipoles are only deviated by $1.9°$ from one another; strontium dipoles have a maximum separation of $6.0°$. The antiferroelectric component of both strontium and titanium acts in the direction of the $\mathbf{c}$ vector (or the $\mathbf{x}' + \mathbf{z}'$ direction).

Imaginary modes: There are no imaginary modes in the present system as this is an end point structure.

Having considered the 10 structures, composing the orthorhombic ancestor systems on and individual basis, we now consider the vibrational frequencies as an overview.

4.5.3 Frequency Analysis

Table 4.5.17 lists all of the vibrational frequencies of the 10 orthorhombic ancestor systems 20–29, together with those of the $Pm\bar{3}m$ system in the same type of cell. These have been included for reference to the preceding section and could be useful if one were looking to compare the results to spectroscopic data.

In table C.3 (page 251), we compare the sets of frequencies for every structure with every other, looking for the maximum deviation. This type of analysis can help confirm or elucidate similarities between structures. The analysis identified four pairs of structures that are very similar to one another and we will briefly make note of these here.

Structures 26 and 22 (for which there is a maximum difference of $2.4\,\mathrm{cm}^{-1}$) are similar in energy and in terms of the lattice lengths, though we note that the angle β on structure 22 deviates from the orthorhombic by $0.1°$, where as 26 is orthorhombic. The octahedra are also similar though structure 22's octahedra rock slightly towards the cell edge, where as 26's rock strictly towards a face. It seems that this difference may not be important.

Structures 27 and 23 (for which there is a maximum difference of $4.9\,\mathrm{cm}^{-1}$) are similar in energy and again, lattice lengths are similar, though β deviates from $90°$ by about $0.1°$ in structure 23. Both structures have a similar rotation about $\mathbf{y}'$ but we note that as with structure 22, 23 has octahedra that rock partially towards a cell edge, while the octahedra in structure 27 rock only towards a face.

Structures 28 and 24 (for which there is a maximum difference of $5.4\,\mathrm{cm}^{-1}$)) are degenerate in energy, have almost identical lattice parameters and octahedra that are qualitatively identical and quantitatively very similar. We have already made comparisons of these two structures in the description of structure 28 (see section 4.5.2.9), we

noted that there was a slight difference in the dipole moment and in the nature of the eigenvectors.

Structures 29 and 25 (for which there is a maximum difference of $2.1\,\mathrm{cm}^{-1}$) are degenerate in energy. The lattice lengths are similar though there are some small differences in the cell angles. We see a similar rotation of octahedra about $\mathbf{y}'$ as well as a similar angular separation from $\mathbf{y}'$. Again, we note that structure 29 has octahedra that lean directly towards a cell wall, while structure 25's octahedra lean slightly towards an edge.

We now draw the section to an end with a summary and some conclusions of what has been learned.

Table 4.5.17: Full frequency listing (in cm^{-1}) of the orthorhombic $Pnma/Imma$ ancestor structures. The cubic $Pm\bar{3}m$ frequencies in the tetragonal/orthorhombic unit cell have also been included here. Blocks of $-$ and $+$ indicate degenerate modes. The labelling is identical to table 4.4.18 though.

Freq. no.	Label	Structure number										
		$Pm\bar{3}m$	20	21	22	23	24	25	26	27	28	29
1	$-$	829.9	817.3	818.4	819.2	819.5	819.2	819.5	819.2	819.7	819.2	819.5
2	$+$	795.9	784.2	785.7	788.0	787.1	785.5	787.7	787.9	787.5	785.4	787.8
3	$-$	747.3	735.1	736.1	735.9	742.2	744.6	739.1	735.9	741.8	744.9	739.6
4	Γ_{15} (TO3)	533.2	529.4	530.8	542.7	535.0	530.7	540.4	541.7	537.8	529.9	540.6
5	Γ_{15} (TO3)	533.2	528.4	529.7	531.1	530.1	528.9	530.8	531.1	530.3	529.7	530.9
6	Γ_{15} (TO3)	533.1	522.1	523.0	529.7	529.2	524.5	529.4	529.1	529.4	524.4	529.7
7	$+$	528.1	519.8	520.8	526.9	526.9	521.3	525.5	526.6	527.4	521.2	526.5
8	$-$	505.5	499.4	509.3	523.4	522.5	509.3	524.9	523.4	523.2	509.4	524.9
9	$-$	505.1	495.2	502.2	512.6	510.2	501.7	510.2	510.9	509.6	501.4	510.4
10	$-$	505.1	490.9	492.2	502.8	504.3	498.9	502.9	502.9	507.9	496.8	503.0
11	$+$	473.8	470.4	479.8	501.7	502.3	492.5	501.5	501.2	502.8	492.2	502.1
12	$+$	473.8	469.7	475.8	489.8	500.3	470.3	501.3	489.7	501.0	470.6	501.4
13	$-$	470.7	468.2	470.2	464.8	465.3	470.2	465.1	465.0	465.1	468.1	465.2
14	$-$	470.7	465.8	457.5	456.4	462.5	465.2	458.0	456.5	462.0	467.1	459.6
15	$+$	465.6	457.4	456.4	453.4	456.5	464.8	456.4	453.4	456.3	465.1	456.4
16	$-$	452.6	450.5	452.0	437.1	442.0	457.9	438.5	438.1	439.9	457.9	438.4
17	$+$	430.2	431.3	431.7	430.8	429.9	430.9	430.5	431.0	429.9	430.9	430.5
18	$+$	430.2	428.2	428.3	427.3	428.4	429.1	427.7	427.1	428.4	429.1	427.7
19	$+$	429.4	426.8	426.6	427.0	424.3	426.4	425.0	427.1	424.3	426.6	425.2
20	$-$	424.9	425.9	422.7	423.5	421.1	423.7	422.0	423.5	421.0	425.0	422.0
21	$-$	424.9	425.9	422.6	408.3	398.2	421.3	401.9	408.7	396.2	421.8	402.1
22	$-$	424.8	422.7	414.1	392.0	395.7	395.5	393.7	393.0	395.9	395.4	393.6
23	$+$	317.3	329.5	330.4	328.8	327.9	329.0	328.5	329.1	328.0	328.9	328.6
24	$+$	317.3	323.8	323.8	323.7	324.7	323.3	324.0	323.8	324.8	323.3	324.1
25	$-$	311.0	321.2	321.2	321.5	320.3	321.1	321.3	321.8	320.4	321.1	321.4
26	$-$	311.0	309.0	309.2	311.5	310.0	308.6	310.3	311.0	309.3	308.6	310.7
27	$+$	274.6	289.9	290.0	291.9	291.4	289.2	291.3	291.5	291.0	289.2	291.3
28	$-$	272.9	287.3	287.5	285.2	282.6	286.3	284.7	286.1	283.1	286.3	284.9
29	$+$	258.5	269.8	270.3	269.5	268.7	268.6	269.3	269.6	268.9	268.6	269.3
30	$+$	258.5	259.5	261.1	260.0	260.4	261.2	260.4	260.4	260.6	261.0	260.5
31	Γ_{25}	228.5	251.0	250.6	253.9	253.9	251.2	253.5	253.6	253.4	251.3	253.8
32	Γ_{25}	228.5	242.0	242.5	244.8	245.6	244.5	245.5	244.8	245.4	244.4	245.4
33	Γ_{25}	227.8	235.1	235.3	241.9	241.8	236.7	241.7	241.2	241.9	236.8	241.9
34	$-$	163.7	180.9	184.9	197.7	193.0	183.1	196.4	196.6	194.9	182.6	196.4
35	$-$	163.7	174.0	175.6	190.3	187.4	175.9	189.7	189.8	188.7	175.7	190.0
36	$-$	163.2	165.5	167.3	172.4	172.2	172.2	172.5	171.2	173.1	172.5	172.4
37	Γ_{15} (TO2)	156.8	164.0	163.7	169.7	168.4	166.5	169.5	169.7	168.8	166.4	169.5
38	Γ_{15} (TO2)	156.7	160.8	160.5	161.3	167.2	163.9	164.6	161.1	167.6	164.0	164.5
39	Γ_{15} (TO2)	156.7	159.0	160.0	160.2	164.0	160.4	161.7	160.4	163.8	160.2	161.6
40	$+$	129.1	145.8	145.8	145.1	143.2	146.3	144.8	145.6	143.4	146.3	144.8
41	$+$	129.1	135.4	135.8	136.6	139.3	139.6	137.4	135.9	138.8	140.3	137.3
42	$+$	129.0	133.4	133.6	136.1	135.6	135.0	137.1	135.3	136.6	134.9	137.0
43	$-$	111.2	124.8	125.4	134.2	133.8	133.8	132.9	133.6	135.2	133.8	132.8
44	$+$	108.8	118.7	119.8	129.0	132.3	124.0	129.5	129.6	132.0	124.0	129.7
45	$+$	108.8	115.5	115.3	127.6	127.1	119.4	125.9	127.0	129.1	119.3	125.8
46	$-$	106.4	114.7	115.3	117.4	123.9	116.4	125.7	116.5	123.8	116.4	125.8
47	$-$	106.4	110.2	109.8	116.7	118.6	112.8	116.7	115.7	118.3	112.6	116.4
48	$+$	102.1	107.9	109.7	114.7	114.7	110.5	115.7	115.6	114.1	110.5	115.3
49	$+$	102.1	105.0	109.6	114.5	112.8	108.0	114.6	113.2	113.4	106.9	115.0
50	$-$	101.5	103.0	107.4	110.6	109.9	106.9	110.5	110.6	110.2	106.8	110.6
51	$+$	13.1	86.8	94.3	104.1	99.0	101.0	102.7	103.1	99.8	101.6	103.6
52		0.2	52.6	52.1	98.8	98.9	92.7	101.1	98.3	99.4	92.0	101.5
53		0.2	37.7	41.5	98.4	94.1	52.6	98.6	97.8	99.1	52.6	98.7
54		0.2	32.0	38.8	53.1	88.5	42.0	69.5	52.5	90.6	41.6	70.6
55	Γ_{15} (TO1)	$67.2i$	4.7	38.1	48.0	59.4	30.5	54.7	48.0	58.7	28.5	54.6
56	Γ_{15} (TO1)	$67.2i$	0.6	0.9	25.5	31.8	29.4	33.5	25.6	31.4	24.0	33.6
57	Γ_{15} (TO1)	$68.7i$	0.5	0.5	$0.1i$	24.1	0.4	24.8	1.3	22.8	0.5	27.0
58	$-$	$79.6i$	$47.3i$	$0.3i$	$0.2i$	$0.3i$	$0.3i$	$0.2i$	$0.3i$	$0.3i$	$0.4i$	$0.6i$
59	$-$	$79.6i$	$63.0i$	$48.9i$	$1.7i$	$0.3i$	$0.3i$	$0.3i$	$1.2i$	$0.4i$	$1.3i$	$0.7i$
60	$-$	$79.6i$	$63.5i$	$54.7i$	$25.0i$	$0.6i$	$46.0i$	$1.5i$	$27.5i$	$0.5i$	$48.5i$	$0.9i$

4.5.4 Summary of Orthorhombic Ancestor Systems

Much of what has been observed in the tetragonal ancestor systems is equally valid for the orthorhombic ancestor systems. We found that the high symmetry orthorhombic ancestor systems were of significantly higher energy than those of the tetragonal ancestor systems. We also note that the lowest energy orthorhombic ancestor system is higher than the ground state system, though the absolute differences in energy between the lowest energy tetragonal and orthorhombic ancestor systems is small (about 0.12 meV, corresponding to ~ 0.28 K). The highest energy orthorhombic ancestor system (structure 20) is 6.58 meV beneath the high symmetry $Pm\bar{3}m$ cubic system (1) and is equivalent to a drop of ~ 15 K. The lowest energy orthorhombic ancestor system (structure 23) is 0.60 meV, corresponding to ~ 1.4 K beneath the highest. As such we may not actually see these phase phase transitions in experiment.

In the tetragonal ancestor system we saw that, ignoring the polar distortions, the changes to the octahedra began with a rotation about $\mathbf{y}'$ of about 5° and were followed with a rocking over either towards a cell face or a cell edge, usually less than 1°. In the case of the orthorhombic ancestor systems, there was an initial rotation (rocking) of the octahedra about a short lattice vector (towards a cell face) of about 5° followed by a rotation about $\mathbf{y}'$ of 1° to 2°. There appeared to be a very small energetic advantage of the octahedra also rocking slightly in the direction of the other face but as there were no structures that were close to rocking directly towards a cell edge (rotation about either the $\mathbf{x}'$ or $\mathbf{z}'$ pseudo-cubic axes), this many be energetically unfavourable.

In general, we note that both tetragonal and orthorhombic ancestor systems tend to rotate on an axis (the $\mathbf{y}'$) and rock over towards a cell face. However the tetragonal ancestor systems favour a strong axial rotation and a weak rocking, while the orthorhombic ancestor systems favour a strong rocking and a weak axial rotation. There appears to be an energy barrier between these two configurations, which may be enforced by the distortions in the lattice that correspond to the changes in the octahedra. The energy barrier between the top level structures from these two dendrimer trees i.e. structures 9 ($I4/mcm$) and 20 ($Pnma/Imma$) was calculated using an 18 point NEB calculation and found to be 0.208 meV when going from structure 20 to 9 and 0.658 meV going from 9 to 20 (see figure 4.2.2, where the barrier has been represented graphically). There was no fitting performed on the NEB data, so the high energy point refers to the highest energy intermediate structure along the elastic band.

By considering the nature of the cell, we can readily understand in both the tetragonal and orthorhombic ancestor systems, why axial rotation about one or other of the $\mathbf{x}'$ or $\mathbf{z}'$ axes has never been the most dominant type of rotation. If we consider the $I4/mcm$ tetragonal system, where the most dominant type of rotation has been about the $\mathbf{y}'$ axis, we note that the sets of octahedra stacked up on top of one another counter-

rotate. This counter-rotation allows maximum separation of oxygen atoms between the stacked pairs of octahedra. If we now consider an example where the rotation is only about one or the other pseudo-cubic axes, then due to the configuration of the cell, the images of the octahedra in the direction of the rotation axis, would be rotating in the same direction (and so not allowing the same separation of oxygen). We therefore see, that the choice of cell enforces an orientation to the types of rotation that can take place. However, when a larger cell was used ($2\times2\times2$ compared to 5 atom cubic) as in structure 38 (see section 4.6.2.9), no (significantly) lower energy state was found than in the tetragonal ancestor structure 14 which implies that the limited cell size, did not impinge on the types of rotation and distortion that can take place (only the orientation of them).

In the transitions from structure 24 to 25 and 28 to 29 we observed a new correlation between octahedral rotations and changes to the cell lengths. These were commented on in section 4.5.2.6 with some additional commentary given in section 4.5.2.10. We knew already that the octahedra of a cell rocking over towards a cell face will usually cause an expansion of the lattice in that direction (by rocking we mean a rotation about a combination of two pseudo-cubic vectors, which in the context of the 20 atom cells means a rotation about the **a** or **c** axes). It is assumed that this expansion is due to a concertina effect of the octahedra. When this edge based rotation is combined with an axial rotation, then we can expect an expansion in a and c (and a change in β). It is expected that this expansion is due to repulsion between oxygen and titanium atoms.

Though phase transition energies were generally greater in the orthorhombic ancestor systems than in the tetragonal, they are still rather small and so they may not be observed in experiment. However, the results illustrate very nicely the types of distortion to which STO is prone.

We now move on to considering the rhombohedral system, for which we used a different 10 atom unit cell.

4.6 Rhombohedral Unit Cell

4.6.1 Introduction

We now consider the final set of structures, which form the rhombohedral ancestor systems. The geometry optimized starting cell has $R\bar{3}c$ symmetry and has been shown, with atom labels in figure 4.6.1. The unit cell is very different from the previous ones considered, which had cell angles of $\sim 90°$. However, the 10 atom unit cell used here is able to encompass most of the atomic motion described in the tetragonal and orthorhombic ancestor systems.

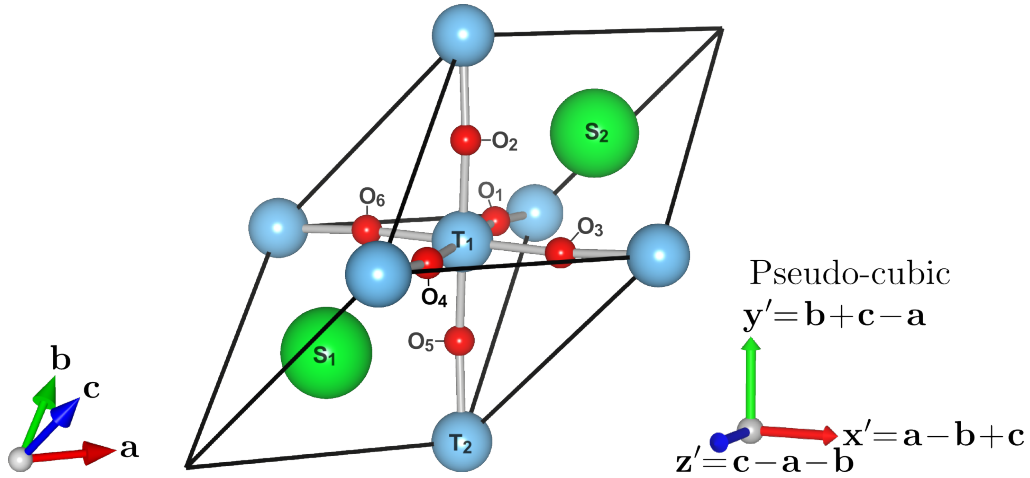

Figure 4.6.1: Structural diagram of the 10 atom $R\bar{3}c$ rhombohedral strontium titanate cell. The direction of the lattice vectors has been shown together with the direction of the pseudo-cubic axis. Green, blue and red balls represent respectively, strontium, titanium and oxygen atoms.

The unit cell in use for this section has angles approximately equal to $60°$ and lattice parameters approximately equal to $\sqrt{2}$ of the cubic. If the cell is actually an ideal cubic system, in the setting shown in figure 4.6.1, then those approximations are exact. For the cell to be rhombohedral, then $\alpha = \beta = \gamma \neq 60°$ and $a = b = c$.

A more detailed version of the dendrimer diagram in figure 4.2.2 has been displayed for the tetragonal ancestor systems in figure 4.6.2.

We will now move through the rhombohedral ancestor dendrimer diagram considering the 8+1 structures in their numerical order. Some consideration of the relationship of the highest symmetry rhombohedral structure ($R\bar{3}m$) to the ideal cubic system ($Pm\bar{3}m$) will be made at the start (a cubic system in a rhombohedral type cell was generated for this purpose). A list of frequencies for the tetragonal ancestor structures can be found in table 4.6.13 on page 223.

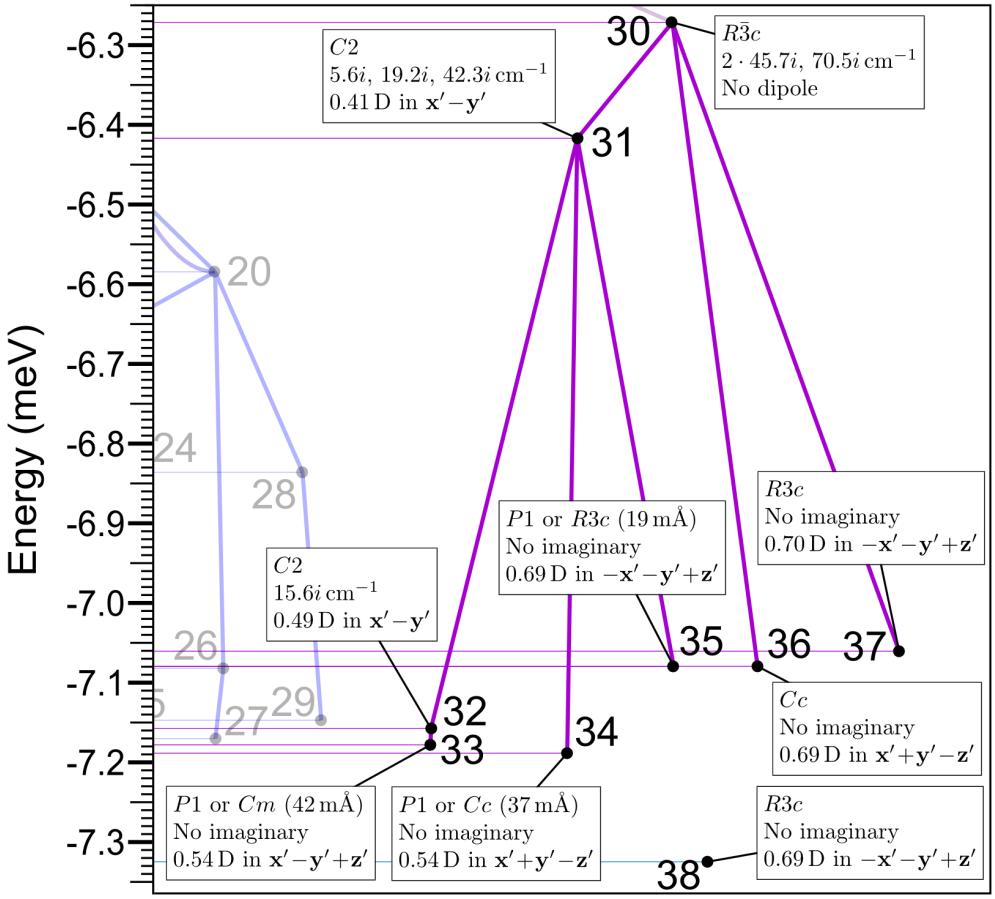

Figure 4.6.2: Dendrimer plot summarizing the rhombohedral ancestor phase transitions. Here we provide a magnified version of figure 4.2.2, with labels showing the space groups, imaginary frequencies and dipole moments of the 8 structures that were considered in this part of the study. Additionally, structure 38, which is based on a $2\times2\times2$ cubic supercell but with rhombohedral symmetry is marked.

4.6.2 The Structures

4.6.2.1 Structure no. 30 $R\bar{3}c$

Transitioning: The present structure is a starting structure, but by comparing it to the same type of cell, put into the cubic symmetry, we can consider the transition from the cubic $Pm\bar{3}m$ system to the rhombohedral $R\bar{3}m$ system. The transition involved rotations only; there was no change in the net dipole, nor were there local dipoles of any significance. The result was a highly symmetrical structure, with a reduced volume and all sticks departing from their equivalent pseudo-cubic axes by $4.2°$.

The cubic symmetry system in the rhombohedral type unit cell have six imaginary modes and 25–27 are the degenerate Γ_{15} (TO1) modes. Degenerate modes 28–30 involve complicated rotational motion of the oxygen atoms only. Modes 28 and 29 (with a frequency of $80.1i\,\mathrm{cm}^{-1}$) were found to be most directly involved in the transition. Mode 28 is inclined at $79°$ to the difference vector and mode 29 is inclined at $15°$ to it;

both modes are depicted in figure 4.6.3.

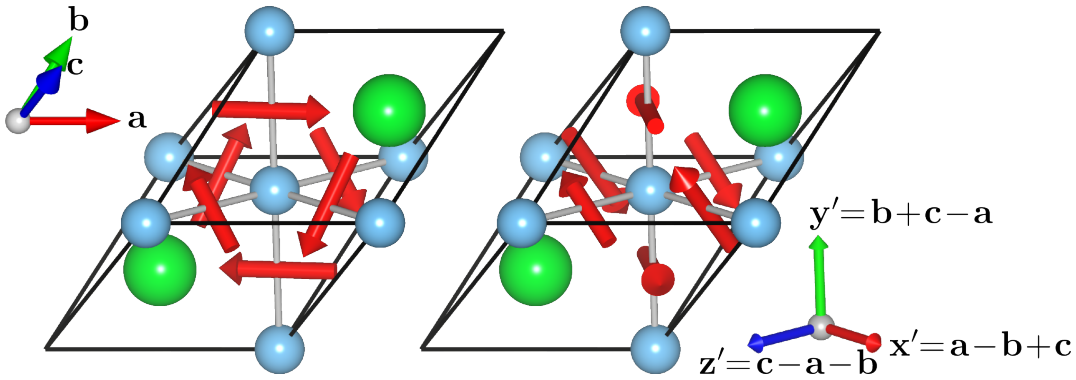

Figure 4.6.3: A representation of the degenerate imaginary modes no. 28 (left) and 29 (right) of the $Pm\bar{3}m$ structure in the rhombohedral setting. Green, blue and red respectively represent strontium, titanium and oxygen. Atoms not vibrating are represented as balls, vibrating atoms are arrows. For clarity, we now show the orientation using both lattice parameters and the pseudo-cubic axes.

In both of these modes, the oxygen atoms move in counter rotating pairs, either end of the octahedral sticks. The eigenvector of mode 28 shows a rotation about the $\mathbf{y}'$ axis and a rotation about the $\mathbf{x}' + \mathbf{z}'$ vector (rocking towards $\mathbf{x}' - \mathbf{z}'$ or to the right as it is drawn on the page). Mode 29's eigenvector also shows a rotation about $\mathbf{y}'$ in the same direction only the rocking is at right angles to mode 28 i.e. away from the page, in the $-\mathbf{x}' - \mathbf{z}'$ direction or about the $\mathbf{x}' - \mathbf{z}'$ vector.

We should note that there is a problem with the calculated frequencies for the translational modes and the Γ_{15} (TO3) modes, which is discussed in more detail in section 4.6.3 and table 4.6.13.

All three of the degenerate modes 28–30 harden during the transition, leaving only three imaginary modes in the $R\bar{3}c$ system. We see that the degenerate modes harden and split to form part of five modes: degenerate modes 19 and 20 ($140.9\,\mathrm{cm}^{-1}$), mode 22 ($117.2\,\mathrm{cm}^{-1}$) and degenerate modes 23 and 24 ($17.2\,\mathrm{cm}^{-1}$). Modes 19 and 20 were only contributed to in a small way by the parent modes 28–30, the angle of inclination was between $83°$ and $89°$. The remaining three modes in the present structure 22, 23 and 24 were each contributed to by the parent modes 28–30, though for each mode in the present structure, one mode from the parent was dominant. Mode 28 in the parent was inclined at $14°$ to mode 24, mode 29 in the parent was inclined at $12°$ to mode 22 and mode 30 in the parent was inclined at $8°$ to mode 23.

Space group: $R\bar{3}m$ (no. 167).

Cell definition (Å and degrees): $a = 5.5081, b = 5.5081, c = 5.5081;$
$\alpha = 60.13, \beta = 60.13, \gamma = 60.13;$

Cell volume: $118.51\,\text{Å}^3$, $V/2V_0 = 0.9982$.

Potential energy (per formula unit): $-79.55696\,\text{eV}$, which is a drop of $6.27\,\text{meV}$ from the parent structure 1 and equivalent to a temperature drop of $\sim 14.5\,\text{K}$.

Polyhedral distortion: From table 4.6.1, we see that the present structure is highly symmetrical. The octahedral deviations from the pseudo-cubic axes are all identical and set at $4.2°$. Unlike the tetragonal and orthorhombic ancestor systems, there is no favoured direction of rotation of the octahedra. The projection of the rotation around each plane of pseudo-cubic axis is $3.0°$. We make this comment as a comparison to the tetragonal and orthorhombic ancestor systems, where we would expect to see rotations about the $\mathbf{y}'$ axis of around $5°$ for the tetragonal ancestors and around $1°$ to $2°$ for the orthorhombic ancestors.

Table 4.6.1: The octahedral tilt and distortion around titanium atom T_1 in structure 30. The octahedral volume was $9.9566\,\text{Å}^3$ which is 1.0063 of the ideal cubic equivalent.

Stick	θ (°)	θ_1 (°)	θ_2 (°)	length l (Å)	l/l_0
$s_{x'}$	4.2262	−2.9939	−2.9939	3.9092	1.0021
$s_{y'}$	4.2262	2.9939	2.9939	3.9092	1.0021
$s_{z'}$	4.2262	2.9939	−2.9939	3.9092	1.0021

The internal angles of the octahedra are all equivalent to one another with s_α, s_β and s_γ values of $89.73°$, $89.73°$ and $90.27°$ respectively.

Dipole (per formula unit): There is virtually no dipole in this system, very small values $\sim 2 \times 10^{-4}\,\text{D}$ are most likely imperfections in the optimization.

Imaginary modes: There are three imaginary modes in the present structure, two of which are degenerate in energy and one non-degenerate; their frequencies are $45.7i\,\text{cm}^{-1}$ for modes 28 and 29 and $70.5i\,\text{cm}^{-1}$ for mode 30. All three imaginary modes are predominantly ferroelectric. The imaginary modes have been described and depicted in table 4.6.2 and figure 4.6.4.

Mode 30, is the simplest to describe as it is purely ferroelectric with the ionic shifts acting in the direction of an octahedral face. Modes 28 and 29 are rather complicated as they involve a ferroelectric shift, and antiferroelectric shift and a distortion to the octahedra themselves.

Mode 28 has a ferroelectric shift, acting between two pseudo-cubic axes (in the $\mathbf{y}' - \mathbf{x}'$) direction. It is not clear that there is any rotational component to the octahedral distortion. However, the $s_{x'}$ and $s_{y'}$ sticks appear to be pushed in opposite directions in the direction of the $\mathbf{z}'$ axis (easiest to determine by looking at table 4.6.2). This last type of distortion has not been noticed in previous sets of eigenvectors.

Mode 29 is essentially the same in nature as mode 28 (they are degenerate) but in this case the net ferroelectric component of the displacement acts along all three

pseudo-cubic axes (in the $\mathbf{x}' + \mathbf{y}' + \mathbf{z}'$ direction).

Table 4.6.2: Eigenvectors for the imaginary modes no. 28 (left), 29 (middle) and 30 (right) of structure no. 30, frequency are $45.7i$, $45.7i$ and $70.5i\,\mathrm{cm}^{-1}$ respectively.

Atom	dx′	dy′	dz′
S_1	0.09	−0.09	0.00
S_2	0.09	−0.09	0.00
T_1	0.26	−0.31	−0.05
T_2	0.31	−0.26	0.05
O_1	−0.22	0.22	0.00
O_2	−0.24	0.23	0.02
O_3	−0.23	0.24	−0.02
O_4	−0.22	0.22	0.00
O_5	−0.24	0.23	0.02
O_6	−0.23	0.24	−0.02

Atom	dx′	dy′	dz′
S_1	0.05	0.05	0.10
S_2	0.05	0.05	0.10
T_1	0.21	0.12	0.33
T_2	0.12	0.21	0.33
O_1	−0.15	−0.15	−0.26
O_2	−0.12	−0.13	−0.27
O_3	−0.13	−0.12	−0.27
O_4	−0.15	−0.15	−0.26
O_5	−0.12	−0.13	−0.27
O_6	−0.13	−0.12	−0.27

Atom	dx′	dy′	dz′
S_1	−0.11	−0.11	0.11
S_2	−0.11	−0.11	0.11
T_1	−0.21	−0.21	0.21
T_2	−0.21	−0.21	0.21
O_1	0.20	0.20	−0.19
O_2	0.20	0.19	−0.20
O_3	0.19	0.20	−0.20
O_4	0.20	0.20	−0.19
O_5	0.20	0.19	−0.20
O_6	0.19	0.20	−0.20

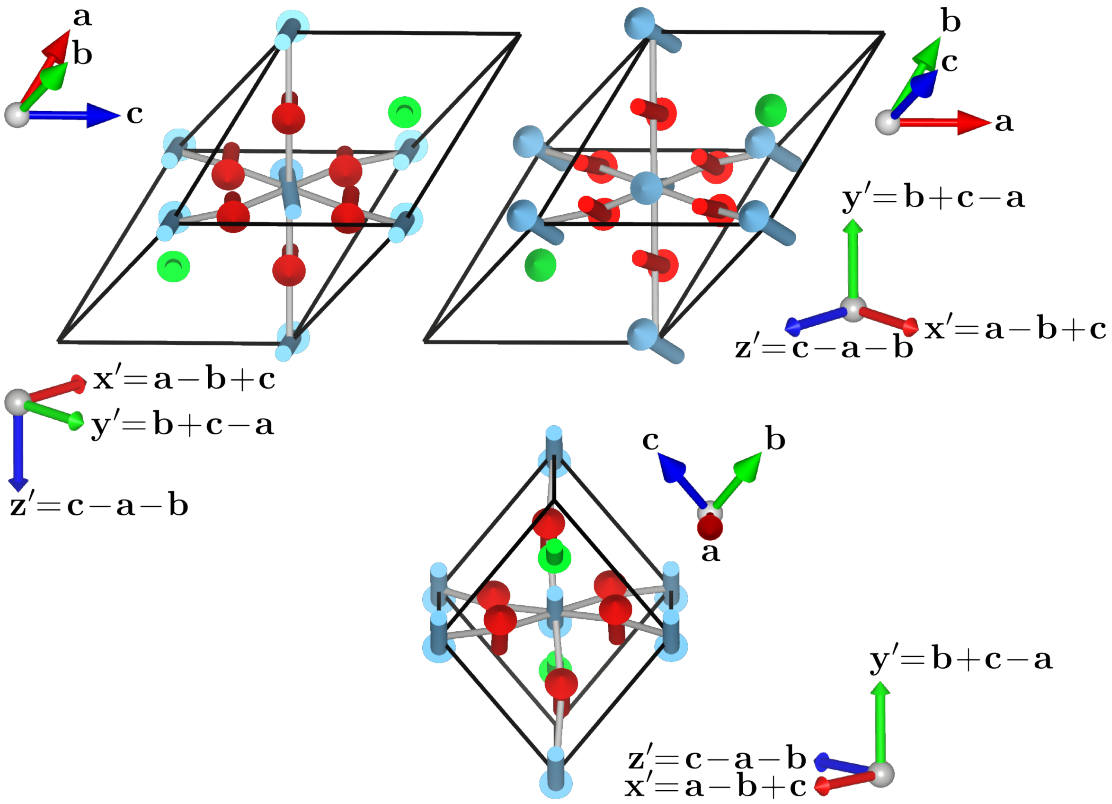

Figure 4.6.4: Graphical representation of the imaginary modes no. 28 (top left), 29 (top right) and 30 (bottom) of structure no. 30. Green, blue and red arrows respectively represent motion of strontium, titanium and oxygen. For each different orientation displayed, we show the orientation using both lattice parameters and the pseudo-cubic axes.

Let us consider the derivation of the three imaginary modes from the normal modes of the cubic structure. Mode 30 in the present structure was inherited almost unchanged from the Γ_{15} (TO1) mode 26 ($70.6i\,\mathrm{cm}^{-1}$) in the parent, parent and child modes were inclined at just 5° to one another. The degenerate modes 28 and 29 in the

present structure inherited their character from three parent modes each. Parent modes 5 ($429.5\,\mathrm{cm}^{-1}$), 18 (Γ_{15} (TO2) with a frequency of $156.1\,\mathrm{cm}^{-1}$) and 25 (Γ_{15} (TO1) with a frequency of $70.6i\,\mathrm{cm}^{-1}$) go into making the present mode 28 ($45.7i\,\mathrm{cm}^{-1}$). Parent modes 7, 16 and 27 respectively are degenerate with the previous set and go into making mode 29. The corresponding angles are $85°$, $82°$ and $11°$ respectively, for both sets of parent modes relative to their respective child mode.

4.6.2.2 Structure no. 31 ($C2$)

Transitioning: The present structure was obtained after optimization by nudging the ions of structure no. 30 in the direction of its eigenvector no. 28, with a frequency of $45.7i\,\mathrm{cm}^{-1}$. The transition was mostly ferroelectric in nature, though there was some antiferroelectric behaviour of the titanium. A small change in the rotation of the octahedra occurred along with some relatively small changes to the cell parameters: c increased the most, while a and b grew evenly (but by less than a thousandth of an Ångström), the rhombohedral symmetry of the parent was reduced to monoclinic symmetry. It is not entirely clear how the ionic shifts are associated with the change in the lattice parameters.

Mode 28 from the parent structure (30) was most directly responsible for the transition and is inclined at $14°$ to the difference vector. Mode 17 in the parent ($163.1\,\mathrm{cm}^{-1}$) was the next most involved, but is inclined at $84°$ to the difference vector. Several other modes played even less substantial rôles in the transition.

Mode 28 split into various parts, most of which were hard and part remained as the new mode 28 (old and new were inclined at $81°$ to one another). We note that the number of imaginary modes is unchanged from the parent to the present structure, which is unusual. We might expect this to occur in the case of imperfect optimization, but the system was converged to within $1\,\mathrm{meV\,Å}^{-1}$. Parent mode 28 most directly hardened to present mode 23 ($84.9\,\mathrm{cm}^{-1}$); the two modes are inclined at $14°$ to one another. All the other modes that mode 28 split into are inclined to it with angles greater than $80°$.

The degeneracy of modes 28 and 29 was broken during the transition. Mode 29 split into three modes: 30, 29 and 24 with frequencies of $42.3i$, $19.2i$ and $58.7\,\mathrm{cm}^{-1}$, and inclined to the original mode with angles of $60°$, $62°$ and $43°$ respectively.

Finally, mode 30 ($70.5i\,\mathrm{cm}^{-1}$) from the parent, also split into multiple parts, many of which were inclined to it with angles greater than $80°$ and two of which had angles lower than $80°$. Mode 30 was the least changed of the imaginary modes during the transition, as the parent and present mode 30s are inclined at $32°$ to one another, though it hardened somewhat to a frequency of $42.3i\,\mathrm{cm}^{-1}$. Parent mode 30 also contributed to mode 24 ($58.7\,\mathrm{cm}^{-1}$) and is inclined at $60°$ to it.

Space group: $C2$ (no. 5).

Cell definition (Å and degrees): $a = 5.5088$, $b = 5.5088$, $c = 5.5102$;
$\alpha = 60.12$, $\beta = 60.12$, $\gamma = 60.17$;

Cell volume: 118.61 Å^3, $V/2V_0 = 0.9990$.

Potential energy (per formula unit): -39.77863 eV, which is a drop of 0.15 meV from the parent structure no. 30 and equivalent to a temperature drop of ~ 0.34 K.

Polyhedral distortion: From table 4.6.3, we see a small distortion to the octahedra, involving a rotation that slightly aligns the $s_{z'}$ stick with the $\mathbf{z}'$, although the change in rotation is only a matter of $0.03°$. The separation of the $s_{x'}$ and $s_{y'}$ sticks from their respective pseudo-cubic axes has increased slightly (about $0.04°$). This second type of displacement is caused by a rotation of the octahedra about the $\mathbf{z}'$ axis.

Table 4.6.3: The octahedral tilt and distortion around titanium atom T_1 in structure 31. The octahedral volume was 9.9653 Å^3 which is 1.0072 of the ideal cubic equivalent.

Stick	θ (°)	θ_1 (°)	θ_2 (°)	length l (Å)	l/l_0
$s_{x'}$	4.2600	−3.0594	−2.9761	3.9115	1.0027
$s_{y'}$	4.2601	2.9761	3.0595	3.9115	1.0027
$s_{z'}$	4.2036	2.9784	−2.9784	3.9081	1.0018

The octahedra themselves have hardly changed from the parent structure (in as much as the analytical tools that have been constructed can determine), the internal angles s_α, s_β and s_γ have values of $89.73°$, $89.73°$ and $90.28°$ respectively. We note that the data were not analysed in a way that lets one determine if octahedral sticks shift relative to one one another. It was considered that this type of distortion might have been observed in the present structure due to the nature of the imaginary mode that led to it.

Dipole (per formula unit): 0.409 D of which the strontium dipoles contribute 0.169 D and the titanium dipoles contribute 0.241 D, both inclined in the same net direction. The overall dipole is given by $0.290\mathbf{x}' - 0.290\mathbf{y}'$. There is a strong antiferroelectric component to the dipole moment as the titanium dipoles are diverged from one another at an angle of $8°$. The difference between the two dipoles gives the antiferroelectric component (twice the antiferroelectric component on a per dipole basis): $-0.014\mathbf{x}' - 0.014\mathbf{y}' - 0.027\mathbf{z}'$ (broadly towards an octahedral face, while the overall dipole is towards an edge). The strontium dipoles are aligned with one another.

Imaginary modes: The system has three imaginary modes 28–30 with frequencies of $5.6i$, $19.2i$ and $42.3i$ cm^{-1}. Mode 28, which has an has an almost zero second derivative is somewhat unusual. Under the harmonic approximation, it is generally impossible for there to be more than three translational (zero) modes in a system where the potential

energy surface is at a stationary point, as it implies that an atom or a group of atoms can move in some path without any energetic consequence. If the potential energy surface near to a stationary point is characterised strongly by higher order terms e.g. a third or fourth order polynomials then an inflection point would be possible. However, in this work, we assume that the low magnitude of mode 28 does not indicate anharmonicity of the energy surface at the stationary point. The eigenvectors of modes 28–30 have been depicted in table 4.6.4 and figure 4.6.5.

Table 4.6.4: Eigenvectors for the imaginary modes no. 28 (left), 29 (middle) and 30 (right) of structure no. 31, frequency are $5.6i$, $19.2i$ and $42.3i\,\mathrm{cm}^{-1}$ respectively.

Atom	$\mathrm{d}x'$	$\mathrm{d}y'$	$\mathrm{d}z'$
S_1	−0.08	0.08	0.00
S_2	−0.18	0.18	0.00
T_1	−0.09	0.07	0.00
T_2	−0.07	0.09	−0.00
O_1	0.07	−0.07	0.00
O_2	0.26	0.10	−0.19
O_3	−0.10	−0.26	0.19
O_4	−0.28	0.28	0.00
O_5	−0.45	0.10	0.19
O_6	−0.10	0.45	−0.19

Atom	$\mathrm{d}x'$	$\mathrm{d}y'$	$\mathrm{d}z'$
S_1	0.03	0.03	0.02
S_2	0.09	0.09	0.13
T_1	0.12	0.08	0.15
T_2	0.08	0.12	0.15
O_1	−0.40	−0.40	−0.09
O_2	−0.07	−0.08	−0.40
O_3	−0.08	−0.07	−0.40
O_4	0.22	0.22	−0.09
O_5	−0.08	−0.08	0.21
O_6	−0.08	−0.08	0.21

Atom	$\mathrm{d}x'$	$\mathrm{d}y'$	$\mathrm{d}z'$
S_1	−0.06	−0.06	0.18
S_2	−0.08	−0.08	0.13
T_1	−0.05	−0.09	0.33
T_2	−0.09	−0.05	0.33
O_1	0.16	0.16	−0.29
O_2	0.11	0.10	−0.25
O_3	0.10	0.11	−0.25
O_4	0.04	0.04	−0.29
O_5	0.12	0.10	−0.36
O_6	0.10	0.12	−0.36

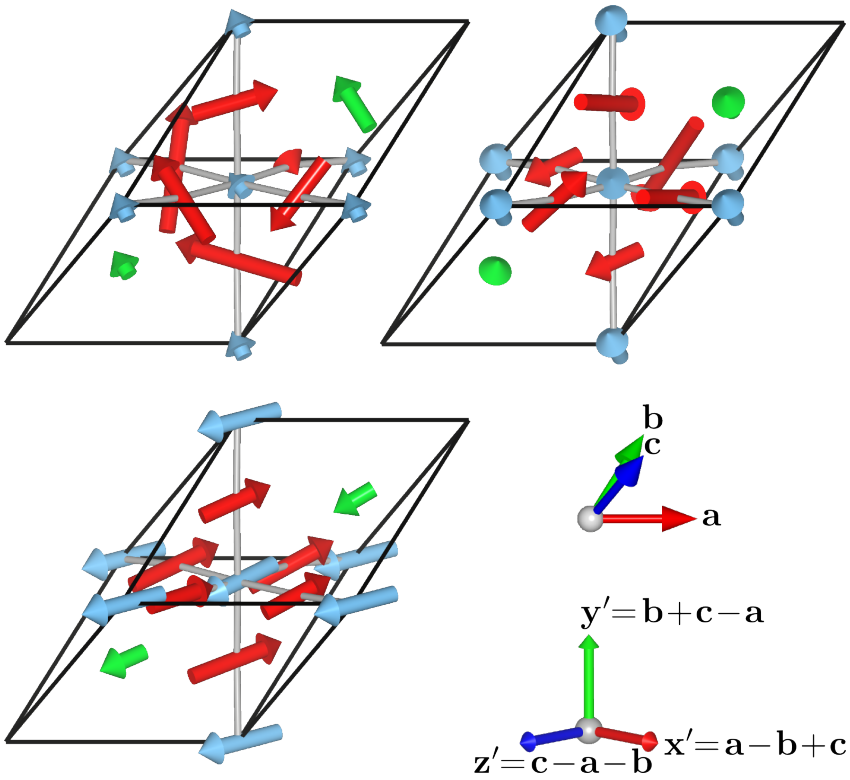

Figure 4.6.5: Graphical representation of the imaginary modes no. 28 (top left), 29 (top right) and 30 (bottom) of structure no. 31. Green, blue and red arrows respectively represent motion of strontium, titanium and oxygen.

The eigenvector of mode 28 is perhaps the hardest to analyse yet encountered. The

titanium ions have a very weak motion in the $\mathbf{y}' - \mathbf{x}'$ direction, with a comparatively large antiferroelectric component acting in the $\mathbf{x}'\mathbf{y}'$-plane. The strontium ions move in the same direction in a perfect diagonal ($\mathbf{y}' - \mathbf{x}'$) but the magnitudes of their motions differ by a factor of about two. One might therefore consider the strontium to have some antiferroelectricity acting in the same direction as the ferroelectric component. The oxygen motion is probably the hardest to interpret and appears to consist of a ferroelectric shift in the same direction as the cations ($\mathbf{y}' - \mathbf{x}'$), with a greater magnitude (so by comparison the cations move backwards in the $\mathbf{x}' - \mathbf{y}'$ direction), and also a set of rotations. The rotation involves a strong rotation about the $\mathbf{z}'$ axis and a weaker rotation (rocking) towards the $\mathbf{y}' - \mathbf{x}'$ direction (or a rocking about a vector in the $\mathbf{x}' - \mathbf{y}'$ direction).

Mode 29 is similar to mode 28. The titanium ions move approximately towards an octahedral face ($\mathbf{x}' + \mathbf{y}' + \mathbf{z}'$), though there is a strong antiferroelectric contribution in the $\mathbf{x}' - \mathbf{y}'$ direction. There is very little motion in the strontium, and we see that one moves around three times as much as the other. The oxygen atoms move overall in the $-\mathbf{x}' - \mathbf{y}' - \mathbf{z}'$ direction (opposite to the cations, so it is like most of the ferroelectric transitions in this respect). The rotation of the oxygen ions is a little simpler for mode 29 than mode 28 and involves a rotation about a vector pointing in the $\mathbf{x}' - \mathbf{y}'$ direction. We might also describe it as a rocking towards the $\mathbf{x}' + \mathbf{y}'$ direction.

Mode 30 involves a ferroelectric motion of the anions and cations, with titanium moving mostly in the $\mathbf{z}'$ direction with a smaller component in the $-\mathbf{x}' - \mathbf{y}'$ direction and the oxygen ions reciprocating. There is also antiferroelectric character in the motion of both of the cations. The octahedra rotate about a vector in the $\mathbf{x}' - \mathbf{y}'$ direction, which was the same vector as mode 29. The rotational motion is more subtle that in mode 29 and in the opposite direction (though the direction of motion is only relevant in the context of the other ionic motions as the potential energy surface is assumed to be symmetrical in the direction of the eigenvector (as compared to the opposite direction)).

Mode 28 in the present structure was derived from two other modes in the parent structure: 28 ($45.7i\,\mathrm{cm}^{-1}$) and 24 ($17.2\,\mathrm{cm}^{-1}$). Mode 24 (the lowest frequency real mode) was actually the most dominant and was inclined at 28° to the present mode 28. Mode 28 in the parent was inclined at 81° to the present mode 28. It would seem that the low magnitude of the present mode 28 may have been a consequence of the combining of a hard mode (24) with a soft mode (28).

Modes 29 and 30 in the present structure mostly comprise three other modes in different ratios: mode 30 ($70.5i\,\mathrm{cm}^{-1}$), mode 29 ($45.7i\,\mathrm{cm}^{-1}$ and degenerate with parent mode 28) and mode 23 ($17.2\,\mathrm{cm}^{-1}$). Present mode 29 is inclined to these with the respective angles of 84°, 62° and 29°, while present mode 30 is inclined to them with angles of 32°, 60° and 81°.

4.6.2.3 Structure no. 32 ($C2$)

Transitioning: The present structure was obtained by nudging structure 31 in the direction of the eigenvector of mode no. 28, which had a frequency of $5.6i\,\mathrm{cm}^{-1}$. The transition involved a small ferroelectric displacement but was mostly a change in the rotation of the octahedra. In this way the transition was of a similar nature to the grandparent to parent transition only with the weighting on the ferroelectric and rotational components of the transition reversed. The space group of the cell was unchanged during the transition. During the transition we observed a significant and equal increase in lattice parameters a and b and a decrease of c.

Mode 28 from the parent structure was inclined at $30°$ to the difference vector and the next most involved mode was no. 22 ($71\,\mathrm{cm}^{-1}$), which was inclined at $71°$ to the difference vector. The other involved modes were all at angles greater than $85°$.

All but one imaginary modes survived the transition. Mode 28 ($5.6i\,\mathrm{cm}^{-1}$) from the parent hardened and became significant parts of three other modes, which are as follows: mode 28 ($39.4\,\mathrm{cm}^{-1}$), mode 23 ($90.3\,\mathrm{cm}^{-1}$) and mode 22 ($120.8\,\mathrm{cm}^{-1}$). The parent mode was inclined to these with angles of $52°$, $78°$ and $52°$ respectively.

Imaginary modes 29 and 30 in the parent, partially hardened, mixed and split to contribute to three modes, one of which is the remaining imaginary mode 30 ($15.6i\,\mathrm{cm}^{-1}$). The modes also contributed to modes 25 ($40.9\,\mathrm{cm}^{-1}$) and 24 ($69.4\,\mathrm{cm}^{-1}$). Present modes 30, 25 and 24 were inclined to mode 29 in the parent with angles of $48°$, $48°$ and $72°$ respectively and inclined to mode 30 with similar angles of $44°$, $53°$ and $74°$ respectively.

Space group: $C2$ (no. 5).

Cell definition (Å and degrees): $a = 5.5175$, $b = 5.5175$, $c = 5.5052$;
$\alpha = 60.11$, $\beta = 60.11$, $\gamma = 59.89$;

Cell volume: $118.61\,\text{Å}^3$, $V/2V_0 = 0.9990$.

Potential energy (per formula unit): $-39.77937\,\mathrm{eV}$, which is a drop of $0.741\,\mathrm{meV}$ from the parent structure no. 31 and equivalent do a temperature drop of $\sim 1.7\,\mathrm{K}$.

Polyhedral distortion: From table 4.6.5, we see that the octahedra have changed their orientation significantly from the parent, though the nature of the change is similar to the change between structure no. 30 (grandparent) and 31 (parent). We see that $s_{z'}$ stick is almost aligned with the $\mathbf{z}'$ axis and that most of the rotation is about this same axis. The nature of the rotation can be characterized by a rotation of $5.4°$ about the $\mathbf{z}'$ axis and a rocking (hinging over an edge) about a vector in the $\mathbf{x}' - \mathbf{y}'$ direction of $0.76°$. This type of rotation is identical to the type seen in the tetragonal ancestor system (see table 4.4.9).

We report the internal angles for the oxygen octahedra surrounding both T_1 and

Table 4.6.5: The octahedral tilt and distortion around titanium atom T_1 in structure 32. The octahedral volume was $9.9752\,\text{Å}^3$ which is 1.0082 of the ideal cubic equivalent.

Stick	θ (°)	θ_1 (°)	θ_2 (°)	length l (Å)	l/l_0
$s_{x'}$	5.4651	−5.4403	−0.5264	3.9116	1.0027
$s_{y'}$	5.4654	0.5265	5.4406	3.9115	1.0027
$s_{z'}$	0.7618	0.5389	−0.5389	3.9117	1.0028

T_2 as there is a juxtaposition of two internal angles between them, s_α, s_β and s_γ are respectively $89.93°$, $89.90°$ and $90.04°$ for T_1 and $89.90°$, $89.93°$ and $90.04°$ for T_2.

Dipole (per formula unit): $0.490\,\text{D}$, of which the strontium contributes $0.212\,\text{D}$ and the titanium contributes $0.278\,\text{D}$, both in the same net direction. The overall dipole moment is given by: $0.346\mathbf{x}' - 0.346\mathbf{y}'$. The titanium ions display a high level of antiferroelectricity with the dipoles diverging by $8°$. The antiferroelectricity of the titanium ions acts mostly in the $-\mathbf{x}' - \mathbf{y}'$ direction, with a small -$\mathbf{z}'$ component. The strontium dipoles are aligned with one another. The magnitudes of the strontium dipoles are not exactly the same but differ by $\sim 6\,\%$. It may be that the small difference is a consequence of inperfect optimization, as the initial nudge used to create the present structure introduced a factor of two difference in the displacment of the strontium ions.

Imaginary modes: Only one imaginary mode remains in this structure and its frequency is $15.6i\,\text{cm}^{-1}$. The mode consists of a ferroelectric motion along the $\mathbf{z}'$ axis and a rotation of the oxygen octahedra about a vector in the $\mathbf{x}' - \mathbf{y}'$ direction. It is described and depicted in table 4.6.6 and figure 4.6.6.

Table 4.6.6: Eigenvectors for the imaginary modes no. 30 of structure no. 32, with a frequency of $15.6i\,\text{cm}^{-1}$.

Atom	d$\mathbf{x}'$	d$\mathbf{y}'$	d$\mathbf{z}'$
S_1	0.02	0.02	0.19
S_2	0.03	0.03	0.20
T_1	0.02	0.02	0.41
T_2	0.02	0.02	0.41
O_1	−0.13	−0.13	−0.24
O_2	0.04	0.03	−0.41
O_3	0.03	0.04	−0.41
O_4	0.20	0.20	−0.24
O_5	0.03	0.03	−0.08
O_6	0.03	0.03	−0.08

Imaginary mode 30 ($15.6i\,\text{cm}^{-1}$) in the present structure was derived mostly from two other modes in the parent structure. Parent mode 30 ($42.3i\,\text{cm}^{-1}$) and 29 ($19.2i\,\text{cm}^{-1}$) are inclined at $44°$ and $48°$ respectively to the present mode (the angles were also given in the transitioning section).

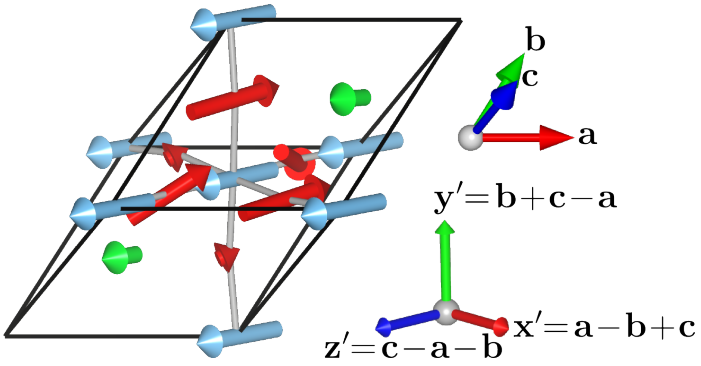

Figure 4.6.6: Graphical representation of the imaginary modes no. 30 of structure no. 32. Green, blue and red arrows respectively represent motion of strontium, titanium and oxygen.

4.6.2.4 Structure no. 33 (Cm or $P1$)

Transitioning: The parent structure was no. 32; the present structure was obtained by nudging the parent in the direction of mode no. 30 ($15.6i\,\mathrm{cm}^{-1}$). The ferroelectric transition increased the overall dipole moment by allowing the titanium to move towards the octahedral face instead of the edge. The octahedra also rotated into a less symmetrical form than the parent structure. We note that a and b have increased a small and equal amount as a consequence of the transition and c has remained the same.

Mode no. 30 in the parent structure is inclined at $43°$ to the difference vector, though a couple of others had a non-trivial rôle in the transition. Real modes 25 ($40.9\,\mathrm{cm}^{-1}$) and 24 ($69.4\,\mathrm{cm}^{-1}$) in the parent structure were inclined to the difference vector at $71°$ and $74°$ respectively.

Mode 30 in the parent structure, upon hardening, split and became a part of at least six other modes with frequencies ranging from 27.9 to $170.2\,\mathrm{cm}^{-1}$. The two most closely related modes were 27 ($27.9\,\mathrm{cm}^{-1}$) and 24 ($80.4\,\mathrm{cm}^{-1}$), which were inclined to the parent mode with angels of $50°$ and $58°$ respectively.

Space group: The lowest non-$P1$ symmetry group is Cm (no. 8), though the structure deviates by $42\,\mathrm{mÅ}$ from the ideal monoclinic system.

Cell definition (Å and degrees): $a = 5.5191$, $b = 5.5191$, $c = 5.5053$;
$\alpha = 60.07$, $\beta = 60.15$, $\gamma = 59.85$;

Cell volume: $118.64\,\mathrm{Å}^3$, $V/2V_0 = 0.9992$.

Potential energy (per formula unit): $-39.77939\,\mathrm{eV}$, which is a drop of $21\,\mu\mathrm{eV}$ from the parent structure and equivalent to a drop in temperature of $\sim 0.05\,\mathrm{K}$. Clearly one would not expect to observe phase transition with energy changes as small as this, but we have made comments on this matter in the previous sections.

Polyhedral distortion: From table 4.6.7, we see that that the nature of the octahedral tilting has become a little less symmetrical than the parent. The octahedra now

lean/rock over, further from the $\mathbf{z}'$ pseudo-cubic axis by $1.4°$, which is approximately double that of the parent structure. This rocking is no longer directly between the $\mathbf{x}'$ and $\mathbf{y}'$ pseudo-cubic axes, but now leans more towards the $\mathbf{x}'$ axis (no longer entirely an edge based hinging). The rotation about the $\mathbf{z}'$ axis is still the most dominant ($5.3°$), but has decreased slightly from the parent by about $0.2°$.

Table 4.6.7: The octahedral tilt and distortion around titanium atom T_1 in structure 33. The octahedral volume was 9.9767 Å^3 which is 1.0084 of the ideal cubic equivalent.

Stick	θ (°)	θ_1 (°)	θ_2 (°)	length l (Å)	l/l_0
$s_{x'}$	5.4459	−5.2762	−1.3619	3.9086	1.0019
$s_{y'}$	5.2901	−0.4202	5.2736	3.9123	1.0029
$s_{z'}$	1.4464	1.3820	0.4267	3.9147	1.0035

The internal angles of the octahedra are $89.81°$, $90.03°$ and $90.00°$ for s_α, s_β and s_γ respectively for T_1 and note that in the present structure, the angles are the same for T_2 with some small variations (the juxtaposition of s_α and s_β that appeared in the parent structure 32 did not appear in the present structure).

Dipole (per formula unit): 0.543 D, of which the strontium contributes 0.236 D and the titanium contributes 0.308 D; the two are inclined at a small angle of $2.2°$ to one another. The imperfect alignment of the strontium and titanium dipoles may be as a consequence of imperfect optimization. The overall dipole per formula unit is $0.238\mathbf{x}' - 0.387\mathbf{y}' + 0.297\mathbf{z}'$ (approximately in the direction of an octahedral face). We observe antiferroelectricity in both the titanium and the strontium dipoles, with titanium dipoles inclined at $5.5°$ to one another and strontium dipoles inclined at $3.6°$ to one another.

Imaginary modes: There are no imaginary modes in the present structure.

4.6.2.5 Structure no. 34 (Cc or $P1$)

Transitioning: The parent structure is number 31 and the present structure was obtained by nudging down the imaginary mode no. 29, with a frequency of $19.2i$ cm^{-1}. The transition involved ferroelectric and rotational motions of the ions and a possible lowering of symmetry from monoclinic to triclinic. The ferroelectric displacement towards an octahedral face resulted in an increase of the dipole moment. The lattice parameters b and c grew while a underwent a very small shrink. The present structure is by a small margin, the lowest in energy of the structures based on a 10 atom unit cell discovered during this research.

Several modes were implicated in the transition and mode 29, which was used to the parent system is inclined at an angle of $43°$ to the difference vector. The two other imaginary modes were involved in the transition, which is indicated by the angle of these modes from the difference vector of $69°$ for mode 30 ($42.3i$ cm^{-1}) and $76°$ for

mode 28 ($5.6i\,\mathrm{cm}^{-1}$). A couple of real modes were also implicated in the transition and they are mode 24 ($58.7\,\mathrm{cm}^{-1}$) and mode 22 ($115.9\,\mathrm{cm}^{-1}$), which are respectively inclined at $76°$ and $74°$ to the difference vector.

All three imaginary modes in the parent system disappeared during the transition, though there was much contamination with other modes. Mode 28 in the parent split and contributed towards six real modes in the present system. The most directly related present modes were 26 ($38.0\,\mathrm{cm}^{-1}$) and 27 ($27.9\,\mathrm{cm}^{-1}$), which are inclined at angles of $45°$ and $65°$ respectively to parent mode 28. Also implicated in a minor way were modes 25, 24 and 22 with frequencies of 69.0, 73.0 and $120.6\,\mathrm{cm}^{-1}$.

Parent mode 29 is perhaps the most shattered mode encountered so far as it splits to become relatively small parts of a large number of modes, the smallest inclination angle of the parent mode to one of the present modes is $54°$, which is for mode 22 ($120.6\,\mathrm{cm}^{-1}$). The other modes cover a wide range of frequencies, with the lowest at $27.9\,\mathrm{cm}^{-1}$.

Parent mode 30 most directly becomes a part of mode 23 ($91.5\,\mathrm{cm}^{-1}$) and has an angle of inclination to it of $36°$, other modes play a smaller involvement.

Space group: Cc (no. 9), with a rather large deviation of $37\,\mathrm{mÅ}$. The symmetry is $P1$ with deviation tolerances lower than this.

Cell definition (Å and degrees): $a = 5.5069$, $b = 5.5173$, $c = 5.5190$;
$\alpha = 59.85$, $\beta = 60.12$, $\gamma = 60.10$;

Cell volume: $118.63\,\mathrm{Å}^3$, $V/2V_0 = 0.9992$.

Potential energy (per formula unit): $-39.77940\,\mathrm{eV}$, a drop of $0.772\,\mathrm{meV}$, corresponding to $\sim 1.8\,\mathrm{K}$ from the parent structure no. 31.

Polyhedral distortion: Table 4.6.8, shows a similar type of octahedral configuration as in structure 33 (see table 4.6.7), though the orientation is different. The rotation can be described as a rotation about the $\mathbf{y}'$ axis of $5.3°$ and a rocking of the octahedra away from the $\mathbf{y}'$ axis of $1.4°$. The rocking involves a combination of an edge based and a corner based hinge i.e. a rotation about a vector between the $\mathbf{z}'$ axis and the $\mathbf{x}' - \mathbf{z}'$. This type of rotation is not quite the same as what might have been predicted by the eigenvector used to nudge structure no. 31 into the present one (a more symmetrical rotation was predicted). Other factors must have come into play during the geometry optimization.

The internal octahedral angles for T_1 are $89.81°$, $90.00°$ and $90.04°$ for s_α, s_β and s_γ respectively.

Dipole (per formula unit): $0.542\,\mathrm{D}$ of which the strontium contributes $0.235\,\mathrm{D}$ and the titanium contributes $0.306\,\mathrm{D}$, both inclined at an angle of $2°$ to one another. The net dipole per formula unit is given by $\mathbf{0.339}' + \mathbf{0.269}' - \mathbf{0.325}'$. Both strontium and

Table 4.6.8: The octahedral tilt and distortion around titanium atom T_1 in structure 34. The octahedral volume was 9.9765 Å^3 which is 1.0084 of the ideal cubic equivalent.

Stick	θ (°)	θ_1 (°)	θ_2 (°)	length l (Å)	l/l_0
$s_{x'}$	5.4300	−1.2751	−5.2812	3.9108	1.0025
$s_{y'}$	1.4151	0.5619	1.2988	3.9140	1.0033
$s_{z'}$	5.3162	5.2877	−0.5545	3.9106	1.0025

titanium dipoles display antiferroelectricity, titanium dipoles are inclined at $6°$ to one another, and strontium dipoles are inclined at $4.6°$ to one another.

Imaginary modes: There were no imaginary modes in the present structure.

4.6.2.6 Structure no. 35 ($R3c$ or $P1$)

Transitioning: The parent structure was no. 31 and the present structure was obtained by nudging its atoms in the direction of its 30^{th} eigenvector and then optimizing. The transition was ferroelectric and rotational in nature though most of the antiferroelectricity in the parent was suppressed. The change in symmetry is hard to classify as the parent was monoclinic, while the present system is either rhombohedral or triclinic. One would expect the symmetry always to go down during a nudge and optimization operation but it is possible that the decisions made by the symmetry finding software were not perfect. It also may be possible for the optimizer to take a convoluted path for finding a higher symmetry structure (or an approximation to it). The rotational nature of the transition was minor involving rotations of no more than $0.5°$ of the octahedra in the parent. During the transition, a and b grew similarly and c grew a smaller amount. a, b and c are now approximately equal. It may also be worth noting that the volume of the cell has now returned to that of the original cubic system.

The parent mode no. 30 is inclined to the difference vector at an angle of $48°$. Additionally Modes 23 ($84.8\,\mathrm{cm}^{-1}$) and 24 ($58.7\,\mathrm{cm}^{-1}$) are involved in the transition, inclined to the difference vector with an angle of $74°$ and $75°$ respectively.

During the transition, all three imaginary modes become hard. Mode 28 ($5.6i\,\mathrm{cm}^{-1}$) hardens and contributes to several modes, the two most significant of which are modes 26 ($28.4\,\mathrm{cm}^{-1}$) and 27 ($23.9\,\mathrm{cm}^{-1}$), which are inclined to the parent mode at angles of $59°$ and $47°$ respectively. The other involved modes in the present system are inclined at angles greater than $80°$ to parent mode 28. Parent mode 29 ($19.2i\,\mathrm{cm}^{-1}$) hardened and contributed to four modes in the present structure: 27, 26, 24 and 23 which have frequencies of 23.9, 28.4, 97.0 and $100.2\,\mathrm{cm}^{-1}$, which are inclined to the parent mode at angles of $67°$, $43°$, $62°$ and $75°$ respectively. Finally mode no. 30, which was most directly involved in the transition, makes a large contribution to the present mode 23 ($100.2\,\mathrm{cm}^{-1}$), and is inclined at $31°$ to it. Parent mode 30 also made smaller

contributions to modes 24 ($97.0\,\mathrm{cm}^{-1}$) and 16 ($174.1\,\mathrm{cm}^{-1}$), with relative angles of $72°$ and $75°$ respectively (angles of $80°$ and above are being ignored).

Space group: $R3c$ (no. 161) with a deviation of $19\,\mathrm{m\AA}$ and $P1$ for tolerances tighter than that*.

Cell definition (Å and degrees): $a = 5.5136$, $b = 5.5128$, $c = 5.5129$; $\alpha = 60.12$, $\beta = 60.07$, $\gamma = 60.09$;

Cell volume: $118.73\,\mathrm{\AA}^3$, $V/2V_0 = 1.0001$.

Potential energy (per formula unit): $-39.77929\,\mathrm{eV}$, which is a drop of $0.663\,\mathrm{meV}$, corresponding to $\sim 1.6\,\mathrm{K}$ from the parent structure.

Polyhedral distortion: Table 4.6.9 shows us a different type of octahedral tilting to structures 30 to 34 as all angular deviations of the sticks from their respective pseudo-cubic axis are large and none are equal. The nature of the rotation is still similar to that of the parent but we can describe the present state in terms of changes from the parent. The octahedra increase their rotation about the $\mathbf{x}'$ axis by $0.5°$ and decrease their rotation about the $\mathbf{y}'$ by $0.4°$.

Table 4.6.9: The octahedral tilt and distortion around titanium atom T_1 in structure 35. The octahedral volume was $9.9794\,\mathrm{\AA}^3$ which is 1.0086 of the ideal cubic equivalent.

Stick	θ (°)	θ_1 (°)	θ_2 (°)	length l (Å)	l/l_0
$s_{x'}$	4.0152	−3.0741	−2.5913	3.9121	1.0029
$s_{y'}$	4.6248	3.4776	3.0622	3.9119	1.0028
$s_{z'}$	4.3311	2.5851	−3.4833	3.9126	1.0030

The internal angles of the octahedron are $89.81°$, $89.73°$ and $90.25°$ for s_α, s_β and s_γ respectively.

Dipole (per formula unit): $0.688\,\mathrm{D}$, of which the strontium contributes $0.314\,\mathrm{D}$ and the titanium contributes $0.374\,\mathrm{D}$, both acting in the same direction. The overall dipole per unit volume is given by $-0.380\mathbf{x}' - 0.401\mathbf{y}' + 0.409\mathbf{z}'$. Very little antiferroelectric character is present in this structure, titanium dipoles are inclined at $1.1°$ to one another and strontium strontium dipoles are inclined at $2.0°$ to one another.

Imaginary modes: The present structure has no imaginary modes.

4.6.2.7 Structure no. 36 (Cc)

Transitioning: The parent structure was no. 30 and the present structure was obtained after nudging in the direction of normal mode no. 29 ($45.7i\,\mathrm{cm}^{-1}$). In structure 30, modes 28 and 29 were degenerate and so the rule would have been to nudge in the

*It was necessary to adjust the n-fold axes tolerance parameter in *Endeavour* to get the non-$P1$ result.

direction of the sum of the two eigenvectors. Examination of the nature of the mode (see figure 4.6.4 on page 206), showed that the ferroelectric component of it had a significant component in all three pseudo-cubic axes, where as mode 28 (which lead to structure 31) only acted in between two pseudo-cubic axes. Though the two modes, are essentially the same in their nature, the different orientation made it interesting as an avenue of study to consider mode 29 unmixed. During the transition, which involved ferroelectric and rotational displacements, we observed a high symmetry rhombohedral structure transform directly to a monoclinic or possibly lower symmetry rhombohedral structure. Lattice parameters a, b, and c all grew and the cell volume is now equivalent to the ideal cubic system (like structure 35).

An unusual event appears to have occurred during geometry optimization. Careful observation of the dipole direction shown in figure 4.6.2 or in the dipole description shown further below shows that that the dipole acts in the wrong direction as compared to the eigenvector used to nudge it. Error is of course the first suspect in such cases but having checked the start (`POSCAR`) and end (`CONTCAR`) structure files with the *getPolar* program (see appendix D.1.3), the dipole direction changes by $\sim 90°$. The geometry optimization ran with a single run, though examination of the output shows that a very large spike in potential energy occurred during the optimization. Spikes in optimization, indicating bad step choices are, however quite common. The cause of the significant change in ferroelectric displacement during the optimization is currently unknown. However, as a consequence, we do not see the expected eigenvectors involved in the transition.

Two modes were identified in facilitating the transition. Imaginary mode no. 30 ($70.5i\,\mathrm{cm}^{-1}$), which is a pure ferroelectric mode is most directly involved, inclined at $36°$ to the the difference vector. Mode 24 ($17.2\,\mathrm{cm}^{-1}$) was the next most involved mode, inclined at $77°$ to the difference vector. Mode 29, which was expected to have facilitated the transition is inclined at $84°$ to the difference vector.

All three imaginary modes hardened during the transition. Mode 28 ($45.7\,\mathrm{cm}^{-1}$) hardened most directly to mode 24 ($100.9\,\mathrm{cm}^{-1}$), they are inclined by $17°$ to each other. Present modes 27 ($25.8\,\mathrm{cm}^{-1}$) and 17 ($168.8\,\mathrm{cm}^{-1}$) also inherited a small amount of character from parent mode 28, but they are inclined at $77°$ and $80°$ to it respectively.

Parent mode 29 ($45.7i\,\mathrm{cm}^{-1}$) most directly hardens to mode 25 ($92.3\,\mathrm{cm}^{-1}$); these are inclined at $32°$. Present mode 23 ($101.5\,\mathrm{cm}^{-1}$) also inherits character from parent mode 29 and they are inclined at $63°$. Modes 26 ($28.1\,\mathrm{cm}^{-1}$) and 18 ($167.9\,\mathrm{cm}^{-1}$) are both inclined at $80°$ to parent mode 28.

Finally, mode 30 ($70.5i\,\mathrm{cm}^{-1}$) hardens, ,with most of its character inherited by mode 23 ($101.5\,\mathrm{cm}^{-1}$), with an inclination angle of $38°$. The following other modes also inherit character from it: 25 ($92.3\,\mathrm{cm}^{-1}$), 22 ($119.7\,\mathrm{cm}^{-1}$) and 16 ($175.2\,\mathrm{cm}^{-1}$)

and the inclination angles are respectively $65°$, $76°$ and $69°$.

Space group: Cc (no. 9). Another possible space group is $R3c$, though the structure deviates by $19\,\text{m}\text{Å}$ from it.

Cell definition (Å and degrees): $a = 5.5126$, $b = 5.5126$, $c = 5.5142$;
$\alpha = 60.08$, $\beta = 60.08$, $\gamma = 60.12$;

Cell volume: $118.74\,\text{Å}^3$, $V/2V_0 = 1.0001$.

Potential energy (per formula unit): $-39.77929\,\text{eV}$, a drop of $-0.808\,\text{meV}$, corresponding to $\sim 1.9\,\text{K}$ from the parent structure.

Polyhedral distortion: The rotation data for this structure is displayed in table 4.6.10. The present octahedral configuration resembles that of structure 31, except that in 31, the octahedra tilted to align better with the $\mathbf{z}'$ axis but here the octahedra pull further away from it. The change in the rotation is quite symmetrical and involves the $s_{z'}$ stick pulling away from the $\mathbf{y}'$ axis, directly between the $\mathbf{x}'$ and $\mathbf{y}'$ pseudo-cubic axes. Additionally a small rotation about the $\mathbf{z}'$ axis, so as to reduce the overall amount of rotation in this direction occurs. As a consequence, the $\theta_{x'}$ and $\theta_{y'}$ values (θ column) are virtually unchanged by the transition.

Table 4.6.10: The octahedral tilt and distortion around titanium atom T_1 in structure 36. The octahedral volume was $9.9799\,\text{Å}^3$ which is 1.0087 of the ideal cubic equivalent.

Stick	θ (°)	θ_1 (°)	θ_2 (°)	length l (Å)	l/l_0
$s_{x'}$	4.2202	−2.7415	−3.2171	3.9127	1.0030
$s_{y'}$	4.2200	3.2169	2.7414	3.9128	1.0030
$s_{z'}$	4.5360	3.2133	−3.2133	3.9113	1.0026

We observe little angular distortion within the octahedra and see that it corresponds the external rotational symmetry: s_α, s_β and s_γ are $89.77°$, $89.77°$ and $90.27°$ respectively.

Dipole (per formula unit): $0.693\,\text{D}$ of which the strontium contributes $0.316\,\text{D}$ and the titanium contributes $0.377\,\text{D}$, both acting in the same direction. The vector for the dipole is $0.410\mathbf{x}' + 0.410\mathbf{y}' - 0.377\mathbf{z}'$. Again, we see very little antiferroelectricity in this structure with titanium dipoles inclined at only $0.3°$ to one another and strontium dipoles inclined at $0.9°$.

Imaginary modes: No imaginary modes are present in this structure.

4.6.2.8 Structure no. 37 ($R3c$)

Transitioning: The parent structure was no. 30 and the present structure was obtained by nudging the atoms in the direction of the ferroelectric mode no. 30 ($70.5i\,\text{cm}^{-1}$) and then optimizing. The transition was entirely ferroelectric in nature (with a very

small rotational aspect) and lowered the symmetry of the cell, without changing the rhombohedral lattice type. The dipole moment strength in the present structure is the strongest of any of the structures presented in the thesis. However, as the structure is not the lowest in energy, we can surmise that such a large dipole is not the optimum configuration for the cell. The cell lengths increase equally and the cell angles decrease a small amount. It is clearer to see in this example that the decrease in the cell angles corresponds to the ferroelectric displacement in the direction of the volume diagonal (or the octahedral faces), as we observed in the cubic, tetragonal and orthorhombic ancestor systems. The present lattice parameters more closely compares to a cubic cell (a cubic supercell could be built from the rhombohedral cell if the cell angles were all $60°$) than the parent structure, which had a greater rhombohedral distortion.

The mode most directly involved with the transition was mode 30, though it was inclined at the surprisingly steep angle of $42°$ to the difference vector. One other mode played a minor involvement, which was no. 18 ($157.5\,\mathrm{cm}^{-1}$), but this mode was inclined at $82°$ to the difference vector. The most probable explanation for the large angle between mode 30 and the difference vector is that the relative displacements of the three different types of ion in the optimized structure were not the same as in the eigenvector used to nudge the parent structure. Further evidence of this hypothesis comes from two places. The first is that the *cds3* program, that was used to compare normal modes, outputs the difference vector between the two structures; a visual check showed that the magnitudes of strontium and titanium displacement were significantly different in the eigenvector and the difference vector. The second piece of evidence is that a translational mode had a significant component in the difference vector (according to the *cds3*). Involvement of translational modes has been excluded from comment in the the thesis so far, though they often appear to have an involvement in the transition. In principle a translational mode cannot be involved in a transition as their zero eigenvalue magnitude indicates a shift of all ions equally. However, *VASP* scales the motions of ions in modes according to the masses of the ions involved. As a consequence the translational modes actually indicate a relative displacement of atoms (all in the same direction).

All three imaginary modes harden during the transition. Parent degenerate modes 28 and 29 ($45.7i\,\mathrm{cm}^{-1}$) harden and most directly contribute respectively to degenerate modes 25 and 24 ($99.2\,\mathrm{cm}^{-1}$); parent and child modes are inclined by $16°$ to each other. Degenerate present modes 26 and 27 ($27.4\,\mathrm{cm}^{-1}$) and 18 and 17 ($168.9\,\mathrm{cm}^{-1}$) also inherit character from parent modes 28 and 29 and are inclined at $78°$ and $79°$ respectively.

Parent mode 30 ($70.5i\,\mathrm{cm}^{-1}$) hardens and becomes a part of three other modes. The most direct inheritor was mode 23 ($100.0\,\mathrm{cm}^{-1}$), but also inheriting were modes

22 ($119.7\,\mathrm{cm}^{-1}$) and 16 ($174.9\,\mathrm{cm}^{-1}$), the relative angles are respectively $27°$, $75°$ and $69°$.

Space group: $R3c$ (no. 161).

Cell definition (Å and degrees): $a = 5.5132$, $b = 5.5132$, $c = 5.5132$; $\alpha = 60.09$, $\beta = 60.09$, $\gamma = 60.09$;

Cell volume: $118.74\,\text{Å}^3$, $V/2V_0 = 1.0001$.

Potential energy (per formula unit): $-39.77929\,\mathrm{eV}$, which is a drop of $0.789\,\mathrm{meV}$, corresponding to $\sim 1.8\,\mathrm{K}$ from the parent structure.

Polyhedral distortion: The octahedral tilting is described in table 4.6.11. We see a uniform rotation about all pseudo-cubic axes, with a slightly increased degree of rotation that in the $R\bar{3}c$ parent.

Table 4.6.11: The octahedral tilt and distortion around titanium atom T_1 in structure 37. The octahedral volume was $9.9798\,\text{Å}^3$ which is 1.0087 of the ideal cubic equivalent.

Stick	θ (°)	θ_1 (°)	θ_2 (°)	length l (Å)	l/l_0
$s_{x'}$	4.3250	−3.0632	−3.0632	3.9123	1.0029
$s_{y'}$	4.3250	3.0632	3.0632	3.9123	1.0029
$s_{z'}$	4.3250	3.0632	−3.0632	3.9123	1.0029

The internal distortion angles of the octahedra display a quarter of a degree distortion with respect to all stick combinations s_α, s_β and s_γ are respectively $89.76°$, $89.76°$ and $90.24°$.

Dipole (per formula unit): $0.698\,\mathrm{D}$ of which the strontium contributes $0.319\,\mathrm{D}$ and the titanium contributes $0.379\,\mathrm{D}$, both acting in the same direction. The overall dipole is given by $-0.402\mathbf{x}' - 0.402\mathbf{y}' + 0.402\mathbf{z}'$. There is no antiferroelectricity in the present structure.

Imaginary modes: No imaginary modes are present in this structure.

4.6.2.9 Structure no. 38 ($R3c$)

Comments: The present structure is based on a $2\times2\times2$ supercell of the cubic system containing 40 atoms. A separate diagram has not been included, though the layout of the cell is shown in the introduction to the thesis (see figure 1.2.2, on page 22 (right)). The structure was optimized as part of a different branch of research (not included in the thesis). We include it here because it had the lowest energy of any of the other structures while not having the lowest symmetry. The energy though is essentially identical to that of structure no. 14 in the tetragonal ancestor system (page 152).

The present structure is identical (or very similar) to structure 37 (above) in terms of space group, volume, octahedral distortion and the nature of the dipole moment. The

only clear point of difference is the potential energy which is 0.24 meV. We consider the possible differences in the potential energy. The present structure was calculated with a Monkhorst-Pack k-point spacing of $4\times4\times4$, while the rest of the rhombohedral ancestor set were calculated with a $8\times8\times8$ spacing. The 10 atoms structure has approximately two times the k-point density as the 40 atom structure, which usually would either lower or keep constant the calculated potential energy. As the 40 atom structure had a lower potential energy (per formula unit) than structure 37, the different k-point density does not seem like a viable explanation. The interactions of the slightly varying tilts in the present structure may enable it to get to a lower energy state. The small difference in dipole moment strength between structure 38 and 37 (the dipole in 37 seems slightly overextended), would account for a small energy change ($\sim 10\,\mu$eV). It may also be that one cannot compare calculations on cells of different sizes at the level of accuracy that is being used here.

Space group: $R3c$ (no. 161).

Cell definition (Å and degrees): $a = 7.8020$, $b = 7.8020$, $c = 7.8020$;
$\alpha = 89.92$, $\beta = 89.92$, $\gamma = 90.08$.

Cell volume: 474.91 Å^3, $V/8V_0 = 1.0000$.

Potential energy (per formula unit): -39.77953 eV, which is a drop of 7.325 meV, corresponding to ~ 17 K compared to the optimized cubic structure.

Polyhedral distortion: The octahedral tilting is described in table 4.6.12. We note the same rotation about all pseudo-cubic axes. The octahedral rotation is almost identical to that of structure no. 37 above.

Table 4.6.12: The octahedral tilt and distortion around a titanium atom in structure 38. The octahedral volume was 9.9783 Å^3 which is 1.0085 of the ideal cubic equivalent.

Stick	θ (°)	θ_1 (°)	θ_2 (°)	length l (Å)	l/l_0
$s_{x'}$	4.3120	3.0536	3.0546	3.9121	1.0028
$s_{y'}$	4.3120	−3.0546	−3.0536	3.9121	1.0028
$s_{z'}$	4.3118	−3.0542	3.0537	3.9121	1.0028

The internal distortion angles of the octahedra display a quarter of a degree distortion with respect to all stick combinations s_α, s_β and s_γ are respectively $89.76°$, $89.76°$ and $90.24°$. Again these distortions are the same as structure no. 37.

Dipole (per formula unit): 0.687 D of which the strontium contributes 0.313 D and the titanium contributes 0.373 D, both acting in the same direction. The overall dipole is given by $-0.396\mathbf{x}' - 0.396\mathbf{y}' + 0.396\mathbf{z}'$. There is virtually no antiferroelectricity in this structure.

Imaginary modes: No imaginary modes are present in this structure.

Having considered the eight structures (not including no. 38), composing the orthorhombic ancestor systems on and individual basis, we now consider the vibrational frequencies as an overview.

4.6.3 Frequency Analysis

In table 4.6.13 we present a list of the phonon frequencies of all of the rhombohedral ancestor structures 30–37. Structure 38, is not included here as it has a different type of unit cell with four times as many atoms. We also include vibrational frequencies calculated for a rhombohedral unit cell arranged into the cubic $Pm\bar{3}m$ configuration. The vibrational modes that have been identified were based on the values for the cubic system (see table 4.3.5), which was in turn based on the works by Wahl et al. [44].

Table 4.6.13: Full frequency listing (in cm^{-1}) of the rhombohedral $R\bar{3}m$ ancestor structures. The frequencies for the cubic $Pm\bar{3}m$ system, factored into the rhombohedral unit cell have also been included here. Blocks of $-$ and $+$ indicate degenerate modes, we discuss the symmetry labelling in more detail in the text.

Freq. no.	Label	Structure number								
		$Pm\bar{3}m$	30	31	32	33	34	35	36	37
1	$+$	750.0	819.1	819.4	818.6	818.8	818.9	819.7	819.7	819.8
2	Γ_{15} (TO3)	498.1	528.1	533.1	530.1	529.9	529.7	530.2	529.8	529.6
3	Γ_{15} (TO3)	498.1	528.1	529.2	527.7	528.9	528.6	529.3	529.6	529.3
4	Γ_{15} (TO3)	498.1	519.5	521.1	524.3	524.2	524.7	528.9	528.4	529.3
5	$-$	429.5	469.6	498.9	507.4	506.3	505.0	511.4	511.4	510.7
6	$-$	429.5	469.6	482.5	481.9	493.3	495.0	508.4	508.8	510.7
7	$-$	429.5	430.2	430.5	428.8	429.1	429.0	429.4	429.2	428.9
8	$+$	428.4	430.2	429.6	428.3	427.4	427.9	428.7	428.9	428.9
9	$+$	428.4	427.2	425.9	425.2	426.1	425.6	424.1	424.0	424.1
10	$-$	424.5	427.2	421.2	423.5	423.3	423.0	420.5	420.8	420.6
11	$-$	424.5	424.7	415.7	412.3	406.0	402.6	396.3	396.3	394.9
12	$-$	424.5	421.8	402.7	399.8	397.7	401.1	394.5	393.8	394.9
13	Γ_{25}	227.7	260.3	262.7	256.4	256.7	256.9	260.8	260.8	260.6
14	Γ_{25}	227.7	236.9	238.9	246.0	246.0	246.3	244.6	244.0	243.9
15	Γ_{25}	227.7	236.9	237.7	243.5	243.7	243.5	242.9	243.4	243.9
16	Γ_{15} (TO2)	156.1	163.1	167.5	168.2	170.2	169.4	174.1	175.2	174.9
17	Γ_{15} (TO2)	156.1	163.1	164.9	167.5	168.4	167.4	168.4	168.8	168.9
18	Γ_{15} (TO2)	156.1	157.5	161.0	164.9	163.3	164.8	168.1	167.9	168.9
19	$+$	129.0	140.9	140.8	141.3	142.1	142.2	142.0	141.6	141.0
20	$+$	129.0	140.9	140.5	137.2	137.3	137.5	140.3	140.4	141.0
21	$+$	129.0	130.5	130.3	135.7	135.6	135.4	131.5	131.5	131.4
22	$-$	$12.9i$	117.2	115.9	120.8	121.1	120.6	119.6	119.7	119.7
23	$-$	$12.9i$	17.2	84.9	90.3	94.4	91.5	100.2	101.5	100.0
24	$-$	$12.9i$	17.2	58.7	69.4	80.4	73.0	97.0	100.9	99.2
25	Γ_{15} (TO1)	$70.6i$	1.7	2.7	40.9	55.9	69.0	95.4	92.3	99.2
26	Γ_{15} (TO1)	$70.6i$	$0.1i$	1.7	39.4	34.6	38.0	28.4	28.1	27.4
27	Γ_{15} (TO1)	$70.6i$	$0.1i$	$0.7i$	3.5	27.9	27.9	23.9	25.8	27.4
28	$+$	$80.1i$	$45.7i$	$5.6i$	$0.4i$	$0.4i$	$0.2i$	$0.3i$	$0.4i$	$0.7i$
29	$+$	$80.1i$	$45.7i$	$19.2i$	$0.7i$	$0.5i$	$0.6i$	$0.4i$	$0.4i$	$0.7i$
30	$+$	$80.1i$	$70.5i$	$42.3i$	$15.6i$	$1.8i$	$0.9i$	$1.0i$	$0.5i$	$0.7i$

We should note two unexpected frequencies for the $Pm\bar{3}m$ configuration. The Γ_{15} (TO3) modes 2–4 have a frequency of $498\,\mathrm{cm}^{-1}$, but from the the five atom and 20 atom unit cell calculations, as well as the data presented in [44], the correct frequency

should be $\sim 535\,\mathrm{cm}^{-1}$ ($533\,\mathrm{cm}^{-1}$ for both calculations in the work presented here and $536\,\mathrm{cm}^{-1}$ in [44]). We note though that the less symmetrical child ancestors of the rhombohedral $Pm\bar{3}m$ structure reproduce the frequency more accurately. The other frequency in question is for the translational modes 22–24, which should in principle be $0\,\mathrm{cm}^{-1}$. The accuracy of these calculations is limited by the plane-wave cut-off energy and numerical noise. Our experience of the calculations in this thesis has shown the frequency of translational modes to vary by as much as $\pm 3\,\mathrm{cm}^{-1}$. In both the high frequency and translational modes, the deviation from the expected value is too large to be explained by the noise or cut-off energy alone. The other gamma point frequencies in the $Pm\bar{3}m$ symmetry rhombohedral type cell, match well with the cubic calculations. The correct frequencies, combined with some careful checking of the structure, suggests that it was not the input structure or differences in the settings that caused the problem.

Examination of the Γ_{15} (TO3) modes shows some unexpected behaviour. The general character of the mode (based on examination of the five atom cubic system) is pure ferroelectric motion of the ions with very little movement of the cations i.e. almost all the motion is in the oxygen ions. In the $Pm\bar{3}m$ rhombohedral case we see that the oxygen ions move as three pairs (oxygens on both ends of an octahedral stick are a pair). Each pair moves in a different direction on a plane with the average direction of motion opposing the cationic motion. The angular separations are significant at 18° or 36° from one another. Examination of the equivalent modes in the $Pm\bar{3}m$ in tetragonal type unit cell actually shows similar deviation of the behaviour of the eigenvectors from the five atom cubic case, despite the similarity of the frequencies. The different character of the eigenvectors may therefore not be relevant in terms of understanding the incorrect frequencies that are generated.

To probe further the unexpected result, the calculation was repeated on a different computer (with a different compilation of *VASP*) and the k-point density was also increased, but neither of these changes changed the result in a significant way. It seems that this difference in the frequencies is an error of some sort. As the error did not appear when $Pm\bar{3}m$ symmetry was applied to the cubic or tetragonal style unit cells or in the present type of cell when rhombohedral symmetry was present, the problem would seem to occur as a response to the highly symmetrical cubic structure being factored into this (rhombohedral) type of cell. There is not the evidence to support a more general conclusion. Perhaps a fault in the *VASP* code is the cause.

As with the previous three sections, we compare the sets of frequencies for, every combination of structures, and for each combination report the maximum deviation as an element in a table (see table C.4 on page 252). From this analysis we identified two sets of structures that were similar.

The first set consists of structures no. 35, 36 and 37, which is unsurprising based on their near degeneracy with one another (see figure 4.6.2 on page 203). The other pair are structures 33 and 34, which is also to have been expected due to their degeneracy. Structure 32 which is energetically similar, fell outside of the group due to its imaginary mode.

We now draw the section to an end with a summary of what has been learned.

4.6.4 Summary of Rhombohedral Ancestor Systems

Examining the first rhombohedral structure (no. 30), we see that despite its octahedral rotation about all three axes, it is much less energetically favourable than the tetragonal (no. 9) and the orthorhombic (no. 20) starting structures. The cell densities were approximately equal and the net dipoles were equal in these structures. This is further evidence that unequal rotations about the pseudo-cubic axes are highly energetically favourable.

The rhombohedral ancestor dendrimer tree has a different configuration to the previous tree structures. The different configuration of the cell has led to the generation of imaginary modes, whereby following any one of them will cause the others to condense.

The initially symmetrically rotated starting structure showed a preference for matching the types of rotation seen in the tetragonal ancestor system i.e. A large rotation ($\sim 5.5°$) about one pseudo-cubic axis and then a smaller one ($\sim 1.0 \pm 0.4°$) away from that same axis causing the octahedra to rock towards the other two axes (in between them). The most obvious distinguishing feature between the two low energy end point structures (33 and 34) and the higher energy end point structures, (35, 36 and 37) is the higher energy structures have an approximately equal rotation about each axis.

As the small differences in rotation between the structures 35 to 37 have resulted in only a very small difference in potential energy between them ($\sim 20\,\mu$eV), it would seem that almost all of the drop in potential energy between these structures and their common parent structure no. 30 is the polarization (and some associated shifts in the lattice parameters).

Based on the lack of imaginary frequencies and the presence of lower energy structures with the same type of unit cell, structures 35 to 37 are all local minima. It is not clear what is causing the energy barrier. Further analysis such as NEB calculations may provide an answer.

4.7 Concluding Remarks

In this chapter, we studied 38 structures in detail, some of which proved to be equivalent to one another. In certain cases the structures were compared to experimental results, though this had limited significance for the non-tetragonal structures. We also performed a detailed analysis of the imaginary and vibrational modes involved in structural transitions within each ancestry of structures i.e. the ones with cubic, tetragonal, orthorhombic and rhombohedral ancestors.

No previous theoretical/computational research has covered such a large number of low-temperature phases of STO. The widest ranging studies to our knowledge covered the cubic $Pm\bar{3}m$ (structure 1 on page 124), the antiferrodistortive tetragonal $I4/mcm$ (structure 9 on page 139) and the ferroelectric tetragonal $P4mm$ (structure 2 on page 125) phases in papers by Blokhin et al. [134] and Sai and Vanderbilt [40]. A ferroelectric distortion of the $I4/mcm$ system is also covered in [40], though the space group was not given. Having explored the energy surface so extensively in the present research, we have painted a picture of the range of local structures that could exist (for short periods) and contribute to the low temperature paraelectric behaviour. We also note that STO, whose ion sizes are so well balanced that it retains cubic structure down to temperatures as low as $105\,\mathrm{K}$, has demonstrated most of the distortions known to exist within the perovskite family i.e. Bravais lattice types, octahedral distortions, ferroelectric/antiferroelectric displacements [46, 47, 135]. As such this study serves as an excellent showcase for perovskites.

We found that the lowest energy structures had monoclinic lattices and that rhombohedral structures were of only slightly higher energy. The most significant factor in lowering the potential energy of the structures from the perfect cubic starting point was octahedral rotation, accounting for an energy change of $\sim 6\,\mathrm{meV}$. The next most important change was the formation of dipoles that acted in the direction of an octahedral face (which accounted for $\sim 0.7\,\mathrm{meV}$). The last significant contributing factor is the symmetry (or equality) of the octahedral rotations. Non-equal rotations about (or angular separations from) the pseudo-cubic axes are more favourable than equal rotations (equal rotations result in the rhombohedral structure). The energy drop associated with equal rotations becoming non-equal is $\sim 0.1\,\mathrm{meV}$. There were changes in the lattice parameters that accompanied these internal structural changes but it is hard to separate the energetic consequences of the lattice parameters changing from the internal changes that caused them.

The energetic contribution of the antiferroelectricity is unknown, as there were not any examples within the results, of antiferroelectricity appearing in the absence of other structural changes. The antiferroelectricity in the most part was generated as a consequence of the motion of the titanium atom within an octahedron, and the

collective counter rotation of the octahedra.

We identified that, of the high symmetry, non-polar structures, the tetragonal was lower in energy than the orthorhombic and rhombohedral, which is in agreement with experimental [22, 30] and other computational observations [136]. No predictions of observed phases have been made as this would require the inclusion of temperature effects. The very low energy differences between saddle point structures, local minima and the ground state structures adds favour to the low temperature paraelectric theory.

We observed that the strontium contributed almost the same to the dipole of the cells as the titanium. Given that the strontium only has half the charge, this implies a larger displacement. The freedom of motion of both cations to move implies that both cations are slightly smaller than the A and B holes in the cage made by the oxygen atoms and that the cage itself must have a certain degree of rigidity independently of the cations in order to allow this. We noted from the observations of the cubic ancestor systems, that both the strontium and titanium probably favour displacing towards octahedral faces but that an effect of correlation causes them to move in the same direction.

For all of the ancestry trees, with the exception of the cubic (which had little freedom to relax), we saw that the volume dropped when symmetry was first broken, but the subsequent symmetry breaking displacements led to an increase in the cell volume. In most cases, the lowest symmetry cells had the same density as the $Pm\bar{3}m$ cell (no. 1). The rhombohedrally distorted cubic descendants were the exceptions as these only increased in volume. Based on these examples, it appears that polar displacements were the driving force behind cell expansion, while non-polar distortions were the driving force of cell contraction.

For all the structures, except the cubic, we reported on the internal distortion angles of the octahedra. It was found that the octahedra distort very little in this way, though they stretch in the direction of the octahedral sticks. The lateral separation of octahedral sticks was not recorded, though this may be a potential extension for future research.

Future extensions to the work may include structural calculations that can take thermal effects into account. The observed crystal structure can be calculated/estimated by combining the thermal motion of atoms over the entire potential energy landscape (of which this investigation may provide a good approximation) with quantum effects. We generally expect to observe higher symmetry structures at higher temperatures and lower symmetry structures at lower temperatures. The heights of potential energy barriers that separate the low symmetry phases is an important factor in determining if a given phase will be stable (larger barriers results in greater stability). However, in cases where the mean thermal energy is close to the barrier height, transition temperatures are governed by the behaviour of the phonon modes.

There is also some uncertainty involved with the comparison of structures based

on different sized unit cells. We observed that the monoclinic structures in the 10 atom cell (33 and 34) were reported as having higher energy than the similar monoclinic structures in the 20 atom cell (e.g. no. 14) and also that the $R3c$ structure in the 40 atom cell (no. 38) was reported with the same energy (per formula unit) as structure 14 (monoclinic). If the cause of this is related to a problem in the methodology, rather than (actual non-symmetrical atomic displacements), then based on the two examples, doubling the unit cell size appears to result in a drop of reported potential energy by ~ 0.1 meV.

Further checking, possibly using the 40 atom $2\times2\times2$ cubic super cell, which can accommodate the symmetry of all of the structures may be useful. Such calculations are very lengthy and frequency calculations have been beyond the capabilities of *HECToR* (the jobs of this size scale badly with processor numbers and only 12 hour queues are allowed). Also of interest would be to attempt calculations of some of the structures of particular interest (low symmetry ones) using hybrid functionals such as HSE06.

We now finish our discussion of the perfect lattice and proceed to discuss defective STO in the next chapter.

Chapter 5

Defect Properties

5.1 Preamble

The importance of the defect properties of STO were described in section 1.3. In our final results chapter we cover three related topics: the development of three new sets of pair potentials; we compare our calculations of vacancy formation and Schottky defect energies, with experiment and other computational studies; we examine the migration of oxygen and strontium between vacancies and calculate the activation barrier.

5.2 Introduction

We now begin our discussion and results for work describing the imperfect lattice. The results presented here are based on classical pair potential (MM) calculations (see section 2.3), all of which have been calculated using the *GULP* code [88, 118]. Work on the hybrid QM/MM model discussed in section 2.5 and for which the pair potentials presented in section 5.3, were originally developed, is still ongoing and not yet ready for publication. In particular we found that there was a problem with the Gaussian type pseudo potentials developed as part of the embedded cluster model and with the underlying methodology for developing them. When fitting the pseudo potentials (manually), only short range (single oxygen bond) interactions were considered. It appears that the longer range effects were important in the model as the atoms in the QM region (region 1) did not have equal eigenvalues, when the lattice was perfect. The result was substantial distortions upon geometry optimization. We are currently developing a new methodology for dealing with this problem.

In the following results sections, we cover three different topics. In section 5.3, we describe a new set of MM pair potentials that were developed to model the orthorhombic phase of strontium titanate. We also present several calculated properties based on the potentials and compare these to experiment and computational results from other studies.

In sections 5.4 and 5.5, we carry out calculations on defective STO using the pair potentials from the previous section. In both cases the Mott-Littleton approach is used (see section 2.3.6 on page 59). In section 5.4, we examine the vacancy formation energies and calculate the Schottky defect energies (see section 1.3.2).

In section 5.5, we carry out calculations to determine the migration barrier for one oxygen atom moving between two adjacent vacancy sites. We perform a similar calculation for strontium and report on the probably transition pathway in both cases.

The results presented in this chapter have been published in [25, 137].

5.3 Classical Pair Potentials

In this section, we cover the development of three new sets of pair potentials for modelling the behaviour of STO. There were two driving factors behind this work. The first was that existing pair potential models overestimated the octahedral rotation angle in the tetragonal system; values of 8° to 10° were typical. The second was originally inspired by the work by Lytle [23] in his experimental determination of an orthorhombic phase at low temperatures (though presently, there is little evidence that this phase occurs).

The Buckingham potentials were fitted with the intention of producing an orthorhombic structure, with octahedral rotation angles close to 2°. The space group was $Pbnm$, which is equivalent to $Pnma$, (see section 4.5.2.1 on page 171). The angle of 2° was chosen based on an assumption that a low temperature orthorhombic structure, would have similar rotation angles to those observed for the tetragonal [22, 30, 121, 122]. The other constraints were the matching of lattice parameters provided by Lytle for the orthorhombic system and for the resultant structure to have no imaginary modes.

Table 5.3.1: Buckingham parameters for three sets of shell model pair potentials of $SrTiO_3$. The cut-off distance for the Buckingham potentials is $15\,$Å. See table 5.3.2 for the corresponding shell potentials.

Interaction	A (eV)	ρ (Å)	C_6 (eV Å^6)
Set 1:			
Sr^{2+} – O^{2-}	843.0	0.36335	1.0
Ti^{4+} – O^{2-}	835.051554	0.382760	9.6
O^{2-} – O^{2-}	22764.30	0.1490	43.0
Set 2:			
Sr^{2+} – O^{2-}	835.0	0.36375	0.0
Ti^{4+} – O^{2-}	838.051554	0.38202	9.8
O^{2-} – O^{2-}	22764.30	0.1490	43.0
Set 3:			
Sr^{2+} – O^{2-}	843.0	0.36335	1.0
Ti^{4+} – O^{2-}	835.02477	0.382760	9.6
O^{2-} – O^{2-}	22764.30	0.1490	43.0

As a starting point for the potential development, we used pair potentials by Akhtar et al. [57]. Initially two sets of potentials were developed, which differed in the rotation angles they produced. Set 1, produced octahedral rotation angles of 5.29° and 2.07°, while potential set 2, produced angles of 4.88° and 1.59°. Note that these angles are determined using an earlier angle determination method based on two subsequent rotations. However, as Glazer [45] pointed out, for small angles such as these, there is little

difference between the two.

Potential set 3 was developed in collaboration with Alexey Sokol (UCL) to deal with a problem with the titanium core and shell charges. It was developed to reproduce the structure of potential set 1, but with much smaller opposing charges on the titanium core and shell. The large charges and strong spring constant were believed to be responsible for convergence problems in a series hybrid QM/MM calculations.

The Buckingham parameters are presented in table 5.3.1 and the core-shell interactions are given in table 5.3.2 (see section 2.3.4.3 on page 55 for reference on Buckingham potentials).

Table 5.3.2: Shell model potentials corresponding to the Buckingham potentials presented in table 5.3.1. Y is the charge on the ion core, the shells have corresponding charges, to produce the overall charge of the ion.

Ion	Y ($\|e\|$)	k_2 ($\mathrm{eV\,\AA^{-2}}$)	k_4 ($\mathrm{eV\,\AA^{-4}}$)
Set 1 & 2:			
Sr^{2+}	1.526	11.671032	50000
Ti^{4+}	−35.863	65974.0	50000
O^{2-}	−2.389	18.41	50000
Set 3:			
Sr^{2+}	1.526	11.671032	50000
Ti^{4+}	−1.0	980.9365	50000
O^{2-}	−2.389	17.600936	50000

We now compare properties of $SrTiO_3$, calculated using the new potentials with those available in the literature (Akhtar et al. [57] and Crawford and Jacobs [59]). Though the potential sets 1 to 3 were developed to model the orthorhombic system, much of the experimental data and modelling work has been on the room temperature cubic phase. For the best comparison of results, the work through the rest of this chapter is based on the cubic phase with a fixed lattice parameter $a = 3.9051\,\mathrm{\AA}$.

In table 5.3.3, we present calculated elastic constants (C_{11}, C_{12} and C_{44}), static dielectric constants ε_s and high frequency dielectric constants ε_∞ (see section 2.3.4.3). The table shows the results from the present work alongside the results of Crawford and Jacobs [59] and Akhtar et al. [57] and experimental results [138–141].

The three new potentials reproduced the experimental elastic and dielectric properties reasonably well, with the exception of the negative static dielectric constant for potential set 3 which indicates an instability arising from a doubly degenerate imaginary frequency of $49i\,\mathrm{cm^{-1}}$. One should consider that these potentials were developed to model the orthorhombic unit cell and can readily be expected to predict instability, when being applied to a cubic system. In the context of the cubic system, potential sets

1 and 2 prove to be sufficiently robust, while potential set 3, fails and should be retained for simulations including explicit account of the thermal motion of the lattice, at least in the room temperature regime.

From the three models, potential 1 gives the best overall agreement with the experimental results. The Crawford and Jacobs potentials produce similar results, with less accurate elastic constants, a good static dielectric constant and a slightly underestimated high frequency dielectric constant. The Akhtar et al. potentials produce more accurate elastic properties and high frequency dielectric constant than the current work, but underestimate the static dielectric constant by approximately $25\,\%$.

Table 5.3.3: Calculated crystal properties of STO in the cubic $Pm\bar{3}m$ phase, compared to calculations and experiment from other works. The lattice parameter a was fixed at 3.9051 Å. The experimental values were taken at 298 K.

	Present work			Other work		
Property	Set 1	Set 2	Set 3	Crawford[a]	Akhtar[b]	Experiment
C_{11} (GPa)	292	293	292	330	301.5	318[c]
C_{12} (GPa)	149	150	149	162	137.4	103[c]
C_{44} (GPa)	149	150	149	161	137.8	124[c]
ε_s	303	512	-468	300.9	216.99	290[d], 291[e]
ε_∞	6.12	6.18	5.85	4.76	5.71	5.57[f]

a Crawford and Jacobs [59].
b Akhtar et al. [57].
c Bell and Rupprecht [138].
d Mitsui and Westphal [139].
e Viana et al. [140].
f Levin et al. [141] measured the refractive index n of 700 nm light. We use the relation $\varepsilon_\infty = n^2$.

We now consider the defect properties of STO, and in particular, oxygen vacancies, which proved to be the active sites involved in a wide range of physical and chemical processes that control the utilization of this material, including its potential application in photocatalysis.

5.4 Formation Energies of Intrinsic Defects

In this section we describe our work on calculating the Schottky defect energies, which were discussed at the start of the thesis in section 1.3.2 (page 30).

Using the Kröger-Vink notation, we can describe the full Schottky defect equation for STO (here we omit charge symbols in the neutral case):

$$\mathrm{Sr_{Sr}} + \mathrm{Ti_{Ti}} + 3\mathrm{O_O} \rightleftharpoons \mathrm{V''_{Sr}} + \mathrm{V''''_{Ti}} + 3\mathrm{V^{\bullet\bullet}_O}. \tag{5.4.1}$$

The energetics of this reaction are compared the vacancy formation energies, with the energy required for the formation of one formula unit of STO:

$$E_{\mathrm{Schottky}} = \tfrac{1}{5}\left(E[\mathrm{V''_{Sr}}] + E[\mathrm{V''''_{Ti}}] + 3E[\mathrm{V^{\bullet\bullet}_O}] + E[\mathrm{SrTiO_3}]\right), \tag{5.4.2}$$

where $E[\,]$ represents the formation energy of the enclosed species.

Titanium is very tightly bound within the lattice and so the full Schottky reaction (requiring the liberation of a titanium) may not occur at a great rate. A competing process, which still maintains charge neutrality is the formation of Schottky-like defects, referred to in this thesis as partial Schottky defects. A partial Schottky defect involves the formation of strontium and oxygen vacancies:

$$\mathrm{Sr_{Sr}} + \mathrm{O_O} \rightleftharpoons \mathrm{V''_{Sr}} + \mathrm{V^{\bullet\bullet}_O}. \tag{5.4.3}$$

In this case, the vacancy formation energies are compared to the lattice energy of a formula unit of strontium oxide SrO in the rocksalt structure, using $5.159\,\text{Å}$ as the lattice parameter [142] (based on a semi-empirical calculation):

$$E_{\mathrm{Partial-Schottky}} = \tfrac{1}{2}\left(E[\mathrm{V''_{Sr}}] + E[\mathrm{V^{\bullet\bullet}_O}] + E[\mathrm{SrO}]\right). \tag{5.4.4}$$

We also define the association energy, which is the energy associated with a strontium and oxygen vacancy being brought adjacent to one another from infinite distance:

$$\mathrm{E_{assoc.}} = E[\mathrm{V''_{Sr}}] + E[\mathrm{V^{\bullet\bullet}_O}] + E[\mathrm{V''_{Sr}} + \mathrm{V^{\bullet\bullet}_O}]. \tag{5.4.5}$$

We used the potentials presented in section 5.3 for performing a series of Mott-Littleton calculations (see section 2.3.6 on page 59) to determine the three vacancy energies and subsequently to evaluate the Schottky, partial Schottky and association energies. In such a calculation, the defect in question would be placed at the centre of the cluster. Region 1, in which atoms are allowed to relax conventionally, had a radius of $10\,\text{Å}$ and region 2a had a radius of $25\,\text{Å}$, which bridges between the full relaxation

Table 5.4.1: Lattice and defect reaction energies for $SrTiO_3$ in the cubic phase and lattice constant ($a = 3.9051$ Å). All energies are in eV.

	Lattice		Vacancy			Schottky		
	$E[SrTiO_3]$	$E[SrO]$	V''_{Sr}	V''''_{Ti}	$V^{\bullet\bullet}_{O}$	Full	Partial	E_{assoc}
Present work:								
Set 1	-149.29	-34.97	20.08	83.66	18.40	1.93	1.75	0.092
Set 2	-149.48	-34.95	20.04	83.60	18.44	1.89	1.77	0.074
Set 3	-149.29	-34.97	20.04	83.46	18.35	1.85	1.71	0.047
Other works:								
Crawford[a]	-150.0	-35.18^*	20.915	84.95	18.28	2.414	2.01^*	—
Akhtar[b]	-149.18	-35.61	20.51	82.23	18.16	1.61	1.53	—
Experiment	—	-33.34[c]	—	—	—	—	2.5[d]	0.34[e]

* Calculated in the present work, using the Crawford and Jacobs [59] potentials.
a Crawford and Jacobs [59].
b Akhtar et al. [57].
c Lide [143].
d Moos and Härdtl [20].
e Cordero et al. [54].

region and the infinite crystal. The lattice parameter of 3.9051 Å was used for setting up the cluster, which was built with cubic symmetry. As the potentials developed in this work were not set up for modelling this system, a constant volume constraint was applied to the optimization.

In table 5.4.1, we present our results of the calculations and compare them to those of Crawford and Jacobs, Akhtar et al. and experiment. Our calculations show a good quantitative match to the previously calculated lattice energies and single defect energies. In the case of the full and partial Schottky defect formation energies, our values are in between the previously reported values, though our partial Schottky defect energies are about 0.7 eV lower than the experimental values. The association energy for the partial Schottky defect formation is lower than expected from experimental reports (close to zero), but is consistent with the high dielectric constant which dampens the electrostatic attraction between charged defects.

Continuing with the Mott-Littleton method, we now present our calculations on oxygen and strontium ion migration.

5.5 Oxygen and Strontium Ion Migration

In section 1.3.3 (page 31), we briefly considered the nature of oxygen and strontium migration in STO. In order to locate and calculate the energy of the migration barrier we perform a transition state search. The Mott-Littleton model is built as described in section 5.4 but with two adjacent vacancies of either oxygen or strontium (we do not model the migration barrier of titanium as titanium migration is not expected to occur due to the large binding energy holding it in place). Directly in between the two vacancies, we place an interstitial ion of the respective type. The transition state search invokes an RFO optimizer (see section 2.4.5.2) to search for a nearby point on the energy surface, with one negative eigenvalue, and thereby indicating a transition point. In figure 5.5.1 we show both types of migration and demonstrate the initial configuration of the interstitial ions.

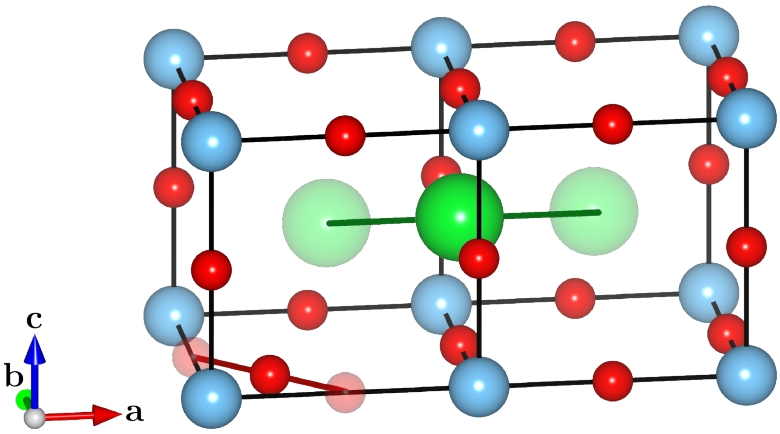

Figure 5.5.1: Approximate oxygen and strontium migration paths, both placed in one diagram for convenience. The faded balls are vacant lattice sites. Green, blue and red represent strontium, titanium and oxygen respectively.

In table 5.5.1, we present the calculated migration barriers and transition point locations, together with calculated values presented by Crawford and Jacobs [59], Akhtar et al. [57] and experiment. The positions of the oxygen saddle points were calculated in a slightly different way to the results presented in [25]. In the present work, the distance between the interstitial oxygen and the nearest titanium was divided by the distance between the titanium and the face diagonal opposing titanium. This fraction was then used as the **a** and **b** fractional coordinates of the transition point. During optimization the lattice in the centre of the cluster distorted slightly and the assumption in [25] that the Ti–Ti diagonal would be exactly $a\sqrt{2}$ Å was inaccurate (a is the lattice parameter). In the present work, the cell face diagonals were 5.618, 5.628 and 5.580 Å for the potential sets 1–3 respectively. The displacements of oxygen from the ideal position $\left(\frac{1}{4}, \frac{1}{4}, 0\right)$ were 0.12, 0.12 and 0.11 Å, towards the titanium for sets 1–3 respectively; Crawford and Jacobs and Akhtar et al. assumed the transition points would be ideal.

Table 5.5.1: Activation barriers for oxygen and strontium migration between neighbouring sites. The mid point between the two oxygen vacancy sites is $\left(\frac{1}{4}, \frac{1}{4}, 0\right)$ (in the present work). The mid point between the two strontium vacancy sites is $\left(0, \frac{1}{2}, \frac{1}{2}\right)$.

	O migration barrier (eV)	O saddle point	Sr migration barrier (eV)	Sr saddle point
Present work:				
Set 1	1.35	$(0.230, 0.230, 0)$	3.20	$\left(0, \frac{1}{2}, \frac{1}{2}\right)$
Set 2	1.25	$(0.230, 0.230, 0)$	3.18	$\left(0, \frac{1}{2}, \frac{1}{2}\right)$
Set 3	0.96	$(0.230, 0.230, 0)$	3.17	$\left(0, \frac{1}{2}, \frac{1}{2}\right)$
Other work:				
Crawford[a]	0.76	$\left(\frac{1}{4}, \frac{1}{4}, \frac{1}{4}\right)$	4.272	$\left(0, \frac{1}{2}, \frac{1}{2}\right)$
Akhtar[b]	0.65	$\left(\frac{1}{4}, \frac{1}{4}, \frac{1}{4}\right)$	2.52	$\left(0, \frac{1}{2}, \frac{1}{2}\right)$
Experiment	0.98[c] 0.65 ± 0.06[d] 1.27 ± 0.13[e]	—	3.5[f]	$\left(0, \frac{1}{2}, \frac{1}{2}\right)$

a Crawford and Jacobs [59].
b Akhtar et al. [57].
c Cordero et al. [54, 144].
d Schwarz and Anderson [55].
e Paladino et al. [56].
f Meyer et al. [145].

Experimental values for the oxygen migration barrier range from 0.65 to 1.27 eV [54–56, 144, 146]. The lower activation barriers appear to be as a consequence of high concentrations of dislocations, which can be reduced in number by annealing, as evidenced by Paladino et al. [56], who performed experiments on both annealed and unannealed crystals. The most modern measurement suggest that an O activation barrier of approximately 1 eV is correct [54, 144]. As can be seen from table 5.5.1, a range of values for the activation barrier can be obtained using the different potential parametrizations, but potential set 3 most closely matches the activation barrier energy. The values presented by Crawford and Jacobs and Akhtar et al. reproduce better the lower experimental values. The calculations presented here showed that the oxygen transition point is slightly closer (~ 0.1 Å) to the nearby titanium than the linear transition path would allow.

All of the strontium migration barriers presented here fall directly in the range set in previous simulations and offer a marked improvement in describing experiment. The corresponding transition points using all the potentials presented in this work occur directly in the middle between the two vacant strontium sites as was expected.

5.6 Concluding Remarks

The work presented in this chapter introduces three new sets of pair potentials offering an improvement upon those that were previously available. The resulting computed properties of the cubic system are in good agreement with experiment.

Preliminary work on defect formation and transport using these models produce consistent results and throws new light on ion transport mechanisms. Moreover, it will act as a starting point for performing higher level QM/MM calculations.

We now draw the defect work to a close by reflecting on our achievements.

Chapter 6

General Discussions and Conclusions

We now bring this thesis to a close and reflect on the various subject matters. At the end of each chapter, we included a separate conclusions section and so we will not attempt to repeat these here. We have now covered a vast body of work, mostly focused on navigating and mapping the intricate potential energy landscape of strontium titanate, but ending in a study of defects.

Our parametrization of the $I4/mcm$ potential energy landscape (chapter 3) has made it possible to carry out cheaply, calculations of potential energy to a good precision and over a large range of input values (via the evaluation of a polynomial). This mathematical description of the potential energy surface allows not only the potential energy, but also any derivatives to be calculated, allowing a diverse range of future research into the field. We used a range of techniques to investigate the minimum of the surface, though the octahedral rotation angle is currently being overestimated by the LDA, PBE and PBEsol functionals. In works by Evarestov et al. [32], LCAO calculations (with a range of functionals, including PBE) resulting in a rotation angle of $\sim 1^{\circ}$, demonstrate that the basis set type can make significant difference on the outcome of calculations on STO. Though the rotation angle calculations made by Evarestov et al. resulted in an underestimate of about a half, it is an improvement over the related results in this thesis and point to a sensible future line of research. The soft nature (mild gradient) of the energy surface, is a probable cause of the sensitivity to the methodology in calculating the structural properties.

Our study of the large number of saddle point and local minima structures (chapter 4) that can exist, demonstrate the complexity of the energy landscape. Our catalogue of STO structures, is more diverse than any we could find in previous work, though some of of the most complete *ab-initio* studies can be found in [32, 40, 134, 147]. The structures and the information they provide on the potential energy surface could help in the construction of an improved quantum mechanical/thermodynamic model of STO at low temperatures. The low barriers between the structures goes some way to explain the paraelectric state that appears to exist at low temperatures. If zero point vibrations

could be neglected, then based on the calculations, a ferroelectric structure with monoclinic or rhombohedral structure would be expected. Overall, we have seen within this study, most of the Bravais lattice types and internal distortions that are known to occur within the perovskite structure i.e. octahedral rotations about three axes and ferroelectric displacements of ions [46, 47, 135].

Finally, we have developed three new sets of pair potentials (chapter 5). The new potentials offer an improvement over the previously available models [57, 59] in terms of the modelling of the oxygen and strontium migration barriers. Additionally, the methodology allowed for an improved estimate on the location of the transition point for oxygen migration between neighbouring sites. This may contribute to the general understanding of the defect chemistry of STO, which may have implications in the development of future fuel cells. As the potentials developed here were developed to reproduce the orthorhombic structure (and will also handle rhombohedral), future investigations could examine oxygen and strontium diffusion in the low temperature systems.

Further research work on the perfect lattice topic might include a more careful comparison of structures calculated using different unit cells, the inclusion of thermal effects and the calculation of free energy. On the defect topic, one of the original goals of this research work was to use *ChemShell* to carry out defect studies on STO. Such calculations would include vacancies and impurities and have the benefits of both a QM level of theory at the local state (the defect) and the response of the surrounding lattice to it. The development of the model has proved to be more involved than originally expected based on some successful calculations on zinc oxide (not part of this work). However, the methodology appears to be almost in place for us to proceed.

Overall the work has considerably enhanced our knowledge of structural and defect properties of this key material.

Appendix A

Additional Formulas and Derivations

A.1 Introduction

In this appendix we describe the mathematical derivation of various principles that were deemed too long to fit in elegantly in the main body of the thesis text.

A.2 Residual Squares Method in One Dimension

In the residual squares method (as implemented in this thesis, see section 3.4.4) used for fitting one-dimensional polynomials, we start by considering a polynomial of n^{th} order in x:

$$f(x) = a_0 + a_1 x + a_2 x^2 + \ldots + a_n x^n = \sum_{j=0}^{n} a_j x^j, \tag{A.2.1}$$

where a_j are the coefficients. We wish to use this polynomial as an approximation to the points within a dataset defined by the corresponding scalars x_i and f_i. The quality of the match of a candidate polynomial is measured by the residual squared:

$$R^2 = \sum_{i=1}^{N} \left(f(x_i) - f_i\right)^2, \tag{A.2.2}$$

where R is the residual, $f(x_i)$ is the polynomial and N is the size of the dataset. A smaller value for R^2 means a higher quality fit, with a value of 0 indicating a perfect fit. This method considers the absolute deviation of all the points in the data set in the f direction, from the approximation made by the polynomial. There is an equal weighting given to the quality of the fit for all points based upon their x coordinate. However, because the difference between the data point and the approximation (in the f direction) is squared, a greater weighting is put on a single point with a large deviation than several points with a small deviation, which is not always ideal. Also, it would be desirable to have the quality of the fit weighted more strongly on points close to the minimum of the curve and this was not implemented here.

We might consider finding a solution (in terms of the coefficients of the polynomial) for $R^2 = 0$. However, in practice an exact solution will not exist, which will cause many linear equation solvers to fail. Instead we minimize R^2 with respect to the coefficients of the polynomial, thereby finding the best fit. The best fit is assumed to be the only stationary point (there could certainly be no maximum) and so we find the first derivative and set it to 0:

$$\frac{\partial R^2}{\partial a_k} = \sum_{i=1}^{N} \left(f(x_i) - f_i\right) \frac{\partial f(x_i)}{\partial a_k} = 0, \tag{A.2.3}$$

where:

$$\frac{\partial f(x_i)}{\partial a_k} = x_i^k \tag{A.2.4}$$

and k is an indexing variable ranging from 0 to N; its distinct from j, as j is used to expand the polynomial.

Subsequently, we expand the polynomials to produce a series of $n+1$ linear equations (one for each unknown coefficient). In the case of a second order polynomial we define:

$$\begin{aligned} a_0 \textstyle\sum 1 \; &+ a_1 \textstyle\sum x_i \; + a_2 \textstyle\sum x_i^2 = \textstyle\sum f_i \\ a_0 \textstyle\sum x_i \; &+ a_1 \textstyle\sum x_i^2 + a_2 \textstyle\sum x_i^3 = \textstyle\sum f_i x_i \\ a_0 \textstyle\sum x_i^2 &+ a_1 \textstyle\sum x_i^3 + a_2 \textstyle\sum x_i^4 = \textstyle\sum f_i x_i^2 \end{aligned} \tag{A.2.5}$$

where all sums are from $i = 1$ to N.

In linear algebra we often solve problems using matrices in terms of:

$$\mathbf{A} \cdot \mathbf{B} = \mathbf{C} \tag{A.2.6}$$

$$\mathbf{B} = \mathbf{A}^{-1} \cdot \mathbf{C} \tag{A.2.7}$$

where $\mathbf{A}$ is a known matrix and $\mathbf{C}$ is a known conformable vector, thus defining the problem. $\mathbf{B}$ is the unknown solution vector i.e. the coefficients that fit the polynomial to the dataset. In the general case for a polynomial of order n, the linear equations expressed in matrix form are:

$$\begin{matrix} \mathbf{A} & & & & \cdot & \mathbf{B} & = & \mathbf{C} \end{matrix}$$

$$\begin{bmatrix} \sum x_i^0 & \sum x_i^1 & \dots & \sum x_i^n \\ \sum x_i^1 & \sum x_i^2 & \dots & \sum x_i^{n+1} \\ \vdots & \vdots & \ddots & \vdots \\ \sum x_i^n & \sum x_i^{n+1} & \dots & \sum x_i^{2n} \end{bmatrix} \cdot \begin{bmatrix} a_0 \\ a_1 \\ \vdots \\ a_n \end{bmatrix} = \begin{bmatrix} \sum f_i x_i^0 \\ \sum f_i x_i^1 \\ \vdots \\ \sum f_i x_i^n \end{bmatrix}. \tag{A.2.8}$$

More concisely we can say:

$$\begin{array}{lll} \mathbf{A} = [A_{jk}]\,; & \mathbf{B} = [B_j]\,; & \mathbf{C} = [C_j]\,; \\ A_{jk} = \sum x_i^{j+k}; & B_j = a_j; & C_j = \sum f_i x_i^j, \end{array} \tag{A.2.9}$$

where j and k are respectively the row and column indices which go from 0 to n, though as the array is symmetric, they can be used interchangeably. Again the sums shown are from i = 1 to N (i.e. a sum over the data points).

Equation (A.2.7) demonstrates a solution finding technique involving the computation of an inverse matrix and the subsequent matrix multiplication with the $\mathbf{C}$ vector to get the solution. This is known as the Gauss-Jordan method [107] but was found to produce poor fits for the data. Instead Cholesky decomposition and back substitution was used [107], which starts with the problem as defined by (A.2.6) but does not directly calculate the inverse matrix. The Cholesky decomposition was shown to improve fits as compared to the Gauss-Jordan method. Both methods were implemented by taking code directly out of *Numerical Recipes* [107].

A.3 Residual Squares Method in Three Dimensions

This section describes how a trivariate or three-dimensional polynomial can be fitted to a data set and then phrased as a set of linear equations, we refer to this in section 3.4.5. It is an extension of the method described in appendix A.2 and it may be helpful to read this first. We start with the description of a trivariate polynomial:

$$f(x,y,z) = a_{000}x^0y^0z^0 + \cdots + a_{123}x^1y^2z^3 + \cdots = \sum_{i,j,k=0}^{n} a_{ijk}x^iy^jz^k, \tag{A.3.1}$$

where x, y and z are the independent variables, a_{ijk} are the coefficients, i, j and k are integers used to index the coefficients and n is the order of the polynomial. The open way in which the specific terms included in (A.3.1) have been described is deliberate. In some cases an order n polynomial would mean that the final term in the sequence would relate to $i = j = k = n$. For the fitting performed in this thesis, it was decided to use a reduced set of terms, such that in an n^{th} order polynomial:

$$i + j + k \leq n. \tag{A.3.2}$$

The set of coefficients associated with these terms more closely resemble the polynomials produced using a Taylor expansion of n^{th} order.

As with the one-dimensional polynomial, the residual squared method is used to

measure a trial polynomial's fitness in describing the data set:

$$\begin{aligned} R^2 &= \sum_{h=1}^{N} \left(f(x_h, y_h, z_h) - f_h\right)^2 \\ &= \sum_{h_x=1}^{N_x} \sum_{h_y=1}^{N_y} \sum_{h_z=1}^{N_z} \left(f(x_{h_x}, y_{h_y}, z_{h_z}) - f_{h_x h_y h_z}\right)^2. \end{aligned} \tag{A.3.3}$$

In (A.3.3), R^2 has been defined in two ways; the upper (simpler) form expresses the data set in list format with h used to index the N data points defined with the corresponding scalars x_h, y_h, z_h and f_h; the lower and more contrived form considers the looping and indexing in the case where the data has been stored in a three-dimensional array (a pseudo regular grid), as this was the approach adopted in the present work. N_x, N_y and N_z define the number of points in the x, y and z directions respectively and the indices h_x, h_y h_z are used to index them. The data set is defined by the scalars x_{h_x}, y_{h_y}, z_{h_z} and $f_{h_x h_y h_z}$.

R^2 is minimized with respect to the coefficients of the polynomial in order to generate a set of linear equations to be solved.

$$\frac{\partial R^2}{\partial a_{pqr}} = \sum_{h=1}^{N} \left(f(x_h, y_h, z_h) - f_h\right) \frac{\partial f(x_h, y_h, z_h)}{\partial a_{pqr}} = 0, \tag{A.3.4}$$

where:

$$\frac{\partial f(x_h, y_h, z_h)}{\partial a_{pqr}} = x_h^p y_h^q z_h^r \tag{A.3.5}$$

and the indexing variables p, q and r have the same ranges as i, j and k but are distinct as they are not used for the expansion of the polynomial.

Rearranging and substituting equations (A.3.1), (A.3.4) and (A.3.5) we get:

$$\begin{aligned} \sum_{h=1}^{N} \left(f(x_h, y_h, z_h)\right) x_h^p y_h^q z_h^r = \sum_{h=1}^{N} \left(\sum_{i,j,k=0}^{n} a_{ijk} x_h^i y_h^j z_h^k \right) x_h^p y_h^q z_h^r = \\ \sum_{h=1}^{N} \sum_{i,j,k=0}^{n} a_{ijk} x_h^{i+p} y_h^{j+q} z_h^{k+r} = \sum_{h=1}^{N} f_h x_h^p y_h^q z_h^r, \end{aligned} \tag{A.3.6}$$

or broken down for three-dimensional arrays:

$$\sum_{h_x=1}^{N_x} \sum_{h_y=1}^{N_y} \sum_{h_z=1}^{N_z} \sum_{i,j,k=0}^{n} a_{ijk} x_{h_x}^{i+p} y_{h_y}^{j+q} z_{h_z}^{k+r} = \sum_{h_x=1}^{N_x} \sum_{h_y=1}^{N_y} \sum_{h_z=1}^{N_z} f_{h_x y z} x_{h_x}^p y_{h_y}^q z_{h_z}^r. \tag{A.3.7}$$

By expanding the sum over i, j and k, such that we include all the terms we wish

to consider, (which for the work in this thesis are described in (A.3.2)) we get the linear equation describing the quality of the fit with respect to coefficient a_{pqr}. By cycling over the same set of values for p, q and r as for i, j and k respectively, we produce a complete set of linear equations that can be solved to find all of the coefficients.

In matrix form the problem can be expressed as:

$$\begin{aligned} \mathbf{A} &= \left[A_{l_{pqr}m_{ijk}}\right]; \quad A_{l_{pqr}m_{ijk}} = \sum_{h=1}^{N} x_h^{i+p} y_h^{j+q} z_h^{k+r}; \\ \mathbf{B} &= \left[B_{l_{pqr}}\right]; \qquad\qquad B_{l_{pqr}} = a_{pqr}; \\ \mathbf{C} &= \left[C_{l_{pqr}}\right]; \qquad\qquad C_{l_{pqr}} = \sum_{h=1}^{N} f_h x_h^p y_h^q z_h^r, \end{aligned} \tag{A.3.8}$$

where the row and column indices for the matrix are l_{pqr} and m_{ijk} (and so are just one integer each). However, for each increment of these two indices, the corresponding p, q, r, i, j and k change to a different set of values that satisfy (A.3.2), until all combinations have been done. This can be achieved with a carefully written counting algorithm. The dimensions of the matrix (and number of coefficients in the trivariate polynomial are given by:

$$0 \leq l_{pqr}, m_{ijk} \leq \frac{2n^3 + 12n^2 + 22n + 12}{12}. \tag{A.3.9}$$

With the problem specified in matrix for, the problem can be passed to a linear solver as described in appendix A.2.

A.4 Calculation of Components of Stick Rotation

Here we describe the mathematics used to calculate the projection vector $\mathbf{v}_p$ of an octahedral stick vector on the plane of another two vectors (pseudo-cubic axis) (please see section 4.2.2.3 for context).

We consider a pair of vectors (which will be assigned the values of pseudo-cubic axis vectors) $\mathbf{x}$ and $\mathbf{y}$ and an additional vector $\mathbf{z}$ which is at right angles to both $\mathbf{x}$ and $\mathbf{y}$. We can express our stick vector $\mathbf{v}$ and the projection vector $\mathbf{v}_p$ in terms of components of these (we follow the convention that $\mathbf{v}$ points in the direction of increasing pseudo-cubic vectors):

$$d\mathbf{x} + e\mathbf{y} + f\mathbf{z} = \mathbf{v}; \tag{A.4.1}$$

$$d\mathbf{x} + e\mathbf{y} = \mathbf{v}_p, \tag{A.4.2}$$

and the following conditions exist:

$$\mathbf{x} \cdot \mathbf{y} \neq 1; \tag{A.4.3}$$

$$\mathbf{x} \cdot \mathbf{z} = \mathbf{y} \cdot \mathbf{z} = 0, \tag{A.4.4}$$

where d, e, and f are as yet uncalculated scalar coefficients. In the above, $\mathbf{x}$, $\mathbf{y}$ and $\mathbf{v}$ are known from the start and though $\mathbf{z}$ is calculable, it is not needed and excluded in the following two equations in which we apply (A.4.4) to equation (A.4.1):

$$d\mathbf{y} \cdot \mathbf{x} + ey^2 = \mathbf{y} \cdot \mathbf{v}; \tag{A.4.5}$$

$$dx^2 + e\mathbf{x} \cdot \mathbf{y} = \mathbf{x} \cdot \mathbf{v}, \tag{A.4.6}$$

where x and y are the magnitudes of their corresponding vectors. Rearranging (A.4.5) in terms of d and substituting into (A.4.6) we get:

$$x^2 \left(\frac{\mathbf{y} \cdot \mathbf{v} - ey^2}{\mathbf{y} \cdot \mathbf{x}} \right) + e\mathbf{x} \cdot \mathbf{y} = \mathbf{x} \cdot \mathbf{v}. \tag{A.4.7}$$

Rearranging to find e, we find:

$$\frac{x^2 \mathbf{y} \cdot \mathbf{v}}{\mathbf{y} \cdot \mathbf{x}} + e \left(\mathbf{x} \cdot \mathbf{y} - \frac{x^2 y^2}{\mathbf{y} \cdot \mathbf{x}} \right) = \mathbf{x} \cdot \mathbf{v}, \tag{A.4.8}$$

$$e = \frac{\mathbf{x} \cdot \mathbf{v} - \frac{x^2 \mathbf{y} \cdot \mathbf{v}}{\mathbf{y} \cdot \mathbf{x}}}{\mathbf{x} \cdot \mathbf{y} - \frac{x^2 y^2}{\mathbf{y} \cdot \mathbf{x}}} = \frac{(\mathbf{x} \cdot \mathbf{v})(\mathbf{y} \cdot \mathbf{x}) - x^2 \mathbf{y} \cdot \mathbf{v}}{(\mathbf{y} \cdot \mathbf{x})^2 - x^2 y^2}. \tag{A.4.9}$$

To find d we substitute e into:

$$d = \frac{\mathbf{x} \cdot \mathbf{v} - e\mathbf{x} \cdot \mathbf{y}}{x^2}, \tag{A.4.10}$$

which is derived from (A.4.6).

With d and e calculated, the projection vector is defined and we can return to the main text (section 4.2.2.3).

Appendix B

Trivariate Polynomial Description of the *I4/mcm* PE Surface

Table B.1: Coefficients for the polynomial fit of the *I4/mcm* potential energy surface as determined by three functionals with a 500 eV plane-wave energy cut-off, see section 3.4.5 and appendix A.3 for an explanation. Potential energy is in eV per formula unit.

i	j	k	LDA	PBE	PBEsol
0	0	0	-4.41101229617457×10^{1}	-4.02011290632576×10^{1}	-3.97555191757377×10^{1}
1	0	0	-1.05285838052736×10^{-1}	-1.00584508029459×10^{-1}	-1.16495490214515×10^{-1}
0	1	0	5.42785926482853×10^{-4}	4.64795406319396×10^{-4}	4.41481494289903×10^{-4}
0	0	1	-2.01671757678449×10^{0}	-1.23411780103313×10^{0}	-1.56037971161573×10^{0}
2	0	0	3.63003926545078×10^{1}	3.25298002269359×10^{1}	3.43361478933185×10^{1}
1	1	0	-3.61996860400445×10^{-3}	1.03509307875118×10^{-3}	-1.27302323639702×10^{-3}
0	2	0	3.27881873055435×10^{1}	2.75813007618967×10^{1}	3.03656885718155×10^{1}
1	0	1	1.74845438784568×10^{1}	1.46594734456375×10^{1}	1.65398678466124×10^{1}
0	1	1	-4.22340686053227×10^{1}	-3.28130436801637×10^{1}	-3.80501361619704×10^{1}
0	0	2	1.03217431506967×10^{2}	9.40147335071457×10^{1}	9.80553319694105×10^{1}
3	0	0	-6.54287695854357×10^{1}	-5.85345455651405×10^{1}	-6.19914731559617×10^{1}
2	1	0	1.56724460950779×10^{-2}	3.43273364802079×10^{-2}	3.39272225211629×10^{-2}
1	2	0	-1.12520796791200×10^{2}	-1.00567223422786×10^{2}	-1.07037111927193×10^{2}
0	3	0	-6.39743175232436×10^{1}	-5.70651778629777×10^{1}	-6.06806493362174×10^{1}
2	0	1	-2.99514172213785×10^{1}	-2.70817903455731×10^{1}	-2.87834139521668×10^{1}
1	1	1	2.41536974996741×10^{2}	2.13316950532086×10^{2}	2.28382428786903×10^{2}
0	2	1	-7.01739669188904×10^{-1}	-7.30731437869059×10^{0}	-3.78907292264542×10^{0}
1	0	2	-1.73316966751539×10^{2}	-1.56420743278155×10^{2}	-1.67515819533842×10^{2}
0	1	2	-6.81853114909131×10^{1}	-7.08948792133535×10^{1}	-6.48884038184336×10^{1}
0	0	3	-2.41872127767637×10^{2}	-1.93030236014860×10^{2}	-2.19992535992528×10^{2}
4	0	0	8.83973247378020×10^{1}	8.02551636807473×10^{1}	8.49927551818270×10^{1}
3	1	0	6.49715339414790×10^{-1}	-1.05654505308680×10^{-1}	1.84371184895537×10^{-1}
2	2	0	1.46797351556493×10^{2}	1.37834363421554×10^{2}	1.43973626551125×10^{2}
1	3	0	1.29460002592579×10^{2}	1.21274984562293×10^{2}	1.25950860404336×10^{2}
0	4	0	1.72147888935557×10^{2}	1.61177844565288×10^{2}	1.67380740693134×10^{2}
3	0	1	3.53202813841552×10^{1}	3.16273613219637×10^{1}	3.35398913311529×10^{1}
2	1	1	-3.44471086593381×10^{2}	-3.17508420727695×10^{2}	-3.35130126090145×10^{2}
1	2	1	-1.85229686687291×10^{2}	-1.54876540700389×10^{2}	-1.71436850568088×10^{2}
0	3	1	-5.86016918393512×10^{1}	-4.43643160168129×10^{1}	-5.34183420019639×10^{1}
2	0	2	1.91993698421341×10^{2}	1.90101421565986×10^{2}	1.94686400112368×10^{2}
1	1	2	-8.79518936024186×10^{1}	-6.84369886152551×10^{1}	-8.05896423648098×10^{1}
0	2	2	3.73613407377350×10^{2}	3.67926747310303×10^{2}	3.72667931597663×10^{2}
1	0	3	3.85213219071706×10^{2}	2.97920562603259×10^{2}	3.55040016391885×10^{2}
0	1	3	1.33555861980178×10^{2}	1.65343737576969×10^{2}	8.33971657349665×10^{1}
0	0	4	1.86372659398275×10^{3}	1.49334685545982×10^{3}	1.78807515759733×10^{3}
5	0	0	-9.73015102583990×10^{1}	-1.00898421494231×10^{2}	-1.00025245188197×10^{2}
4	1	0	-5.00663989928235×10^{0}	-1.76852262764954×10^{0}	-2.53333157515727×10^{0}

Table B.1: (continues on the next page)

Table B.1: (continued from previous page)

i	j	k	LDA	PBE	PBEsol
3	2	0	-1.32189983410860×10^{2}	-1.40312286249875×10^{2}	-1.40572618356350×10^{2}
2	3	0	-1.20272275613396×10^{2}	-1.24274723218970×10^{2}	-1.25597759215101×10^{2}
1	4	0	-1.70136271742749×10^{2}	-1.72021363252432×10^{2}	-1.71375281283280×10^{2}
0	5	0	-2.58185315873862×10^{2}	-2.40322443264068×10^{2}	-2.50475297984935×10^{2}
4	0	1	-3.77593648413015×10^{1}	-3.76826451299967×10^{1}	-3.80691570864150×10^{1}
3	1	1	3.43395655708492×10^{2}	3.55410700152230×10^{2}	3.55593148007988×10^{2}
2	2	1	3.23847740945910×10^{2}	2.91170658352240×10^{2}	3.13008255984721×10^{2}
1	3	1	1.59225654951279×10^{2}	1.41073256729599×10^{2}	1.57141317639021×10^{2}
0	4	1	-2.37512633779903×10^{2}	-2.34306072193957×10^{2}	-2.40799380126052×10^{2}
3	0	2	-1.30312059451524×10^{2}	-1.25593266204239×10^{2}	-1.28462354167730×10^{2}
2	1	2	1.75814810659971×10^{2}	1.56517276028819×10^{2}	1.70182742774691×10^{2}
1	2	2	-3.73144749459736×10^{2}	-3.90754783455807×10^{2}	-3.88373719517881×10^{2}
0	3	2	-3.09291458486823×10^{2}	-3.41167115329888×10^{2}	-3.27417038667479×10^{2}
2	0	3	-3.26662369958290×10^{2}	-3.95967094660928×10^{2}	-3.83275833255675×10^{2}
1	1	3	2.46096262705035×10^{2}	3.22367118418436×10^{2}	3.09174533887127×10^{2}
0	2	3	4.37030262006381×10^{2}	2.78330957224450×10^{2}	3.23276546218983×10^{2}
1	0	4	-3.18922445063106×10^{3}	-2.32294106668834×10^{3}	-2.76189348117886×10^{3}
0	1	4	-1.62899931131593×10^{3}	-1.92337754347353×10^{3}	-1.11007914042444×10^{3}
0	0	5	-7.14388983218297×10^{3}	-6.23060829805580×10^{3}	-8.22496025957779×10^{3}
6	0	0	6.34542290920187×10^{1}	9.24040394645507×10^{1}	7.48499365534588×10^{1}
5	1	0	9.40359728043500×10^{0}	6.02222983226292×10^{0}	5.15169175278962×10^{0}
4	2	0	7.11525740367249×10^{1}	1.07272788398593×10^{2}	9.31838496626876×10^{1}
3	3	0	6.00794415978815×10^{1}	8.95013132322048×10^{1}	8.32788186309114×10^{1}
2	4	0	4.73967409340317×10^{1}	5.31305484476453×10^{1}	4.76028044564685×10^{1}
1	5	0	2.70029539616580×10^{2}	2.35507364830611×10^{2}	2.40239926107397×10^{2}
0	6	0	-5.68686171897092×10^{2}	-5.62553644601129×10^{2}	-5.69025019688703×10^{2}
5	0	1	2.52243505092173×10^{1}	3.57902561692108×10^{1}	3.00831689801870×10^{1}
4	1	1	-1.99707682792757×10^{2}	-2.60425195550898×10^{2}	-2.28950432573871×10^{2}
3	2	1	-3.03757703625445×10^{2}	-3.56238231521695×10^{2}	-3.30476906245167×10^{2}
2	3	1	-2.07492060162494×10^{2}	-2.29115262344689×10^{2}	-2.19817730008804×10^{2}
1	4	1	1.60815717067985×10^{2}	1.39927947922839×10^{2}	1.38794352011715×10^{2}
0	5	1	4.23417184161023×10^{2}	3.82911155008424×10^{2}	4.34873009770777×10^{2}
4	0	2	8.80417080743295×10^{1}	1.14506383856653×10^{2}	9.56612473840984×10^{1}
3	1	2	-1.46712512001060×10^{2}	-2.18166758557205×10^{2}	-1.93904423522402×10^{2}
2	2	2	2.80489127831785×10^{2}	3.37848450877173×10^{2}	2.89073136555468×10^{2}
1	3	2	5.98981727108881×10^{2}	6.04343220396064×10^{2}	5.76723541274444×10^{2}
0	4	2	1.32221243636317×10^{3}	1.40621152215896×10^{3}	1.45738198698690×10^{3}
3	0	3	-1.23591286447202×10^{2}	-2.00235965981266×10^{2}	-1.65303210404828×10^{2}
2	1	3	-4.20616690997289×10^{1}	2.17563212610248×10^{1}	3.30347111740054×10^{1}
1	2	3	-6.84523043348959×10^{2}	-5.41176131473256×10^{2}	-4.93630336110303×10^{2}
0	3	3	-1.00219219065123×10^{3}	-7.82069201179512×10^{2}	-8.88824387314994×10^{2}
2	0	4	2.09799175683335×10^{3}	2.40186442184191×10^{3}	2.33471574203775×10^{3}
1	1	4	-1.45960782947544×10^{3}	-1.85624348871062×10^{3}	-1.68137523258246×10^{3}
0	2	4	-6.01136772020013×10^{2}	-1.21183804013962×10^{1}	-1.35301984059267×10^{2}
1	0	5	9.27785329160580×10^{3}	6.10330123353403×10^{3}	7.38263747220007×10^{3}
0	1	5	8.73959219922494×10^{3}	9.50686211951123×10^{3}	5.89001872922364×10^{3}
0	0	6	8.64048884878122×10^{3}	1.21975582205270×10^{4}	1.84147392443654×10^{4}

Appendix C

Frequency Based Structure Comparison

C.1 Introduction

Using a custom written tool (*compFreq*) that takes in lists of frequencies from structures with the same numbers of atoms, we introduce another method for comparing the similarity of the structures. *compFreq*, described in appendix D.1.10, compares frequencies that are equivalent in ranking and for each pair of structures reports the greatest deviation of frequency. Similar structures will have a low deviation of frequencies. This type of analysis can be useful in comparing complex structures, where different but equivalent atomic motions can disguise the similarity of them.

The comparisons for the different unit cells has been laid out in the following sections.

C.2 Cubic

Please see section 4.3 for reference to the cubic ancestor structures (1–8), compared in table C.1 and see table 4.3.5 for the original list of frequencies.

From analysing the data, we find seven pairings of structures that match within eight wave-numbers. The reason for choosing a cut-off of eight was based on two ideas, firstly there was a general opinion that the difference in frequencies between equivalent structures should be a just a few wave-numbers. Secondly, from looking at the spectrum of deviations we see a moderately smooth spread before eight and after 55 (cm^{-1}) but a discontinuity between them. We took the discontinuity to be a marker of similar and dissimilar structures.

We see two groups of similar structures, based on the matching together of pairs of systems. The blue group is for the monoclinic structures 3 and 6 and the red group is for the rhombohedral structures 4, 5, 7 and 8.

Table C.1: The maximum deviation between lists of equivalently ranking frequencies for the cubic ancestor structures (cm^{-1}). The close matches have been coloured and colour coded to denote different groupings.

Structure	2	3	4	5	6	7	8
1	107	98	95	95	102	95	99
2		70	67	68	78	67	72
3			55	60	8	61	62
4				5	56	5	7
5					61	1	4
6						61	63
7							5

C.3 Tetragonal

Please see section 4.4 for reference to the tetragonal ancestor structures (9–19), compared in table C.2 and see table 4.4.18 for the original list of frequencies.

Analysing the frequency comparison data for the tetragonal system proved harder than in the cubic system. Unlike the cubic structures, there was no strong discontinuity in frequency differences, but rather a fairly smooth spread. The lack of any hard distinction is most likely caused by the increased diversity in the way that the atoms within the tetragonal unit cell can move. One set of structures has been highlighted in red and represents all of the end point structures except structure 12, the greatest frequency deviation found in this set is $10.3\,cm^{-1}$. In common, these structures (11, 14, 17 and 19) all have a monoclinic lattice type, the highest dipole moments (between 0.53 and $0.56\,D$), no imaginary modes and non-zero and approximately equal values of $\theta_{x'_{xy}}$ and $\theta_{y'_{yz}}$, indicating a rocking over of the octahedra, hinging mostly around an edge (instead of a vertex). Structure 12 which was the only end point structure falling outside of this group hinges mostly around a vertex.

There are some other parings of structures such as 13 with 16, which also have some common traits such as similar energy, one imaginary mode of similar magnitude and similar dipole strengths and directions, though not always the same type of octahedral rotations (we might also include structure 18 in this group). The similarities of groups become more vague here though.

Table C.2: The maximum deviation between lists of equivalently ranking frequencies for the tetragonal ancestor structures (cm^{-1}). One set of close matches have been coloured in red to show their grouping.

Structure	10	11	12	13	14	15	16	17	18	19
9	56	59	58	57	64	56	58	65	58	61
10		42	42	40	42	23	42	42	42	42
11			14	23	7	38	22	10	23	8
12				27	21	29	26	22	26	18
13					30	35	9	28	11	29
14						38	29	13	30	8
15							35	39	38	36
16								27	19	28
17									28	6
18										29

C.4 Orthorhombic

Please see section 4.5 for reference to the orthorhombic ancestor structures (20–29), compared in table C.3 and see table 4.5.17 for the original list of frequencies.

With the orthorhombic ancestor systems, it was possible to identify a discontinuity in the sets of frequency differences for the different structures. A jump between about 5 and $18\,cm^{-1}$ was found and so structures with a lower maximum difference in frequencies than $6\,cm^{-1}$ were considered to be similar. This form of analysis identified four pairs of similar structures, which have been colour differently in table C.3.

Table C.3: The maximum deviation between lists of equivalently ranking frequencies for the orthorhombic ancestor structures (cm^{-1}). The close matches have been coloured and colour coded to denote different groupings.

Structure	21	22	23	24	25	26	27	28	29
20	47	61	63	63	63	62	63	62	63
21		57	54	49	57	56	58	48	57
22			35	46	25	2	37	46	27
23				47	19	36	5	48	18
24					46	45	49	5	46
25						26	21	47	2
26							38	45	27
27								49	20
28									48

We will make some further consideration of the similar structures in the main text of the thesis (section 4.5.3).

C.5 Rhombohedral

Please see section 4.6 for reference to the rhombohedral ancestor structures (30–37), compared in table C.4 and see table 4.6.13 for the original list of frequencies.

As with the previous structures, the list of maximum differences between lists of frequencies was put into order. There was no clear discontinuity in the data, though there was a sudden change in the gradient (discontinuity in the first derivative) between the fourth and fifth lowest frequency comparison. The cut-off was chosen to be in between a 13 and 24 cm^{-1} frequency difference. Two sets of similar structures have been identified and coloured differently in table C.4.

Table C.4: The maximum deviation between lists of equivalently ranking frequencies for the rhombohedral structures (cm^{-1}). The close matches have been coloured and colour coded to denote different groupings.

Structure	31	32	33	34	35	36	37
30	68	73	77	74	94	91	97
31		38	53	66	93	90	96
32			24	28	54	51	58
33				13	39	36	43
34					26	28	30
35						4	4
36							7

We make some further consideration of the similar structures in the main text of the thesis (section 4.6.3).

Appendix D

Analytical Computer Codes Used in the Course of the Thesis

D.1 Custom Codes

Here we list the computer codes that were developed in connection with the completion of the work described in this thesis and provide brief descriptions of their functionality. The codes are working versions of software that were not intended for open publication. The source code can be made available upon request.

D.1.1 interpPos (*Interpolate Positions*)

interpPos is a code used to generate the structure images used in Nudged Elastic Band calculations for *VASP*, see section 2.4.5.3. The code takes as input, two end point structures described using fractional coordinates in the *VASP* structure format. *interpPos* then linearly interpolates the (a) atomic positions, (b) lattice vectors and (c) the universal scaling factor (as referred to in the *VASP* manual [68] and referred to as V_p in the thesis) which is assumed to be positive. A specified number of structures are produced and put into separate enumerated directories as is the expected set-up for a NEB calculation. For more information see section 4.2.1 on page 112.

D.1.2 cds3 (*Compare Different Structures 3*

cds3 is intended to compare two similar structures with one another and analyse the vibrational modes of each in order to determine which modes are involved in the transition between the two structures. It takes as input, the output (`OUTCAR`) files from frequency calculations run with the *VASP* code. *cds3* reads from the `OUTCAR` files, the lattice parameters, atomic coordinates and the eigenvectors that describe the vibrational modes. A proximity check to map the atoms from structure B (the second, as input at the command line) onto structure A. The eigenvectors of structure A are compared to a difference vector which points from structure A to structure B. For each eigenvector in structure A, angular separation and the component of the eigenvector against the

difference vector is reported. For more information see section 4.2.2.1.

D.1.3 getPolar (*Get Polarization*)

getPolar analyses a *VASP* structure file and reports information about its polarization properties. It assumes that the first two element types will be strontium and titanium respectively and that the titanium atoms will each have six nearest neighbour oxygen atoms and that strontium atoms will each have 12 nearest neighbour oxygen atoms (though this can easily be reconfigured in the source code). It calculates the polarization of each cation and reports its magnitude and direction in Debye units. For more information see section 4.2.2.4.

D.1.4 rotAngles2 (*Rotation Angles 2*)

rotAngles2 Takes as input a *VASP* structure file and also expects a description of three pseudo-cubic vectors, defined in terms of the cell vectors. It uses these to determine the orientation (rotation) and internal distortion of the octahedra within the cell. It also provides information on the lattice parameters, volume and octahedral volumes of the cell. The way that octahedral rotations are calculated is given in section 4.2.2.3.

D.1.5 findMinima2 (*Find all Minima 2*)

findMinima2 is a code that reads in a formatted list of structural parameters for the $I4/mcm$ energy landscape calculations, for which it expects the points to be on a regular grid. It puts the data into a three-dimensional array and then identifies minima based on a comparison with nearest neighbours (see section 3.4.2).

D.1.6 volMatFit (*Volume Matrix with Fitting*)

volMatFit builds upon findMinima2 in that it uses the same data entry engine. However, it uses a one-dimensional polynomial fitting algorithm to flatten the data in the direction of volume. For every point on the plane of ratio and angle, it reports the minimum potential energy and the volume corresponding to it. Contour plots can be produced from the output data (see section 3.4.4)

D.1.7 thetaMatFit2 (*Theta Matrix Fitting 2*)

thetaMatFit2 also adopts the data entry engine of findMinima2. The code is philosophically similar to *volMatFit* in that it fits one-dimensional contour plots in order to flatten a three-dimensional data set into two dimensions, in this case flattening with respect to angle to give a data set with volume and ratio as axes. In addition to this, it also performs linear interpolation in the direction of volume. Volume was not calculated in even increments (rather a volume parameter that scales all the lattice vectors), the linear interpolation is required to get the contour plotting software to produce a good image. The code is mentioned in the text in section 3.4.4.

D.1.8 multiVariateFit (*Multivariate polynomial Fitting*)

multiVariateFit currently a somewhat bloated code. It performs several functions as more and more functionality has been bolted on to the end. It also takes in data using the input engine of *volMatFit*. Subsequently, it uses Cholesky decomposition to fit a three-dimensional polynomial to the data set (see section 3.4.5 and appendix A.3) and outputs the coefficients. It then decomposes the polynomial into one-dimensional functions such that comparisons with Landau theory can be made (see section 3.4.6). Finally it produces data sets to determine the expectation octahedral rotation angle, based on a calculation of the wave function, associated with the potential energy surface (see section 3.4.7).

D.1.9 genPOSCARs (*Generate POSCAR structure files*)

genPOSCARs a program to generate large numbers of systematically named *VASP* structure files describing the $I4/mcm$ space group. The program linearly changes the volume parameter, ratio and octahedral rotation angle to produce a three-dimensional array of structures with varying properties. It is intended for use to generate a three-dimensional data set, before any of the fitting programs can process the results.

D.1.10 compFreq (*Compare Frequencies*)

compFreq is a program used to compare lists of frequencies with one another, assuming the lists are conformable. For every combination of two frequency lists, it will compare each pair of equivalent frequencies and return the greatest deviation between the two lists. It outputs the maximum deviations in a comparison table (see appendix C).

D.1.11 carLpun (*CAR file to Label a PUN file*)

carLpun is a tool made to help with the labelling of atoms within *ChemShell*. The graphical visualization package Materials Studio can output `.car` files, which can be labelled via atom selection and changing the atom types. carLpun takes a punch file that has been labelled in this way and uses it to label a *ChemShell* fragment file. These files usually have the extension `.pun`, hence the name.

D.1.12 writeMSI, writeXYZ (*Write an MSI/XYZ file*)

writeMSI and *writeXYZ* expect as input a *ChemShell* structure file (see appendix D.3.2), also known as a fragment and usually given the extension `.pun`. These two codes will output equivalent structure files using the MSI or XYZ format having the same file name as the original file but with the appropriate file extension. The MSI file format is native to *Material Studio* [148]. The XYZ file format is one of the simplest structural description formats available and can be generated by *ChemShell*, interpreted and written to by Material Studio and is the file format used by *compareXYZ*, see appendix D.2.3.

D.2 Other Custom Codes

In addition to computer codes written specifically for this work, several other codes written by members of my research team were made use of. These codes are listed and briefly described below. The authors should be contacted for access to this software.

D.2.1 neb-analysis (*Nudged Elastic Band Analysis*)

neb-analysis is a small Unix script file written by Aron Walsh, currently at the University of Bath, to look within the multiple output files produced by a NEB calculation performed by *VASP* and produce a listing of energies of the different structures such that a graph can be plotted.

D.2.2 Construct

Construct is a program written by Alexy Sokol of University College London, to build embedded cluster models (the atomic coordinates and correction charges), for use with *ChemShell* (see section 2.5.5).

D.2.3 compareXYZ

compareXYZ is a code written by Alexey Sokol to compare structure files, written in the `.xyz` format.

D.2.4 murn (*Murnaghan (equation of state)*)

murn is a program by an unknown author for calculating the Murnaghan equation of state of a data set. In essence, it fits a third order, one-dimensional polynomial to a dataset, in a way that weights the quality of the fit, to describe accurately the minimum.

D.3 Large External Codes

Though they have been well mentioned during the course of this thesis, for completeness, the main codes that were used for performing the majority of the processing for the results in the thesis are listed and described here.

D.3.1 VASP (*Vienna Ab-initio Simulation Package*)

VASP is a package for carrying out plane-wave periodic DFT calculations using several contemporary functionals. It can perform geometry optimizations, Nudged Elastic Band and frequency calculations. Please see [66–68, 72, 73, 79, 83–85] for further information.

D.3.2 ChemShell (*Chemistry Shell*)

ChemShell is a shell environment for carrying out computational chemistry calculations. It has interfaces with a range of other Quantum Mechanical and Molecular Mechanical codes including *GAMESS-UK* (see appendix D.3.3) and *GULP* (see appendix D.3.4). It also provides an environment for carrying out hybrid embedded cluster QM/MM calculations involving a central region of interest modelled by a QM code and an outer region modelled by a MM code (see section 2.5). *ChemShell* also includes a variety of custom written geometry optimization methods that allow much flexibility in calculations (though these are based around more ubiquitous optimization methods). See [1–3] for further information.

D.3.3 GAMESS-UK (*General purpose Ab-initio Electronic Structure program for performing SCF - United Kingdom*)

GAMESS-UK is a package for carrying out periodic and non-periodic DFT and HF calculations using non-periodic basis sets e.g. Gaussian type basis sets are very commonly used. The package is highly configurable and can perform geometry optimization and nudged elastic band calculations. Please see [116, 117] for further information.

D.3.4 GULP (*General Utility Lattice Program*)

GULP is a package for carrying out classical Molecular Mechanical forcefield type calculations, using the Shell Model. It can carry out geometry optimizations, Nudged Elastic Band and Mott-Littleton calculations. See [88, 118] for further information.

References

(1) P. Sherwood, A. H. de Vries, M. F. Guest, G. Schreckenbach, C. R. A. Catlow, S. A. French, A. A. Sokol, S. T. Bromley, W. Thiel, A. J. Turner, S. Billeter, F. Terstegen, S. Thiel, J. Kendrick, S. C. Rogers, J. Casci, M. Watson, F. King, E. Karlsen, M. Sjøvoll, A. Fahmi, A. Schäfer, and C. Lennartz, "QUASI: A General Purpose Implementation of the QM/MM Approach and its Application to Problems in Catalysis", *Journal of Molecular Structure (Theochem)*, 2003, **632**, 1–28.

(2) A. A. Sokol, S. T. Bromley, S. A. French, C. R. A. Catlow, and P. Sherwood, "Hybrid QM/MM Embedding Approach for the Treatment of Localized Surface States in Ionic Materials", *International Journal of Quantum Chemistry*, 2004, **99**, 695–712.

(3) P. Sherwood, *ChemShell Website*, `http://www.chemshell.org`, 2011.

(4) Q. Ma, F. Tietz, D. Sebold, and D. Stöver, "Y-Substituted $SrTiO_3$-YSZ Composites as Anode Materials for Solid Oxide Fuel Cells: Interaction Between SYT and YSZ", *Journal of Power Sources*, 2010, **195**, 1920–1925.

(5) J. Gerblinger and H. Meixner, "Fast Oxygen Sensors Based on Sputtered Strontium Titanate", *Sensors and Actuators B*, 1991, **4**, 99–102.

(6) J. G. Mavroides, J. A. Kafalas, and D. F. Kolesar, "Photoelectrolysis of Water in Cells with $SrTiO_3$ Anodes", *Applied Physics Letters*, 1976, **28**, 241–243.

(7) F. T. Wagner and G. A. Somorjai, "Photocatalytic and Photoelectrochemical Hydrogen Production on Strontium Titanate Single Crystals", *Journal of the American Chemical Society*, 1980, **102**, 5494–5502.

(8) S. A. Hayward and E. K. H. Salje, "Cubic-Tetragonal Phase Transition in $SrTiO_3$ Revisited: Landau Theory and Transition Mechanism", *Phase Transitions*, 1999, **68**, 501–522.

(9) S. C. Kehr, Y. M. Liu, L. W. Martin, P. Yu, M. Gajek, S.-Y. Yang, C.-H. Yang, M. T. Wenzel, R. Jacob, H.-G. von Ribbeck, M. Helm, X. Zhang, L. M. Eng, and R. Ramesh, "Near-Field Examination of Perovskite-Based Superlenses and Superlens-Enhanced Probe-Object Coupling", *Nature Communications*, 2011, **2**, 249.

(10) Y. Xin, J. Jiang, K. Huo, T. Hu, and P. K. Chu, "Bioactive $\mathrm{SrTiO_3}$ Nanotube Arrays: Strontium Delivery Platform on Ti-Based Osteoporotic Bone Implants", *ACS Nano*, 2009, **3**, 3228–3234.

(11) Y.-S. Ham and J.-H. Koh, "The Dielectric Characteristics of Screen Printed $\mathrm{SrTiO_3}$-Epoxy Composite Thick Films on the Cu Plate PCB Substrates", *Ferroelectrics*, 2009, **382**, 85–91.

(12) C. Jorel, C. Vallée, P. Gonon, E. Gourvest, C. Dubarry, and E. Defay, "High Performance Metal-Insulator-Metal Capacitor Using a $\mathrm{SrTiO_3/ZrO_2}$ Bilayer", *Applied Physics Letters*, 2009, **94**, 253502.

(13) Y. Nakano and N. Ichinose, "Oxygen Adsorption and VDR Effect in $\mathrm{(Sr,Ca)TiO_{3-}}_x$ Based Ceramics", *Journal of Materials Research*, 1990, **5**, 2910–2922.

(14) T. Menke, R. Dittmann, P. Meuffels, K. Szot, and R. Waser, "Impact of the Electroforming Process on the Device Stability of Epitaxial Fe-Doped $\mathrm{SrTiO_3}$ Resistive Switching Cells", *Journal of Applied Physics*, 2009, **106**, 114507.

(15) M. L. D. de Graaf, *Mineralogy of Russia*, `http://maurice.strahlen.org/yakutia/murun_massif.htm`, 2010.

(16) Commercial Crystal Laboratories, Inc., *Strontium Titanate Substrates*, `http://www.crystalguru.com/PhotoGallery/StrontiumTitanate/StrontiumTitanateSubstrates.htm`, 2010.

(17) J. A. Noland, "Optical Absorption of Single-Crystal Strontium Titanate", *Physical Review*, May 1954, **94**, 724–724.

(18) R. Moos, W. Menesklou, and K. H. Härdtl, "Hall Mobility of Undoped N-Type Conducting Strontium Titanate Single Crystals Between 19 K and 1373 K", *Applied Physics A*, 1995, **61**, 389–395.

(19) N.-H. Chan, R. K. Sharma, and D. M. Smyth, "Nonstoichiometry in $\mathrm{SrTiO_3}$", *Journal of the Electrochemical Society*, 1981, **128**, 1762–1769.

(20) R. Moos and K. H. Härdtl, "Defect Chemistry of Donor-Doped and Undoped Strontium Titanate Ceramics Between 1000° and 1400°C", *Journal of the American Ceramic Society*, 1997, **80**, 2549–2562.

(21) A. F. Wells, *Structural Inorganic Chemistry*, Oxford University Press, 5th edn., 1995.

(22) K. Tsuda and M. Tanaka, "Refinement of Crystal Structure Parameters using Convergent-Beam Electron Diffraction: the Low-Temperature Phase of $SrTiO_3$", *Acta Crystallographica Section A*, 1995, **51**, 7–19.

(23) F. W. Lytle, "X-Ray Diffractometry of Low-Temperature Phase Transformations in Strontium Titanate", *Journal of Applied Physics*, 1964, **35**, 2212–2215.

(24) S. V. Bogdanov, A. M. Kashtanova, and K. V. Kiseleva, "Concerning the Phase Transitions in $SrTiO_3$", English (translation), *Bulletin, Academy of Sciences of the USSR*, 1965, **29**, 902–906.

(25) C. R. A. Catlow, Z. X. Guo, M. Miskufova, S. A. Shevlin, A. G. H. Smith, A. A. Sokol, A. Walsh, D. J. Wilson, and S. M. Woodley, "Advances in Computational Studies of Energy Materials", *Philosophical Transactions of the Royal Society A*, 2010, **368**, 3379–3456.

(26) M. A. Saifi and L. E. Cross, "Dielectric Properties of Strontium Titanate at Low Temperature", *Physical Review B*, 1970, **2**, 677–684.

(27) H. Kronmüller and S. Parkin, *Handbook of Magnetism and Advanced Magnetic Materials*, Wiley, 2007, vol. 4, (contains article: M. Johnsson and P. Lemmens, "Crystallography and Chemistry of Perovskites").

(28) K. A. Müller and W. Berlinger, "Static Critical Exponents at Structural Phase Transitions", *Physical Review Letters*, 1971, **26**, 13–16.

(29) W. G. Nilsen and J. G. Skinner, "Raman Spectrum of Strontium Titanate", *The Journal of Chemical Physics*, 1968, **48**, 2240–2248.

(30) H. Unoki and T. Sakudo, "Electron Spin Resonance of Fe^{3+} in $SrTiO_3$ with Special Reference to the 110°K Phase Transition", *Journal of the Physical Society of Japan*, 1967, **23**, 546–552.

(31) A. Okazaki and M. Ono, "Determination of the Crystal Structure of Perovskitees with the Space Group $I4/mcm$", *Journal of the Physical Society of Japan*, 1978, **45**, 206–211.

(32) R. A. Evarestov, E. Blokhin, D. Gryaznov, E. A. Kotomin, and J. Maier, "Phonon Calculations in Cubic and Tetragonal Phases of $SrTiO_3$: A Comparative LCAO and Plane-Wave Study", *Physical Review B*, 2011, **83**, 134108.

(33) L. Rimai and G. A. deMars, "Electron Paramagnetic Resonance of Trivalent Gadolinium Ions in Strontium and Barium Titanates", *Physical Review*, 1962, **127**, 702–710.

(34) G. H. Kwei, A. C. Lawson, S. J. L. Billinge, and S. W. Cheong, "Structures of the Ferroelectric Phases of Barium Titanate", *The Journal of Physical Chemistry*, 1993, **97**, 2368–2377.

(35) H. A. Jahn and E. Teller, "Stability of Polyatomic Molecules in Degenerate Electronic States I—Orbital Degeneracy", *Proceedings of the Royal Society A*, 1937, **161**, 220–235.

(36) U. Müller, *Inorganic Structural Chemistry*, ed. G. Meyer and A. Nakamura, Wiley, 2nd edn., 1993.

(37) A. S. Bhalla, R. Guo, and R. Roy, "The Perovskite Structure — A Review of its Role in Ceramic Science and Technology", *Materials Research Innovations*, 2000, **4**, 3–26.

(38) H. E. Weaver, "Dielectric Properties of Single Crystals of $\mathrm{SrTiO_3}$ at Low Temperatures", *Journal of Physics and Chemistry of Solids*, 1959, **11**, 274–277.

(39) V. V. Lemanov, "Improper Ferroelastic $\mathrm{SrTiO_3}$ and What We Know Today About Its Properties", *Ferroelectrics*, 2002, **265**, 1–21.

(40) N. Sai and D. Vanderbilt, "First-Principles Study of Ferroelectric and Antiferrodistortive Instabilities in Tetragonal $\mathrm{SrTiO_3}$", *Physical Review B*, 2000, **62**, 13942–13950.

(41) K. A. Müller, W. Berlinger, and E. Tosatti, "Indication for a Novel Phase in the Quantum Paraelectric Regime of $\mathrm{SrTiO_3}$", *Zeitschrift für Physik B*, 1991, **84**, 277–283.

(42) K. A. Müller and H. Burkard, "$\mathrm{SrTiO_3}$: An Intrinsic Quantum Paraelectric Below 4 K", *Physical Review B*, 1979, **19**, 3593–3602.

(43) O. E. Kvyatkovskiĭ, "Quantum Effects in Incipient and Low-Temperature Ferroelectrics (A Review)", *Physics of the Solid State*, 2001, **43**, 1401–1419.

(44) R. Wahl, D. Vogtenhuber, and G. Kresse, "$\mathrm{SrTiO_3}$ and $\mathrm{BaTiO_3}$ Revisited Using the Projector Augmented Wave Method: Performance of Hybrid and Semilocal Functionals", *Physical Review B*, 2008, **78**, 104116.

(45) A. M. Glazer, "The Classification of Tilted Octahedra in Perovskites", *Acta Crystallographica Section B*, 1972, **28**, 3384–3392.

(46) A. M. Glazer, "Simple Ways of Determining Perovskite Structures", *Acta Crystallographica Section A*, 1975, **31**, 756–762.

(47) N. W. Thomas, "The Compositional Dependence of Octahedral Tilting in Orthorhombic and Tetragonal Perovskites", *Acta Crystallographica Section B*, 1996, **52**, 16–31.

(48) M. T. Dove, "Theory of Displacive Phase Transitions in Minerals", *American Mineralogist*, 1997, **82**, 213–244.

(49) J. F. Scott, "Soft-Mode Spectroscopy: Experimental Studies of Structural Phase Transitions", *Reviews of Modern Physics*, 1974, **46**, 83–128.

(50) L. D. Landau, "Zur Theorie der Phasenumwandlungen. I.", *Physikalische Zeitschrift der Sowjetunion*, 1937, **11**, 26–47, (English translation in: D. ter Haar, *Collected Papers of L. D. Landau*, Pergamon Press, 1965, pp. 193–209).

(51) L. D. Landau, "Zur Theorie der Phasenumwandlungen. II.", *Physikalische Zeitschrift der Sowjetunion*, 1937, **11**, 545–555, (English translation in: D. ter Haar, *Collected Papers of L. D. Landau*, Pergamon Press, 1965, pp. 209–216).

(52) M. C. Gallardo, J. Jiménez, J. del Cerro, and E. K. H. Salje, "The Structural Phase Transition in $\mathrm{SrTiO_3}$ Under Uniaxial Stress in the [110] Direction: A Calorimetric Study", *Journal of Physics: Condensed Matter*, 1996, **8**, 83–90.

(53) E. K. H. Salje, M. C. Gallardo, J. Jiménez, F. J. Romero, and J. del Cerro, "The Cubic-Tetragonal Phase Transition in Strontium Titanate: Excess Specific Heat Measurements and Evidence for a Near-Tricritical, Mean Field Type Transition Mechanism", *Journal of Physics: Condensed Matter*, 1998, **10**, 5535–5543.

(54) F. Cordero, A. Franco, V. R. Calderone, P. Nanni, and V. Buscaglia, "Anelastic Relaxation in $\mathrm{SrTiO_3}$ with O Vacancies and H", *Materials Science and Engineering A*, 2006, **442**, 55–58.

(55) D. B. Schwarz and H. U. Anderson, "Determination of Oxygen Chemical Diffusion Coefficients in Single Crystal $\mathrm{SrTiO_3}$ by Capacitance Manometry", *Journal of Electrochemical Society*, 1975, **122**, 707–710.

(56) A. E. Paladino, L. G. Rubin, and J. S. Waugh, "Oxygen Ion Diffusion in Single Crystal $\mathrm{SrTiO_3}$", *Journal of Physics and Chemistry of Solids*, 1965, **26**, 391–397.

(57) M. J. Akhtar, Z.-U.-N. Akhtar, R. A. Jackson, and C. R. A. Catlow, "Computer Simulation Studies of Strontium Titanate", *Journal of the American Ceramic Society*, 1995, **78**, 421–428.

(58) G. V. Lewis and C. R. A. Catlow, "Defect Studies of Doped and Undoped Barium Titanate Using Computer Simulation Techniques", *Journal of Physics and Chemistry of Solids*, 1986, **47**, 89–97.

(59) J. Crawford and P. Jacobs, "Point Defect Energies for Strontium Titanate: A Pair-Potentials Study", *Journal of Solid State Chemistry*, 1999, **144**, 423–429.

(60) A. Szabo and N. S. Ostlund, *Modern Quantum Chemistry*, Dover Publications, Inc., 1996.

(61) R. G. Parr and W. Yang, *Density-Functional Theory of Atoms and Molecules*, Oxford Science Publications, 1994.

(62) J. K. Labonowski, *Simplified Introduction to ab initio Basis Sets. Terms and Notation*, `http://www.ccl.net/cca/documents/basis-sets/basis.html`, Ohio Supercomputer Center, 2010.

(63) A. R. Leach, *Molecular Modelling Principles and Applications*, Prentice Hall, 2nd edn., 2001, pp. 30–34.

(64) D. Marx and J. Hutter, *Modern Methods and Algorithms of Quantum Chemistry Proceedings*, ed. J. Grotendorst, John von Neumann Institut für Computing, 2nd edn., 2000, vol. 3.

(65) P. Pulay, "Ab initio Calculation of Force Constants and Equilibrium Geometries in Polyatomic Molecules. I. Theory", *Molecular Physics*, 2002, **100**, 57–62.

(66) G. Kresse and J. Furthmüller, "Efficiency of ab-initio Total Energy Calculations for Metals and Semiconductors using a Plane-Wave Basis Set", *Computational Materials Science*, 1996, **6**, 15–50.

(67) G. Kresse and J. Furthmüller, "Efficient Iterative Schemes for ab initio Total-Energy Calculations using a Plane-Wave Basis Set", *Physical Review B*, 1996, **54**, 11169–11186.

(68) G. Kresse, M. Marsman, and J. Futhmüller, *VASP the Guide*, `http://cms.mpi.univie.ac.at/vasp/vasp/vasp.html`, 2010.

(69) N. W. Ashcroft and N. D. Mermin, *Solid State Physics*, ed. D. G. Crane, Harcourt College Publishers, College edn., 1976.

(70) H. J. Monkhorst and J. D. Pack, "Special Points for Brillouin-—one Integrations", *Physical Review B*, 1976, **13**, 5188–5192.

(71) D. R. Hamann, M. Schlüter, and C. Chiang, "Norm-Conserving Pseudopotentials", *Physical Review Letters*, 1979, **43**, 1494–1497.

(72) P. E. Blöchl, "Projector Augmented-Wave Method", *Physical Review B*, 1994, **50**, 17953–17979.

(73) G. Kresse and D. Joubert, "From Ultrasoft Pseudopotentials to the Projector Augmented-Wave Method", *Physical Review B*, 1999, **59**, 1758–1775.

(74) C. C. J. Roothaan, "New Developments in Molecular Orbital Theory", *Reviews of Modern Physics*, 1951, **23**, 69–89.

(75) L. H. Thomas, "The Calculation of Atomic Fields", *Mathematical Proceedings of the Cambridge Philosophical Society*, 1927, **23**, 542–548.

(76) E. Fermi, "Un Metodo Statistice per la Determinazione di Alcune Proprieta dell'Atomo", Italian, *Rendiconti Lincei*, 1927, **6**, 602–607, (English translation in: E. Fiorini and G. Gallavotti, "The Accademia dei Lincei to E. Fermi on the Occasion of the 110th Anniversary of His Birthday", *Rendiconti Lincei*, 2011, **22**, 277–306).

(77) E. Fermi, "Eine Statistische Methode zur Bestimmung einiger Eigenschaften des Atoms und ihre Anwendung auf die Theorie des Periodischen Systemsder Elemente", German, *Zeitschrift für Physik A*, 1928, **48**, 73–79.

(78) E. Fermi, "Sulla Deduzione Statistica di Alcune Proprieta dell'Atomo. Applicazione alla Teoria del Systema Periodico degli Elementi", Italian, *Rendiconti Lincei*, 1928, **7**, 342–346.

(79) J. P. Perdew and A. Zunger, "Self-Interaction Correction to Density-Functional Approximations for Many-Electron Systems", *Physical Review B*, 1981, **23**, 5048–5079.

(80) P. Hohenberg and W. Kohn, "Inhomogeneous Electron Gas", *Physical Review*, 1964, **136**, B864–B871.

(81) M. Hazelwinkel, *Encyclopaedia of Mathematics*, Kluwer Academic Publishers, 1990, vol. 5, pp. 336–336.

(82) W. Kohn and L. J. Sham, "Self-Consistent Equations Including Exchange and Correlation Effects", *Physical Review*, 1965, **140**, A1133–A1138.

(83) J. P. Perdew, K. Burke, and M. Ernzerhof, "Generalized Gradient Approximation Made Simple", *Physical Review Letters*, 1996, **77**, 3865–3868.

(84) J. P. Perdew, K. Burke, and M. Ernzerhof, "Errata: Generalized Gradient Approximation Made Simple [Phys. Rev. Lett. 77, 3865 (1996)]", *Physical Review Letters*, 1997, **78**, 1396–1396.

(85) J. P. Perdew, A. Ruzsinszky, G. I. Csonka, O. A. Vydrov, G. E. Scuseria, L. A. Constantin, X. Zhou, and K. Burke, "Restoring the Density-Gradient Expansion for Exchange in Solids and Surfaces", *Physical Review Letters*, 2008, **100**, 136406.

(86) A. D. Becke, "Density-Functional Thermochemistry. V. Systematic Optimization of Exchange-Correlation Functionals", *The Journal of Chemical Physics*, 1997, **107**, 8554–8560.

(87) P. J. Wilson, T. J. Bradley, and D. J. Tozer, "Hybrid exchange-correlation functional determined from thermochemical data and ab initio potentials", *The Journal of Chemical Physics*, 2001, **115**, 9233–9242.

(88) J. D. Gale and A. L. Rohl, "The General Utility Lattice Program (GULP)", *Molecular Simulation*, 2003, **29**, 291–341.

(89) H. M. Evjen, "On the Stability of Certain Heteropolar Crystals", *Physical Review*, 1932, **39**, 675–687.

(90) R. E. Johnson and S. Ranganathan, "Generalized Approach to Ewald Sums", *Physical Review E*, 2007, **75**, 056706.

(91) E. Madelung, "Das Elektrische Feld in Systemen von Regelmäßig Angeordneten Punktladungen", German, *Physikalische Zeitschrift*, 1918, **19**, 524–532.

(92) D. Frenkel and B. Smit, *Understanding Molecular Simulation*, Academic Press, 2nd edn., 2002.

(93) R. A. Jackson and C. R. A. Catlow, "Computer Simulation Studies of Zeolite Structure", *Molecular Simulation*, 1988, **1**, 207–224.

(94) R. A. Buckingham, "The Classical Equation of State of Gaseous Helium, Neon and Argon", *Proceedings of the Royal Society A*, 1938, **168**, 264–283.

(95) M. Born and J. E. Mayer, "Zur Gittertheorie der Ionenkristalle", German, *Zeitschrift für Physik A*, 1932, **75**, 1–18.

(96) J. E. Jones, "On the Determination of Molecular Fields. II. From the Equation of State of a Gas", *Proceedings of the Royal Society A*, 1924, **106**, 463–477.

(97) J. E. Jones and A. E. Ingham, "On the Calculation of Certain Crystal Potential Constants, and on the Cubic Crystal of Least Potential Energy", *Proceedings of the Royal Society A*, 1925, **107**, 636–653.

(98) P. A. Madden and M. Wilson, "'Covalent' Effects in 'Ionic' Systems", *Chemical Society Reviews*, 1996, **25**, 339–350.

(99) B. G. Dick and A. W. Overhauser, "Theory of the Dielectric Constants of Alkali Halide Crystals", *Physical Review*, 1958, **112**, 90–103.

(100) S. M. Tomlinson, C. M. Freeman, C. R. A. Catlow, H. Donnerberg, and M. Leslie, "Atomistic Simulation Studies of Technologically Important Oxides", *Journal of the Chemical Society, Faraday Transactions 2*, 1989, **85**, 367–383.

(101) A. M. Stoneham and J. H. Harding, "Interatomic Potentials in Solid State Chemistry", *Annual Review of Physical Chemistry*, 1986, **37**, 53–80.

(102) N. F. Mott and M. J. Littleton, "Conduction in Polar Crystals. I. Electrolytic Conduction in Solid Salts", *Transactions of the Faraday Society*, 1938, **34**, 485–499.

(103) C. R. A. Catlow, "Mott-Littleton Calculations in Solid-State Chemistry and Physics", *Journal of the Chemical Society, Faraday Transactions 2*, 1989, **85**, 335–340.

(104) E. Larsen and G. N. La Mar, "The Angular Overlap Model. How to Use it and Why", *Journal of Chemical Education*, 1974, **51**, 633–640.

(105) S. M. Woodley, C. R. A. Catlow, J. D. Gale, and P. D. Battle, "Development of a New Force Field for Open Shell Ions: Application to Modelling of $\mathrm{LaMnO_3}$", *Chemical Communications*, 2000, 1879–1880.

(106) S. M. Woodley, P. D. Battle, C. R. A. Catlow, and J. D. Gale, "Development of a New Interatomic Potential for the Modeling of Ligand Field Effects", *The Journal of Physical Chemistry B*, 2001, **105**, 6824–6830.

(107) W. H. Press, S. A. Teukolsky, W. T. Vetterling, and B. P. Flannery, *Numerical Recipes*, Cambridge University Press, 3rd edn., 2007.

(108) A. Banerjee, N. Adams, and J. S. R. Shepard, "Search for Stationary Points on Surfaces", *The Journal of Physical Chemistry*, 1985, **89**, 52–57.

(109) D. Sheppard, R. Terrell, and G. Henkelman, "Optimization Methods for Finding Minimum Energy Paths", *The Journal of Chemical Physics*, 2008, **128**, 134106.

(110) G. Henkelman, B. P. Uberuaga, and H. Jónsson, "A Climbing Image Nudged Elastic Band Method for Finding Saddle Points and Minimum Energy Paths", *The Journal of Chemical Physics*, 2000, **113**, 9901–9904.

(111) R. W. Grimes, C. R. A. Catlow, and A. M. Stoneham, "A Comparison of Defect Energies in MgO Using Mott-Littleton and Quantum Mechanical Procedures", *Journal of Physics: Condensed Matter*, 1989, **1**, 7367–7384.

(112) J. M. Vail, A. H. Harker, J. H. Harding, and P. Saul, "Calculations for Electronic Point Defects with Self-Consistent Lattice Polarisation: the $\mathrm{F^+}$ Centre in MgO", *Journal of Physics C*, 1984, **17**, 3401–3414.

(113) J. H. Harding, A. H. Harker, P. B. Keegstra, R. Pandey, J. M. Vail, and C. Woodward, "Hartree-Fock Cluster Computations of Defect and Perfect Ionic Crystal Properties", *Physica B+C*, 1985, **131**, 151–156.

(114) A. H. Edwards, P. V. Sushko, A. L. Shluger, and V. B. Sulimov, "Embedding Techniques for Irradiation-Induced Defects in Crystalline SiO_2", *IEEE Transactions on Nuclear Science*, 2002, **49**, 1383–1388.

(115) J. L. Pascual and L. Seijo, "Ab initio Model Potential Embedded Cluster Calculations Including Lattice Relaxation and Polarization: Local Distortions on Mn^{2+}-Doped CaF_2", *The Journal of Chemical Physics*, 1995, **102**, 5368–5376.

(116) M. F. Guest, I. J. Bush, H. J. J. van Dam, P. Sherwood, J. M. H. Thomas, J. H. van Lenthe, R. W. A. Havenith, and J. Kendrick, "The GAMESS-UK Electronic Structure Package: Algorithms, Developments and Applications", *Molecular Physics*, 2005, **103**, 719–747.

(117) Computing for Science Ltd., *GAMESS-UK Website*, `http://www.cfs.dl.ac.uk`, 2011.

(118) J. D. Gale, *GULP Website*, `http://projects.ivec.org/gulp/`, 2011.

(119) A. A. Sokol, *Construct*, A Component of ChemShell, A program written by Alexey Sokol of University College London for generating ChemShell style QM/MM clusters., 2005.

(120) W. Jost, "Diffusion and Electrolytic Conduction in Crystals (Ionic Semiconductors)", *The Journal of Chemical Physics*, 1933, **1**, 466–475.

(121) K. A. Müller, W. Berlinger, and F. Waldner, "Characteristic Structural Phase Transition in Perovskite-Type Compounds", *Physical Review Letters*, 1968, **21**, 814–817.

(122) Q. Hui, M. G. Tucker, M. T. Dove, S. A. Wells, and D. A. Keen, "Total Scattering and Reverse Monte Carlo Study of the 105 K Displacive Phase Transition in Strontium Titanate", *Journal of Physics: Condensed Matter*, 2005, **17**, S111–S124.

(123) J. M. Kiat and T. Roisnel, "Rietveld Analysis of Strontium Titanate in the Müller State", *Journal of Physics: Condensed Matter*, 1996, **8**, 3471–3475.

(124) E. Koch, *Solving the Schrödinger Equation in One Dimension*, `http://iffwww.iff.kfa-juelich.de/~ekoch/DFT/qm1d.html`, 2011.

(125) R. C. Powell, *Symmetry, Group Theory, and the Physical Properties of Crystals*, ed. W. Beiglböck, J. Ehlers, K. Hepp, and H. Weidenmüller, Springer, 2010.

(126) K. Brandenburg and H. Putz, *Endeavour - Structure Solution from Powder Diffraction*, `http://www.crystalimpact.com/endeavour/Default.htm`, 2010.

(127) H. Putz, J. C. Schön, and M. Jansen, "Combined Method for ab initio Structure Solution from Powder Diffraction Data", *Journal of Applied Crystallography*, 1999, **32**, 864–870.

(128) R. Hundt, J. C. Schön, A. Hannemann, and M. Jansen, "Determination of Symmetries and Idealized Cell Parameters for Simulated Structures", *Journal of Applied Crystallography*, 1999, **32**, 413–416.

(129) A. Hannemann, R. Hundt, J. C. Schön, and M. Jansen, "A New Algorithm for Space-Group Determination", *Journal of Applied Crystallography*, 1998, **31**, 922–928.

(130) K. Momma and F. Izumi, "VESTA: A Three-Dimensional Visualization System for Electronic and Structural Analysis", *Journal of Applied Crystallography*, 2008, **41**, 653–658.

(131) K. Momma and F. Izumi, *VESTA Website*, `http://www.geocities.jp/kmo_mma/crystal/en/vesta.html`, 2011.

(132) D. K. Swanson and R. C. Peterson, "Polyhedral Volume Calculations", *The Canadian Mineralogist*, 1980, **18**, 153–156.

(133) Q. Zhang, T. Cagin, and W. A. Goddard III, "The Ferroelectric and Cubic Phases in $\mathrm{BaTiO_3}$ Ferroelectrics are also Antiferroelectric", *Proceedings of the National Academy of Sciences*, 2006, **103**, 14695–14700.

(134) E. Blokhin, D. Gryaznov, E. Kotomin, R. Evarestov, and J. Maier, "A Comparative Hybrid DFT Study of Phonons in Several $\mathrm{SrTiO_3}$ Phases", *Integrated Ferroelectrics*, 2011, **123**, 18–25.

(135) N. W. Thomas and A. Beitollahi, "Inter-Relationship of Octahedral Geometry, Polyhedral Volume Ratio and Ferroelectric Properties in Rhombohedral Perovskites", *Acta Crystallographica Section B*, 1994, **50**, 549–560.

(136) A. I. Lebedev, "Ab initio Calculations of Phonon Spectra in $\mathrm{ATiO_3}$ Perovskite Crystals ($\mathrm{A} = \mathrm{Ca, Sr, Ba, Ra, Cd, Zn, Mg, Ge, Sn, Pb}$)", *Physics of the Solid State*, 2009, **51**, 362–372.

(137) A. Walsh, C. R. A. Catlow, A. G. H. Smith, A. A. Sokol, and S. M. Woodley, "Strontium Migration Assisted by Oxygen Vacancies in $\mathrm{SrTiO_3}$ from Classical and Quantum Mechanical Simulations", *Physical Review B*, 2011, **83**, 220301.

(138) R. O. Bell and G. Rupprecht, "Elastic Constants of Strontium Titanate", *Physical Review*, 1963, **129**, 90–94.

(139) T. Mitsui and W. B. Westphal, "Dielectric and X-Ray Studies of $\mathrm{Ca}_x\mathrm{Ba}_{1-x}\mathrm{TiO_3}$ and $\mathrm{Ca}_x\mathrm{Sr}_{1-x}\mathrm{TiO_3}$", *Physical Review*, 1961, **124**, 1354–1359.

(140) R. Viana, P. Lunkenheimer, J. Hemberger, R. Böhmer, and A. Loidl, "Dielectirc Spectroscopy in $SrTiO_3$", *Physical Review B*, 1994, **50**, 601–604.

(141) S. B. Levin, N. J. Field, F. M. Plock, and L. Merker, "Some Optical Properties of Strontium Titanate Crystal", *Journal of the Optical Society of America*, 1955, **45**, 737–739.

(142) O. Madelung, *Semiconductors: Data Handbook*, Springer, 3rd edn., 2004.

(143) D. R. Lide, *CRC Handbook of Chemistry and Physics*, CRC Press, 89th edn., 2009.

(144) F. Cordero, A. Franco, V. R. Calderone, P. Nanni, and V. Buscaglia, "Anelastic Spectroscopy for Studying O Vacancies in Perovskites", *Journal of the European Ceramic Society*, 2006, **26**, 2923–2929.

(145) R. Meyer, R. Waser, J. Helmbold, and G. Borchardt, "Observation of Vacancy Defect Migration in the Cation Sublattice of Complex Oxides by ^{18}O Tracer Experiments", *Physical Review Letters*, 2003, **90**, 105901.

(146) A. E. Paladino, "Oxidation Kinetics of Single-Crystal $SrTiO_3$", *Journal of the American Ceramic Society*, 1965, **48**, 476–478.

(147) E. Heifets, E. Kotomin, and V. A. Trepakov, "Calculations for Antiferrodistortive Phase of $SrTiO_3$ Perovskite: Hybrid Density Functional Study", *Journal of Physics: Condensed Matter*, 2006, **18**, 4845–4851.

(148) Accelrys Software Inc., *Material Studio Website*, `http://accelrys.com/products/materials-studio/`, 2005.